Functional Electrolytes for Advanced Electrochemical Performance in Sodium and Potassium Secondary Batteries

Huan Yang

2020

Table of Contents

Chapter 1

General Introduction

1.1 Energy Storage Systems

The issue of global warming caused by the greenhouse gases declared a serious environmental issue in the latter half of the 1980s.[1] Our society is still working on reducing the emissions of CO_2 by targeting its source, such as industrial and transport systems, and even ordinary life styles critically affect the earth environment.[2] Unfortunately, the greenhouse gas emissions are expected to increase in the future due to the increasing demand for vehicles and household electricity consumption in emerging economies. The growth of awareness on the environmental deterioration problem has spurred the deployment of renewable energy, such as solar and wind power over the past decades.[3-6]

Ongoing research is directed towards alternative energy conversion and storage solutions to confront the present energy crisis.[7] Energy storage technologies are of significance to compensate for their intermittent nature and facilitate their integration into the grid. The energy storage system (ESS) based on batteries has the possibility to eventually be the alternatives as they do not have any tailpipe emissions.

The decade between 2003-2014 witnessed an exciting growth in energy storage research, some of which have rapidly evolved into viable choices for the battery industry, such as secondary batteries based on lithium, sodium, potassium, magnesium, calcium, and aluminum ions.[8-16] The comparison of selected information on the battery systems mentioned above are listed in Table 1-1.

1.2 Na and K secondary batteries

Among the secondary battery family, lithium secondary batteries have been widely studied and dominate the global secondary battery market for portable and automotive energy storage technologies. However, the applicability of Li secondary batteries [17] in the conventional application especially for the large-scale energy storage system, such as grid-scale energy storage devices, remains under debate, which is critical towards the application of load leveling for renewable energy [18]. The foreseeing shortage and the rising cost of lithium resources have led to the urging of alternative energy storage devices to relieve the heavy reliance on lithium-ion batteries (LIBs). [11, 19-21]

Sodium-ion battery (SIB) is one of the possible candidates to replace LIBs because of their relatively high energy density owing to the low Na^+/Na redox potential (–2.71 V vs. standard hydrogen electrode (SHE) [22, 23]. In particular, SIBs are emerging energy storage devices in large scale applications [24] owing to the greater availability of Na resources relative to Li ones.[22] Among ESS, SIBs are expected to precede LIBs in the near future with high natural abundance, low cost, and even distribution of sodium resources.[19]

Potassium-ion batteries (PIBs) also have a great potential as in the case of SIBs, as the redox potential of K^+/K (–2.93 V vs. standard hydrogen electrode) is lower than that of Na^+/Na (–2.71 V) and close to that of Li^+/Li (–3.04 V). This demonstrates the prospects of a battery with a competitive energy density and high voltage operation capabilities.[25-27] Although K^+ has a larger ionic radius of 1.38 Å compared to Li^+ (0.76 Å) and Na^+ (1.02 Å), it has the smallest Stokes radius in certain solvents due to the weaker Lewis acidity of K^+, which is favorable to the transport behavior within the electrolyte and charge transfer at the electrolyte–electrode interface for PIBs.[28, 29]

1.3 Electrolyte for secondary batteries

In the battery studies, the importance of electrolytes has been less valued than the electrode materials considering the most effective design and cost consideration. Among all battery components, an electrolyte is served as the medium for the transfer of charges sandwiched between positive and negative electrodes in secondary batteries. While the recent understandings about electrolytes revealed that the properties of electrolytes profoundly affect batteries performance in many aspects. The formula, structure, even the component ratio of electrolytes could dominate the Coulombic efficiency, capacity retention, rate capability, cycling efficiency, etc. at various temperatures. The properties of electrolytes, such as ionic conductivity, volatility, flammability, and compatibility with other cell components, determine the optimal cell performance in different ways. The required properties of the qualified electrolytes could be attributed to three distinct but interdependent factors: i) ion transport property, which is related to the ionic conductivity [31-34], transference number [35-39], salt diffusivity as well as activity coefficients [40, 41], ii) solvation property to metal ions (salt concentration is in the neighborhood of 1.0

mol dm^{-3} (M) [42] or highly concentrated systems [43], where the neat ionic liquid is an extreme case, iii) stability and compatibility including electrochemical window, redox product for forming solid electrolyte interphase (SEI), and safety in use, etc.

The choice of electrolyte components is affected by diverse needs, dependent on the electrode materials and operating environment in use. In addition to layout new electrolyte components, a significant contribution is required to the new understandings of interphases on both the electrodes.

1.3.1 Salt and solvent

Ideal electrolytes for secondary batteries with a metal shuttle ion commonly are generally recognized with the following requirements at any rate: i) the salt could be completely dissolved and highly dissociated in the solvent, ii) the solvated ions have high ion mobility in the solution, iii) the anion component should be stable against redox decomposition on both electrode sides and inert to electrolyte solvent, iv) both the cation and anion should remain inert to all parts in the cell and be thermally and electrochemically stable in use. Based on the vast experimental and simulative results in previous works,[44, 45] PF_6^- salts are used in the majority of current secondary battery systems owing to its advantages on well-balanced properties with battery environment and electrolyte components. Recently, the stature of PF_6^- has been shaken by the arising amount of study on bis(trifluoromethylsulfonyl)amide salt. In the past decades, tremendous efforts have been made to develop alternative salts, such as $LiBF_4$ [46], $LiAsF_6$ [47], $LiClO_4$ [48], lithium bis(fluorosulfonyl)amide (LiFSA) [49], and lithium bis(trifluoromethylsulfonyl)imide (LiTFSA) [50] in LIBs case. Among them, LiTFSA salt is potentially regarded as a good alternative to $LiPF_6$. Many comparative studies between $LiPF_6$ and LiTFSA have been reported that LiTFSA could improve both the electrochemical and thermal stabilities as an electrolyte in secondary batteries.[51, 52] Table 1-2 lists some examples of salts along with their basic physical properties.

Electrolytes for secondary batteries are provided by dissolving salts into solvents. Commercialized batteries mainly contain carbonate ester-based solvents. In order to achieve the facile ion transportation, a solvent with high relative permittivity (ε) and low viscosity (η) are required. Ethylene carbonate (EC) is widely recognized as a good solvent with a high relative permittivity, but it cannot be used by itself because of its high melting point. All cyclic esters have high relative permittivity (ε = 40-90) and rather high viscosities (η = 1.7-2.0 cP), while all acyclic esters are weakly polar (ε = 3-6) and low viscous (η =0.4-0.7 cP). As a compromise, a series of acyclic carbonate or carboxylic esters are mixed with EC to simultaneously achieve a high relative permittivity and low viscosity. The most commonly used acyclic carbonate are dimethyl carbonate (DMC), diethyl carbonate (DEC), and ethylmethyl carbonate (EMC).[35] In accordance with the demands on relative permittivity and viscosity, an ideal solvent for electrolytic solutions should meet the following favorable conditions; i) a wide liquid phase temperature range, satisfying a low melting point (T_m) and high boiling point (T_b), ii) a high safety without toxicity and high flash point (T_f), iii) an inertness at the cathode and anode and other parts of the cell during cell operation. The availability of a vast number of candidate solvents has been reported in past decades.[35, 53] The most commonly used solvents, along with their physical properties, are listed in Table 1-3 and Figure 1-1.

From a broader perspective, an interfacial stability at both the anode and cathode is required for organic solvents. As far, the major research on the interfacial behavior is recognized to be important in relation to formation of a stable SEI but still less explored, especially in operando conditions. In most cases, one can only rely on computational means to investigate how the target ion moves through the interphase and how these interphases interact with the electrolytes.

1.3.2 Ionic liquid

Organic solvent-based electrolytes are used in most secondary batteries today despite their volatility and flammability, which carries a significant risk of fire or explosion. Hence, a rational design, including high safety and long-term durability, is a current challenge for this purpose.

Ionic liquids (ILs) are exclusively composed of ionic species [54] and considered as good electrolytes to improve safety and durability issues owing to their low volatility, low flammability, and wide electrochemical window [55, 56]. The suitability of IL electrolytes in battery devices has been frequently discussed over the past decade.[57-60] ILs are now considered to be safer alternatives to conventional organic electrolytes and to be compatible with operation over a wide temperature range. The use of ionic liquid electrolytes for secondary batteries can improve safety issues and enables intermediate temperature operation for better electrochemical performance.[61-63] The intermediate temperature operation of secondary batteries could utilize waste heat and improve battery performance by enhancing ion transport and electrode reaction rates.[64, 65]

Figures 1-2 and 1-3 summarize the ionic species used for ILs, especially those of interest for application to Na secondary batteries, along with their abbreviations.[56, 61, 66-92]. Clarifying the intrinsic thermal, physical and electrochemical properties of ILs are crucial to select proper ILs for particular applications. For the application on batteries, ILs based on sulfonylamides such as FSA^- (bis(fluorosulfonyl)amide) and $TFSA^-$ (bis(trifluoromethylsulfonyl)amide) have been examined because of their relatively high ionic conductivity and superior electrochemical compatibility with battery components (e.g., Al substrate and various electrode materials)[53, 93, 94]. The FSA^- anion forms less viscous ILs than $TFSA^-$ and other chemically inert anions.[95-99] Low viscosity is required to operate energy storage devices at room-to-intermediate temperatures because of the resulting high ionic conductivity.[100, 101] The electrochemical behavior of FSA^- also enables its use as a good film provider at the negative electrode in LIBs;[102-105] advantages of the FSA-based ILs to form stable SEI have been widely recognized in both Li and Na systems, which is in contrast to the TFSA-based ILs [78, 103].

Among the ILs research field, the relatively high ionic conductivity and electrochemical stability are always the target of research, but another important challenge is extension of the liquid temperature range by improving thermal stability and reducing melting point (or disappearance of a melting point by glass formation).

1.3.3 Additive for organic electrolyte

The SEI layer is usually formed through decomposition of electrolytic solutions during the first charge/discharge cycle of a battery, and the composition of the SEI layer largely determines the performance of the battery. Addition of effective additives (even a few percent or less) decomposing during or prior to SEI formation in liquid electrolytes protects the electrode surface from further side-reactions. Improvement of the performance of additives has been widely recognized as one of the most effective way to form stable SEI.

So far, significant efforts have been dedicated to design advanced electrolytes with additives from different aspects that facilitate the formation of a robust inorganic-rich SEI on the electrode surface [106] and the optimization of additive formulation to reduce the growth rate of SEI.[107] As evidenced in the commercialized LIBs, finding a functional additive with excellent film-forming properties could be an effective and economical approach to obtain satisfactory electrochemical performance.[108-110]

1.4 Aims of Study

An improved secondary battery system, LIB, NIB, or PIB, requires a compatible and harmonious coexistence of components inside the working device. The electrolyte and its concomitant interphases serve as the essential component of any electrochemical device. Based on the backgrounds mentioned above, the present study aims at i) structural design of cation and anion in ILs to widen the operable temperature range and to develop high energy and power densities in the aspect of electrolyte formula and ii) investigation of a new additive in traditional organic electrolytes for SIBs and PIBs to improve their performance. The content of each chapter is briefly provided below.

Chapter 2 describes experimental details generally required for this thesis.

In Chapter 3, the thermal and physical behavior of Na[FSA]−[C_2C_1pyrr][FSA] (C_2C_1pyrr: *N*-ethyl-*N*-methylpyrrolidinium as shown in Figure 1-4) IL system are investigated by mixing Na[FSA] and [C_2C_1pyrr][FSA]. The relationship between viscosity and molar ionic conductivity is discussed by fractional Walden rule. The electrochemical properties of the Na[FSA]−[C_2C_1pyrr][FSA] IL are evaluated at 298 and 363 K. The charge-discharge behavior and long term cycleability of a NASICON-type cathode, $Na_3V_2(PO_4)_3$/C (NVPC) in the IL is evaluated. The NVPC/NVPC symmetric cell is employed to investigate the rate performance of this electrode material at various Na[FSA] concentrations.

In Chapter 4, structural effect of the anion in ILs is discussed between FSA^- to FTA^-, including that on the temperature range. The use of the asymmetric FTA^- is beneficial to expand the liquid phase range because asymmetric molecules hinder the ordered packing of ions to generate a crystalline phase.[111] The electrochemical properties of this IL is investigated at 298–363 K to evaluate the suitability of the IL electrolyte for wide-temperature Na secondary battery applications. The charge-discharge behavior of hard carbon in the IL is evaluated. The salt concentration dependency of the rate capability and cyclability is also examined.

The limited cycleability and inferior Coulombic efficiency of a graphite negative electrode are two major obstacles to their practical utilization in PIBs. In Chapter 5, improvement of effects of the KDFP (KPO_2F_2) additive into a typical KPF_6 organic electrolyte on interfacial properties of the graphite electrode is described. The structural variation of potassium-graphite intercalation compound by potassiation/depotassiation is studied by *ex-situ* X-ray diffraction (XRD) analysis. The SEI layer on graphite and K metal electrodes are analyzed by X-ray photoelectron spectroscopy (XPS).

In Chapter 6, the electrochemical behavior of NaDFP ($NaPO_2F_2$) as an additive in 1 M $NaPF_6$ in EC/DMC is investigated. Charge-discharge tests of a hard carbon electrode in $NaPF_6$ electrolyte with and without the NaDFP additive are carried out to evaluate rate and cycle performance. For comparison, fluoroethylene carbonate (FEC), a commonly used film-forming additive, was also tested in the same conditions.

In Chapter 7, thermal and structural properties of NaDFP are investigated. As described in the subsequent chapter, NaDFP is an effective additive to SIBs. The

NaDFP is characterized by thermogravimetric and single-crystal X-ray diffraction (SCXRD) analysis for the first time.

Table 1-1 Comparison of selected information on Li, Na, K, Mg, Ca, and Al. [8-16, 112]

Characteristics	Li	Na	K	Mg	Ca	Al
Ionic radius (Å)	0.76	1.02	1.38	0.76	0.99	0.54
Atomic mass	6.9	23.0	39.1	24.3	40.1	27.0
Density of metal (g cm^{-3})	0.534	0.968	0.862	1.740	1.540	2.700
Standard redox potential (V vs. SHE)	–3.04	–2.71	–2.94	–2.37	–2.87	–1.68
Valence	+1	+1	+1	+2	+2	+3
Elemental abundance (wt%)^{a}	0.0065	2.74	2.47	2.00	3.45	7.73
Specific capacity (mAh g^{-1})^{b}	3860	1166	685	2206	1337	2980

[a] Element distribution in the earth crust.[113] [b] Specific capacity of the corresponding metal electrode based on its charged state.

Table 1-2. Electrolytes in LIBs, SIBs, and PIBs[a]

Salt	MW	T_m / K	T_{dec} / K in solution	Corrosion	σ / mS cm^{-1} (1M at 298 K) in PC	in EC/DMC	Ref
$LiBF_4$	93.9	566	>373	N	3.4	4.9	[31] [32]
$LiPF_6$	151.9	473	≈353	N	5.8	10.7	[114]
$LiAsF_6$	195.9	613	>373	N	5.7	11.1	[115]
$LiClO_4$	106.4	509	>373	N	5.6	8.4	[114]
LiOTf	155.9	>573	>373	Y	1.7		[116]
LiFSA	186.9	408	>473	Y		12	[49] [101]
LiTFSA	286.9	507	>373	Y	5.1	9.0	[50] [117]
$NaPF_6$	167.9	575	>373	N		9.8	[118]
$NaClO_4$	122.4	747	>423	N		8.0	[119]
NaFSA	203.0	395	>473	N		9.0	[120]
NaTFSA	303.0	536	>423	N			[121]
KPF_6	184.1	848		N		11.5	[118]
KFSA	219.1	642		N		4.09	[122]

[a] MW: molecular weight, T_m: melting temperature of the neat salt, T_{dec}: decomposition temperature in solution, Corrosion: aluminium corrsion at high potential, σ: ionic conductivity. The symbols Y and N in the Corrosion column denote Yes and No to aluminium corrosion at high potential.

Table 1-3. Selected properties of some organic solvents for electrochemical devices[a] [35, 53] (see Figure 1-1 for their structures)

Solvent	MW	T_m / K	T_b / K	η / cP at 298 K	ε at 298 K	d / g cm^{-3} at 298 K
EC	88	309.4	521	1.90(313 K)	89.78	1.321
PC	102	224.2	515	2.53	64.92	1.200
BC	116	220	513	3.2	53	1.199
γBL	86	229.5	477	1.73	39	1.199
γVL	100	242	481	2.0	34	1.057
NMO	101	288	543	2.5	78	1.17
DMC	90	277.6	364	0.59(293 K)	3.107	1.063
DEC	118	198.7	399	0.75	2.805	0.969
EMC	104	220	383	0.65	2.958	1.006
EA	88	189	350	0.45	6.02	0.902
MB	102	189	375	0.6		0.898
EB	116	180	393	0.71		0.878
DMM	76	168	314	0.33	2.7	0.86
DME	90	215	357	0.46	7.2	0.86
DEE	118	199	394			0.84
THF	72	164	339	0.46	7.4	0.88

[a] MW: molecular weight, T_m: melting temperature, T_b: boiling temperature, ε: relative permittivity, d: density.

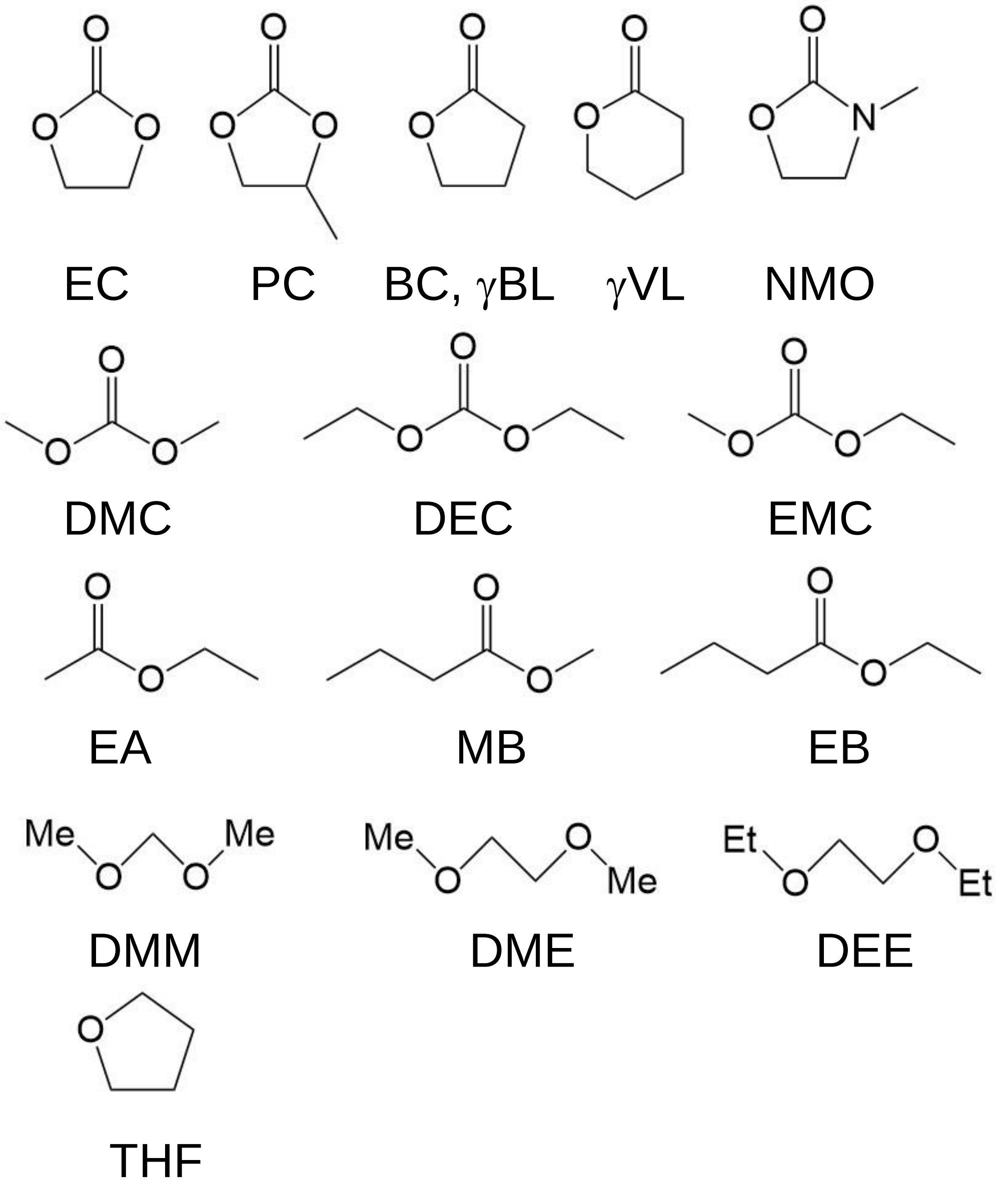

Figure 1-1 The structures of selected solvents for electrochemical devices.

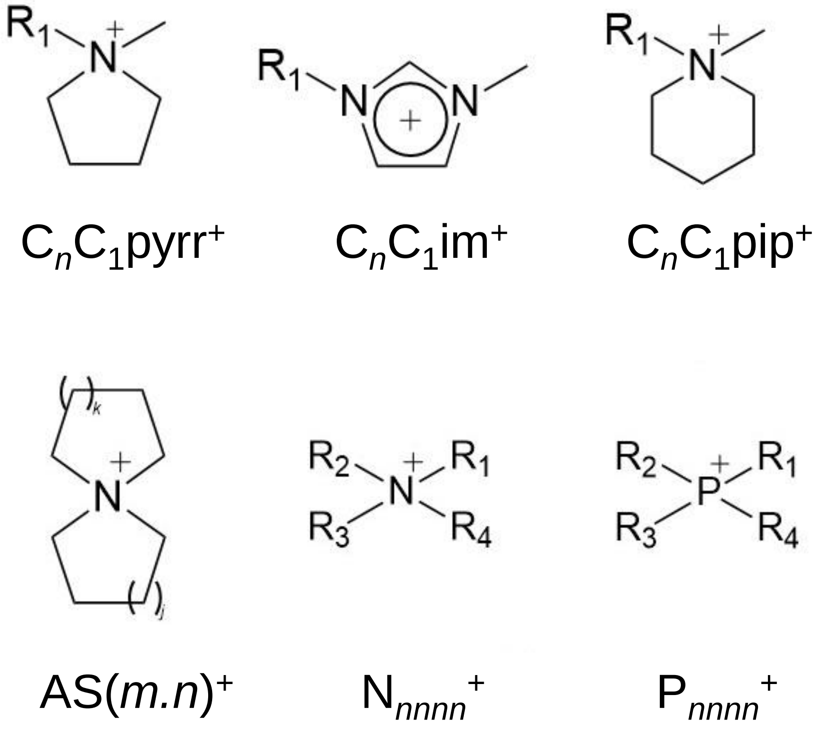

Figure 1-2 Structures of cations for ILs. Abbreviations: $C_nC_1im^+$ = 1-alkyl-3-methylimidazolium, $C_nC_1pyrr^+$ = *N*-alkyl-*N*-methylpyrrolidinium, $C_nC_1pip^+$ = *N*-alkyl-*N*-methylpiperidinium, $AS[m.n]^+$ = azoniaspiro[*m*,*n*]nonane, N_{nnnn}^+ = tetraalkylammonium, and P_{nnnn}^+ = tetraalkylphosphonium.

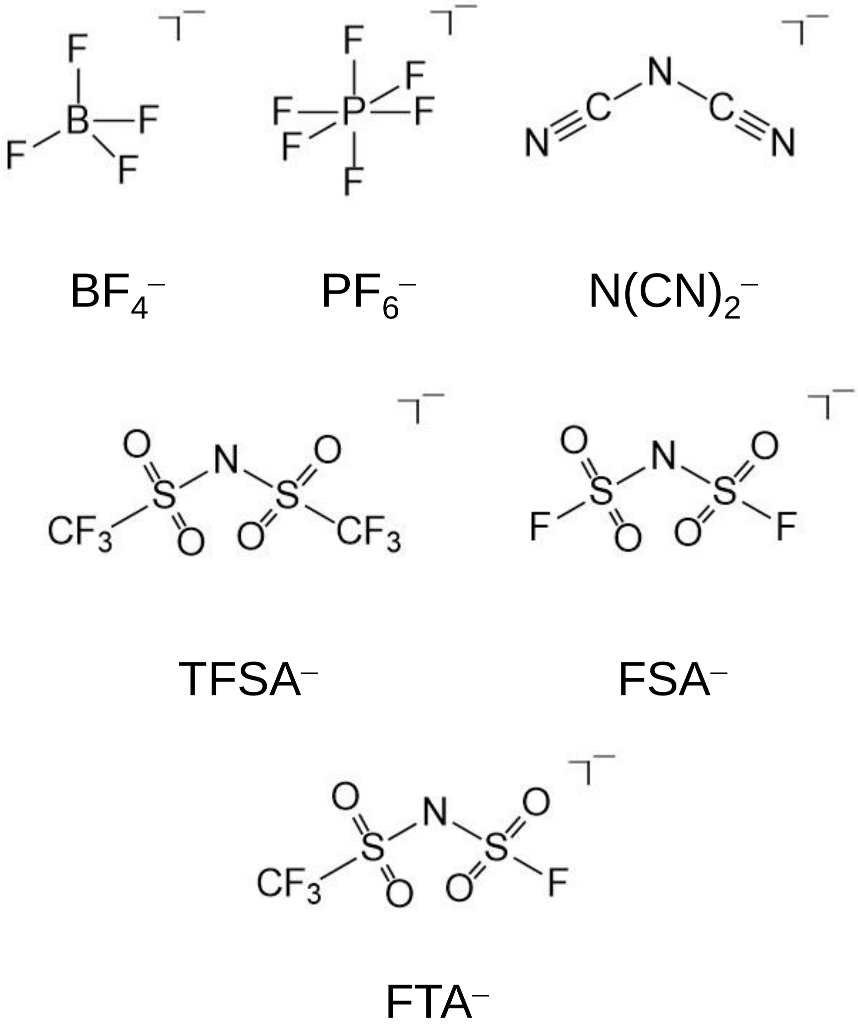

BF_4^- PF_6^- $N(CN)_2^-$

$TFSA^-$ FSA^-

FTA^-

Figure 1-3 Structure of anions for ILs. Abbreviations: FSA^- = bis(fluorosulfonyl)amide, $TFSA^-$ = bis(trifluoromethylsulfonyl)amide, and FTA^- = (fluorosulfonyl)(trifluoromethylsulfonyl)amide.

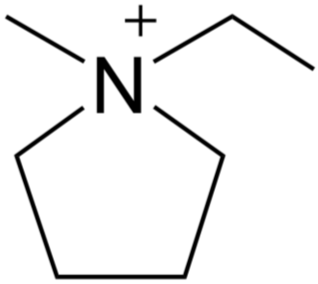

Figure 1-4 Structure of *N*-ethyl-*N*-methylpyrrolidinium cation ($C_2C_1pyrr^+$).

References

[1] A. Raval, V. Ramanathan, Nature, 342 (1989) 758-761.

[2] S. Kawatsu, J. Power Sources, 71 (1998) 150-155.

[3] G. Boyle, Renewable Energy, Open University., 2004.

[4] J. Twidell, T. Weir, Renewable Energy Resources, Routledge, 2015.

[5] H. Lund, Energy, 32 (2007) 912-919.

[6] I. Dincer, Renewable Sustainable Energy Rev., 4 (2000) 157-175.

[7] H. D. Yoo, E. Markevich, G. Salitra, D. Sharon, D. Aurbach, Mater. Today, 17 (2014) 110-121.

[8] K. Mizushima, P. Jones, P. Wiseman, J. B. Goodenough, Mater. Res. Bull., 15 (1980) 783-789.

[9] M.-S. Balogun, Y. Luo, W. Qiu, P. Liu, Y. Tong, Carbon, 98 (2016) 162-178.

[10] Y. Wen, K. He, Y. Zhu, F. Han, Y. Xu, I. Matsuda, Y. Ishii, J. Cumings, C. Wang, Nat. Commun., 5 (2014) 1-10.

[11] W. Luo, J. Wan, B. Ozdemir, W. Bao, Y. Chen, J. Dai, H. Lin, Y. Xu, F. Gu, V. Barone, Nano Lett., 15 (2015) 7671-7677.

[12] N. Singh, T. S. Arthur, C. Ling, M. Matsui, F. Mizuno, Chem. Commun., 49 (2013) 149-151.

[13] M. Wang, C. Jiang, S. Zhang, X. Song, Y. Tang, H.-M. Cheng, Nat. Chem., 10 (2018) 667-672.

[14] N. Jayaprakash, S. Das, L. Archer, Chem. Commun., 47 (2011) 12610-12612.

[15] S.-W. Kim, D.-H. Seo, X. Ma, G. Ceder, K. Kang, Adv. Energy. Mater., 2 (2012)

710-721.

[16] H. Pan, Y.-S. Hu, L. Chen, Energy Environ. Sci., 6 (2013) 2338-2360.

[17] E. A. Olivetti, G. Ceder, G. G. Gaustad, X. Fu, Joule, 1 (2017) 229-243.

[18] B. Dunn, H. Kamath, J. M. Tarascon, Science, 334 (2011) 928-935.

[19] J.-M. Tarascon, Nat. Chem., 2 (2010) 510.

[20] D. Larcher, J.-M. Tarascon, Nat. Chem., 7 (2015) 19-29.

[21] K. Matsumoto, J. Hwang, S. Kaushik, C.-Y. Chen, R. Hagiwara, Energy Environ. Sci., 12 (2019) 3247-3287.

[22] N. Yabuuchi, K. Kubota, M. Dahbi, S. Komaba, Chem. Rev., 114 (2014) 11636-11682.

[23] J. Song, B. Xiao, Y. Lin, K. Xu, X. Li, Adv. Energy Mater., (2018) 1703082.

[24] J.-Y. Hwang, S.-T. Myung, Y.-K. Sun, Chem. Soc. Rev., 46 (2017) 3529-3614.

[25] K. Lei, F. Li, C. Mu, J. Wang, Q. Zhao, C. Chen, J. Chen, Energy Environ. Sci., 10 (2017) 552-557.

[26] S. Komaba, T. Hasegawa, M. Dahbi, K. Kubota, Electrochem. Commun., 60 (2015) 172-175.

[27] J. C. Pramudita, D. Sehrawat, D. Goonetilleke, N. Sharma, Adv. Energy Mater., 7 (2017) 1602911.

[28] Y. Matsuda, H. Nakashima, M. Morita, Y. Takasu, J. Electrochem. Soc., 128 (1981) 2552-2556.

[29] L. Wang, J. Yang, J. Li, T. Chen, S. Chen, Z. Wu, J. Qiu, B. Wang, P. Gao, X. Niu, J. Power Sources, 409 (2019) 24-30.

[30] M. Faraday, Philos. Trans. R. Soc. London, (1834) 77-122.

[31] M. S. Ding, J. Electrochem. Soc., 151 (2004) A40-A47.

[32] M. S. Ding, T. R. Jow, J. Electrochem. Soc., 151 (2004) A2007-A2015.

[33] Y. Aihara, T. Bando, H. Nakagawa, H. Yoshida, K. Hayamizu, E. Akiba, W. S. Price, J. Electrochem. Soc., 151 (2004) A119-A122.

[34] M. Ding, K. Xu, S. Zhang, K. Amine, G. Henriksen, T. Jow, J. Electrochem. Soc., 148 (2001) A1196-A1204.

[35] K. Xu, Chem. Rev., 104 (2004) 4303-4418.

[36] L. Niedzicki, M. Kasprzyk, K. Kuziak, G. Żukowska, M. Armand, M. Bukowska, M. Marcinek, P. Szczeciński, W. Wieczorek, J. Power Sources, 192 (2009) 612-617.

[37] J. Zhao, L. Wang, X. He, C. Wan, C. Jiang, J. Electrochem. Soc., 155 (2008) A292-A296.

[38] A. Ghosh, C. Wang, P. Kofinas, J. Electrochem. Soc., 157 (2010) A846-A849.

[39] S. Zugmann, M. Fleischmann, M. Amereller, R. M. Gschwind, H. D. Wiemhöfer, H. J. Gores, Electrochim. Acta, 56 (2011) 3926-3933.

[40] L. O. Valøen, J. N. Reimers, J. Electrochem. Soc., 152 (2005) A882-A891.

[41] S. Stewart, J. Newman, J. Electrochem. Soc., 155 (2008) A458-A463.

[42] J. M. Bockris, A. Reddy, M. Gamboa-Aldeco, L. Peter, Platinum Met. Rev., 46 (2002) 15-17.

[43] P. Y. Zavalij, S. Yang, M. S. Whittingham, Acta Crystallogr., Sect. B: Struct. Sci., Cryst. Eng. Mater., 60 (2004) 716-724.

[44] P. Johansson, P. Jacobsson, J. Power Sources, 153 (2006) 336-344.

[45] Z. Zeng, W.-I. Liang, H.-G. Liao, H. L. Xin, Y.-H. Chu, H. Zheng, Nano Lett., 14 (2014) 1745-1750.

[46] C. Jung, Solid State Ionics, 179 (2008) 1717-1720.

[47] E. Zinigrad, E. Levi, H. Teller, G. Salitra, D. Aurbach, P. Dan, J. Electrochem. Soc., 151 (2004) A111-A118.

[48] M. Castriota, E. Cazzanelli, I. Nicotera, L. Coppola, C. Oliviero, G. A. Ranieri, J. Chem. Phys., 118 (2003) 5537-5541.

[49] A. Abouimrane, J. Ding, I. Davidson, J. Power Sources, 189 (2009) 693-696.

[50] C. W. Walker Jr, J. D. Cox, M. Salomon, J. Electrochem. Soc., 143 (1996) L80-L82.

[51] G. G. Eshetu, S. Grugeon, G. Gachot, D. Mathiron, M. Armand, S. Laruelle, Electrochim. Acta, 102 (2013) 133-141.

[52] M. Dahbi, F. Ghamouss, F. Tran-Van, D. Lemordant, M. Anouti, J. Power Sources, 196 (2011) 9743-9750.

[53] K. Xu, Chem. Rev., 114 (2014) 11503-11618.

[54] M. Watanabe, M. L. Thomas, S. Zhang, K. Ueno, T. Yasuda, K. Dokko, Chem. Rev., 117 (2017) 7190-7239.

[55] J. P. Hallett, T. Welton, Chem. Rev., 111 (2011) 3508-3576.

[56] H. Ohno, Electrochemical Aspects of Ionic Liquids, John Wiley & Sons, 2005.

[57] F. Béguin, V. Presser, A. Balducci, E. Frackowiak, Adv. Mater., 26 (2014) 2219-2251.

[58] D. R. MacFarlane, N. Tachikawa, M. Forsyth, J. M. Pringle, P. C. Howlett, G. D.

Elliott, J. H. Davis, M. Watanabe, P. Simon, C. A. Angell, Energ. Environ. Sci., 7 (2014) 232-250.

[59] M. V. Fedorov, A. A. Kornyshev, Chem. Rev., 114 (2014) 2978-3036.

[60] H. Liu, Y. Liu, J. Li, Phys. Chem. Chem. Phys., 12 (2010) 1685-1697.

[61] M. Forsyth, G. M. Girard, A. Basile, M. Hilder, D. MacFarlane, F. Chen, P. Howlett, Electrochim. Acta, 220 (2016) 609-617.

[62] K. Matsumoto, E. Nishiwaki, T. Hosokawa, S. Tawa, T. Nohira, R. Hagiwara, J. Phys. Chem. C, 121 (2017) 9209-9219.

[63] H. Yang, J. Hwang, Y. Wang, K. Matsumoto, R. Hagiwara, J. Phys. Chem. C, 123 (2019) 22018-22026.

[64] J. Hwang, K. Matsumoto, R. Hagiwara, Adv. Sustainable Syst., 2 (2018) 1700171.

[65] X. Lin, M. Salari, L. M. R. Arava, P. M. Ajayan, M. W. Grinstaff, Chem. Soc. Rev., 45 (2016) 5848-5887.

[66] M. Forsyth, H. Yoon, F. Chen, H. Zhu, D. R. MacFarlane, M. Armand, P. C. Howlett, J. Phys. Chem. C, 120 (2016) 4276-4286.

[67] N. Wongittharom, T.-C. Lee, C.-H. Wang, Y.-C. Wang, J.-K. Chang, J. Mater. Chem. A, 2 (2014) 5655-5661.

[68] R. Hagiwara, Y. Ito, J. Fluorine Chem., 105 (2000) 221-227.

[69] H. Xue, R. Verma, M. S. Jean’ne, J. Fluorine Chem., 127 (2006) 159-176.

[70] M. Galiński, A. Lewandowski, I. Stępniak, Electrochim. Acta, 51 (2006) 5567-5580.

[71] K. Matsumoto, R. Hagiwara, J. Fluorine Chem., 128 (2007) 317-331.

[72] R. Hagiwara, J. S. Lee, Electrochemistry, 75 (2007) 23-34.

[73] A. E. Visser, N. J. Bridges, R. D. Rogers, Ionic Liquids: Science and Applications, ACS Publications, 2012.

[74] K. Matsumoto, Y. Okamoto, T. Nohira, R. Hagiwara, J. Phys. Chem. C, 119 (2015) 7648-7655.

[75] D. Monti, E. Jónsson, M. R. Palacín, P. Johansson, J. Power Sources, 245 (2014) 630-636.

[76] F. Wu, N. Zhu, Y. Bai, L. Liu, H. Zhou, C. Wu, ACS Appl. Mater. Interfaces, 8 (2016) 21381-21386.

[77] C. R. Pope, M. Kar, D. R. MacFarlane, M. Armand, M. Forsyth, L. A. O'Dell, ChemPhysChem, 17 (2016) 3187-3195.

[78] T. Hosokawa, K. Matsumoto, T. Nohira, R. Hagiwara, A. Fukunaga, S. Sakai, K. Nitta, J. Phys. Chem. C, 120 (2016) 9628-9636.

[79] K. Matsumoto, R. Taniki, T. Nohira, R. Hagiwara, J. Electrochem. Soc., 162 (2015) A1409-A1414.

[80] M. Hilder, M. Gras, C. R. Pope, M. Kar, D. R. MacFarlane, M. Forsyth, L. A. O’Dell, Phys. Chem. Chem. Phys., 19 (2017) 17461-17468.

[81] K. Matsumoto, T. Hosokawa, T. Nohira, R. Hagiwara, A. Fukunaga, K. Numata, E. Itani, S. Sakai, K. Nitta, S. Inazawa, J. Power Sources, 265 (2014) 36-39.

[82] M. Hilder, P. C. Howlett, D. Saurel, E. Gonzalo, A. Basile, M. Armand, T. Rojo, M. Kar, D. R. MacFarlane, M. Forsyth, Electrochim. Acta, 268 (2018) 94-100.

[83] F. Makhlooghiazad, R. Yunis, D. Mecerreyes, M. Armand, P. C. Howlett, M. Forsyth, Solid State Ionics, 312 (2017) 44-52.

[84] C.-H. Wang, Y.-W. Yeh, N. Wongittharom, Y.-C. Wang, C.-J. Tseng, S.-W. Lee, W.-S. Chang, J.-K. Chang, J. Power Sources, 274 (2015) 1016-1023.

[85] T. Vogl, C. Vaalma, D. Buchholz, M. Secchiaroli, R. Marassi, S. Passerini, A. Balducci, J. Mater. Chem. A, 4 (2016) 10472-10478.

[86] S. Noor, N. Su, L. Khoon, N. Mohamed, A. Ahmad, M. Yahya, H. Zhu, M. Forsyth, D. MacFarlane, Electrochim. Acta, 247 (2017) 983-993.

[87] H. Yoon, H. Zhu, A. Hervault, M. Armand, D. R. MacFarlane, M. Forsyth, Phys. Chem. Chem. Phys., 16 (2014) 12350-12355.

[88] P. J. Fischer, M. P. Do, R. M. Reich, A. Nagasubramanian, M. Srinivasan, F. E. Kühn, Phys. Chem. Chem. Phys., 20 (2018) 29412-29422.

[89] S. A. M. Noor, P. C. Howlett, D. R. MacFarlane, M. Forsyth, Electrochim. Acta, 114 (2013) 766-771.

[90] S. Brutti, M. Navarra, G. Maresca, S. Panero, J. Manzi, E. Simonetti, G. Appetecchi, Electrochim. Acta, 306 (2019) 317-326.

[91] J. S. Moreno, G. Maresca, S. Panero, B. Scrosati, G. Appetecchi, Electrochem. Commun., 43 (2014) 1-4.

[92] M. Hilder, P. C. Howlett, D. Saurel, E. Gonzalo, M. Armand, T. Rojo, D. R. Macfarlane, M. Forsyth, J. Power Sources, 349 (2017) 45-51.

[93] A. Basile, M. Hilder, F. Makhlooghiazad, C. Pozo-Gonzalo, D. R. MacFarlane, P. C. Howlett, M. Forsyth, Adv. Energy Mater., 8 (2018) 1703491.

[94] X.-F. Luo, A. S. Helal, C.-T. Hsieh, J. Li, J.-K. Chang, Nano Energy, 49 (2018) 515-522.

[95] A. Best, A. Bhatt, A. Hollenkamp, J. Electrochem. Soc., 157 (2010) A903-A911.

[96] H. Yoon, P. Howlett, A. Best, M. Forsyth, D. MacFarlane, J. Electrochem. Soc., 160 (2013) A1629-A1637.

[97] A. I. Bhatt, P. Kao, A. S. Best, A. F. Hollenkamp, J. Electrochem. Soc., 160 (2013) A1171-A1180.

[98] O. Borodin, W. Gorecki, G. D. Smith, M. Armand, J. Phys. Chem. B, 114 (2010) 6786-6798.

[99] A. Budi, A. Basile, G. Opletal, A. F. Hollenkamp, A. S. Best, R. J. Rees, A. I. Bhatt, A. P. O'Mullane, S. P. Russo, J. Phys. Chem. C, 116 (2012) 19789-19797.

[100] S. M. Zakeeruddin, M. Grätzel, Adv. Funct. Mater., 19 (2009) 2187-2202.

[101] H.-B. Han, S.-S. Zhou, D.-J. Zhang, S.-W. Feng, L.-F. Li, K. Liu, W.-F. Feng, J. Nie, H. Li, X.-J. Huang, J. Power Sources, 196 (2011) 3623-3632.

[102] W. Xu, J. Wang, F. Ding, X. Chen, E. Nasybulin, Y. Zhang, J.-G. Zhang, Energ. Environ. Sci., 7 (2014) 513-537.

[103] I. A. Shkrob, T. W. Marin, Y. Zhu, D. P. Abraham, J. Phys. Chem. C, 118 (2014) 19661-19671.

[104] A. Basile, A. F. Hollenkamp, A. I. Bhatt, A. P. O'Mullane, Electrochem. Commun., 27 (2013) 69-72.

[105] M. Ishikawa, T. Sugimoto, M. Kikuta, E. Ishiko, M. Kono, J. Power Sources, 162 (2006) 658-662.

[106] L. Fan, R. Ma, Q. Zhang, X. Jia, B. Lu, Angew. Chem., Int. Ed., 58 (2019) 10500 –10505.

[107] J. Zhao, X. Zou, Y. Zhu, Y. Xu, C. Wang, Adv. Funct. Mater., 26 (2016) 8103-8110.

[108] S. Mai, M. Xu, X. Liao, J. Hu, H. Lin, L. Xing, Y. Liao, X. Li, W. Li, Electrochim. Acta, 147 (2014) 565-571.

[109] J. Self, D. S. Hall, L. Madec, J. Dahn, J. Power Sources, 298 (2015) 369-378.

[110] X. Zuo, M. Zhao, X. Ma, X. Xiao, J. Liu, J. Nan, Electrochim. Acta, 245 (2017) 705-714.

[111] S. Jeremias, M. Carewska, L. Conte, S. Passerini, G. B. Appetecchi, RSC Adv., 3 (2013) 17755-17761.

[112] M. D. Slater, D. Kim, E. Lee, C. S. Johnson, Adv. Funct. Mater., 23 (2013) 947-958.

[113] S. R. Taylor, S. M. McLennan, The Continental Crust: Its Composition and Evolution, United States: N. p., 1985.

[114] M. Schmidt, U. Heider, A. Kuehner, R. Oesten, M. Jungnitz, N. Ignat'ev, P. Sartori, J. Power Sources, 97 (2001) 557-560.

[115] L. Doucey, M. Revault, A. Lautié, A. Chaussé, R. Messina, Electrochim. Acta, 44 (1999) 2371-2377.

[116] M. Ue, S. Mori, J. Electrochem. Soc., 142 (1995) 2577-2581.

[117] L. A. Dominey, V. R. Koch, T. J. Blakley, Electrochim. Acta, 37 (1992) 1551-1554.

[118] S. Amara, J. Toulc'Hoat, L. Timperman, A. Biller, H. Galiano, C. Marcel, M. Ledigabel, M. Anouti, ChemPhysChem, 20 (2019) 581-594.

[119] J. Y. Jang, H. Kim, Y. Lee, K. T. Lee, K. Kang, N.-S. Choi, Electrochem. Commun., 44 (2014) 74-77.

[120] R.-S. Kühnel, D. Reber, C. Battaglia, ACS Energy Lett., 2 (2017) 2005-2006.

[121] G. G. Eshetu, S. Grugeon, H. Kim, S. Jeong, L. Wu, G. Gachot, S. Laruelle, M. Armand, S. Passerini, ChemSusChem, 9 (2016) 462-471.

[122] S. Liu, J. Mao, Q. Zhang, Z. Wang, W. K. Pang, L. Zhang, A. Du, V. Sencadas, W. Zhang, Z. Guo, Angew. Chem. Int. Ed., 59 (2020) 3638-3644.

Chapter 2

Experimental

2.1 Apparatus and Material Handling

Moisture and air-sensitive materials were handled in a glove box (Miwa Manufacturing Co., Ltd., MS3-P60S-N) under dried and deoxygenated argon gas (99.995%) with a gas-refining instrument. The dew point (below 193 K, monitored by 10.6 ppm) and oxygen content (below 1 ppm, monitored by Oxygen Analyzer DF-150E, General Electric Company) in the atmosphere were controlled during the experiment. Some materials which are stable to dry air were handled in a dry air atmosphere in an open dry chamber (Daikin Industries, Ltd., HRW-60AR). The dew point (below 213 K) was monitored during the experiment. All the experimental tools were washed with deionized water, acetone, or ethanol, and were completely dried in an oven at 363 K before use. The weight of electrodes and samples were measured in the glove box using electric balances (CPA225D, Sartorius; WMC25-SH, Mettler Toledo).

Figures 2-1 and 2-2 show the vacuum line and schematic drawing of the drying vessel, respectively, which were mainly used for drying the materials and impregnating separators and electrodes with ionic liquids (ILs). The vacuum line was made of corrosion-resistant stainless-steel pipes (SUS316, 1/2 inch o.d.) connected by the stainless steel unions and valves with a Kel-F (polychlorotrifluoroethylene) tip (Swagelok Co.). Tetrafluoroethylene-perfluoroalkylvinylether copolymer (PFA) tube

(1/4 inch o.d.) was used as the connecting part to a vacuum vessel. The line was connected to a rotary vacuum pump through a Pyrex glass cold trap, which was cooled down with liquid nitrogen. The pressure was monitored by Bourdon and Pirani gauges. The highest degree of vacuum was below 1 Pa in this system.

KPO_3 and KPF_6 (Aldrich, purity > 99%) were dried under vacuum for 24 h at 353 K before use. Potassium difluorophosphate, KDFP (KPO_2F_2), was synthesized by the reaction of KPO_3 and KPF_6 in the molar ratio of 2:1 by heating the starting mixture at 593 K in a platinum crucible placed in a Ni reactor over three days. The schematic illustration of the platinum crucible in a Ni reactor is shown in Figure 2-3.

2.2 Synthesis and fabrication of electrolyte

The preparative methods of two kinds of electrolyte, ILs and organic electrolyte, will be provided in each chapter with details. For the synthesis of ILs, the starting materials were dried under vacuum line for 24 h at 353 K prior to use. The synthetic process was conducted in the dry chamber. The obtained organic phase was separated from mixture and washed several times with deionized water. Then the solvent was removed by a rotary evaporator. The schematic illustration of the rotary evaporator is shown in Figure 2-4. The product was purified again by the column filling with activated alumina and ethanol. The schematic illustration of the column is shown in Figure 2-5. Then the residual activated alumina particles and other impurity in the mixture was filtered out by filter paper with a funnel. The final product was dried in vacuo at 353 K for 24 h.

2.3 Physicochemical characterizations

2.3.1 Thermogravimetry

Thermogravimetric (TG) analysis was performed using a Thermo Plus EVO II TG 8120 (Rigaku) instrument. Samples were loaded on Al pans. The measurement chamber was flashed with Ar gas for 20 minutes at a flow volume of 0.2 L min^{-1} prior to measurement. Then the measurement chamber was flashed with Ar gas and evacuated at the same time so that a flow volume of 0.1 L min^{-1} was maintained for the measurement. The temperature was elevated from 298 to 773 K at a scanning rate of 5 K min^{-1}.

2.3.2 Differential scanning calorimetry

Differential scanning calorimetry was performed by a DSC-8230 Thermo Plus EVO II Series (Rigaku Corp.). In Chapter 3, unless otherwise noted, the measurement was performed from 173 to 393 K (173 to 523 K for [C_2C_1pyrr][FSA] single salt, and 173 to 403 K for x(Na[FSA] = 0.90)) at a scanning rate of 5 K min^{-1}. In Chapter 4, the measurement was performed from 173 to 423 K at a scanning rate of 5 K min^{-1}. The samples for DSC were sealed in an airtight Al cell under the atmosphere of dry Ar. Each transition temperature was determined using the tangent intersection method.

2.3.3 Viscosity measurement

Viscosities were measured with an electromagnetically spinning viscometer EMS-100 (Kyoto Electronics Manufacturing Co., Ltd.). Samples were sealed in glass tubes with a spherical Al probe (2 mm in diameter) in the glove box. The Al probe was immersed in *ca.* 1 mL electrolyte sample and set in the attached thermostatic chamber. The temperature was varied from 403 to 303 K at an interval of 10 K. At each temperature, the glass tube was kept in the chamber for 10 min before measurement and the measurement was repeated for 10 times at each temperature.

2.3.4 Ionic conductivity

The ionic conductivity was measured by an AC impedance technique using a 3532-80 impedance analyzer (Hioki E.E. Corp.). Samples were sealed in a T-shaped cell with two stainless steel disc electrodes in the glove box and placed in a temperature-controlled thermostatic chamber (SU-242, ESPEC). The schematic illustration of the T-shaped cell is shown in Figure 2-6. The frequency was set from 20 kHz to 100 Hz. Ionic conductivity, σ, was calculated by the Eq. 2-1, where R is the measured resistance, and K is the constant of the T-shaped cell obtained by measuring the resistance of 5 wt% KCl aqueous solution at 298 K. The value of constant K is 12.85 cm^{-1}.

$$\sigma = {}^{K}\!/_{R} \tag{2-1}$$

The temperature was varied from 363 K to 273 K at an interval of 10 K. At each temperature, the cell was kept for 1 h before measurement.

2.3.5 Density measurement

The density was measured with an oscillating U-tube density meter (DMA 4500 M, Anton Paar GmbH). Tetradecane (Wako Pure Chemical Industries, purity >99%) was used as a standard due to its stability upon heating.

2.4 Material characterization

2.4.1 Physicochemical characterizations X-ray diffraction

The structures of prepared KDFP, NaDFP, and graphite electrode in Chapters 5 and 6 were characterized by XRD with a Rigaku SmartLab diffractometer with Ni-filtered Cu-*K*α radiation (1.5418 Å; 40 kV and 30 mA) and a silicon strip high-speed detector (Rigaku D/teX Ultra 250). For prepared KDFP and NaDFP, the well-ground sample was spread on a sample holder covered by a transparent wrap film (poly(vinyl chloride (PVC, HITACHI). For the samples of ex-situ XRD in Chapter 5, graphite electrodes were rinsed with EC/DEC to remove the electrolyte and placed in an air-tight cell with Be windows to avoid exposure to air. XRD patterns were recorded under an Ar atmosphere at room temperature.

2.4.2 Single-crystal X-ray diffraction analysis

Single-crystal X-ray diffraction was performed using the diffractometer R-axis Rapid II (Rigaku Corporation) equipped with an imaging plate area detector controlled by the program RAPID AUTO 2.40 [1]. A crystal with the size of $0.10\times0.10\times0.10$ mm^3 were mounted in quartz capillaries under the dry argon and sealed using an oxygen torch and placed to the stream of cold nitrogen. A graphite-monochromated Mo*K*α radiation (λ = 0.71073 Å; 50 kV–40 mA) was used. Data collection was performed at 113 K. Integration, scaling, and absorption corrections were performed using RAPID AUTO 2.40 software. The structure was solved using SIR-92 [2] and refined by SHELXL-97 [3] linked to Win-GX [4]. Anisotropic displacement factors were introduced for non-hydrogen atoms and hydrogen atoms were treated using an appropriate riding model.

2.4.3 Raman spectroscopy

Raman spectra were collected by DXR3 Smart Raman (Thermo Fisher Scientific) using a 532 nm diode-pumped solid-state laser for fresh and (de)potassiated graphite electrodes in Chapter 5. The samples for Raman spectroscopy were sealed in a glass cell and isolated from air.

2.4.4 X-ray Photoelectron Spectroscopy

The elemental compositions and chemical states of the SEI layer on the K metal electrode and graphite electrode were investigated by X-ray photoelectron spectroscopy (XPS; JEOL, JPS-36310, Mg $K\alpha$ source). Depth profiles of these electrodes were obtained by a combination with the Ar-ion etching apparatus. The accelerating voltage and current of etching were fixed at 800 V and 19.0 mA, respectively.

2.4.5 IR (Infrared spectroscopy)

Infrared spectra were obtained by a Fourier transform infrared spectrometer (ALPHA I, Bruker Optics Laboratories, Inc.) equipped with an attenuated total reflection (ATR) module in the dry chamber.

2.5 Electrochemical measurement

2.5.1 Three-electrode cell

A conventional three-electrode cell configuration under Ar atmosphere at 298 K with a specific working electrode, a Pt wire counter electrode, and a Ag^+/Ag reference electrode. The reference electrode is composed of Ag wire immersed in 0.05 mol kg^{-1} $AgSO_3CF_3$/electrolyte solution (0.5 M KPF_6-EC/DEC (1:1, v:v) with or without additive) filled in a glass tube with porous frit. For electrochemical stability of the electrolyte test, an Al and Pt disk electrode with 8 mm diameter were used as working electrode (Figure 2-7). For K^+ ion intercalation/deintercalation, a graphite electrode (carbon black, carboxyl methylcellulose (CMC), and styrene-butadiene rubber (SBR) at a weight ratio of 80:10:5:5) with 0.25 cm^{-2} area was used as a working electrode (Figure 2-8).

2.5.2 Coin cell

The half cells were assembled using 2032 type coin cells with a potassium / Na foil counter electrode and a graphite/hard carbon/$Na_3V_2(PO_4)_3$ working electrode. Borosilicate glass microfiber filter (Whatman GF/A, the thickness of 260 μm) was used as the separator. For IL electrolytes, the separators were impregnated with ILs under vacuum at 363 K for 1 day. For organic electrolytes, the electrolyte was added by pipette onto separators.The dosage of the electrolyte for each coin cell was around 120 μL. All the cells were assembled in the Ar-filled glove box.

In Chapter 3, a carbon-coated $Na_3V_2(PO_4)_3$ material ($Na_3V_2(PO_4)_3$:Super C65:PTFE=80:15:5, where Super C65 is a conductive additive and PTFE is a binder) was used as cathode in half cell to test the electrochemical performance of ILs. In Chapter 4, hard carbon (HC, Carbotron P, Kureha Battery Materials Japan Co., Ltd) was used as an active material. The HC electrodes were prepared in the following manner. HC (96 wt%) powder and PAI binder (4 wt%) were uniformly mixed in NMP by a solid/liquid ratio of 0.52, and the obtained slurry was coated onto Al foil. The HC electrodes were dried in vacuum at 473 K for 12 h before being transferred into an Ar-filled glove box. In Chapter 5, graphite working electrode was prepared by mixing the active material (graphite, SNO-10 (10 μm mean diameter), SEC Carbon) with carbon black, carboxyl methylcellulose (CMC), and styrene-butadiene rubber (SBR) at a weight ratio of 80:10:5:5. The slurry was then pasted onto Cu foil and dried in a vacuum oven at 383 K for 10 h before cell assembling. In Chapter 7, the HC (85 wt%) powder, AB (10 wt%), and PVDF binder (5 wt%) were uniformly mixed in NMP with a solid/liquid ratio of 0.50, and the obtained slurry was coated onto Al foil. Then, the HC electrodes were dried under vacuum at 473 K for 12 h before being transferred into an Ar-filled glove box.

2.5.3 Charge-discharge test

Galvanostatic charge-discharge properties were measured by two-electrode coin cells. The schematic illustration of the two-electrode coin cells is shown in Figure 2-9. The electrode potential was controlled and recorded by a potentiostat (Hokuto Denko Co., Ltd., HZ-5000). The operating temperature was controlled by an SU-241 thermostatic chamber (ESPEC Corp.). Galvanostatic charge-discharge tests were conducted at various current rates from 0.1C to 400C at 363 K. All the tests were started after maintaining the equilibrium state at operating temperature for 3 h.

2.5.4 Electrochemical impedance spectroscopy

Electrochemical impedance spectroscopy (EIS) measurements were carried out using a Bio-Logic VSP (Bio-Logic) at 363 K over a frequency range from 100 kHz to 1 mHz with an AC perturbation voltage of 10 mV. The temperature was controlled by an ESPEC Environment Test Chamber. The 2032-type coin cells were utilized for impedance measurements of half-cell, Na/Na symmetric cell and $Na_3V_2(PO_4)_3$/ $Na_3V_2(PO_4)_3$ symmetric cell (Figure 2-10).

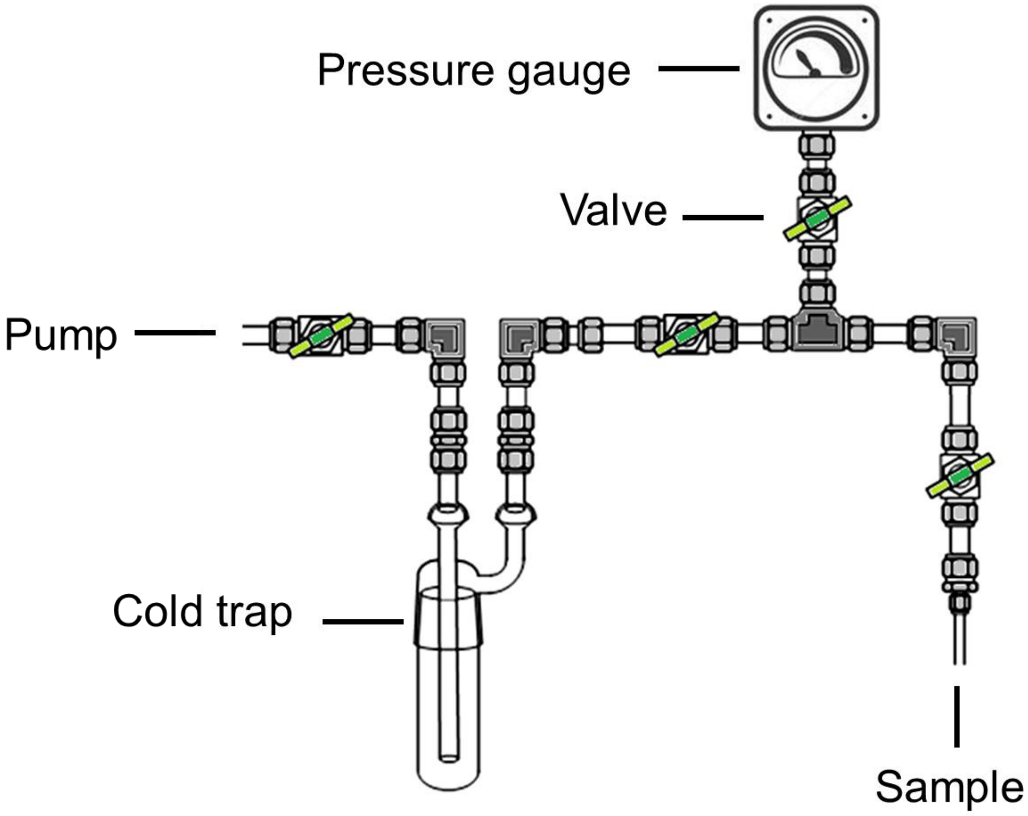

Figure 2-1 A schematic illustration of a vacuum line.

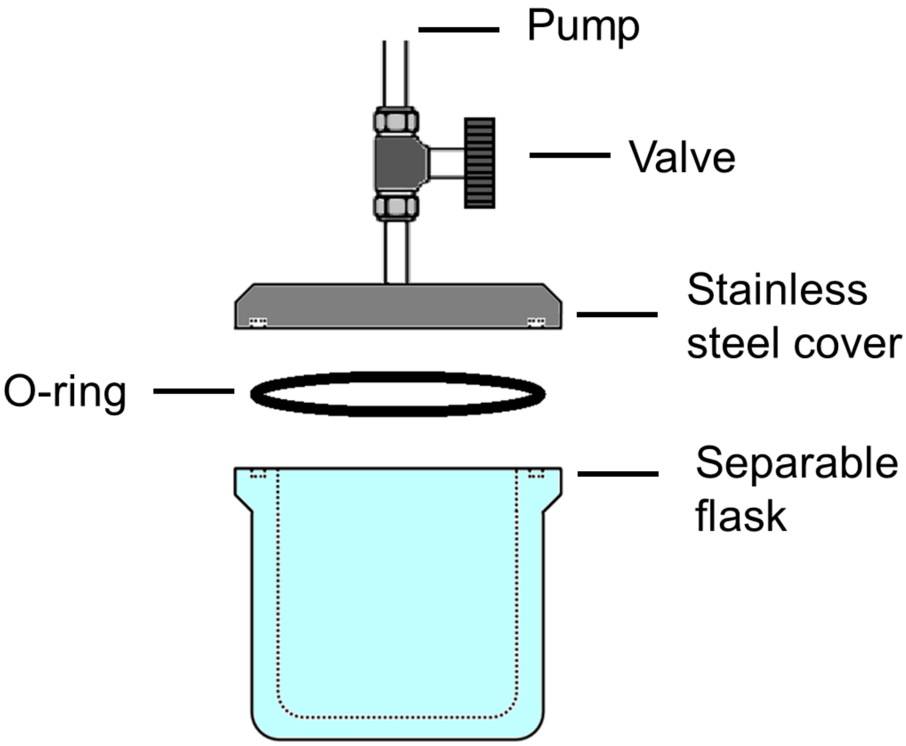

Figure 2-2 A schematic illustration of a vessel for vacuum drying.

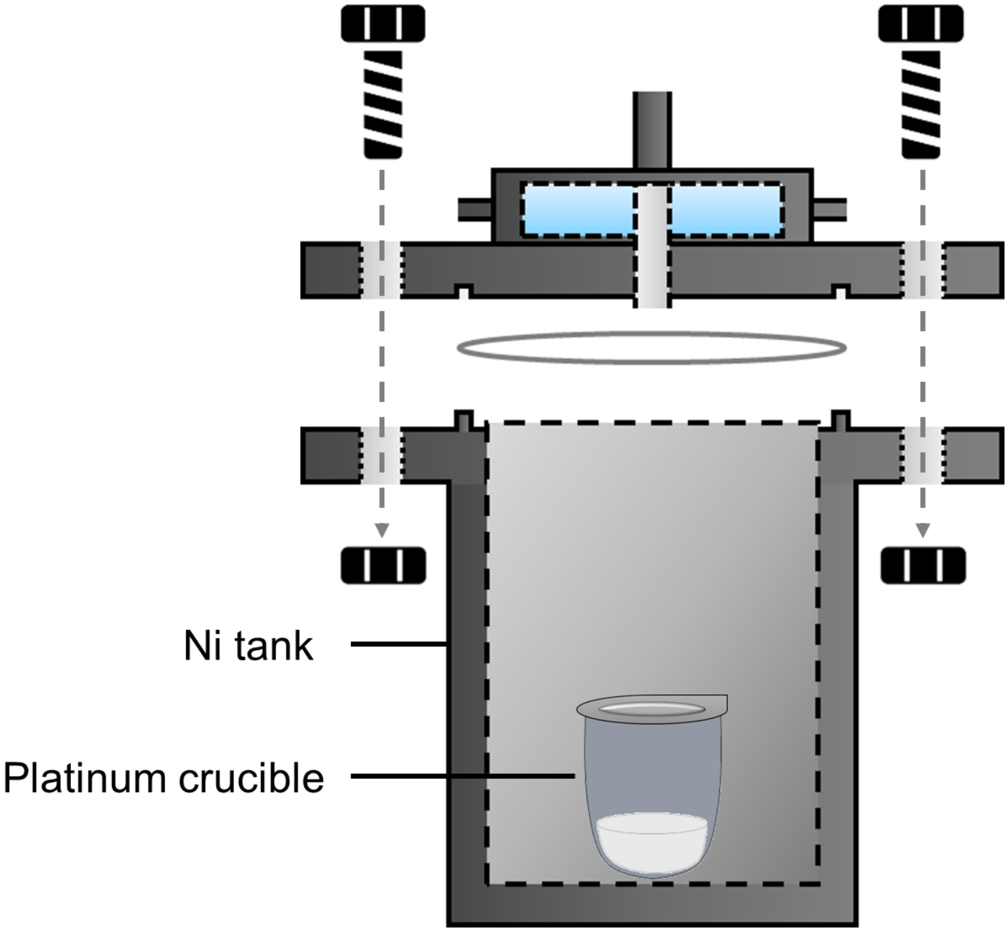

Figure 2-3 A schematic illustration of the platinum crucible in a Ni reactor.

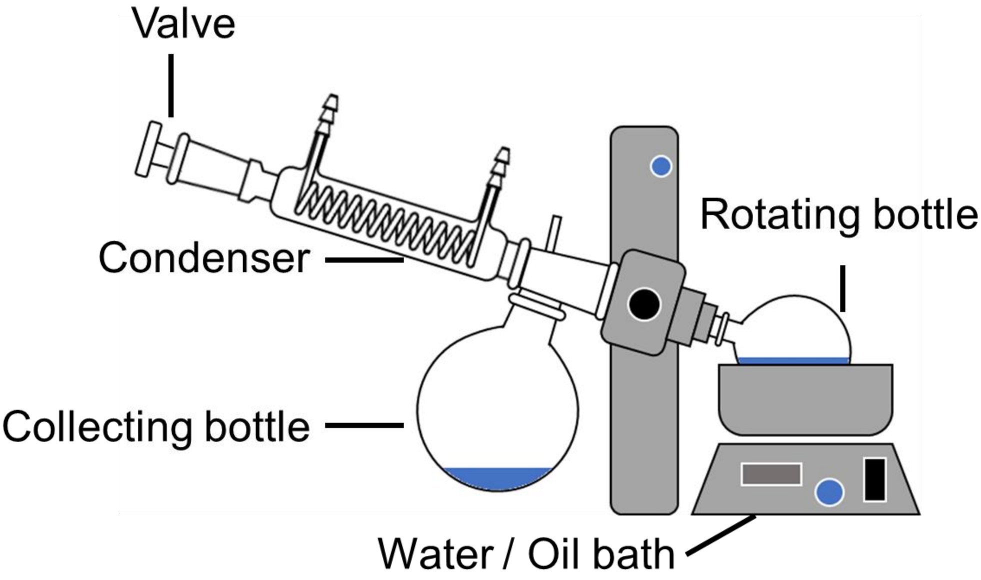

Figure 2-4 A schematic illustration of a rotary evaporator.

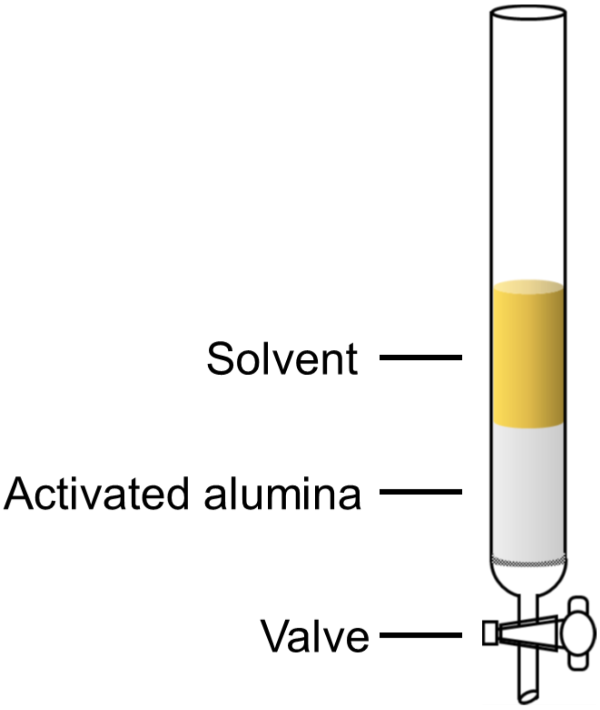

Figure 2-5 A schematic illustration of an activated alumina column.

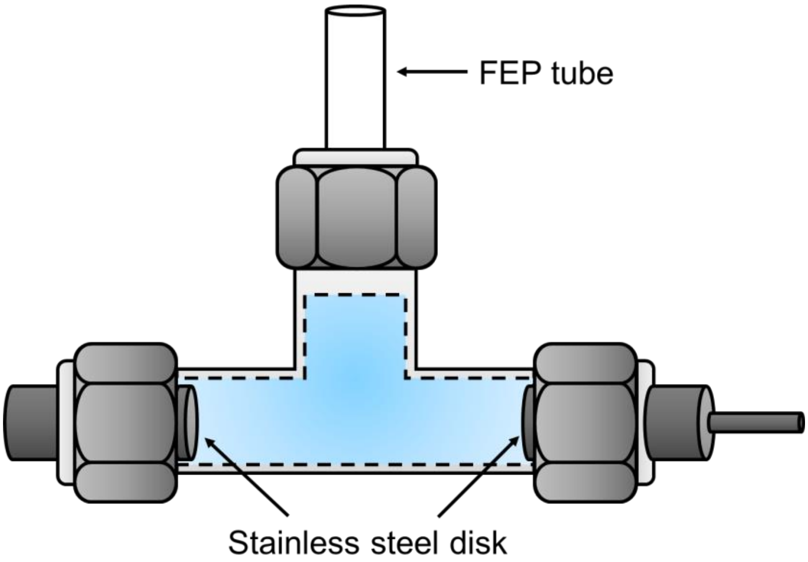

Figure 2-6 A schematic drawing of the cell for ionic conductivity measurements of solid-state samples.

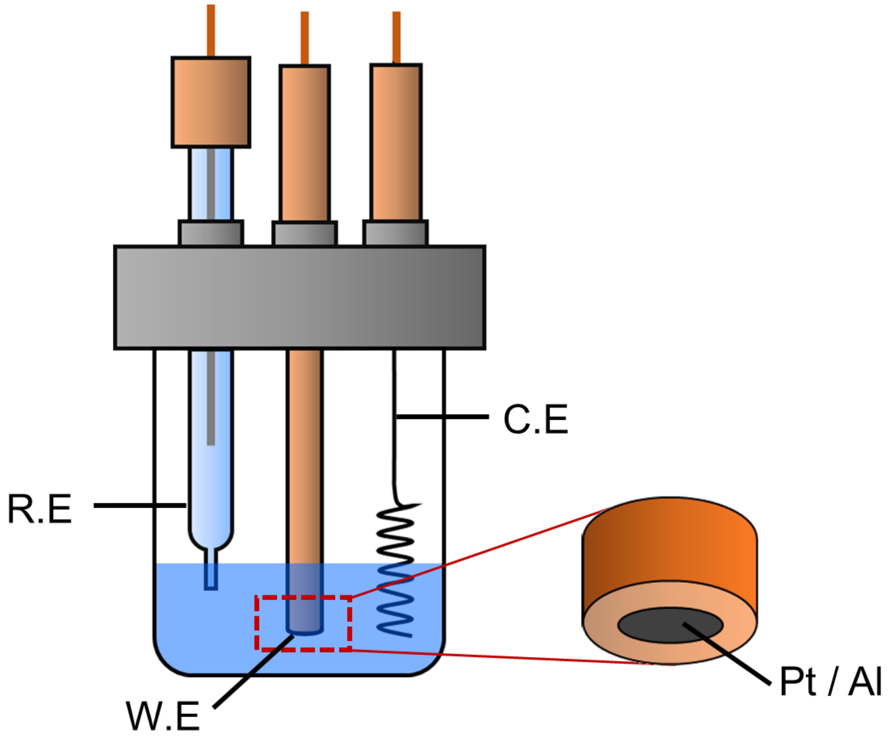

Figure 2-7 A schematic drawing of the three-electrode beaker cell for cyclic voltammetry: Pt or Al disk was used as working electrode. W.E.: working electrode, C.E.: counter electrode, and R.E.: reference electrode.

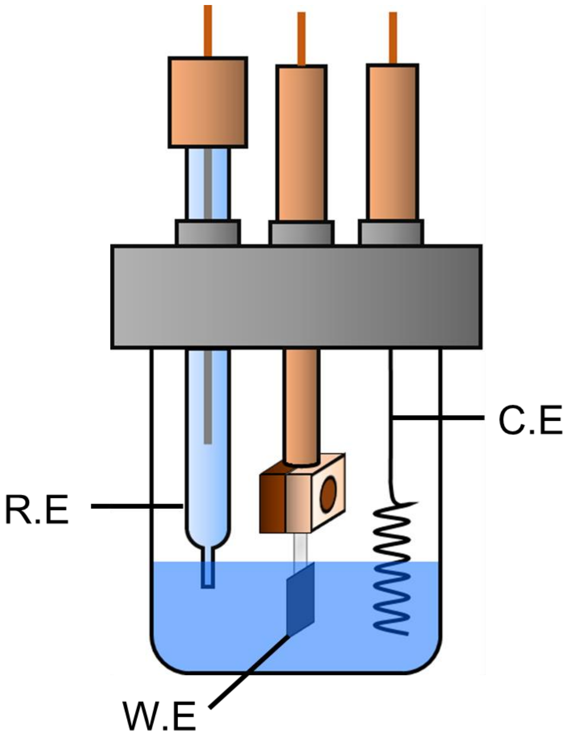

Figure 2-8 A schematic drawing of the three-electrode beaker cell for cyclic voltammetry: graphite is used as working electrode. W.E.: working electrode, C.E.: counter electrode, and R.E.: reference electrode.

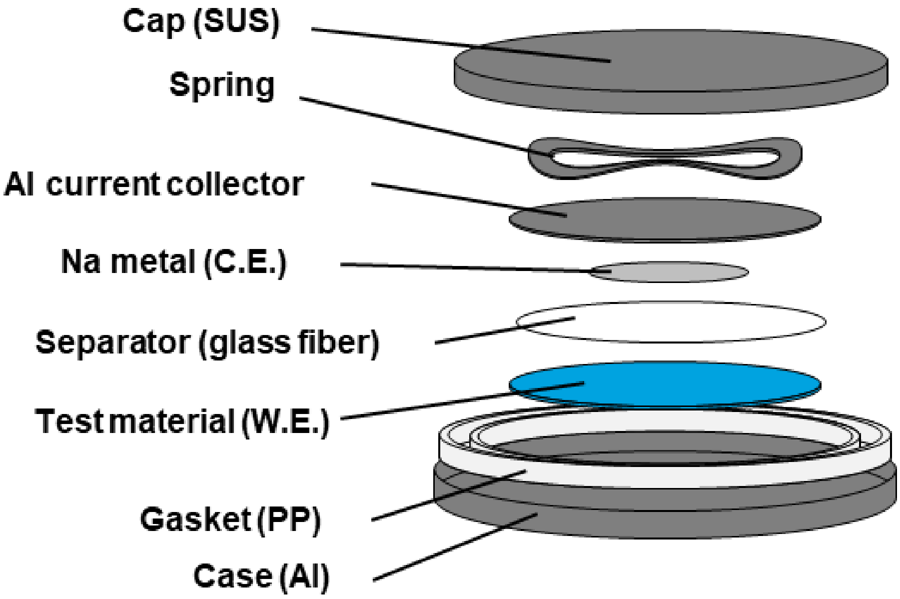

Figure 2-9 A schematic drawing of the two-electrode coin cell for galvanostatic charge–discharge tests. W.E.: working electrode, C.E.: counter electrode.

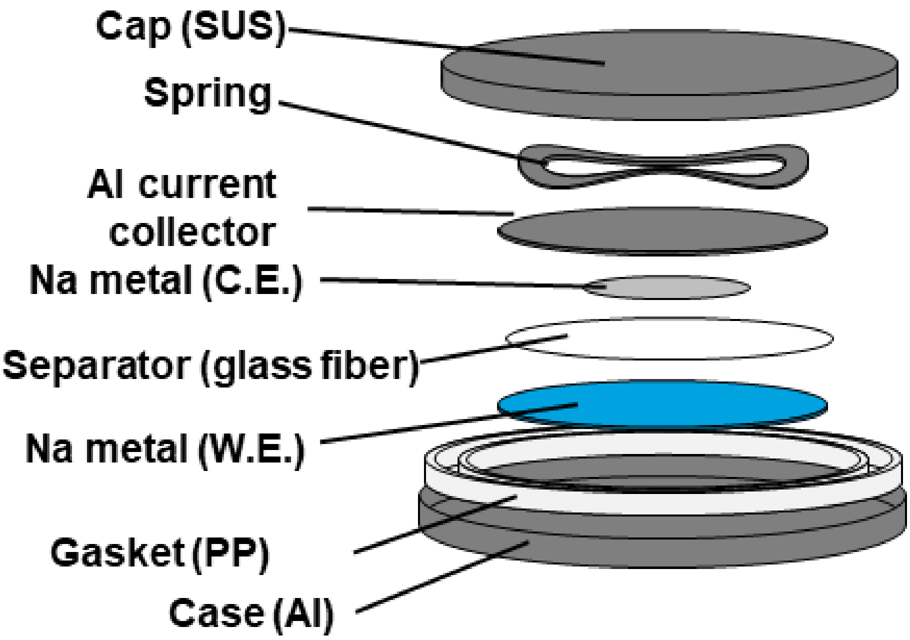

Figure 2-10 A schematic drawing of the symmetric cell with two Na metal for EIS.

References

[1] RAPID AUTO, version 2.40; Rigaku Corporation: Tokyo, Japan, 2006.

[2] A. Altomare, G. Cascarano, C. Giacovazzo, A. Guagliardi, J. Appl. Crystallogr., 26 (1993) 343-350.

[3] G.M. Sheldrick, Acta Crystallogr., Sect. A: Found. Crystallogr., 64 (2008) 112-122.

[4] L.J. Farrugia, J. Appl. Crystallogr., 32 (1999) 837-838.

Chapter 3

N-Ethyl-*N*-Methylpyrrolidinium Bis(fluorosulfonyl)amide Ionic Liquid Electrolytes for Sodium Secondary Batteries: Effects of Na Ion Concentration

3.1 Introduction

Ionic liquids (ILs) contain only ionic species and are characterized by unique properties such as non-flammability, non-volatility, high thermal and electrochemical stability, wide electrochemical windows and wide liquid temperature ranges that include room temperature.[1] These properties allow ILs to be used as electrolytes in energy-related devices such as secondary batteries, electrochemical capacitors, fuel cells and dye-sensitized solar cells.[2-8] The safety advantages of ILs are evident due to their unique properties. Bis(trifluoromethylsulfonyl)amide ($TFSA^-$) and bis(fluorosulfonyl)amide (FSA^-) are typical IL anions that possess high chemical and electrochemical stability and form salts with low melting points.[9, 10] Many ILs based on $TFSA^-$ and FSA^- have been reported to date.[11-17] Some reports claim that FSA^--based ILs form a robust solid-electrolyte interphase (SEI) on Li^0, which suppresses dendrite formation in Li batteries.[18-22]

Some physical and electrochemical investigations have described the potential of Na[FSA]–[C_3C_1pyrr][FSA] (C_3C_1pyrr: *N*-methyl-*N*-propylpyrrolidinium) and

Na[FSA]–[C_2C_1im][FSA] (C_2C_1im: 1-ethyl-3-methylimidazolium) as IL electrolytes in Na secondary batteries.[23-27] These studies have revealed that the Na mole fraction is an important factor affecting battery operation and that the optimal Na fraction depends on temperature and the electrochemical reaction.[25, 26, 28] The rate capability of positive electrode materials is more difficult to evaluate, because polarization of the Na counter electrode in a two-electrode cell is significant even at elevated temperatures.[29, 30] Evaluation of electrode materials covering a wide range of Na compositions is required to establish the optimal Na salt concentration in practical cells. This need prompted us to investigate and characterize new IL electrolytes based on $C_2C_1pyrr^+$ and FSA^-. It is notable that organic ionic plastic crystals are also attractive materials possessing a plastic crystalline phase observed over a wide temperature range, which is advantageous for its applications in electrochemical devices.[27] Organic ionic plastic crystal phase often appears along with ILs, especially in the case of onium salts with a relatively spherical cation (e.g. $C_2C_1pyrr^+$).[31] The thermal and physical properties of the Na[FSA]–[C_2C_1pyrr][FSA] system are reported in this study. A Na[FSA]–[C_2C_1pyrr][FSA] phase diagram constructed from differential scanning calorimetry (DSC) results is used to establish the optimal temperature range of the electrolyte. In addition to the basic physicochemical and electrochemical properties of Na[FSA]–[C_2C_1pyrr][FSA], we have investigated the Na metal deposition/dissolution behavior and the effects of molar fraction of Na[FSA], *x*(Na[FSA]), on the rate and cycle performance of $Na_3V_2(PO_4)_3$/C (NVPC, “C” denotes carbon coat), which is a widely studied positive electrode material in sodium secondary batteries.[32, 33] A NVPC/NVPC symmetric cell is also evaluated to address concerns regarding the effect of the Na metal counter electrode on cell performance.

3.2 Experimental

Na[FSA] (Mitsubishi Materials Electronic Chemicals Co., Ltd., purity >99%) was dried under vacuum for 24 h at 353 K prior to use. [C_2C_1pyrr][FSA] was synthesized from K[FSA] (Mitsubishi Materials Electronic Chemicals Co., Ltd., purity >99%) and [C_2C_1pyrr]Br (Sigma-Aldrich, purity 99%) by a metathesis reaction as follows.[31] The starting materials, K[FSA] (33.88 g, 154.5 mmol) (Mitsubishi Materials Electronic Chemicals Co., Ltd., purity>99%) and [C_2C_1pyrr]Br (25.00 g, 128.8 mmol) (Sigma-Aldrich, purity 99%), were separately dissolved in deionized water. K[FSA] was added dropwise to the aqueous solution of [C_2C_1pyrr]Br. The mixture was stirred at room temperature for 24 h. The precipitated viscous liquid was dissolved in dichloromethane (Wako Pure Chemical Industries, purity 99%). The organic phase was washed several times with deionized water until the Br^- content was below the detectable level by an $AgNO_3$ test. Additionally, the products were purified with an active alumna column in ethanol. The solvent was removed by a rotary evaporator and the final product was obtained by evaporation at 323 K for 48 h (yield = 70.1%). The synthetic process of [C_2C_1pyrr][FSA] is shown in Figure 3-1. The water content of [C_2C_1pyrr][FSA] measured by Karl-Fisher titration (899 Coulometer, Metrohm) was < 30 ppm. The K and Br impurity contents were below their detectable limits (K^+ < 63 ppm, Br^{-} < 1 ppm) by X-ray fluorescence (XRF) spectroscopy (Rigaku, EDX-300, at a voltage of 50 kV and current of 2 mA. Samples were sealed in a plastic cell with a proline window and placed in a He flow during measurements). Powdery Na[FSA] and waxy $[C_2C_1pyrr][FSA]$ were weighed to the desired molar ratio and mixed together. The mixture was completely dissolved in super-dry acetonitrile (Wako Pure Chemical Industries, purity 99.5%, H_2O <10 ppm). The solvent was removed under vacuum at 333 K to obtain a homogeneous sample. All the samples were stored in the glove box at room temperature.

Charge/discharge behavior was measured using a HJ1001SD8 device (Hokuto Denko) following storage of the cells at a target temperature in the thermostatic chamber for at least 3 h. Electrochemical stability was examined using a VSP-300 electrochemical system (Bio-Logic) using a two-electrode coin cell comprising a Pt- or Al-plate working electrode (13-mm in diameter, 0.20-mm in thickness) and a Na metal counter electrode. Cyclic voltammetry was performed at 5 mV s^{-1} at 298 and 363 K. Sodium deposition/dissolution was performed at a current density of 0.1 mA cm^{-2} in Na[FSA]-$[C_2C_1pyrr][FSA]$ electrolyte with x(Na[FSA]) = 0.3–0.7 at 298 and 363 K using Al working and Na counter electrodes. 0.08 C cm^{-2} Na metal was deposited on the Al substrate, and 0.02 C cm^{-2} Na dissolution/deposition was repeated until the electrode potential reached 0.5 V vs. Na^{+}/Na during dissolution. The average cycle efficiency of Na deposition/dissolution ($\varepsilon_{\mathrm{cycle}}$) is described by Eq. 3-1:

$$\varepsilon_{\mathrm{cycle}} = N_{\mathrm{eff}} \cdot Q_{\mathrm{cycle}} / (Q_{\mathrm{ex}} + N_{\mathrm{eff}} \cdot Q_{\mathrm{cycle}}) \tag{3-1}$$

where N_{eff} is the number of cycles until the electrode potential reaches 0.5 V vs. Na^+/Na, Q_{cycle} is the electric charge for Na deposition/dissolution (0.2 C cm^{-2}), and Q_{ex} is the extra amount of electricity theoretically unused (0.8 C cm^{-2}). The cathode in the half-cell for rate and cycle tests was the carbon-coated $Na_3V_2(PO_4)_3$ material ($Na_3V_2(PO_4)_3$:Super C65:PTFE=80:15:5, where Super C65 is a conductive additive and PTFE is poly-(tetrafluoroethylene), a binder) reported in previous work.[34] NVPC served as the anode and cathode in the symmetric cell used to determine the influence of the anode on the half-cell performance. The theoretical capacities of NVPC serving as a positive or negative electrode via the V^{3+}/V^{4+} and V^{3+}/V^{2+} redox reactions are unequal (117.6 mAh g^{-1} and 55.0 mAh g^{-1}, respectively). Thus, a positive-to-negative mass loading ratio of 1:2.5 was used to maintain capacity at the negative electrode. Mass loadings of 1.2 and 3.0 mg cm^{-2} were used for the positive and negative electrodes, respectively (0.785 cm^2 area for both the electrodes).

3.3 Results and Discussion

The thermal stability of Na[FSA]–[C_2C_1pyrr][FSA] was investigated by TG (see Table 3-1 and Figure 3-2). The [C_2C_1pyrr][FSA] single salt exhibits a thermal decomposition temperature of 578 K based on a 5 wt% loss, which is similar to the reported value (576 K).[31] The 1:1 mixture exhibits a small decrease in weight near 430 K, which is followed by a small step loss at 485 K and a major decrease at 530 K (Figure 3-2). The mixture has a lower decomposition temperature than the single salt, which accords with the accelerated decomposition of [C_2C_1pyrr][FSA] in the presence of Na^+ that is attributed to the lower decomposition temperature of neat Na[FSA].[34, 35]

The phase behavior of Na[FSA]–[C_2C_1pyrr][FSA] at x(Na[FSA]) = 0–1.0 was investigated by DSC (Figure 3-3 and Table 3-2). Figure 3-4 shows the phase diagram of the Na[FSA]–[C_2C_1pyrr][FSA] system. The upper limit of DSC measurements was 393 K except for neat [C_2C_1pyrr][FSA], because decomposition of the 1:1 mixture begins at approximately 400 K according to TG analysis. Thus, T_m cannot be determined at x(Na[FSA]) = 0.10–0.25, and a dashed line is drawn to illustrate the behavior in this region. The DSC curve of the [C_2C_1pyrr][FSA] single salt exhibits solid-solid phase transitions at 205 and 257 K upon heating, followed by melting at 478 K. This behavior agrees with a previous report.[31] Samples with x(Na[FSA]) = 0.1−0.3 are sticky and waxy. These are considered to be mixtures of liquid and a plastic crystalline material based on the fact that neat [C_2C_1pyrr][FSA] forms a plastic crystal phase between 255 and 478 K.[31] No crystallization occurs at x(Na[FSA]) = 0.3−0.5, and only a glass transition is observed during DSC measurements. The glass transition temperature increases with increasing x(Na[FSA]) in the range of x(Na[FSA]) = 0.3−0.9. As previously proposed for ILs,[36] the glass transition temperature correlates with ionic motion and conductivity. This trend is observed in the present case, where ionic conductivity decreases with increasing x(Na[FSA]) (see below for details). A pair of transition peaks appear near 250 K at x(Na[FSA]) = 0.6 and continue to be observed at x(Na[FSA]) = 0.7−0.9. Similar behavior has been reported in the high x(Na[FSA]) range of the Na[FSA]–[C_3C_1pyrr][FSA] system [37] and has been interpreted to indicate the existence of a metastable phase [23]. The onset and end temperatures of melting, T_{m1}' and T_{m2}', for the metastable phase are listed in Table 3-2. The T_{m1}' is greater than T_{m1} at x(Na[FSA]) = 0.6−0.9. The present case suggests that the metastable phase is caused by crystallization of one of the Na[FSA] polymorphs, because analogous metastable phases are observed at similar temperatures regardless of the organic cation structure, and a variety of polymorphic behavior is known for FSA salts [37]. The remaining Na[FSA] in the solid-liquid mixture at x(Na[FSA]) = 0.7−0.9 melts above 305 K. According to this phase diagram, a broad liquid temperature range from low to intermediate temperatures is achieved at $0.3 \leq x$(Na[FSA]) ≤ 0.7. Especially, the liquid phase observed from room to intermediate temperature at x(Na[FSA]) > 0.5, which has not been in encountered in previous studies of Na[FSA]–[C_3C_1pyrr][FSA] and Na[FSA]–[C_2C_1im][FSA] systems,[23, 26] enables us to examine the effects of high Na^+ concentrations on electrode behavior.

Temperature dependences of the viscosity, ionic conductivity, and density of the Na[FSA]−[C_2C_1pyrr][FSA] system are shown in Figures 3-5, 3-6 and 3-7, respectively. Tables 3-3 and 3-4 contain experimental data for viscosity and ionic conductivity. The changes in viscosity and ionic conductivity exhibit concave and convex behavior, respectively. Temperature dependence of viscosity and ionic conductivity for the Na[FSA]–[C_2C_1pyrr][FSA] IL system obey the Vogel-Tammann-Fulcher (VTF) equation [38-40] (Eq. 3-2 and 3-3):

$$\eta(T) = A_{\eta}T^{1/2}\exp(\frac{B_{\eta}}{T-T_{0\eta}}) \tag{3-2}$$

$$\sigma(T) = A_{\sigma}T^{-1/2}\exp(-\frac{B_{\sigma}}{T-T_{0\sigma}}) \tag{3-3}$$

where η and σ are viscosity and ionic conductivity, respectively, and A_{η}, B_{η}, $T_{0\eta}$, A_{σ}, B_{σ}, *and* $T_{0\sigma}$ are refined VTF parameters as shown in Tables 3-5 and 3-6. ($R^2 > 0.99$). The ionic conductivity at Na[FSA] = 0.3 is 1.39 mS cm^{-1} at 298 K and increases to 23.72 mS cm^{-1} at 363 K. These values are similar to those of Na[FSA]–[C_3C_1pyrr][FSA] at the same composition and temperature (e.g., 1.9 mS cm^{-1} at x(Na[FSA]) = 0.3 at 298 K),[26] whereas the imidazolium-based Na[FSA]–[C_2C_1im][FSA] system yields higher ionic conductivities (5.55 mS cm^{-1} at x(Na[FSA]) = 0.3 at 298 K).[23] The difference results from the intrinsic difference in fluidity between imidazolium- and pyrrolidinium-based ILs (8.0 and 16.6 mS cm^{-1} for [C_3C_1pyrr][FSA] and [C_2C_1im][FSA], respectively). The general trends in viscosity and ionic conductivity agree with the behavior of previous IL systems.

The density of Na[FSA]–[C_2C_1pyrr][FSA] is linearly dependent on temperature from 283 to 363 K (Figure 3-7). The density is fit to Eq. 3-4 from the refined parameters, A and B, based on the data shown in Table 3-7:

$$\rho = AT + B \tag{3-4}$$

Density decreases with increasing temperature and decreasing x(Na[FSA]). The molar concentration of Na[FSA] at different x(Na[FSA]) values in the

Na[FSA]–[C_2C_1pyrr][FSA] system is calculated from the density and formula weights summarized in Table 3-8 and Figure 3-8. The Na[FSA] molar concentration at x(Na[FSA]) = 0.7 reaches 5.42 mol L^{-1} at 298 K and 5.22 mol L^{-1} at 363 K. A large Na[FSA] concentration is advantageous since it improves electrochemical performance by increasing the supply of Na^+ ions to the electrode.

For many ionic liquids, molar ionic conductivity (λ), calculated from ionic conductivity and molar concentration, is correlated with viscosity according to the Walden rule[41-47]. Figure 3-9 shows the temperature dependence of molar ionic conductivity (λ) for the Na[FSA]–[C_2C_1pyrr][FSA] IL system with several molar fractions of Na[FSA]. If an electrolyte obeys the Walden rule, the product of its molar conductivity and viscosity is constant (Eq. 3-5).[47] Figure 3-10 shows the Walden plots of logarithmic molar conductivity versus logarithmic reciprocal viscosity. For the guide, the dash line runs from the corner to the corner of a square diagram.[41, 48] When the gradient of the Walden plot is smaller than unity, the relationship between the molar conductivity and the viscosity can be described by the fractional Walden rule, which can be expressed by Eq. 3-6:[41, 48]

$$\lambda\eta = C \tag{3-5}$$

$$\lambda\eta^{\alpha} = C' \tag{3-6}$$

where C and C' are temperature constant. The parameter α is the decoupling constant ranges from zero to unity, corresponding to the gradient of the plot. It has been reported that the parameter α is independent of temperature, pressure, ionic masses, and time; experimentally, it appears to be a function of ion size and shape.[49] Table 3-9 lists the *α* and *C′* value of the fractional Walden plot for Na[FSA]–[C_2C_1pyrr][FSA] IL system. For the Na[FSA]−[C_2C_1pyrr][FSA] ionic liquids, the value of α shows the maximum point at *x*(Na[FSA]) = 0.50 and 0.60 (0.91 for *x*(Na[FSA]) = 0.30, 0.94 for *x*(Na[FSA]) = 0.40, 0.96 for *x*(Na[FSA]) = 0.50, 0.96 for *x*(Na[FSA]) = 0.60, and 0.86 for *x*(Na[FSA]) = 0.70). These values are very similar to those reported previously for neat ionic liquids.[48, 50] The *C′* parameter corresponds to the vertical intercept in the Walden plot, and a small *C′* value means a shift of the plot to the bottom in the graph and occurs by greater association of the ions in an ionic liquid.[49] The *C′* parameter exhibits the maximum point at *x*(Na[FSA]) = 0.50. Typically, data for ionic liquids fall below the diagonal dashed line because of the strong interaction between ions in the purely ionic medium, resulting in the movement of most ions at least partially “correlated” with their immediate neighbors.[49]

Figure 3-11 shows combined cyclic voltammograms of Al (at positive and negative potentials) and Pt (positive potentials) plate electrodes in Na[FSA]-[C_2C_1pyrr][FSA] (*x*(Na[FSA])= 0.3-0.7) at 298 and 363 K in a two-electrode cell with a Na metal counter electrode. At negative potentials, the cathodic and anodic currents near 0 V vs. Na^+/Na at the Al electrode correspond to electrodeposition and electrodissolution, respectively, of Na metal. Figure 3-11 shows that the slopes of the cyclic voltammetric traces of Na deposition and dissolution increase with increasing *x*(Na[FSA]) reflect a decrease in the charge-transfer resistance, R_{ct}, of the electrode reaction. This behavior is confirmed in Figure 3-12 by the electrochemical impedance spectroscopy (EIS) results for symmetric Na/Na cells, where the radius of the semicircles in the Nyquist plots decreases with increasing x(Na[FSA]). The results are not influenced by the bulk resistance, which is small and does not significantly change as a function of x(Na[FSA]). The charge transfer resistance, R_{ct}, semicircles decrease in radius as the Na[FSA] mole fraction increases from 0.3 to 0.6, which is resulted from the sufficient Na^+ supply helps to from robust SEI protecting IL from further decomposition on the Na metal. Then the semicircle becomes large at x(Na[FSA]) = 0.7, on account of the high polarization of the Na metal counter electrode. Figure 3-11 also shows that the anodic limit, where irreversible decomposition of the IL electrolyte occurs on the Pt electrode is beyond 5.0 V vs Na+/Na. This result confirms the suitability of the system as a state-of-the-art positive electrode at 298 and 363 K.

Figure 3-13 displays the voltage profiles during Na metal deposition/dissolution in Na[FSA]-[C_2C_1pyrr][FSA] with x(Na[FSA]) = 0.3–0.7 at 298 and 363 K. The $\varepsilon_{\mathrm{cycle}}$ was evaluated according to Eq. 3-1. Figure 3-14 shows the effects of temperature and Na[FSA] mole fraction on $\varepsilon_{\mathrm{cycle}}$. An increase in temperature improves $\varepsilon_{\mathrm{cycle}}$ at all x(Na[FSA]) values. The effect of suppression of dendritic electrodeposition exceeds that of electrolyte decomposition at elevated temperatures, which results in a large $\varepsilon_{\mathrm{cycle}}$ at 363 K.[51, 52] The $\varepsilon_{\mathrm{cycle}}$ increases with increasing x(Na[FSA]) at 298 and 363 K and reaches a maximum at x(Na[FSA]) = 0.6. The formation of SEI is related to the decomposition of electrolyte on Na metal. The SEI film formed by reduction of FSA^-–based electrolytes is minimal, which accords with the fact that a high fraction of

Na^+ in the electrolyte is preferable.[22, 53] Because an increase in x(Na[FSA]) provides a stable supply of Na^+ at the electrode, the resultant inorganic compound formation is considered to facilitate SEI-layer stabilization and suppresses dendrite formation. Further analytical insights are required to confirm the SEI formation mechanism in the future. A similar interpretation was made in a previous work with a different IL system.[28] The decrease in $\varepsilon_{\mathrm{cycle}}$ at x(Na[FSA]) = 0.7 likely results from the different properties of SEI layer. This interpretation is supported by EIS results with symmetric Na/Na cells, which reveal a greater interfacial resistance at this x(Na[FSA]) level. The trend of $\varepsilon_{\mathrm{cycle}}$ in the deposition/dissolution test is different from that of Coulombic efficiency observed in the cyclic voltammetric tests (Figures 3-11). The difference in methodology, which results in the different contact period between the deposited Na metal and electrolyte, probably causes this inconsistency.

The effect of x(Na[FSA]) on the rate capability of the Na[FSA]-[C_2C_1pyrr][FSA] system was tested with Na/NVPC cells. The resulting rate capabilities at 298 and 363K are shown in Figure 3-15. Cells were charged galvanostatically at 11.7 mA g^{-1} (0.1 C) and discharged at current densities from 11.7 mA g^{-1} (0.1 C) to 4.68 $\times 10^3$ mA g^{-1} (400 C) (three cycles for each rate) followed by three 0.1 C charge–discharge cycles to confirm retention of soundness of the cell. Discharge curves of Na/NVPC cells at 363 K during rate capability tests are shown in Figure 3-16. The highest capacity is observed at x(Na[FSA]) = 0.6. The capacity difference among electrolytes with x(Na[FSA]) = 0.3–0.7 is enhanced progressively with increasing discharge rate. Discharge curves obtained at 40 C and the corresponding differential capacity vs. voltage plots (d*Q*/d*V*) are shown in Figure 3-17. Figure 3-17(a) shows that polarization is greatly alleviated by increasing *x*(Na[FSA]) from 0.3 to 0.6, which highlights the influence of *x*(Na[FSA]) on IL behavior. A similar trend has been observed for the $Na_2FeP_2O_7$ positive electrode in the Na[FSA]-[C_2C_1im][FSA] system.[29] The internal resistance, which includes the bulk and interfacial impedance, decreases with increasing Na salt concentration despite the low ionic conductivity present at high *x*(Na[FSA]).[54] Thus, the potential of the reduction peak in the d*Q*/d*V* plots during discharge moves to more positive values upon increasing *x*(Na[FSA]) from 0.3 to 0.6. At *x*(Na[FSA]) = 0.7, the rate capability diminishes and the peak in the d*Q*/d*V* plot shifts to a less positive voltage. As encountered in Na metal deposition/dissolution (Figure 3-13), this behavior results from greater polarization of the Na counter electrode at *x*(Na[FSA]) = 0.7. The capacity retention (0.1C) of all cells after testing is higher than 99% (Figure 3-15).

The stable cycling performance of Na/NVPC cells at *x*(Na[FSA]) = 0.3–0.7 and 363 K, which maintain 99.9% efficiency throughout 2000 cycles, is illustrated in Figure 3-18. The capacity retention increases with increasing *x*(Na[FSA]) until *x*(Na[FSA]) = 0.6, but decreases at *x*(Na[FSA]) = 0.7. As shown in Figures 3-19 (a) and (b), the polarization decreases with increasing *x*(Na[FSA]) until *x*(Na[FSA]) = 0.6, but increases at *x*(Na[FSA]) = 0.7 according to the discharge curves and corresponding d*Q*/d*V* plots at 70% capacity retention relative to the first cycle. Cells with Na[FSA]–[C_2C_1pyrr][FSA] electrolyte containing Na[FSA] (*x*(Na[FSA]) = 0.3, 0.4, 0.5, 0.6 and 0.7 achieve the capacity retentions of 44.4, 71.2, 79.0, 88.5, and 78.7%, respectively, after 3000 cycles at 2 C. The optimum cycling performance was achieved at *x*(Na[FSA]) = 0.6, which provides satisfactory capacity retention (80% retention after 4000 cycles) and high average coulombic efficiency (>99.5%).

As shown above and in the previous work, Na electrode polarization is significant in IL electrolytes.[29, 30] This can be greatly reduced by increasing the operating temperature, but still causes unfavorable effects at high rates. The NVPC/NVPC symmetric cells were assembled to exclude the influence of the Na metal counter electrode in the half-cell and to evaluate the effects of *x*(Na[FSA]) on NVPC electrode performance. The cathode and anode in the NVPC symmetric cell operate via the V^{3+}/V^{4+} and V^{3+}/V^{2+} redox processes described below [55]:

$$\text{(Positive) } Na_3V_2(PO_4)_3 \rightleftarrows NaV_2(PO_4)_3 + 2e^- + 2Na^+ \qquad (3\text{-}7)$$

$$\text{(Negative) } Na_3V_2(PO_4)_3 + e^- + Na^+ \rightleftarrows Na_4V_2(PO_4)_3 \qquad (3\text{-}8)$$

$$\text{(Total) } 3Na_3V_2(PO_4)_3 \rightleftarrows NaV_2(PO_4)_3 + 2Na_4V_2(PO_4)_3 \qquad (3\text{-}9)$$

Although the theoretical capacity ratio of NVPC as positive and negative electrode materials is 2.0:1.0, a 1.0:2.5 mass ratio was used in this study considering their practical capacity values. Figure 3-20 shows that the rate capability and charge–discharge curves of the NVPC/NVPC symmetric cells at *x*(Na[FSA]) = 0.3–0.7, at 363 K. The rate capability increases monotonously with increasing *x*(Na[FSA]) from 0.3 to 0.7. Although the values at *x*(Na[FSA]) = 0.6 and 0.7 are comparable, the discharge capacity at *x*(Na[FSA]) = 0.7 slightly exceeds that at

x(Na[FSA]) = 0.6. The change of coordination environment of the sodium ion as pointed out in the previous work [25] would be one of the factors on this behavior. This clearly demonstrates that the half-cell test using a Na metal counter electrode cannot evaluate the performance of a target material in the present system, and the large Na[FSA] mole fraction provides an advantage in rate capability at 363 K. It should be noted that the present rate capabilities include the contribution of the redox activity of V^{3+}/V^{2+} on the anode side in addition to that of V^{4+}/V^{3+} on the cathode side. However, the rate results could reflect the V^{4+}/V^{3+} contribution to the capacity retention is more than the case for the Na/NVPC half-cell, considering the smaller R_{ct} of the NVPC/NVPC symmetric cell than that of the Na/Na symmetric cell (Figure 3-21).

3.4 Conclusions

The thermal, physical, and electrochemical properties of the binary Na[FSA]-[C_2C_1pyrr][FSA] system have been investigated. A phase diagram constructed from DSC results reveals that a wide temperature range over 100 K around room temperature is achieved at a broad compositions of $0.3 \leq x$(Na[FSA]) ≤ 0.7. Valid VTF and Walden plot behavior was established. Sodium deposition/dissolution cycling efficiency increases with increasing temperature and increasing x(Na[FSA]) at $0.3 \leq x$(Na[FSA]) ≤ 0.6. The Na ion concentration in the IL significantly influences the rate and cycle capability of a Na/NVPC half-cell. The optimum electrochemical performance of a Na[FSA]–[C_2C_1pyrr][FSA] half-cell operating at 363 K occurs at 60 mol% Na[FSA] and is characterized by superior charge/discharge rates under various operating conditions with good cycling stability over 4000 cycles. NVPC symmetric cell rate tests indicate that the half-cell test using Na counter electrode is not fully appropriate for evaluating the rate capability of NVPC and that the Na[FSA]–[C_2C_1pyrr][FSA] system based on V^{3+}/V^{4+} and V^{2+}/V^{3+} activities improves rate capability upon increasing Na[FSA] from 0.3 to 0.7. The high Na ion concentration in the Na[FSA]–[C_2C_1pyrr][FSA] system allows the application of this IL electrolyte as high-rate Na secondary batteries especially under an environment with waste heat.

Table 3-1. Decomposition temperature (T_d) of Na[FSA], [C_2C_1pyrr][FSA], and Na[FSA]–[C_2C_1pyrr][FSA] (x(Na[FSA]) = 0.50)[a]

	T_d / K
Na[FSA]	587
[C_2C_1pyrr][FSA]	578
Na[FSA]–[C_2C_1pyrr][FSA] (x(Na[FSA]) = 0.50)	485

[a] T_d was determined as the temperature where the weight loss was 5 %.

Table 3-2. Thermal properties of the Na[FSA]–[C_2C_1pyrr][FSA] system^a

x(Na[FSA])	T_g / K	$T_{s–s}$ / K	T_{m1} / K	T_{m2} / K	T_{m1}'/ K	T_{m2}'/ K
0	n.d.	205 & 257	474	480	n.d.	n.d.
0.10	n.d.	205 & 257	n.d.	n.d.	n.d.	n.d.
0.20	n.d.	205 & 255	n.d.	n.d.	n.d.	n.d.
0.27	n.d	206 & 258	n.d.	n.d.	n.d.	n.d.
0.30	188	n.d.	n.d.	n.d.	n.d.	n.d.
0.40	198	n.d.	n.d.	n.d.	n.d.	n.d.
0.50	211	n.d.	n.d.	n.d.	n.d.	n.d.
0.60	214	n.d.	241	266	n.d.	n.d.
0.70	216	n.d.	240	272	n.d.	n.d.
0.75	217	n.d.	242	309	254	277
0.80	218	n.d.	240	370	253	278
0.85	220	n.d.	237	386	254	277
0.90	221	n.d.	230	393	254	278
1.00	n.d.	375	391	401		

^{a} T_{m1}: the onset temperature of melting, T_{m2}: the end temperature of melting, T_{m1}': the onset temperature of melting for the metastable phase, T_{m2}': the end temperature of melting for the metastable phase, $T_{s–s}$: solid–solid transition temperature, T_g: glass transition temperature and n.d.: not detected.

Table 3-3. Viscosity (mPa s) for the Na[FSA]–[C_2C_1pyrr][FSA] IL system

Temperature / K	*x*(Na[FSA])				
	0.30	0.40	0.50	0.60	0.70
303	150	346	779	2059	5830
313	97.2	205	414	959	2300
323	66.1	130	240	495	1040
333	46.9	85.9	153	280	526
343	34.5	59.5	102	171	292
353	26.2	43.1	70.8	113	175
363	20.5	33.3	51.7	77.7	112
373	16.5	26.4	39.2	55.6	76.2
383	13.4	21.1	30.4	41.2	53.0
393	11.1	17.8	23.8	31.6	37.7
403	9.35	14.8	19.4	24.8	--

Table 3-4. Ionic conductivity (mS cm^{-1}) for the Na[FSA]–[C_2C_1pyrr][FSA] IL system

Temperature / K	x(Na[FSA])				
	0.30	0.40	0.50	0.60	0.70
283	0.76	0.36	0.14	0.04	0.01
293	1.38	0.70	0.33	0.10	0.04
303	2.33	1.23	0.65	0.24	0.11
313	3.55	2.01	1.18	0.50	0.25
323	5.01	3.08	1.96	0.93	0.50
333	6.79	4.46	3.06	1.60	0.89
343	8.91	6.20	4.51	2.53	1.48
353	11.3	8.32	6.34	3.78	2.29
363	14.0	10.9	8.56	5.43	3.35
373	16.7	13.7	11.2	7.39	4.64
383	20.2	17.2	14.2	9.71	6.21
393	23.7	20.4	17.5	12.5	8.00
403	--	25.4	21.1	15.5	--

Table 3-5. VTF fitting parameters of viscosity for the Na[FSA]–[C_2C_1pyrr][FSA] IL system

x(Na[FSA])	$10^3 \times A_\eta$ / mPa s $K^{-1/2}$	B_η / K	$T_{0\eta}$ / K
0.30	5.05	1151	148
0.40	7.56	1059	169
0.50	10.59	992	184
0.60	5.00	1194	184
0.70	2.41	1362	188

Table 3-6. VTF fitting parameters of ionic conductivity for the Na[FSA]–[C_2C_1pyrr][FSA] IL system

x(Na[FSA])	$10^{-4} \times A_\sigma$ / mS cm^{-1} K$^{1/2}$	B_σ / K	$T_{0\sigma}$ / K
0.30	1.90	837	167
0.40	6.43	1240	147
0.50	2.51	861	192
0.60	2.82	915	200
0.70	1.74	865	209

Table 3-7. Density (g cm^{-3}) for the Na[FSA]–[C_2C_1pyrr][FSA] IL system and its fitting parameters for Eq. 3-4

Temperature / K	x(Na[FSA])				
	0.3	0.4	0.5	0.6	0.7
283	1.52	1.57	1.63	1.71	1.80
293	1.51	1.56	1.63	1.70	1.79
303	1.50	1.55	1.62	1.69	1.78
313	1.49	1.54	1.61	1.68	1.77
323	1.48	1.53	1.60	1.67	1.76
333	1.47	1.52	1.59	1.66	1.75
343	1.46	1.51	1.58	1.65	1.74
353	1.46	1.51	1.57	1.64	1.73
A/10^4 gcm^{-3} K^{-1}	-8.82	-9.04	-9.38	-9.66	-10.26
B / gcm^{-3}	1.77	1.82	1.90	1.98	2.08

Table 3-8. Molar concentration (mol L^{-1}) for the Na[FSA]–[C_2C_1pyrr][FSA] IL system

Temperature / K	*x*(Na[FSA])				
	0.30	0.40	0.50	0.60	0.70
283	1.71	2.43	3.29	4.28	5.47
293	1.70	2.42	3.27	4.25	5.44
303	1.69	2.41	3.25	4.23	5.41
313	1.68	2.39	3.23	4.20	5.38
323	1.67	2.38	3.21	4.18	5.34
333	1.66	2.36	3.19	4.15	5.31
343	1.65	2.35	3.17	4.13	5.28
353	1.64	2.34	3.15	4.11	5.25
363	1.63	2.32	3.14	4.08	5.22

Table 3-9. The α *and C′* value of the fractional Walden plot for the Na[FSA]–[C_2C_1pyrr][FSA] IL system

x(Na[FSA])	α	Log (C'/S cm^2 mol^{-1})
0.30	0.91	−0.21
0.40	0.94	−0.18
0.50	0.96	−0.14
0.60	0.96	−0.21
0.70	0.86	−0.31

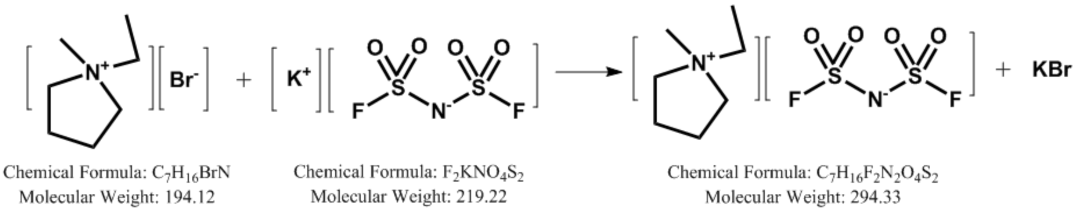

Figure 3-1. The synthetic process of [C_2C_1pyrr][FSA]

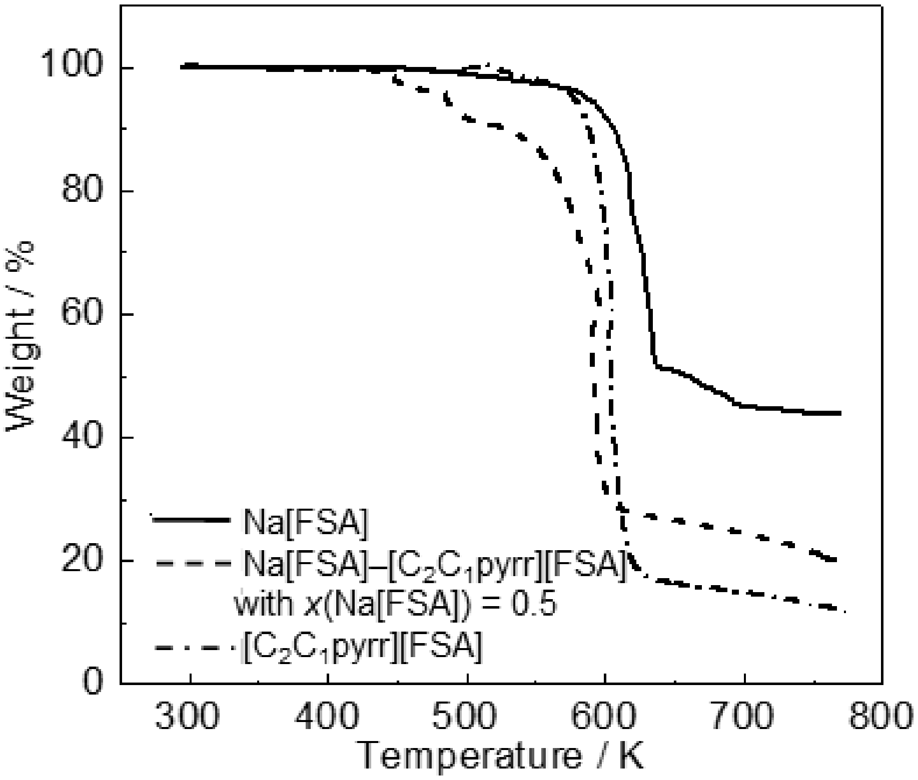

Figure 3-2. TG curves of the Na[FSA]–[C_2C_1pyrr][FSA] IL system. Scan rate: 5 K min^{-1}.

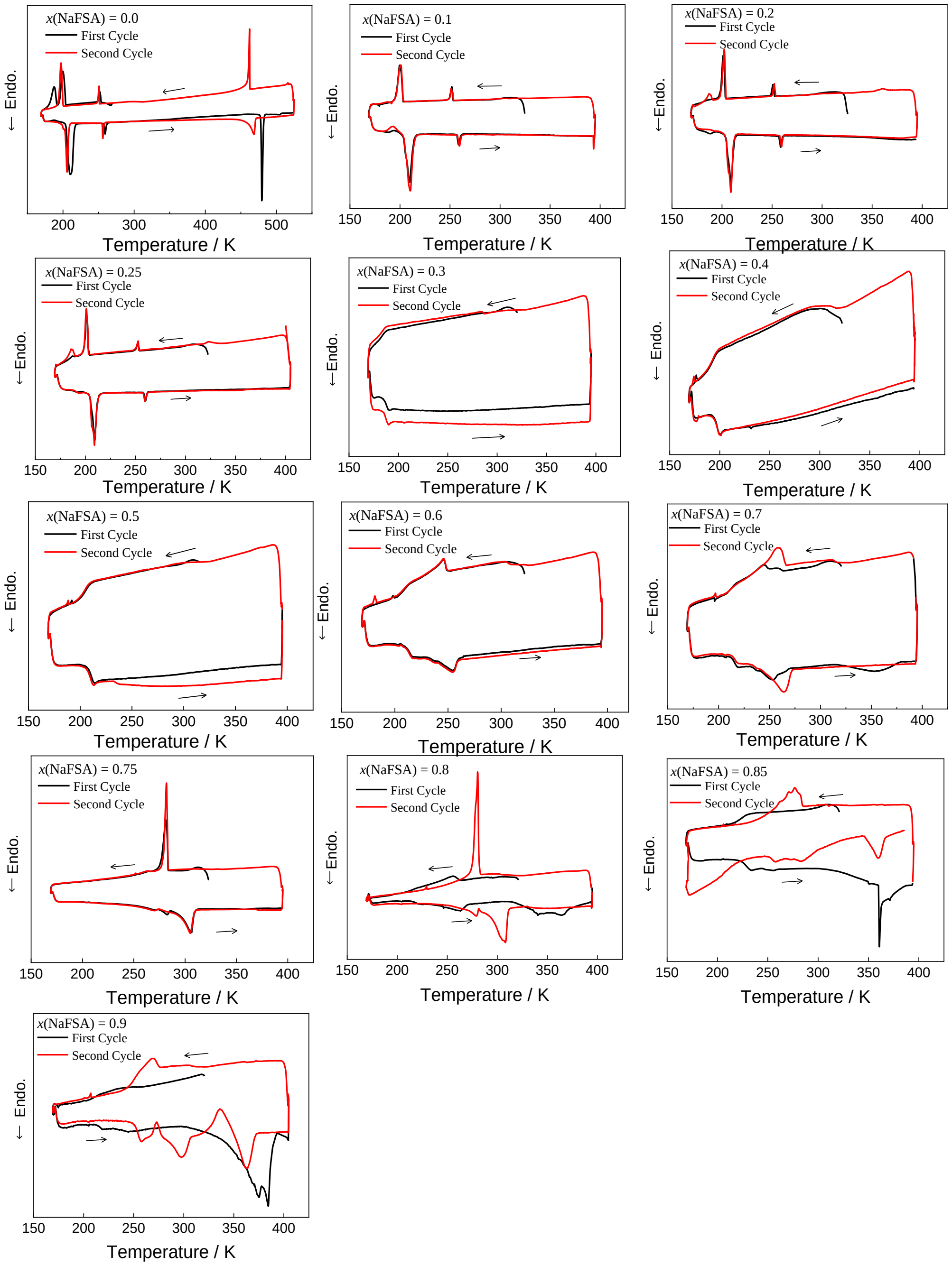

Figure 3-3. DSC curves of the Na[FSA]–[C_2C_1pyrr][FSA] system at x(Na[FSA]) = 0.0–0.9. Scan rate: 5 K min^{-1}.

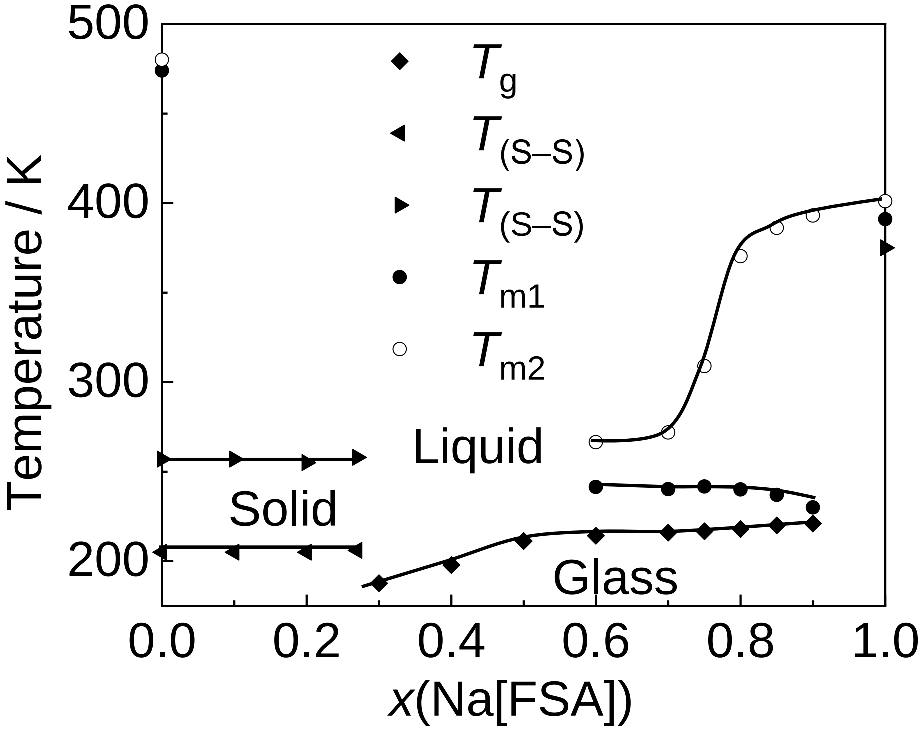

Figure 3-4. Phase diagram of the Na[FSA]-[C_2C_1pyrr][FSA] system. T_{m1}: onset temperature of melting, T_{m2}: end temperature of melting, $T_{s–s}$: solid–solid transition temperature, and T_g: glass transition temperature.

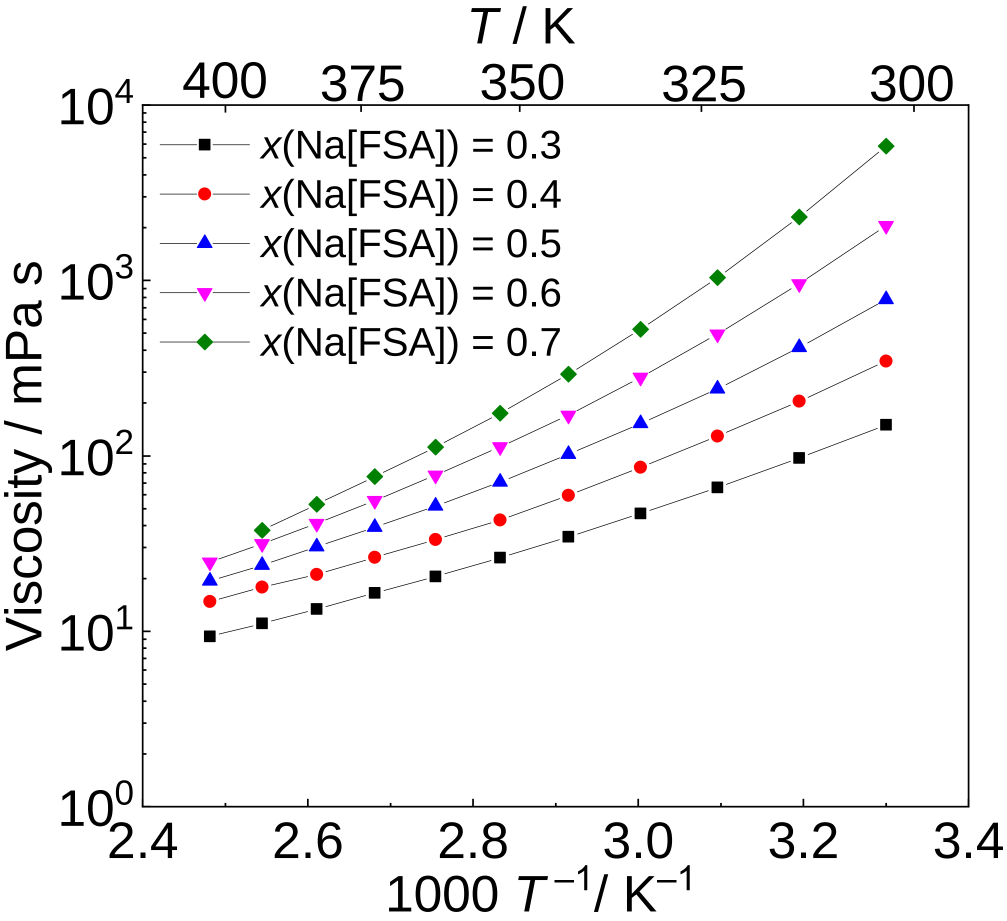

Figure 3-5. Temperature dependence of Na[FSA]–[C_2C_1pyrr][FSA] viscosity at x(Na[FSA]) = 0.30–0.70.

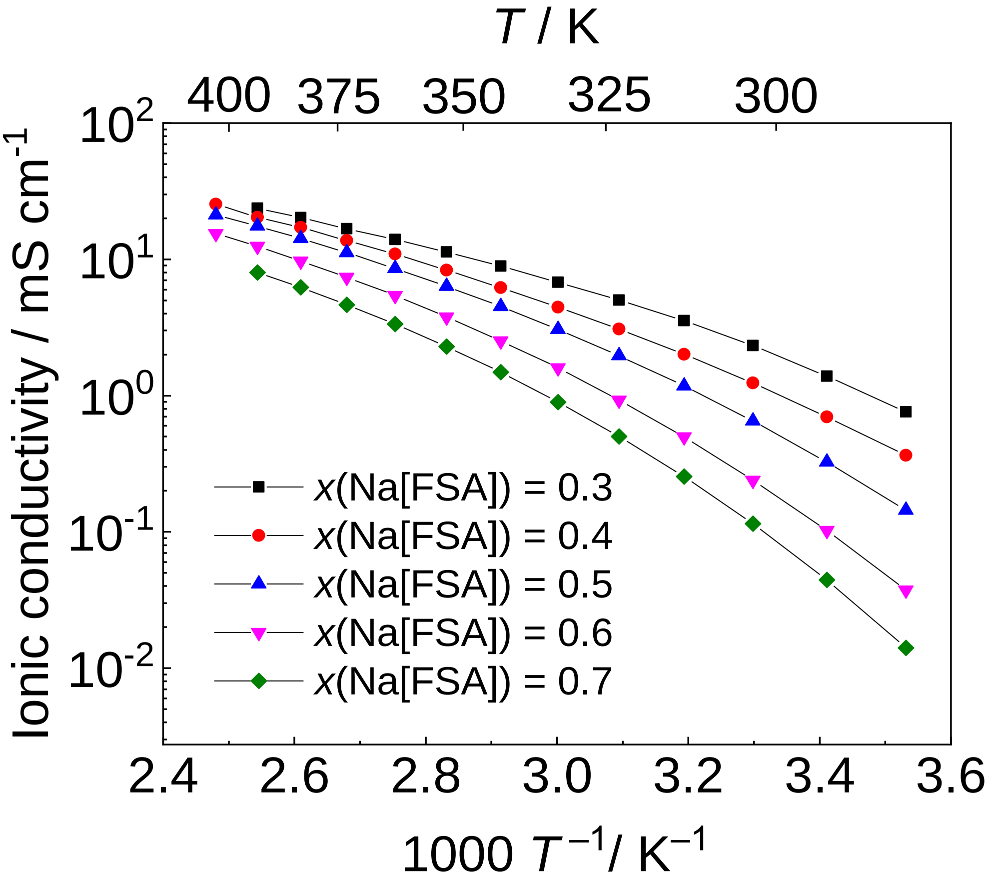

Figure 3-6. Temperature dependence of Na[FSA]–[C_2C_1pyrr][FSA] ionic conductivity at x(Na[FSA]) = 0.30–0.70.

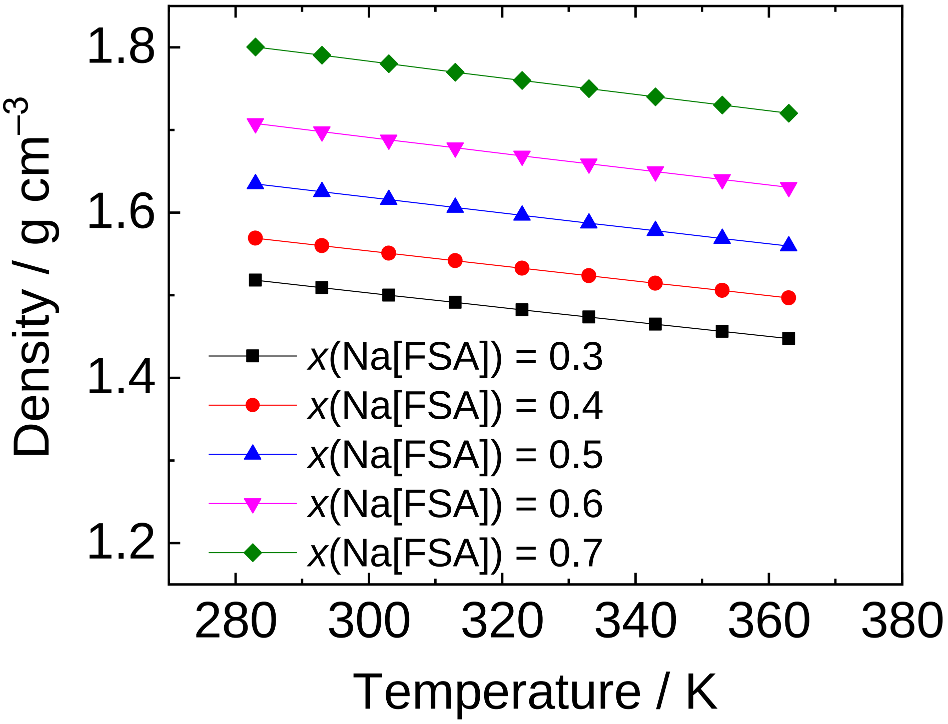

Figure 3-7. Temperature dependence of Na[FSA]–[C_2C_1pyrr][FSA] density at x(Na[FSA]) = 0.30–0.70.

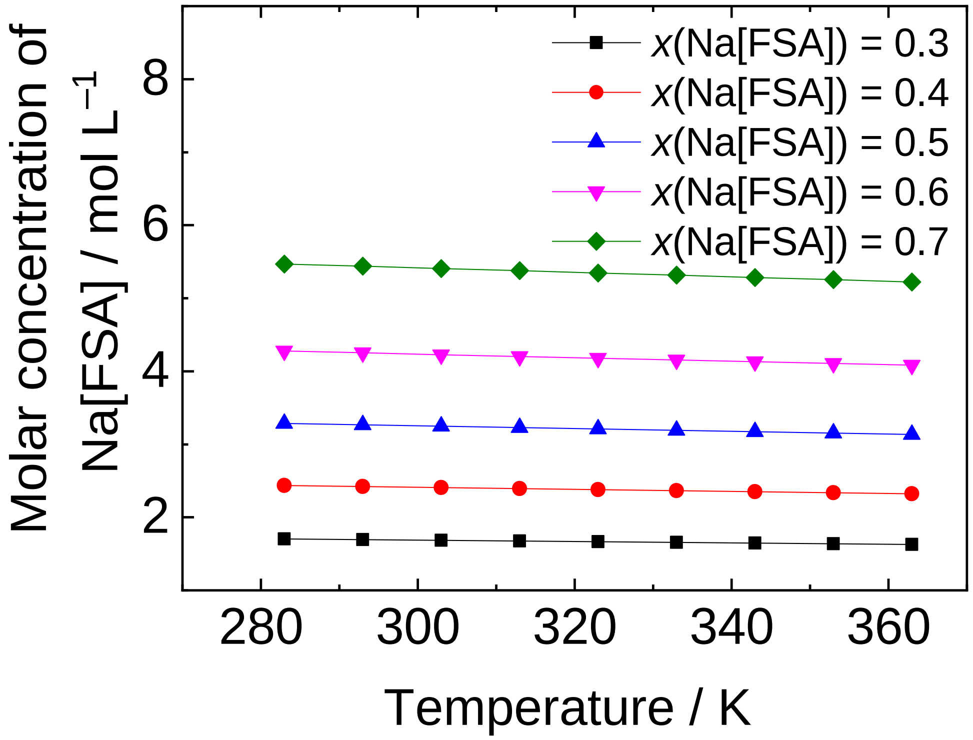

Figure 3-8. The molar concentration for the Na[FSA]–[C_2C_1pyrr][FSA] IL system.

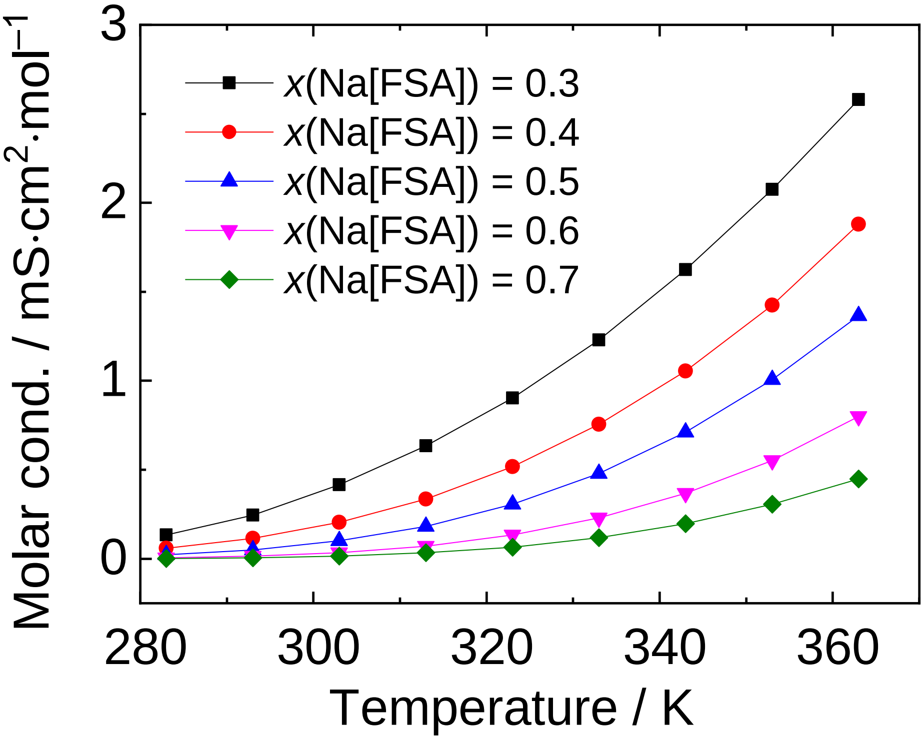

Figure 3-9 The temperature dependence of molar ionic conductivity (λ) for the Na[FSA]–[C_2C_1pyrr][FSA] IL system with several molar fractions of Na[FSA].

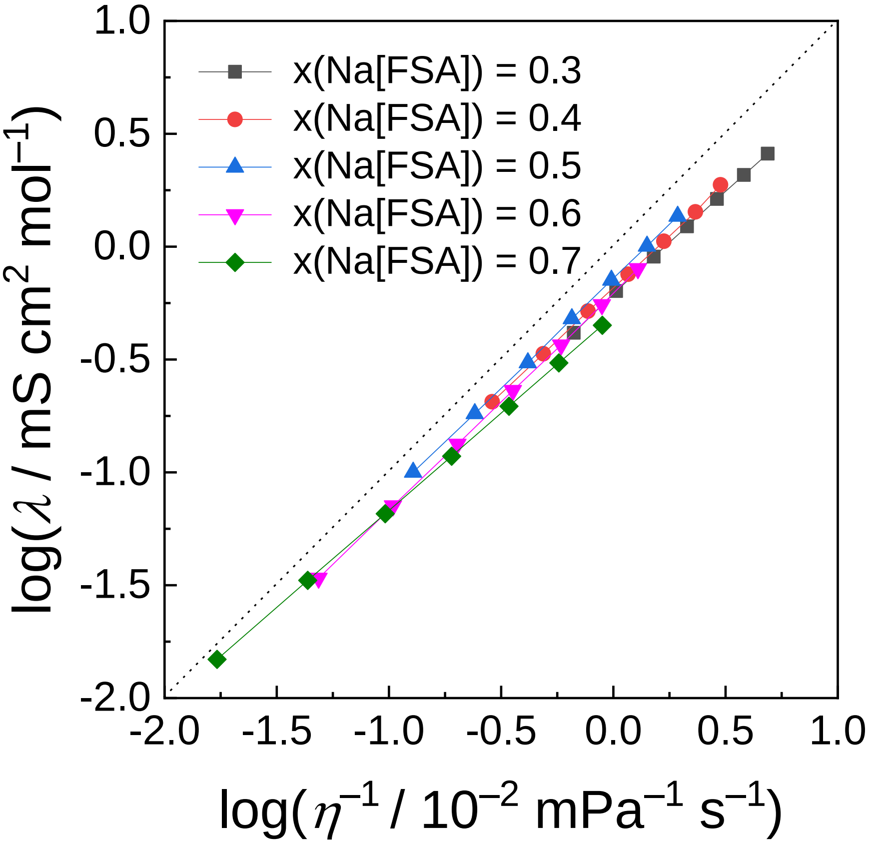

Figure 3-10. Walden plot for the Na[FSA]–[C_2C_1pyrr][FSA] IL system for *x*(Na[FSA]) = 0.3–0.7.

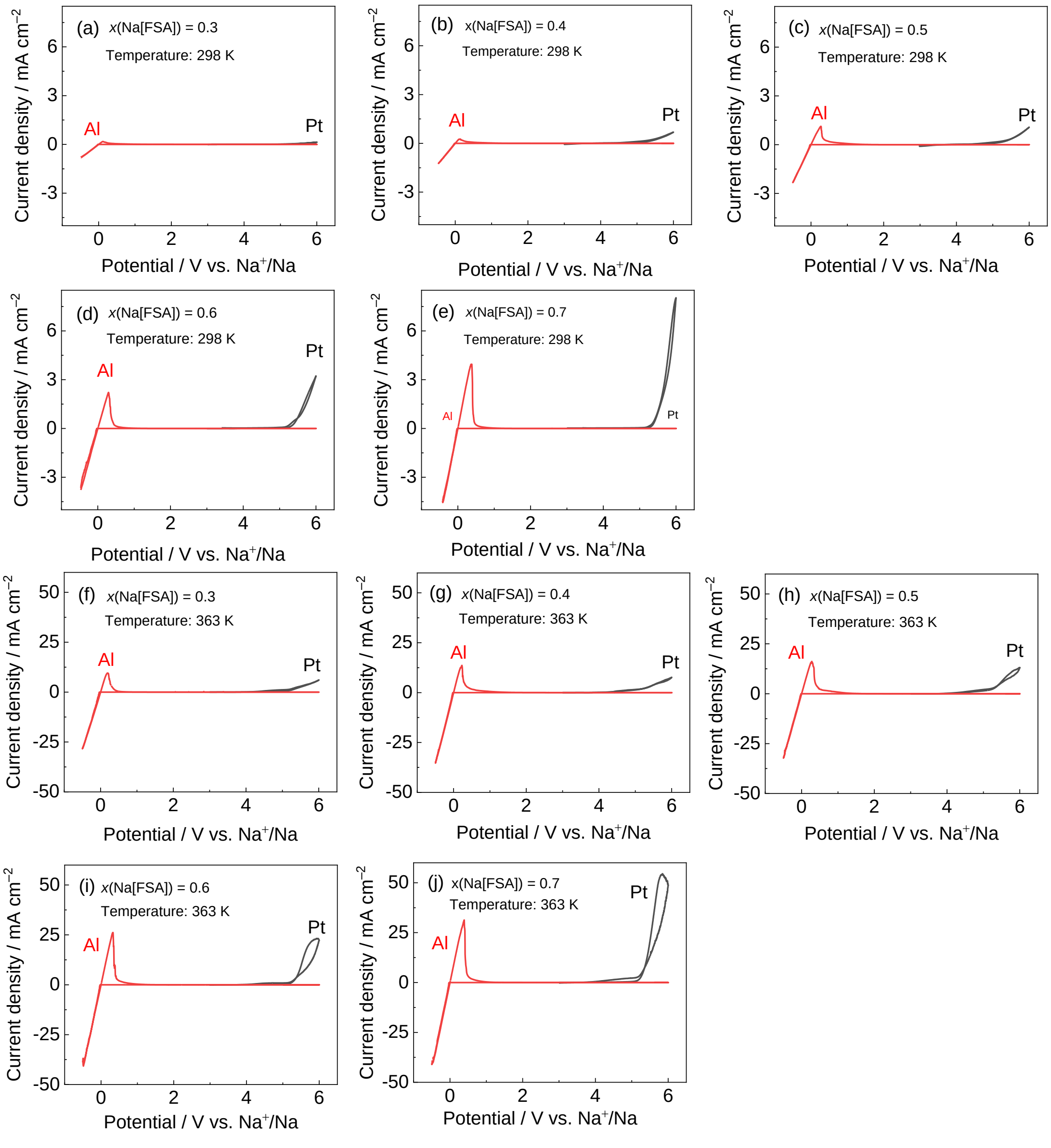

Figure 3-11. Combined cyclic voltammograms of Al (positive and negative potential region) and Pt plates (positive potential region) electrodes in the Na[FSA]–[C$_2$C$_1$pyrr][FSA] system (x(Na[FSA]) = 0.3–0.7) at (a–e) 298 K and (f–j) 363 K. Scan rate: 5 mV s^{-1}.

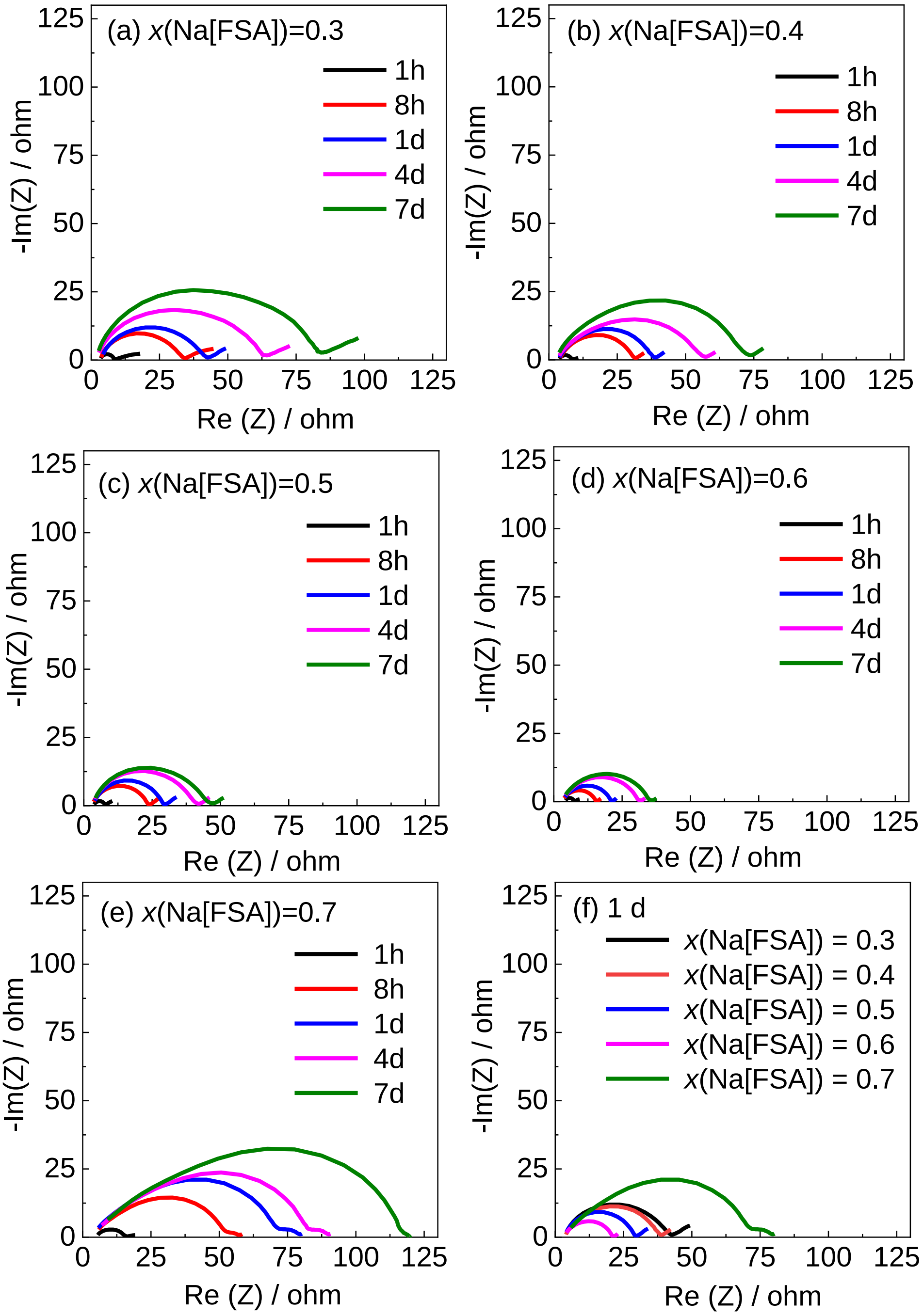

Figure 3-12. (a–e) Nyquist plots of Na/Na symmetric cells in Na[FSA]-[C_2C_1pyrr][FSA] (x(Na[FSA]) = 0.3–0.7) at 363 K over 7 d. Nyquist plots (f) at x(Na[FSA]) = 0.3–0.7 after 1 d. AC perturbation: 10 mV, frequency range: 10 mHz to 100 kHz.

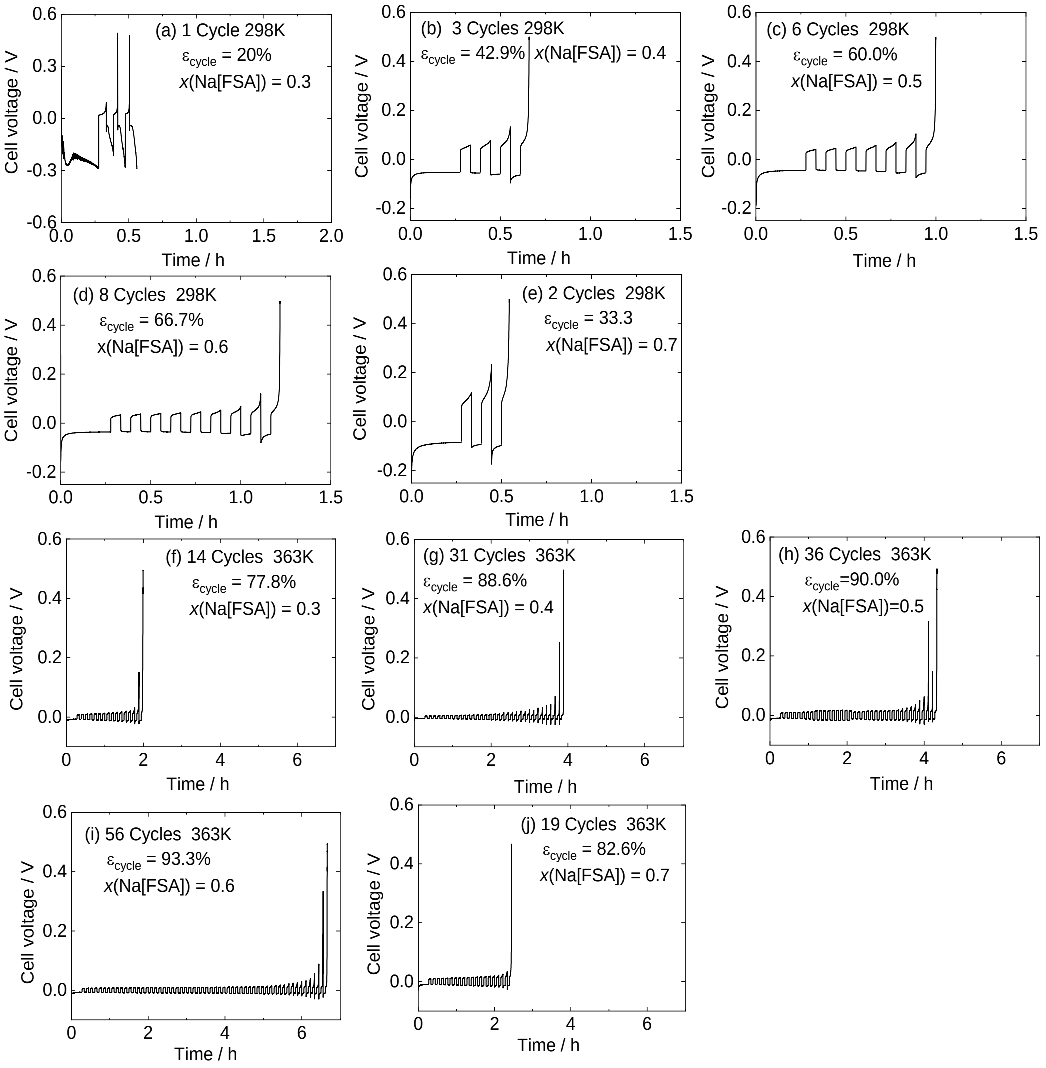

Figure 3-13. Voltage profiles during Na deposition/dissolution in Na[FSA]-[C_2C_1pyrr][FSA] at (a–e) 298 and (f–j) 363 K for x(Na[FSA]) = 0.3–0.7. The working and counter electrodes were Al and Na plates, respectively. 0.08 C cm^{-2} Na was deposited on the Al substrate, and 0.02 C cm^{-2} Na deposition and dissolution was repeated until the electrode potential reached 0.5 V vs. Na^+/Na during dissolution.

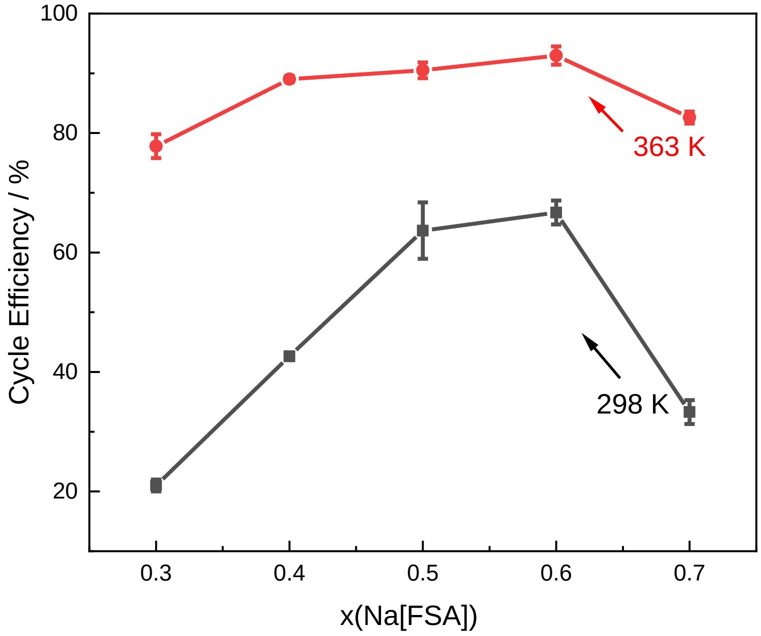

Figure 3-14. Cycle efficiency ($\varepsilon_{\text{cycle}}$) of Na metal deposition/dissolution in Na[FSA]-[C_2C_1pyrr][FSA] in the range of x(Na[FSA]) = 0.3–0.7 at 298 and 363 K.

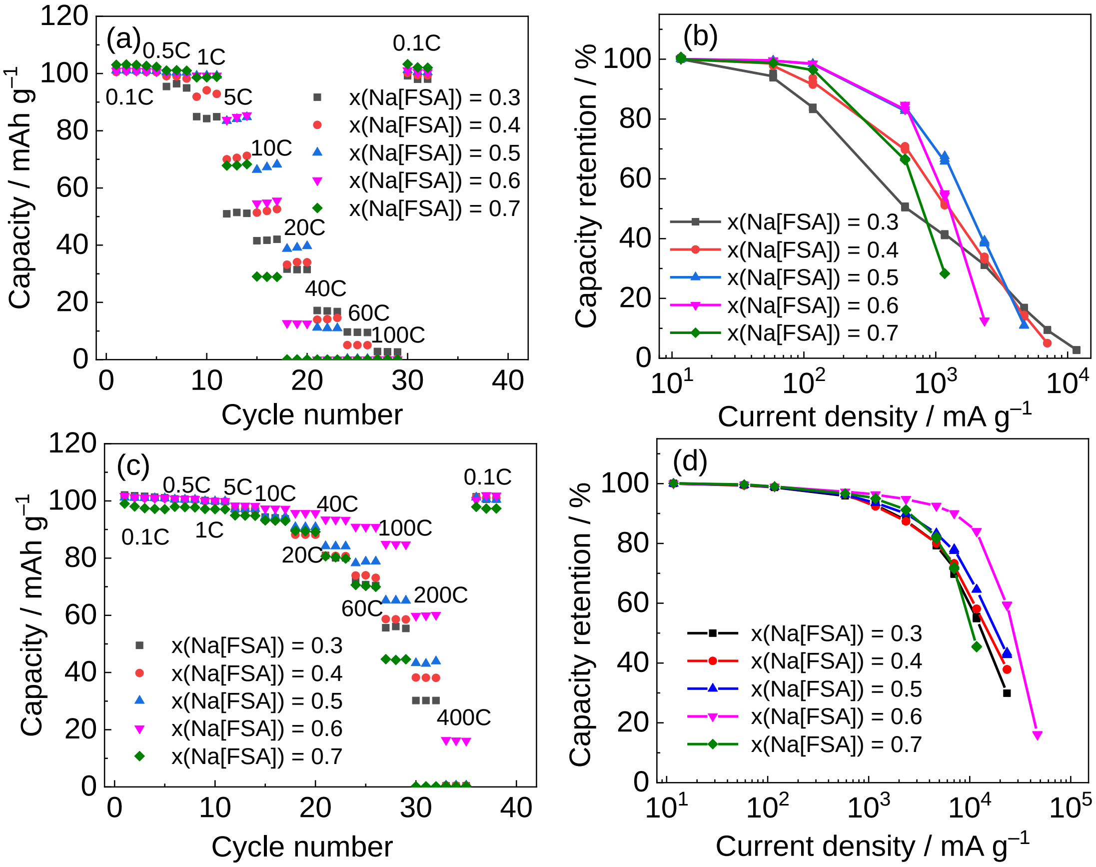

Figure 3-15. Rate capability of the Na/NVPC cells at (a, b) 298 K and (c, d) 363 K. Electrolyte: Na[FSA]–[C_2C_1pyrr][FSA] (x(Na[FSA]) = 0.3–0.7). Charge rate: 0.1C, discharge rates: 0.1C–400C, cut-off voltages: 2.4–3.8 V.

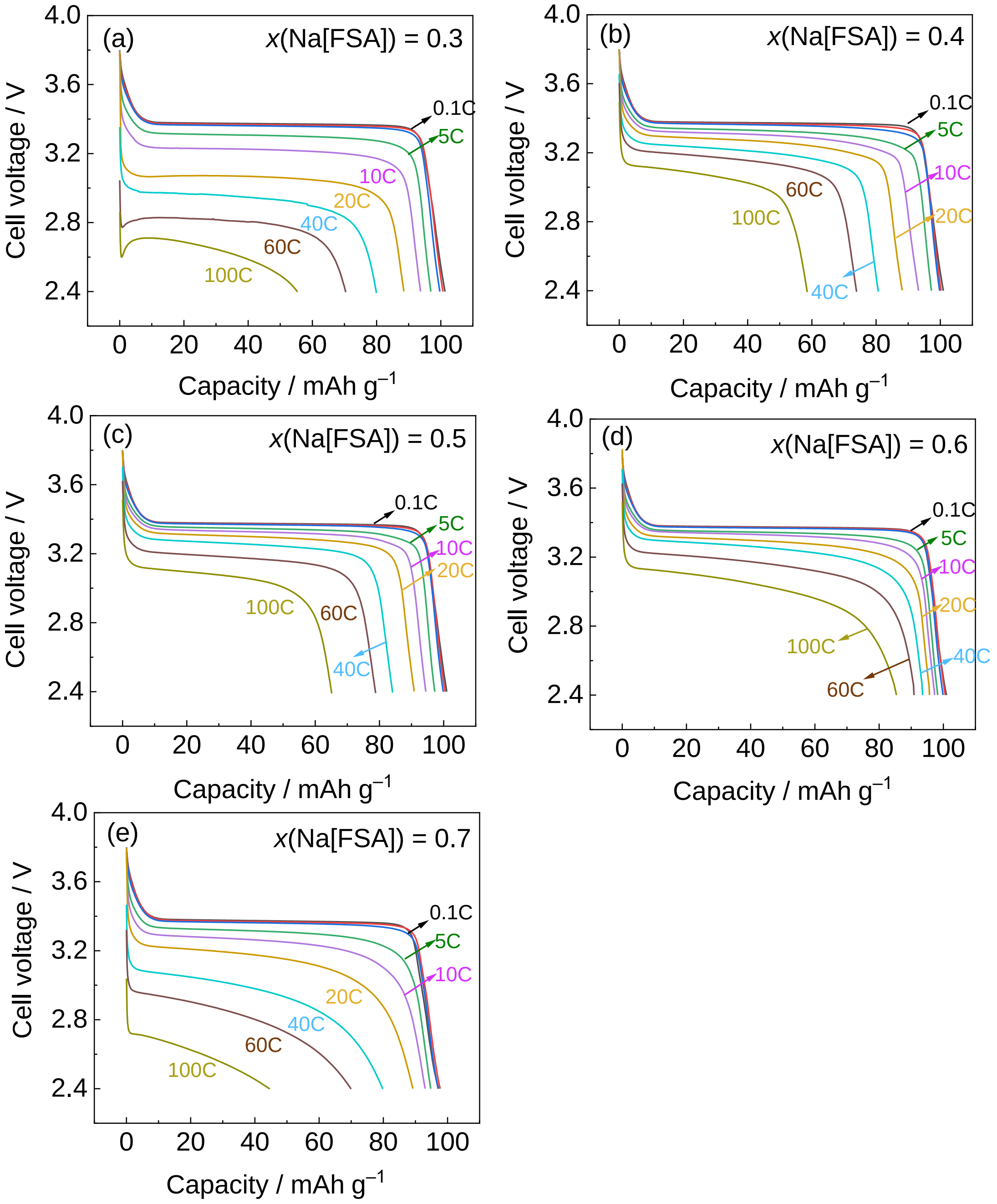

Figure 3-16. Discharge curves of Na/NVPC cells at 363 K during rate capability tests. Discharge rate ranges from 0.1C to 100C with the cutoff voltages of 2.4–3.8 V. Electrolyte: (a-e) Na[FSA]–[C_2C_1pyrr][FSA] (x(Na[FSA]) = 0.3–0.7).

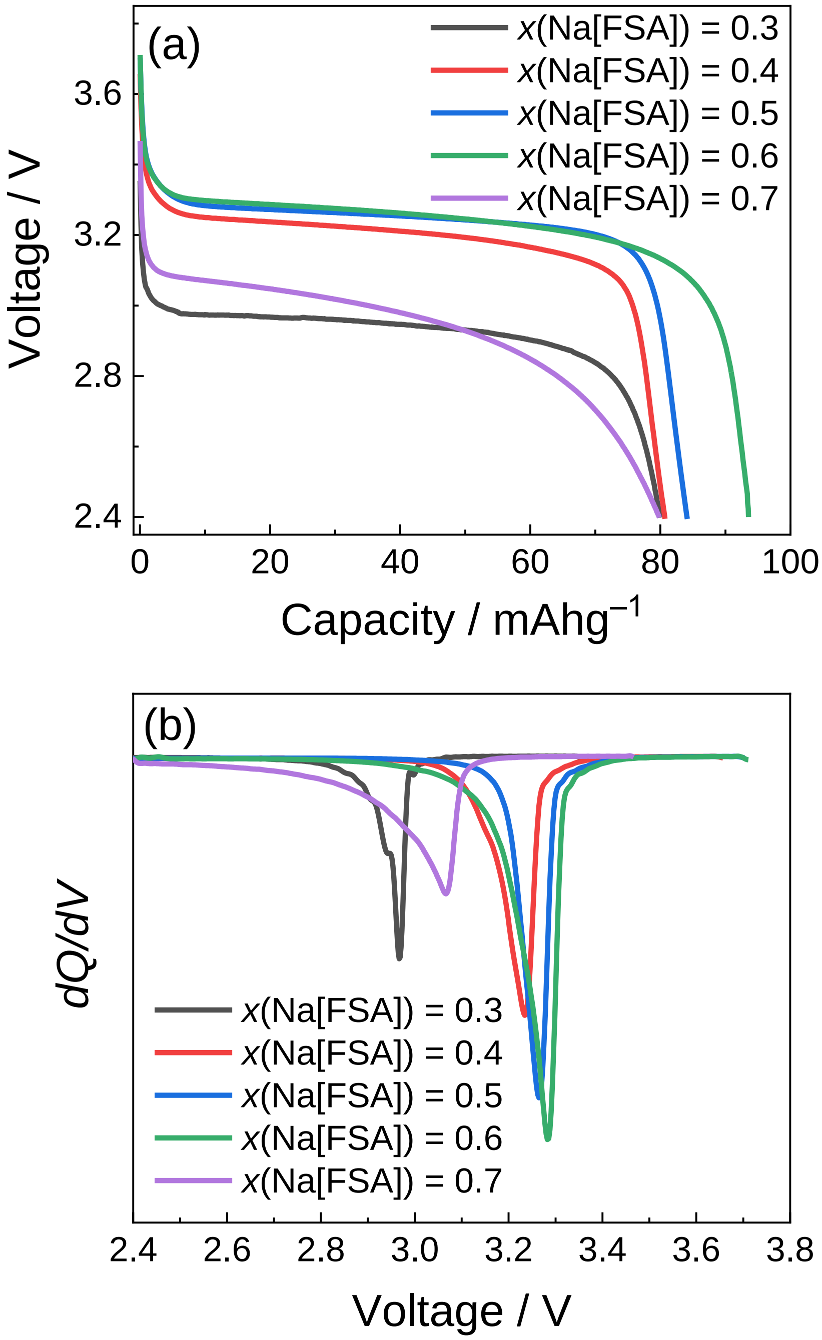

Figure 3-17. (a) The discharge curves of Na/NVPC cells at 363 K operated at 40C and (b) the corresponding (dQ/dV) plot. Electrolyte: Na[FSA]–[C_2C_1pyrr][FSA] (x(Na[FSA]) = 0.3–0.7).

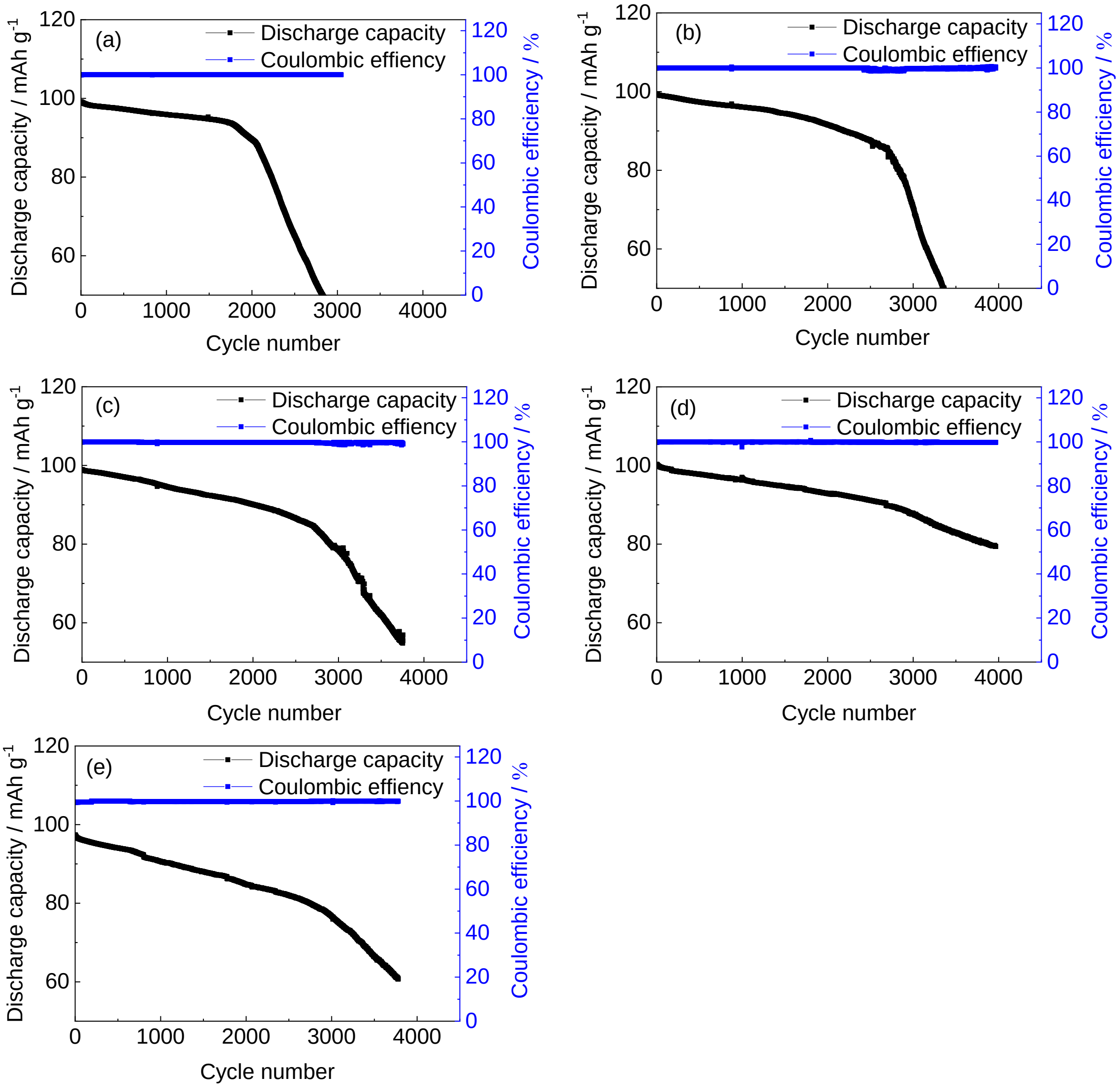

Figure 3-18. Cycling performance of Na/NVPC cells at 363 K. Electrolyte: Na[FSA]–$[C_2C_1pyrr]$[FSA] with *x*(Na[FSA]) = (a) 0.3, (b) 0.4, (c) 0.5, (d) 0.6, and (e) 0.7. Charge–discharge rate: 2 C. Cut-off voltages: 2.4–3.8 V.

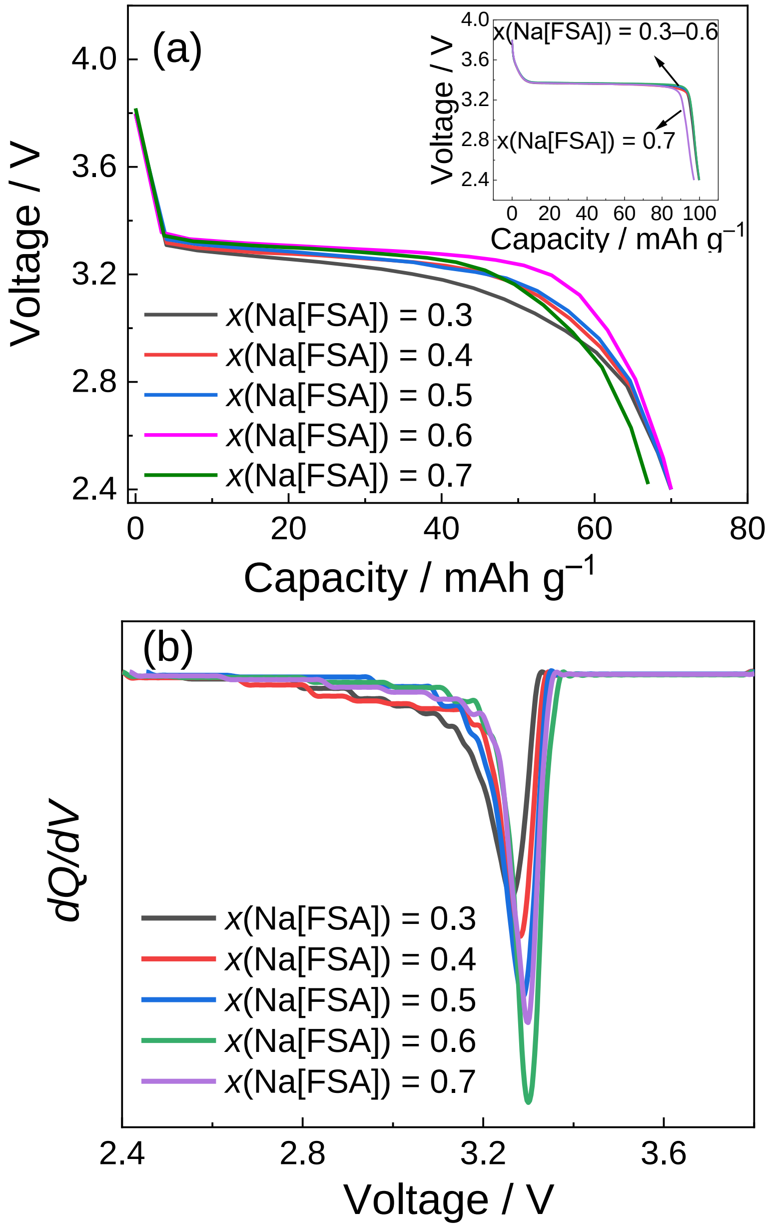

Figure 3-19. (a) The charge/discharge behavior and (b) corresponding dQ/dV curves of Na/NPVC cells during cycle tests. The curves are those at a capacity retention of 70% for each concentration of x(Na[FSA]) range from x(Na[FSA]) = 0.3–0.7 based on the first cycle. Voltage range: 2.4–3.8 V.

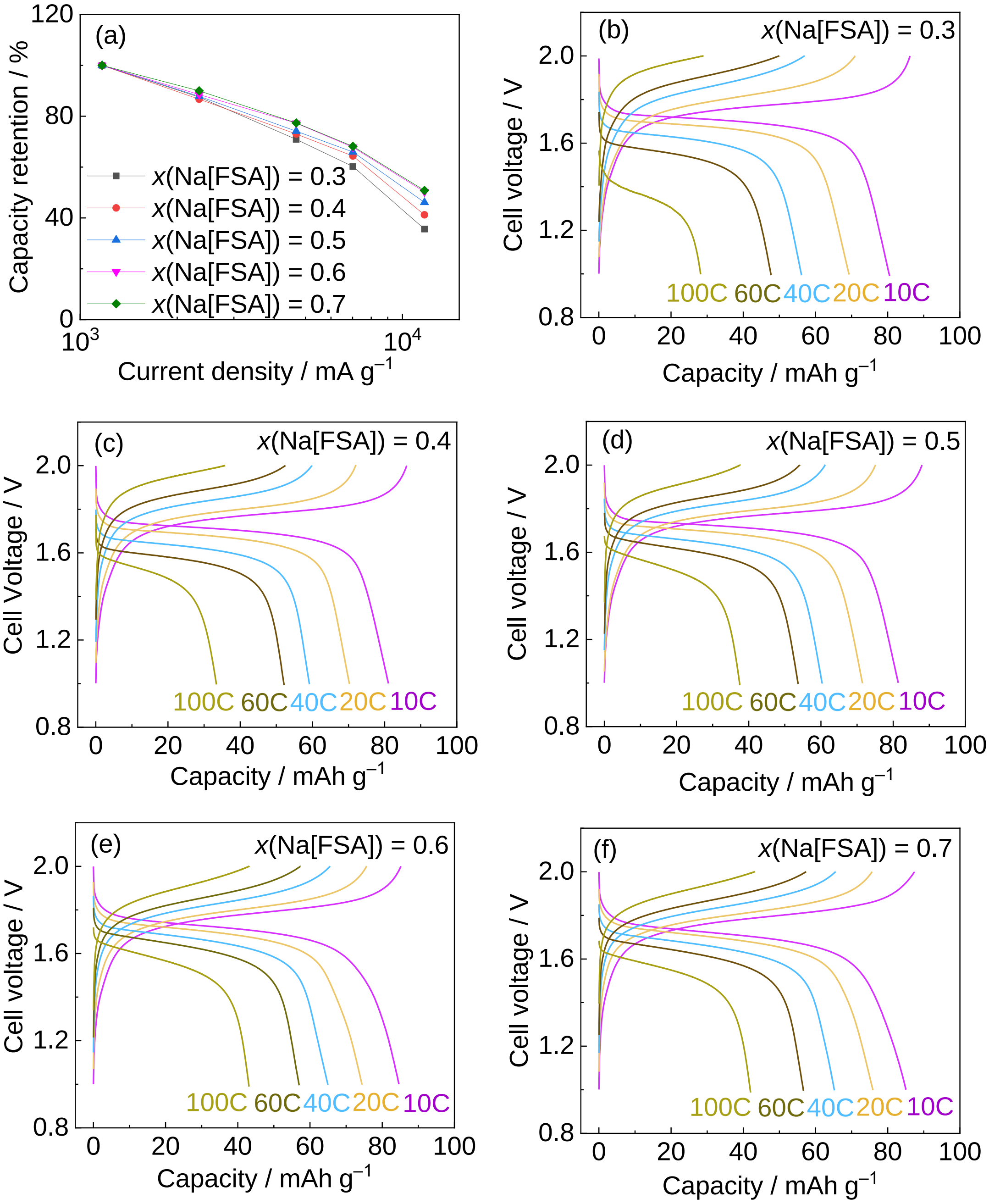

Figure 3-20. Electrochemical measurements of the NVPC/NVPC symmetric cell at 363K. (a) Rate capability from 10 to 100 C at cutoff voltages of 1.0–2.0 V and (b, f) charge–discharge curve of the NVPC/NVPC symmetric cells at x(Na[FSA]) = 0.3–0.7 at 363K during rate capability tests. Rate ranges from 10C to 100C with the cutoff voltages of 1.0–2.0 V.

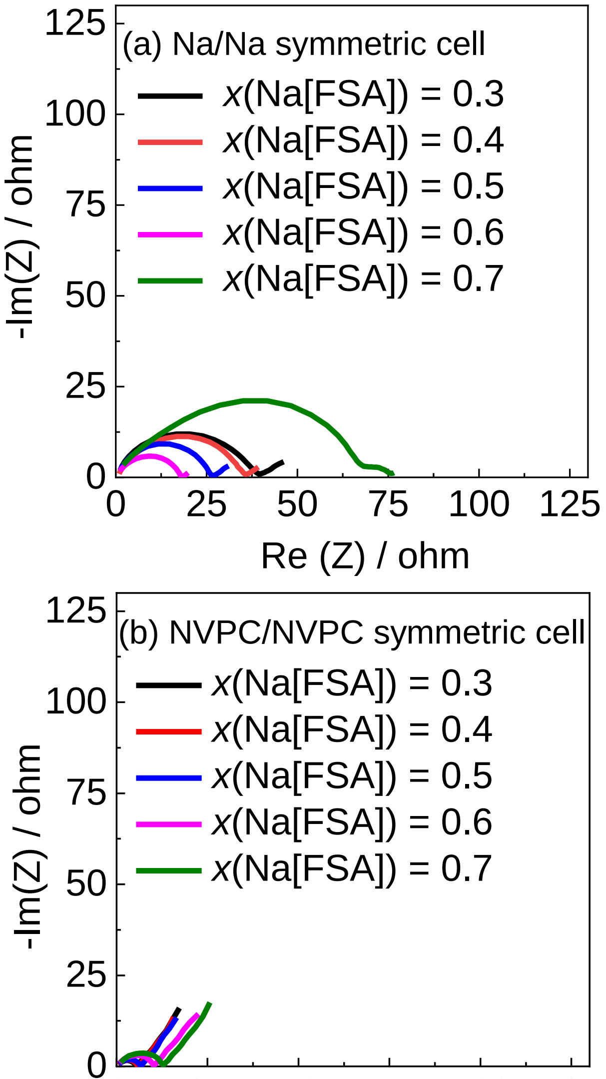

Figure 3-21. Nyquist plots of (a) the Na/Na symmetric and (b) NVPC/NVPC symmetric (SOC = 0.5) cells in Na[FSA]–[C_2C_1pyrr][FSA] (x(Na[FSA]) = 0.3–0.7) at 363 K (1 d after cell assembling). AC perturbation: 10 mV, frequency range: 10 mHz to 100 kHz. R_b is set as zero to compare R_{ct} in all the plots.

References

[1] J. P. Hallett, T. Welton, Chem. Rev., 111 (2011) 3508-3576.

[2] J. S. Wilkes, Green Chem., 4 (2002) 73-80.

[3] P. Wasserscheid, W. Keim, Angew. Chem. Int. Ed., 39 (2000) 3772-3789.

[4] R. Hagiwara, Y. Ito, J. Fluorine Chem., 105 (2000) 221-227.

[5] T. Welton, Chem. Rev., 99 (1999) 2071-2084.

[6] R. Hagiwara, J. S. Lee, Electrochemistry, 75 (2007) 23-34.

[7] H. Ohno, Electrochemical Aspects of Ionic Liquids, John Wiley & Sons, 2005.

[8] M. Watanabe, M. L. Thomas, S. Zhang, K. Ueno, T. Yasuda, K. Dokko, Chem. Rev., 117 (2017) 7190-7239.

[9] J. N. Canongia Lopes, K. Shimizu, A. A. Pádua, Y. Umebayashi, S. Fukuda, K. Fujii, S.-i. Ishiguro, J. Phys. Chem. B, 112 (2008) 9449-9455.

[10] L. Xue, C. W. Padgett, D. D. DesMarteau, W. T. Pennington, Solid State Sci., 4 (2002) 1535-1545.

[11] A. Noda, K. Hayamizu, M. Watanabe, J. Phys. Chem. B, 105 (2001) 4603-4610.

[12] S. Seki, N. Kihira, T. Kobayashi, Y. Kobayashi, Y. Mita, K. Takei, H. Miyashiro, S. Kuwabata, Electrochemistry, 77 (2009) 690-692.

[13] H. Matsumoto, H. Sakaebe, K. Tatsumi, M. Kikuta, E. Ishiko, M. Kono, J. Power Sources, 160 (2006) 1308-1313.

[14] K. Hayamizu, S. Tsuzuki, S. Seki, K. Fujii, M. Suenaga, Y. Umebayashi, J. Chem. Phys., 133 (2010) 194505.

[15] K. Tsunashima, A. Kawabata, M. Matsumiya, S. Kodama, R. Enomoto, M.

Sugiya, Y. Kunugi, Electrochem. Commun., 13 (2011) 178-181.

[16] S. Seki, Y. Ohno, Y. Mita, N. Serizawa, K. Takei, H. Miyashiro, ECS Electrochem. Lett., 1 (2012) A77-A79.

[17] J. Shimada, M. Shimada, T. Sugahara, K. Tsunashima, A. Tani, Y. Tsuchida, M. Matsumiya, J. Chem. Eng. Data 63 (2018) 3615-3620.

[18] A. Basile, A. F. Hollenkamp, A. I. Bhatt, A. P. O'Mullane, Electrochem. Commun., 27 (2013) 69-72.

[19] N. Schweikert, A. Hofmann, M. Schulz, M. Scheuermann, S. T. Boles, T. Hanemann, H. Hahn, S. Indris, J. Power Sources, 228 (2013) 237-243.

[20] A. I. Bhatt, P. Kao, A. S. Best, A. F. Hollenkamp, J. Electrochem. Soc., 160 (2013) A1171-A1180.

[21] W. Xu, J. Wang, F. Ding, X. Chen, E. Nasybulin, Y. Zhang, J.-G. Zhang, Energ. Environ. Sci., 7 (2014) 513-537.

[22] I. A. Shkrob, T. W. Marin, Y. Zhu, D. P. Abraham, J. Phys. Chem. C, 118 (2014) 19661-19671.

[23] K. Matsumoto, T. Hosokawa, T. Nohira, R. Hagiwara, A. Fukunaga, K. Numata, E. Itani, S. Sakai, K. Nitta, S. Inazawa, J. Power Sources, 265 (2014) 36-39.

[24] K. Matsumoto, Y. Okamoto, T. Nohira, R. Hagiwara, J. Phys. Chem. C, 119 (2015) 7648-7655.

[25] M. Forsyth, H. Yoon, F. Chen, H. Zhu, D. R. MacFarlane, M. Armand, P. C. Howlett, J. Phys. Chem. C, 120 (2016) 4276-4286.

[26] C. Ding, T. Nohira, R. Hagiwara, K. Matsumoto, Y. Okamoto, A. Fukunaga, S.

Sakai, K. Nitta, S. Inazawa, J. Power Sources, 269 (2014) 124-128.

[27] A. Basile, M. Hilder, F. Makhlooghiazad, C. Pozo-Gonzalo, D. R. MacFarlane, P. C. Howlett, M. Forsyth, Adv. Energy Mater., 8 (2018) 1703491.

[28] M. Hilder, P. C. Howlett, D. Saurel, E. Gonzalo, A. Basile, M. Armand, T. Rojo, M. Kar, D. R. MacFarlane, M. Forsyth, Electrochim. Acta, 268 (2018) 94-100.

[29] J. Hwang, K. Matsumoto, R. Hagiwara, J. Phys. Chem. C, 122 (2018) 26857−26864.

[30] C.-H. Wang, C.-H. Yang, J.-K. Chang, Chem. Commun., 52 (2016) 10890-10893.

[31] M. Yoshizawa-Fujita, E. Kishi, M. Suematsu, T. Takekawa, M. Rikukawa, Chem. Lett., 43 (2014) 1909-1911.

[32] Z. Jian, C. Yuan, W. Han, X. Lu, L. Gu, X. Xi, Y. S. Hu, H. Li, W. Chen, D. Chen, Adv. Funct. Mater., 24 (2014) 4265-4272.

[33] Z. Jian, L. Zhao, H. Pan, Y.-S. Hu, H. Li, W. Chen, L. Chen, Electrochem. Commun., 14 (2012) 86-89.

[34] J. Hwang, K. Matsumoto, R. Hagiwara, Adv. Sustainable Syst., 2 (2018) 1700171.

[35] K. Kubota, T. Nohira, T. Goto, R. Hagiwara, Electrochem. Commun., 10 (2008) 1886-1888.

[36] M. Hirao, H. Sugimoto, H. Ohno, J. Electrochem. Soc., 147 (2000) 4168-4172.

[37] K. Matsumoto, T. Oka, T. Nohira, R. Hagiwara, Inorg. Chem., 52 (2012) 568-576.

[38] K. Matsumoto, E. Nishiwaki, T. Hosokawa, S. Tawa, T. Nohira, R. Hagiwara, J.

Phys. Chem. C, 121 (2017) 9209-9219.

[39] K. Liu, Y.-X. Zhou, H.-B. Han, S.-S. Zhou, W.-F. Feng, J. Nie, H. Li, X.-J. Huang, M. Armand, Z.-B. Zhou, Electrochim. Acta, 55 (2010) 7145-7151.

[40] H.-B. Han, S.-S. Zhou, D.-J. Zhang, S.-W. Feng, L.-F. Li, K. Liu, W.-F. Feng, J. Nie, H. Li, X.-J. Huang, J. Power Sources, 196 (2011) 3623-3632.

[41] W. Xu, E. I. Cooper, C. A. Angell, J. Phys. Chem. B, 107 (2003) 6170-6178.

[42] P. Walden, H. Ulich, G. Busch, Phys. Chem, 123 (1926) 429-434.

[43] R. Hagiwara, K. Matsumoto, Y. Nakamori, T. Tsuda, Y. Ito, H. Matsumoto, K. Momota, J. Electrochem. Soc., 150 (2003) D195-D199.

[44] Y. Yoshida, K. Muroi, A. Otsuka, G. Saito, M. Takahashi, T. Yoko, Inorg. Chem. , 43 (2004) 1458-1462.

[45] W. Xu, C. A. Angell, Science, 302 (2003) 422-425.

[46] D. R. MacFarlane, M. Forsyth, E. I. Izgorodina, A. P. Abbott, G. Annat, K. Fraser, Phys. Chem. Chem. Phys., 11 (2009) 4962-4967.

[47] M. Yoshizawa, W. Xu, C. A. Angell, J. Am. Chem. Soc., 125 (2003) 15411-15419.

[48] K. R. Harris, J. Phys. Chem. B, 114 (2010) 9572-9577.

[49] K. J. Fraser, E. I. Izgorodina, M. Forsyth, J. L. Scott, D. R. MacFarlane, Chem. Commun., (2007) 3817-3819.

[50] C. Schreiner, S. Zugmann, R. Hartl, H. J. Gores, J. Chem. Eng. Data 55 (2009) 1784-1788.

[51] K. Matsumoto, R. Taniki, T. Nohira, R. Hagiwara, J. Electrochem. Soc., 162

(2015) A1409-A1414.

[52] T. H. T. Nohira, Kazuhiko Matsumoto, Rika Hagiwara, Denki Kagaku, 86 (2018) 293-297.

[53] T. Hosokawa, K. Matsumoto, T. Nohira, R. Hagiwara, A. Fukunaga, S. Sakai, K. Nitta, J. Phys. Chem. C, 120 (2016) 9628-9636.

[54] C.-Y. Chen, T. Kiko, T. Hosokawa, K. Matsumoto, T. Nohira, R. Hagiwara, J. Power Sources, 332 (2016) 51-59.

[55] L. S. Plashnitsa, E. Kobayashi, Y. Noguchi, S. Okada, J.-i. Yamaki, J. Electrochem. Soc., 157 (2010) A536-A543.

Chapter 4

Physicochemical and Electrochemical Properties of Na[FTA]-[C_3C_1pyrr][FTA] Ionic Liquid for Na Secondary Batteries

4.1 Introduction

Ionic liquids (ILs) are considered as good electrolytes to achieve a superior electrochemical performance owing to their unique properties [1, 2]. A number of recent studies highlight the desire to use ILs in wide temperatures within mobile applications and further electric vehicle (EV) market [3-5]. The use of asymmetric cation or anion is one of the feasible methods to extend a liquid temperature range of ILs to the lower side because asymmetric molecules hinder closer approach of ions to strongly interact and generate a solid phase [6, 7]. Among various organic cations, asymmetric pyrrolidinium-based and imidazolium-based cations showed high potentials as electrolytes in Na secondary battery studies [8, 9].Regarding the anions, compared to widely used symmetric FSA^- and $TFSA^-$ anions, the asymmetric (fluorosulfonyl)(trifluoromethylsulfonyl)amide (FTA) anion has a potential to reduce melting point or prevent solidification in the same manner without losing advantages observed for FSA and TFSA ILs [6, 10].

In previous studies, several FSA^--based ILs were investigated for Na secondary batteries, including inorganic and inorganic-organic hybrid systems such as Na[FSA]-K[FSA] [11], Na[FSA]-[C_3C_1pyrr][FSA] [12, 13], and Na[FSA]-[C_2C_1im][FSA] [14] [15]. TFSA-based ILs, Na[TFSA]-[C_2C_1im][TFSA] [16], Na[TFSA]-[C_4C_1im][TFSA] [16], and

Na[TFSA]-[C_4C_1pyrr][TFSA] [17], were also studied as Na secondary battery electrolytes, but their use is limited because of the instability against reduction as mentioned above. Concerning the FTA-based IL electrolytes for energy storage devices, their performance in Li-ion batteries and supercapacitors were demonstrated in previous works [18, 19], which suggested wide temperature range and high stability against Al corrosion. However, there is no systematic study on the physicochemical and electrochemical properties of FTA-based ILs available for Na secondary batteries. The aim of the present study is to investigate thermal, physical, and electrochemical characterization of the Na[FTA]-[C_3C_1pyrr][FTA] system. This includes their application as electrolytes for intermediate-temperature operating Na secondary batteries as proposed in previous works [20, 21] because intermediate operation using waste heat and hot environment is energetically efficient and enhance battery performance but requires safe electrolytes such as ILs. Battery performance of the FTA-based ILs will be discussed with the hard carbon (HC) electrode which is one of the most studied and promising negative electrode materials. Its performance in ILs was investigated in previous works, exhibiting a reasonably high discharge capacity and long cycle life, especially at intermediate temperatures [22, 23].

4.2 Experimental

Neat [C_3C_1pyrr][FTA] was synthesized by ion exchange between aqueous solutions of [C_3C_1pyrr]Br (IoLiTec, purity > 99%) and Na[FTA] (Provisco CS Ltd. purity > 98%) in the molar ratio of [C_3C_1pyrr]Br:Na[FTA] = 1:1.2. After 24-hour stirring, a water immiscible phase of [C_3C_1pyrr][FTA] formed. Subsequently, the obtained [C_3C_1pyrr][FTA] was purified with deionized water for several times to remove water-soluble byproduct (NaBr) until the Br content in the aqueous solution became below the detectable level by an $AgNO_3$ test using 1 mol L^{-1} $AgNO_3$ aqueous solution. Finally, $[C_3C_1pyrr][FTA]$ was extracted from the aqueous solution with dichloromethane (Wako Pure Chemical Industries, purity 99%) and dried under vacuum at 353 K. The Br content in the final product was below its detectable limit ($Br^- < 1$ ppm) according to X-ray fluorescence spectroscopy (Rigaku, EDXL-300). The Na[FTA]-$[C_3C_1pyrr][FTA]$ ILs were prepared by mixing Na[FTA] in the range of molar fraction of Na[FTA] (x(Na[FTA])) of 0–0.9 with $[C_3C_1pyrr][FTA]$.

The Na metal deposition/dissolution was evaluated by voltage profiles and electrochemical impedance spectroscopy (EIS) of Na/Na symmetric cells. In addition, an Al working electrode with 13 mm in diameter and 0.2 mm of thickness were used to test the cycle efficiency of Na metal deposition/dissolution process performed at a current density of 0.1 mA cm^{-2} in the Na[FTA]-$[C_3C_1pyrr][FTA]$ IL electrolytes with x(Na[FSA]) = 0.1–0.4 at 363 K.

Hard carbon (Carbotron P, Kureha Battery Materials Japan Co., Ltd) was used as an active material. HC electrodes were prepared in the following manner. The HC (96 wt%) powder and PAI binder (4 wt%) were uniformly mixed in NMP by a solid/liquid ratio of 0.52, and the obtained slurry was coated onto Al foil. The HC electrodes were dried in vacuum at 473 K for 12 h before being transferred into an Ar-filled glove box. Electrochemical characterization of the HC electrodes using the Na[FTA]-$[C_3C_1pyrr][FTA]$ ILs was carried out using a 2032-type coin cell, fabricated with the HC working electrode and Na counter electrode. A glass fiber filter (Whatman, GF-A, 260 μm) was used as a separator. The specific capacity of the charge-discharge process was calculated based on the mass of active material. Rate capability was tested at constant current rates of 20–2000 mA (g-HC)$^{-1}$ within a voltage range of 0.005–1.5 V. The cycle tests were performed at a constant current rate of 200 mA (g-HC)$^{-1}$ in the same voltage range with the rate capability test.

4.3 Results and Discussion

Figure 4-1 shows DSC curves at x(Na[FTA]) = 0.0–0.9, and the corresponding phase diagram of the Na[FTA]-[C_3C_1pyrr][FTA] system. As shown in Figure 4-2, the decomposition temperature (T_{dec}) of the neat [C_3C_1pyrr][FTA] (the temperature at which the weight loss exceeds 1 wt%) is 500 K, which is slightly lower than the previous report (558 K) [6]. Table 4-1 summarizes thermal transition temperatures based on the DSC results. In the x(Na[FTA]) range of 0.0–0.4, only the glass transition is observed in the DSC curves. The glass transition temperature is 170 K for the neat [C_3C_1pyrr][FTA], which well-agrees with the previous report (166 K) [6] and monotonously increases to reach 209 K at x(Na[FTA]) = 0.5 which is kept almost constant at the composition above. Such a trend of glass transition temperature increase with an increasing fraction of alkali metal ion was also observed in a lithium system (Li[FTA]-[C_3C_1pyrr][FTA]) [18]. Crystallization does not occur in this region including the neat [C_3C_1pyrr][FTA], which is considred to be caused by the asymmetric structure of FTA$^-$ preventing it from efficient packing of ions to acquire interaction enough to generate periodic structures [6]. As a result, a wide liquid temperature range is observed from x(Na[FTA]) = 0.0 to 0.4. The absence of crystallization behavior at such a low Na salt fraction was not observed in the previously studied FSA systems [12, 15]. At x(Na[FTA]) = 0.5 and 0.6, a weak and broad peak appears around 320–330 K, but it disappears in the second DSC cycle (the peaks are pointed out in Figure 4-1(f) and (g)). According to visual observation, the samples at x(Na[FTA]) = 0.0 to 0.4 are clear liquid at room temperature, whereas the samples become cloudy and highly viscous above x(Na[FTA]) = 0.5, implying that Na[FTA] is already saturated in [C_3C_1pyrr][FTA] at x(Na[FTA]) of 0.5. During the heating in the first cycle of DSC at x(Na[FTA]) of 0.5 and 0.6, the residual solid Na[FTA] dissolves into the liquid phase, resulting in the weak endothermic peaks at 312 and 333 K, respectively. However, there is no corresponding exothermic peak of precipitation in the second cooling because of supersaturation. For x(Na[FTA]) of 0.7–0.9, the solid phase becomes a major component according to visual observation and a pair of exothermic and endothermic peaks, resulting from the melting of the solid phase and solidification of the melt, are observed in DSC curves. In summary, as shown in Figure 4-1 (k), the phase diagram of the Na[FTA]-[C_3C_1pyrr][FTA] system is composed of glass transition and solid/liquid transition without showing any intermediate compound. The x(Na[FTA]) range of 0.0–0.4 that has a wide liquid-phase temperature range is selected for further investigation including transport and electrochemical measurements.

Figure 4-3 shows the temperature-dependence of density (a), viscosity (b), and ionic conductivity (c) for the Na[FTA]-[C_3C_1pyrr][FTA] system. The density values and fitting parameters are listed in Table 4-2. For the x(Na[FTA]) range of 0.0–0.4, linear relations were obtained between the density and x(Na[FTA]), as well as density and temperature; densities increase with increasing x(Na[FTA]) and decreasing temperature. The temperature dependence of density is fitted by the Eq. 3-4.

Table 4-3 lists the molar concentration of Na[FTA] (mol L^{-1}) in the Na[FTA]-[C_3C_1pyrr][FTA] system calculated from the density results and formula weight data. The x(Na[FTA]) at 0.1, 0.2, 0.3, and 0.4 correspond to 0.4, 0.9, 1.4, and 2.0 mol L^{-1} at 298 K respectively, which is concentrated enough to comply with the requirement for practical cells.

Viscosities and ionic conductivities of the investigated ILs are listed in Tables 4-4 and 4-5, respectively. At 298 K, ionic conductivity decreases with increasing x(Na[FTA]) from 6.5 mS cm^{-1} at x(Na[FTA]) = 0 to 0.45 mS cm^{-1} at x(Na[FTA]) = 0.4. Comparison of the Na and lithium IL systems shows that the Na system has a slightly higher or equivalent ionic conductivities compared to the lithium system (for example, at 298 K, 4.2 mS cm^{-1} for Na[FTA]-[C_3C_1pyrr][FTA] at x(Na[FTA]) = 0.1 and 3.7 mS cm^{-1} for Li[FTA]-[C_3C_1pyrr][FTA] at x(Li[FTA]) = 0.1). The ionic conductivities of the Na[FTA]-[C_3C_1pyrr][FTA] system show slightly lower values than those of the Na[FSA]-[C_3C_1pyrr][FSA] system [12] conceivably due to the substitution of fluorine atom by a bulky trifluoromethyl group. This disadvantage can be compensated by intermediate-temperature operation, as ionic conductivity rapidly increases with increasing temperature (for instance, 2.4 mS cm^{-1} at 298 K, 9.4 mS cm^{-1} at 338 K, and 18.4 mS cm^{-1} at 368 K for x(Na[FTA]) of 0.2). Temperature dependence of viscosity and ionic conductivity obey the Vogel-Tammann-Fulcher(VTF) equation [24-26], which can be fitted by Eqs. 3-2 and 3-3 with the fitting parameters A_η, B_η, $T_{0\eta}$, A_σ, B_σ, and $T_{0\sigma}$ ($R^2 > 0.999$; refer to Tables 4-6 and 4-7).

Deviation from the linear Arrhenius behavior in Figure 4-3 (concave for viscosity and convex for ionic conductivity) was widely observed for pure ILs and metal ion containing

ILs in previous works [27-30]. The $T_{0\eta}$ and $T_{0\sigma}$ parameters are the ideal glass-transition temperature and usually lower than the glass-transition temperature observed by DSC analysis. $T_{0\eta}$ and $T_{0\sigma}$ increase with the increasing x(Na[FTA]), which show the same trends against x(Na[FTA]) with the T_g observed in Figure 4-1.

Concerning ion transport properties of electrolytes, the correlation between molar ionic conductivity (λ) and viscosity (η) is expressed by the fractional Walden rule, which is represented by Eq. 3-6.[31-33]

Figure 4-4 shows the Walden plots of the Na[FTA]-[C_3C_1pyrr][FTA] system. A deviation of the gradient from unity is confirmed. The α value, decoupling constant, agrees with the Walden plot gradient. The C' parameter agrees with the Walden plot intercept. The greater ion association in ionic liquids leads to a shift of Walden plot to the bottom, which exhibits a smaller C' value [31]. For the Na[FTA]-[C_3C_1pyrr][FTA] ionic liquids, the range of α value is from 0.92 to 0.96; the range of logC' is from −0.11 to −0.24, as listed in Table 4-8. These two parameters do not exhibit an obvious trend with the increase of x(Na[FTA]).

The anodic stability of the Na[FTA]-[C_3C_1pyrr][FTA] ILs was identified by linear sweep voltammetry (LSV) using a coin-cell with Pt working and Na counter electrodes. Figure 4-5 (a, b) shows the LSV results at 298 and 363 K. When the current flowing through the cell reached 0.1 mA cm^{-2}, the corresponding potential is recognized as an anodic limit [6]. The anodic potential limit of 5.4–5.5 V vs. Na^+/Na is observed at 298 K at any x(Na[FTA]). In this case, decomposition of component ions causes oxidation currents at the anodic limit, and Na^+ ion concentration seems to have a minor influence on it, agreeing with the other IL systems [34]. However, the Na[FTA]-[C_3C_1pyrr][FTA] ILs become less stable against anodic decomposition at elevated temperature; the anodic limit is 5.1–5.3 V vs. Na^+/Na at 363 K, reflecting the lower kinetic barrier to oxidize the ILs. The wide anodic limit over 5 V vs. Na^+/Na still fits the requirement for a practical positive electrode material in Na secondary batteries.

Compatibility of Al electrodes as current collectors for positive electrodes was investigated by cyclic voltammetry in the Na[FTA]-[C_3C_1pyrr][FTA] IL at different *x*(Na[FTA]). As shown in Figure 4-6, the IL with the *x*(Na[FTA]) range of 0.1–0.4 shows similar anodic behavior. The anodic current of 3–4 μA cm^{-2} in the first anodic scan is attributed to the formation of the passivation layer. During this anodic reaction, Al surface is oxidized and forms species containing sulfonyl-amide. Different from organic solutions, the solubility of this species into ILs is low, and further anodic reaction is limited [19, 35]. The negligible currents (less than 1 μA cm^{-2} at 5.5 V vs. Na^+/Na) in the subsequent cycles prove the high compatibility of Al current collector to the Na[FTA]-[C_3C_1pyrr][FTA] ILs.

Sodium metal deposition-dissolution test of Na/Na symmetric cells is a facile method to examine the electrochemical performance in terms of overpotential for different electrolytes. The performance of various electrolyte compositions is exclusively evaluated at the Na electrodes, without introducing any positive electrode [13, 36]. Besides, among the battery community, metal electrodes are widely used as counter electrodes for half cell tests in mostly laboratory-scaled researches. Therefore, clarifying the contribution of Na counter electrodes on electrochemical performance in a given electrolyte is also inevitable. The deposition-dissolution was cycled in the *x*(Na[FTA]) range of 0.1–0.4 with a sequence of constant currents of 10, 50, 100, 500, 1000, and 3000 μA cm^{-2} for 10 cycles at each current density. For each cycle, 8-min deposition (or dissolution) and 2-min rest were applied (20 min per cycle). The obtained voltage profiles at 298 and 363 K are shown in Figure 4-7. The recorded overpotential of the Na/Na cells is attributed to several factors, including bulk resistance of Na-ion transport, resistance of surface film on Na electrodes, and charge transfer resistance [13, 37]. At 298 K, the polarization significantly decreases and is stabilized with increasing x(Na[FTA]) in spite of the lower ionic conductivity at high x(Na[FTA]). The major reason for this trend is the lower interfacial resistance at high x(Na[FTA]), agreeing with previous reports [13, 37, 38]. The polarization of the Na/Na symmetric cells decreases dramatically at 363 K (note the difference in the range of the horizontal axis in Figure 4-7). Only the overpotential of 0.04–0.09 V was observed even at 1000 μA cm^{-2}. Although the ion mobility in the IL electrolyte is increased at elevated temperature (see temperature dependence of ionic conductivity above), enhanced interfacial properties, including ion migration in SEI films and charge transfer, mainly contribute to this behavior [23, 39]. The concentration dependence is not obvious at 363 K, and similar polarization values, which are lower than that at x(Na[FTA]) = 0.1, were obtained for x(Na[FTA]) of 0.2–0.4. In brief summary, elevated temperature promotes the Na metal deposition-dissolution, whereas x(Na[FTA]) also has an impact on reducing polarization. Further discussions will be given with EIS results in the next section.

Figure 4-8 shows the EIS results of Na symmetric cells in the Na[FTA]-[C_3C_1pyrr][FTA] ILs in the temperature range of 298–363 K. These Nyquist plots are recorded after three charge/discharge cycles at a current density of 10 μA cm^{-2} for 8 min during each charge and discharge period in order to form a stable SEI layer. A slightly depressed semicircle was obtained at all x(Na[FTA]) values and temperatures. This may indicate that multiple factors contribute to resistances at electrolyte/Na interface, including naturally formed passivation layer, SEI film, and charge transfer. However, it is hard to distinguish them clearly in the case of Na electrodes. Figure 4-8 (d) shows the simplified equivalent circuit used for fitting. The R_{bulk} and R_{int} parameters are the electrolyte and interfacial resistances (including resistance of surface films and charge transfer), respectively.

The fitting results are listed in Table 4-9. The diffusion components were not fitted here as it made the fitting unstable. The large R_{int} with the characteristic frequencies of 150–10 Hz suggests that charge transfer dominates the interfacial behavior at 298 K [37] and explains the huge polarization of the Na symmetric cells at 298 K (see Figure 4-7). Regarding the effect of Na ion concentration, a negative correlation was observed for R_{int}; R_{int} decreases as x(Na[FTA]) increases, coinciding with the voltage profiles of Na symmetric cells at current densities of 10–500 μA cm^{-2} at 298 K.. Furthermore, the characteristic frequency shifts from 17.1 Hz (x(Na[FTA]) = 0.1) to 125 Hz (x(Na[FTA]) = 0.4) at 298 K.

At 333 and 363 K, Na symmetric cells with x(Na[FTA]) = 0.1–0.4 exhibit a remarkable decrease in R_{int} and R_{bulk} with increasing temperature. Elevated temperatures can activate the interfacial electrochemical process, which agrees with the low polarization of the Na/Na symmetric cells at 363 K (Figure 4-7). In addition, the characteristic frequencies of the semicircles shift to 3000–20000 Hz at elevated temperature. Because the semicircle ascribed to the impedance of the surface film is observed at a higher frequency than that of charge transfer, this change indicates that the major contribution to the impedance represented by the semicircle in the present Nyquist plots shifts from that originated from charge transfer process to that from the surface film [37]. Concerning transport properties of the investigated ILs, R_{bulk} is smaller than R_{int} at 298 and 333 K, however, the R_{bulk}/R_{int} ratio is relatively large at 363 K. When considering the total resistance of $R_{bulk} + R_{int}$, the values of 9.06, 5.75, 5.28, and 6.40 ohm were obtained for x(Na[FTA]) of 0.1, 0.2, 0.3 and 0.4 respectively, at 363 K. Na symmetric cells at x(Na[FTA]) = 0.1 shows the largest resistance among all the tested x(Na[FTA]). Similar values of total resistance were obtained in x(Na[FTA]) of 0.2–0.4, which coincides with the similar polarizations in the deposition/dissolution tests of Na/Na symmetric cells at 363 K (Figure 4-7 (d, f, h)).

Since the results of Na metal deposition/dissolution and EIS based on Na/Na symmetric cells have difficulties in the estimation of Na metal deposition/dissolution efficiency, Na metal deposition/dissolution test on Al electrode was also examined. Figure 4-9 shows the voltage profiles during Na metal deposition/dissolution test in Na[FTA]-[C_3C_1pyrr][FTA] with x(Na[FTA]) = 0.1–0.4 at 363 K. For comparison, Na[FSA]-[C_3C_1pyrr][FSA] (x(Na[FSA]) = 0.1) and Na[TFSA]-[C_3C_1pyrr][TFSA] (x(Na[TFSA]) = 0.1) were also tested in the same condition (the Na salt fraction of 0.1 was selected because of the limited solubility of Na[TFSA] into [C_3C_1pyrr][TFSA], the solution became cloudy with x(Na[TFSA]) higher than 0.3). The cycle efficiency of Na deposition/dissolution (ε_{cycle}) was evaluated by Eq. 3-1.

An increase in x(Na[FTA]) from 0.1 to 0.3 alleviate the overpotential of each Na metal deposition/dissolution cycle from 0.03 to 0.01 V. The maximum ε_{cycle} is achieved at x(Na[FTA]) = 0.2 (92.5%) and 0.3 (92.2%), in contrast to 86.2% at x(Na[FTA]) = 0.1. The benefit of SEI formation by a high fraction of Na^+ in the electrolyte deriving from a stable supply of Na^+ at the electrode. Consequently, high x(Na[FTA]) facilitates SEI-layer stabilization and suppresses dendrite formation giving a high $\varepsilon_{\mathrm{cycle}}$ as a result. The $\varepsilon_{\mathrm{cycle}}$ at x(Na[FTA]) = 0.4 slightly decreases to 91.1%, but the overpotential of Na metal deposition/dissolution cycles could still be held around 0.01 V. The Na[FSA]-[C_3C_1pyrr][FSA] electrolyte at x(Na[FSA]) = 0.1 exhibits a similar $\varepsilon_{\mathrm{cycle}}$ value to that of the Na[FTA]-[C_3C_1pyrr][FTA] electrolyte at x(Na[FTA]) = 0.1 with a smaller overpotential. On the other hand, the Na[TFSA]-[C_3C_1pyrr][TFSA] (x(Na[TFSA]) = 0.1) apparently shows an inferior $\varepsilon_{\mathrm{cycle}}$ with large overpotential. Instability of the TFSA system against reduction was suggested in previous works [40], which was interpreted by the formation of unstable radical anion according to an electron paramagnetic resonance analysis [41]. Comparison of the present three cases with FTA^-, FSA^-, and $TFSA^-$ indicates that even substitution of one trifluoromethyl group with F atom [40] results in formation of stable SEI [42] on Na metal.

Performance of the Na[FTA]-[C_3C_1pyrr][FTA] system was further studied in terms of the reversibility of HC negative electrode. Figure 4-10 shows the charge-discharge curves of Na/HC cells with the IL at x(Na[FTA]) of 0.1–0.4 at 363 K (charge-discharge rate: 20 mA g^{-1}) and the corresponding dQ/dV plot. The first charge-discharge curves can be classified into several parts. A short plateau is observed at 1.3–1.0 V during the initial charge (sodiation), which is attributed to the reductive decomposition of the electrolyte and SEI film formation [23]. The following sloping region from 1.2 to 0.1 V and the plateau below 0.1 V is assigned to Na^+ insertion/extraction between graphene layers and nanopore within HC, respectively, according to the previous work [43]. The subsequent initial discharge curve has the corresponding electrochemical behavior. The Na/HC cells show similar discharge capacities of 260–270 mAh g^{-1} from the initial cycles regardless of x(Na[FTA]), whereas the initial charge capacities are significantly larger than that. The discharge capacities obtained in this study are similar to that obtained with the same HC material in different ILs in a previous work [31].

The Coulombic efficiencies of the initial five cycles at x(Na[FTA]) of 0.1–0.4 are listed in Table 4-10. The Na/HC cell at x(Na[FTA]) = 0.1 exhibits a high Coulombic efficiency of 81.3% in the first cycle and quickly reaches a stable state in the subsequent cycles (Coulombic efficiency > 99%). The Coulombic efficiency decreases with increasing x(Na[FTA]), giving the initial Coulombic efficiency of 65.4% at x(Na[FTA]) = 0.4. Even in the fifth cycle, the Coulombic efficiency does not efficiently improve at x(Na[FTA]) = 0.4 (92.4%), indicating the unstable SEI formation at high x(Na[FTA]). In an organic electrolyte (Na[FSA]-succinonitrile), a different behavior was observed; an increase of Na[FSA] concentration stabilizes the Na/HC cell and leads to the higher Coulombic efficiency [44]. These results imply that particular irreversible reactions, triggered by increasing x(Na[FTA]), occur during the charging process on HC. The corresponding dQ/dV plots of the first and fifth cycles in Figure 4-10 was applied to confirm the voltage location of this particular irreversible reaction. As shown in Figure 4-10 (f), during the first charge, the peak of SEI formation located around 1.2 V monotonously shifted to high voltage value with increasing x(Na[FTA]), indicating the increasing x(Na[FTA]) is preferable for the SEI film formation with lower reaction barrier. However, a broad peak around 0.6 V becomes more and more obvious with increasing x(Na[FTA]) and disappears in the following cycles (Figure 4-10 (h)), which confirms additional irreversible reactions including severe decomposition of ILs occurs especially at x(Na[FTA]) = 0.4. Electrolyte decomposition was also observed during the initial charging for the HC electrode in an organic electrolyte, resulting in the constant deterioration of cycle performance from the early cycles [43]. Such a decomposition peak does not appear with FSA^- but does with $TFSA^-$ (see Figure 4-10 (f)), indicating that the CF_3 group on the sulfonylamide causes this decomposition reaction in this voltage range. Further research is needed for clarifying the reduction mechanism of FTA^--based ILs.

Figure 4-11 shows the rate capability of the Na/HC cells at x(Na[FTA]) = 0.1–0.4 at 363 K. The data with Na[FSA] and Na[TFSA] are also shown for comparison (x(Na[FSA]) = 0.1 and x(Na[TFSA]) = 0.1). As shown in Figure 4-11, the capacity gradually decreases with an increasing rate up to 200 mA g^{-1}. A capacity of 230–270 mAh g^{-1} was obtained within this range of charge-discharge rates. In contrast, at high charge-discharge rates, x(Na[FTA]) considerably influences the discharge capacities of the Na/HC cells; with increasing rate, the Na/HC cell at x(Na[FTA]) of 0.3 provides the highest discharge capacities among all the investigated x(Na[FTA]) values. Figure 4-12 shows charge-discharge curves of the Na/HC cell with the Na[FTA]-[C_3C_1pyrr][FTA] IL during the rate test at 363 K giving the discharge capacity of 238 mAh g^{-1} at 200 mA g^{-1} (Coulombic efficiency > 99%) with about 91% capacity retention based on the initial capacity at 20 mA g^{-1}. The charge-discharge capacities of HC remain similar within a rate range of 20–200 mA g^{-1}. At higher rates, the capacity of the plateau region around 0.1 V is gradually decreased, and polarization becomes more and more severe with increasing rate, as shown in the dQ/dV plots (Figure 4-13), whereas capacity acquired during the sloping region is less sensitive to the rate. The capacity decay at high rates is governed by the polarization based on interfacial reactions (Na metal and HC electrodes) and ion transport in the electrolyte. As was observed in the results of the Na/Na symmetric cell tests, the polarization at the Na metal electrode does not notably differ above x(Na[FTA]) of 0.3. Thus, the rate performance is dependent on the interfacial reaction at the HC electrode and ion transport. Because the high R_{bulk} at high x(Na[FTA]) (corresponding to the low ionic conductivity at high x(Na[FTA]) in Table 4-5) works against the rate performance, the appearance of the maximum rate performance at x(Na[FTA]) = 0.3 suggests the improved interfacial reaction at the HC electrode at high x(Na[FTA]). Although the rate performance for the FTA and FSA IL, x(Na[FTA]) = 0.1 and x(Na[FSA]) = 0.1, are similar to each other, the rate performance of the TFSA IL (x(Na[TFSA]) = 0.1) is obviously inferior. The proper evaluation for the TFSA system requires a trustable counter electrode because of the high polarization and low $\varepsilon_{\mathrm{cycle}}$ mentioned for the Na metal electrode (Figure 4-9).

Figure 4-14 shows the cycling performance of the Na/HC cell with the IL at x(Na[FTA]) = 0.1–0.4 at 200 mA g^{-1}. Capacity retentions of 84.2, 93.1, and 97.0% are achieved at 363 K after 400 cycles for x(Na[FTA]) = 0.1, 0.2 and 0.3, respectively, providing 99.9% average Coulombic efficiency. The discharge capacity at x(Na[FTA]) = 0.4 is constantly deteriorated from the early cycles with the capacity retentions of 48.2% at the 200th cycle. The capacity retention increases with increasing x(Na[FTA]) = 0.1–0.3, however, decreases at x(Na[FTA]) = 0.4. Figure 4-15 shows the charge-discharge curves and corresponding dQ/dV plots of the 200th cycle, which can be compared with the 5th cycle (see Figure 4-10 for dQ/dV plots of the 5th cycle), illustrating the influence of x(Na[FTA]) on cycle capability. For x(Na[FTA]) = 0.1–0.3, a clear and long plateau was observed around 0.1 V at the 200th cycle in Figure 4-15 (a, b, and c). Combining the corresponding dQ/dV plots at the 200th cycle in Figure 4-15 (e), the polarization of x(Na[FTA]) = 0.2–0.3 is alleviated comparing with x(Na[FTA]) = 0.1 indicating high concentration of Na[FTA] have a positive impact on cycle performance. In contrast, the capacity obtained in the plateau region of x(Na[FTA]) = 0.4 is considerably reduced at the 200th cycle, while the capacity in the sloping region based on Na^+ insertion is similar at any x(Na[FTA]). The capacity achieved at the plateau is attributed to the reversible Na insertion into the nanopores, in which the plateau features are affected by the x(Na[FTA]) in the present IL system. High x(Na[FTA]) of 0.4 has difficulties in the Na insertion into the nanopores, which could be related to the unfavorable decomposition of ILs during the formation of SEI film in the first cycle as shown in Figure 4-10 (f). Details on the decomposition process is not clear in the current stage, but the decomposition products slowly deposit during cycling may block the nanopores of HC. Since the insertion of Na^+ into the nanopores is essential to the capacity of the HC negative electrode, high x(Na[FTA]) out of a certain range should be avoided for long term stability.

4.4 Conclusions

This chapter described the thermal, transport, and electrochemical properties of the Na[FTA]-[C_3C_1pyrr][FTA] ILs in view of their applications as electrolytes in Na secondary batteries. Intermediate temperature operation is one of the targets of this work and thus electrochemical behavior was investigated at 298 and 363 K. According to DSC results, a wide liquid temperature range that holds the pure liquid phase even at 170–209 K is observed in x(Na[FTA]) = 0.0–0.4. Absence of crystallization behavior in such a low Na salt fraction was not observed for the previously known FSA^- systems and is attributed to the asymmetric structure of FTA^-. Neat $[C_3C_1pyrr][FTA]$ exhibits an ionic conductivity of 6.46 and 30.9 mS cm^{-1} at 298 K and 368 K, respectively. The viscosity and ionic conductivity obeys fractional Walden rule for x(Na[FTA]) = 0.0–0.4. The high anodic limit above 5 V vs. Na^+/Na and high compatibility with an Al electrode substrate were confirmed. Na symmetric cells show better performance with the increase of x(Na[FTA]) and temperature. The Na metal deposition/dissolution test on the Al substrate reveals the inferior SEI formation ability and less electrochemical stability of C–F bond of FTA anion than FSA anion. The electrochemical tests of HC electrodes showed that discharge capacities around 260–270 mAh g^{-1} are delivered at a low rate of 20 mA g^{-1} at 363 K with Coulombic efficiency decreasing with the increase of x(Na[FTA]). A higher rate capability and stable cycle performance maintaining 97.0% capacity retention at the 400th cycle were confirmed at x(Na[FTA]) of 0.3, which is considered to result from the balance of the interfacial reaction and ion transport. The wide liquid temperature range derived from FTA^- is a remarkable characteristic as IL electrolytes for Na secondary batteries, and incorporation of different cationic frames is an interesting future study. The physicochemical properties of FTA-based ILs are somewhere between those of FSA- and TFSA-based ILs, whereas the electrochemical stability against reduction related to stable SEI formation was observed as for FSA-based ILs. Further studies fully making use of these advantages are required to design practical batteries.

Table 4-1. DSC transition temperatures for the Na[FTA]-[C_3C_1pyrr][FTA] system.[a]

x(Na[FSA])	T_g / K	T_m / K
0	170	--.
0.1	178	--
0.2	183	--
0.3	196	--
0.4	209	--
0.5	217	312
0.6	218	333
0.7	213	358
0.8	221	395
0.9	217	392

[a] T_g: glass transition temperature and T_m: melting point.

Table 4-2. Density (g cm^{-3}) of the Na[FTA]-[C_3C_1pyrr][FTA] system. The symbols *A* and *B* are the constants in Eq. 3-4 for the temperature dependence of density.

***T* / K**	***x*(Na[FSA])**				
	0	**0.1**	**0.2**	**0.3**	**0.4**
278	1.4068	1.4407	1.4791	1.5218	1.5718
288	1.3994	1.4319	1.4700	1.5124	1.5620
298	1.3898	1.4230	1.4609	1.5030	1.5522
308	1.3813	1.4142	1.4518	1.4936	1.5426
318	1.3728	1.4054	1.4427	1.4843	1.5330
328	1.3643	1.3968	1.4338	1.4750	1.5234
338	1.3559	1.3882	1.4249	1.4658	1.5139
348	1.3477	1.3796	1.4160	1.4565	1.5045
358	1.3391	1.3710	1.4068	1.4469	1.4952
$A \times 10^4$ /g cm^{-3} K^{-1}	–8.5105	–8.7097	–9.0285	–9.3432	–9.5717
B / g cm^{-3}	1.6437	1.6826	1.7300	1.7815	1.8375

Table 4-3. Molar concentrations (mol dm^{-3}) of the Na[FTA]-[C_3C_1pyrr][FTA] system.

***T* / K**	***x*(Na[FSA])**				
	0	**0.1**	**0.2**	**0.3**	**0.4**
278	0	0.414	0.877	1.397	1.988
288	0	0.412	0.872	1.388	1.975
298	0	0.409	0.866	1.380	1.963
308	0	0.407	0.861	1.371	1.951
318	0	0.404	0.855	1.363	1.939
328	0	0.402	0.850	1.354	1.927
338	0	0.399	0.845	1.345	1.915
348	0	0.397	0.839	1.337	1.903
358	0	0.394	0.834	1.328	1.891

Table 4-4. Viscosities (mPa s) of the Na[FTA]-[C_3C_1pyrr][FTA] system.

***T* / K**	***x*(Na[FSA])**					
	0	**0.1**	**0.2**	**0.3**	**0.4**	**0.5**
278	87	190	315	1030	3960	--
288	58	115	177	488	1530	--
298	40	74	107	259	720	--
308	29	50	69	150	364	11200
318	22	35	47	93	196	1130
328	17	26	33	62	119	495
338	13	19	24	43	77	240
348	11	15	19	31	54	135
358	9	12	14	23	39	89

Table 4-5. Ionic conductivities (mS cm^{-1}) of the Na[FTA]-[C_3C_1pyrr][FTA] system.

***T* / K**	***x*(Na[FSA])**				
	0	**0.1**	**0.2**	**0.3**	**0.4**
238	0.23	--	--	--	--
248	0.54	0.23	--	--	--
258	1.1	0.51	0.18	--	--
268	1.9	0.99	0.41	--	--
278	3.1	1.7	0.82	0.30	--
288	4.6	2.8	1.5	0.62	0.21
298	6.5	4.2	2.4	1.1	0.45
308	9.0	6.0	3.6	1.9	0.84
318	11.9	8.2	5.2	3.0	1.5
328	15.1	10.8	7.1	4.3	2.3
338	18.5	13.9	9.4	6.1	3.5
348	22.4	17.4	12.1	8.1	5.0
358	26.4	21.3	15.1	10.5	6.8
368	30.9	25.8	18.4	13.2	8.9

Table 4-6. VTF fitting parameters of viscosity for the Na[FTA]-[C_3C_1pyrr][FTA] ILs.

x(Na[FTA])	**10^3 x A_η / mPa s $K^{-1/2}$**	**B_η / K**	**$T_{0\eta}$ / K**
0.0	4.22	1105	123
0.1	2.72	1256	127
0.2	3.20	1181	142
0.3	4.33	1101	163
0.4	5.02	1098	176

Table 4-7. VTF fitting parameters of ionic conductivity for the Na[FTA]-[C_3C_1pyrr][FTA] ILs.

x(Na[FSA])	**10^4 x A_σ / mS cm^{-1} $K^{1/2}$**	**B_σ / K**	**$T_{0\sigma}$ / K**
0.0	1.73	720	155
0.1	4.04	1013	138
0.2	2.28	857	162
0.3	2.19	856	176
0.4	2.03	850	190

Table 4-8. Linear fitting parameters for the fractional Walden plots in Figure 4-4.

x(Na[FSA])	**α**	**Log (C'/S cm^2 mol^{-1})**
0.0	0.9645	-0.1593
0.1	0.9249	-0.1151
0.2	0.9550	-0.2376
0.3	0.9486	-0.2186
0.4	0.9472	-0.2410

Table 4-9. Fitting results of the EIS for the Na/Na symmetric cells with the Na[FTA]-[C_3C_1pyrr][FTA] system (Figure 4-8).[a]

x(Na[FTA])		0.1	0.2	0.3	0.4
298 K	R_{bulk} / Ω	7.2	12	23	40
	R_{int} / Ω	7758	2938	1432	996
	C.F. / Hz	17.1	55.5	84.5	125
	Q / F $s^{\alpha-1}$	1.46×10^{-6}	2.03×10^{-6}	2.62×10^{-6}	2.65×10^{-6}
	α	0.93	0.89	0.91	0.90
333 K	R_{bulk} / Ω	2.7	3.5	4.2	11
	R_{int} / Ω	48	33	25	15
	C.F. / Hz	2906	2906	4306	6306
	Q / F $s^{\alpha-1}$	3.84×10^{-6}	3.19×10^{-6}	4.26×10^{-6}	7.02×10^{-6}
	α	0.89	0.94	0.91	0.88
363 K	R_{bulk} / Ω	3.43	2.58	2.62	4.22
	R_{int} / Ω	5.63	3.17	2.66	2.18
	C.F. / Hz	1.4×10^{4}	1.4×10^{4}	2.1×10^{4}	2.1×10^{4}
	Q / F $s^{\alpha-1}$	4.44×10^{-6}	3.36×10^{-6}	7.91×10^{-6}	42.2×10^{-6}
	α	0.93	1	0.94	0.82

[a] *C.F.*, Q, and α denote characteristic frequency, CPE parameter, and CPE exponent, respectively.

Table 4-10. Coulombic efficiencies (%) of the Na/HC cells with *x*(Na[FTA]) = 0.1−0.4 at the charge-discharge rate of 20 mA g^{-1} from the initial to fifth cycles.

***x*(Na[FTA])**	**0.1**	**0.2**	**0.3**	**0.4**
1st.	81.3	78.3	73.8	65.4
2nd	98.4	96.1	90.9	83.3
3rd	98.7	96.8	92.9	86.0
4th	98.9	97.2	93.3	89.4
5th	99.1	97.3	93.7	92.4

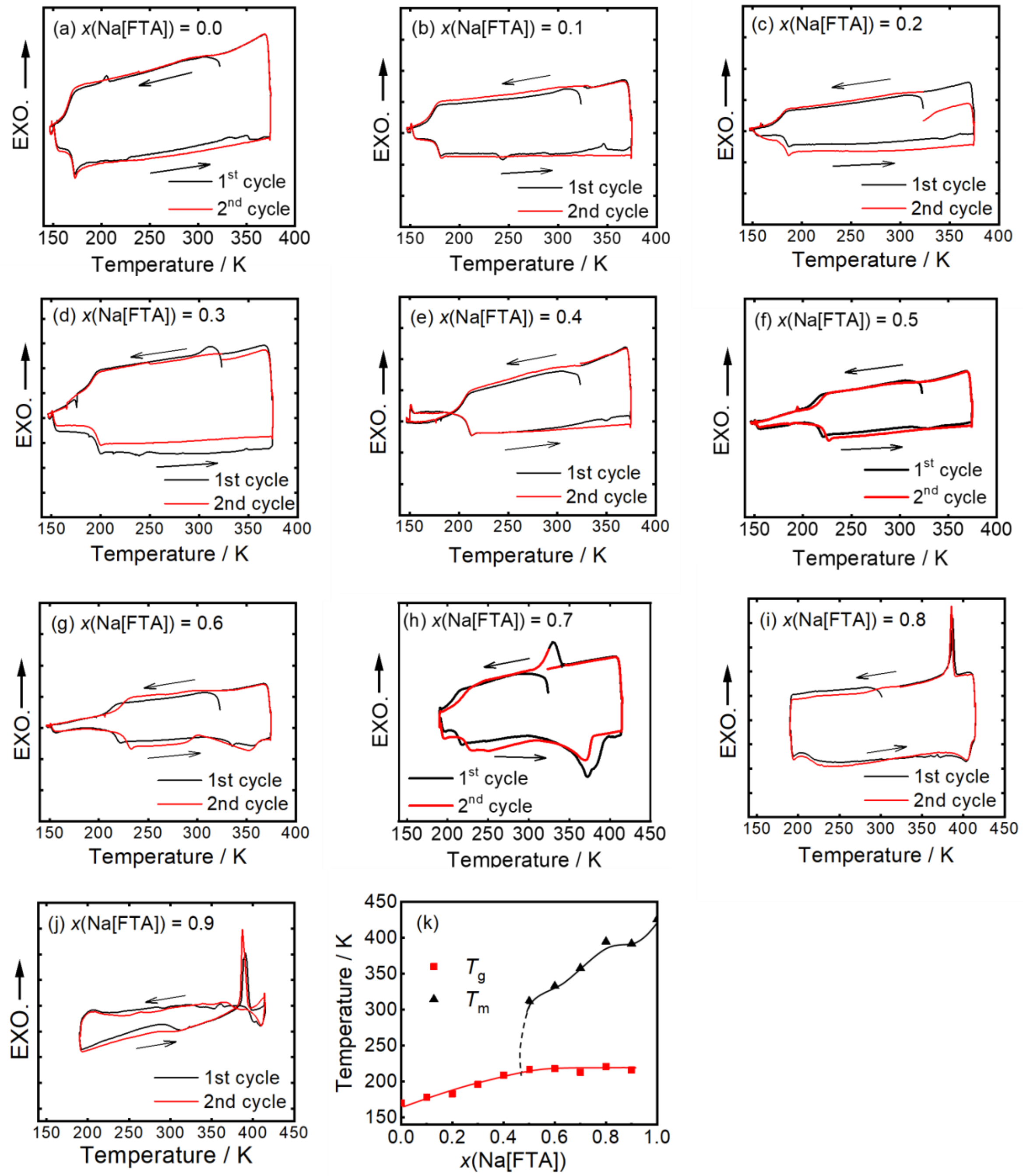

Figure 4-1. (a-j) DSC curves at x(Na[FTA]) = 0.0–0.9, and (k) the resultant phase diagram for the Na[FTA]-[C_3C_1pyrr][FTA] system. T_g: glass transition temperature, and T_m: melting point. T_g and T_m were determined from the first cycle.

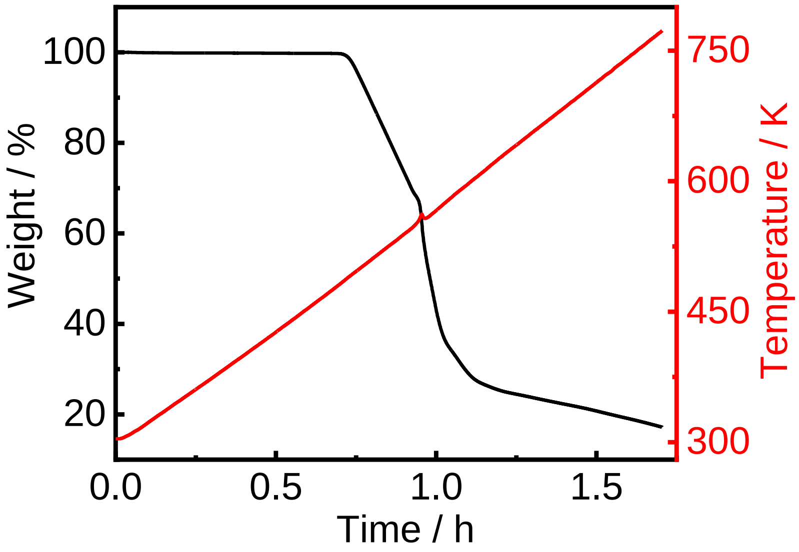

Figure 4-2. TG curves of the Na[FTA]-[C_3C_1pyrr][FTA] IL system. Scan rate: 5 K min^{-1}.

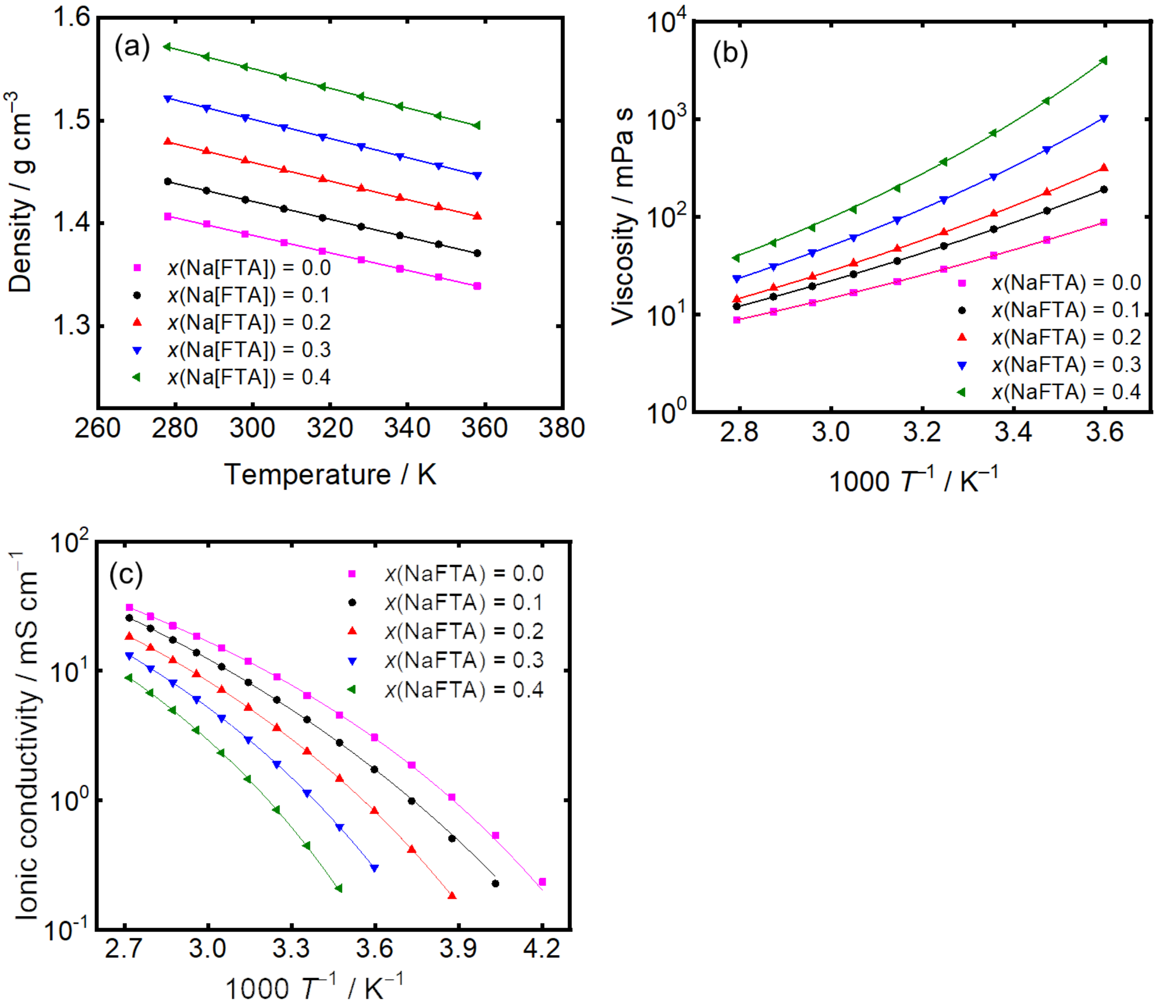

Figure 4-3. Temperature dependence of (a) density, (b) viscosity, and (c) ionic conductivity of the Na[FTA]-[C$_3$C$_1$pyrr][FTA] ILs in the *x*(Na[FTA]) range of 0.0–0.4.

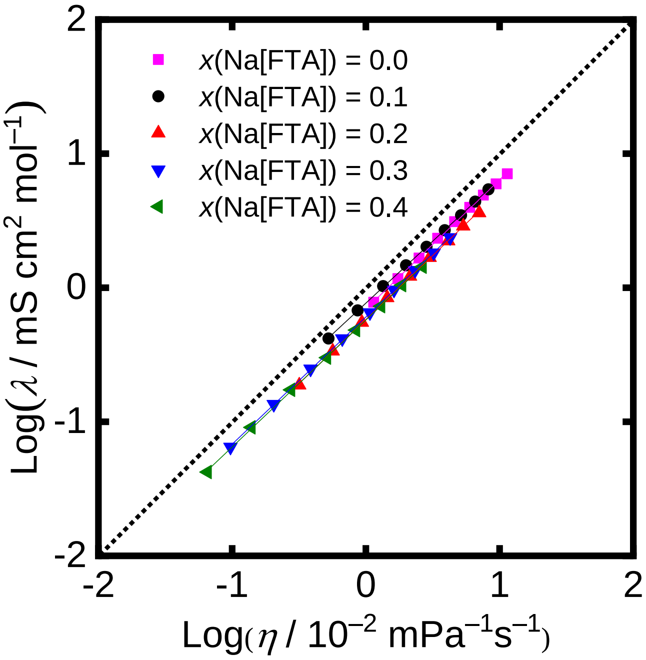

Figure 4-4. Walden plots of the Na[FTA]-[C_3C_1pyrr]-[FTA] ILs for *x*(Na[FTA]) = 0.0−0.4. The dashed line is a visual guide representing α = 1 in Eq. 3-6.

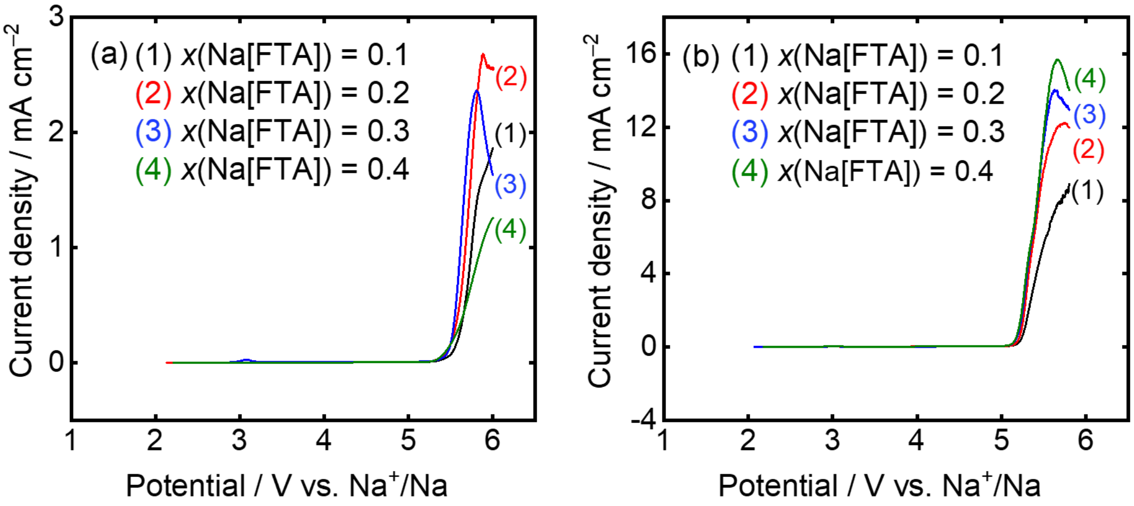

Figure 4-5. Linear sweep voltammograms of a Pt electrode at a scan rate of 1 mV s^{-1} in the Na[FTA]-[C_3C_1pyrr][FTA] ILs at x(Na[FTA]) = 0.1−0.4 at (a) 298 K and (b) 363 K.

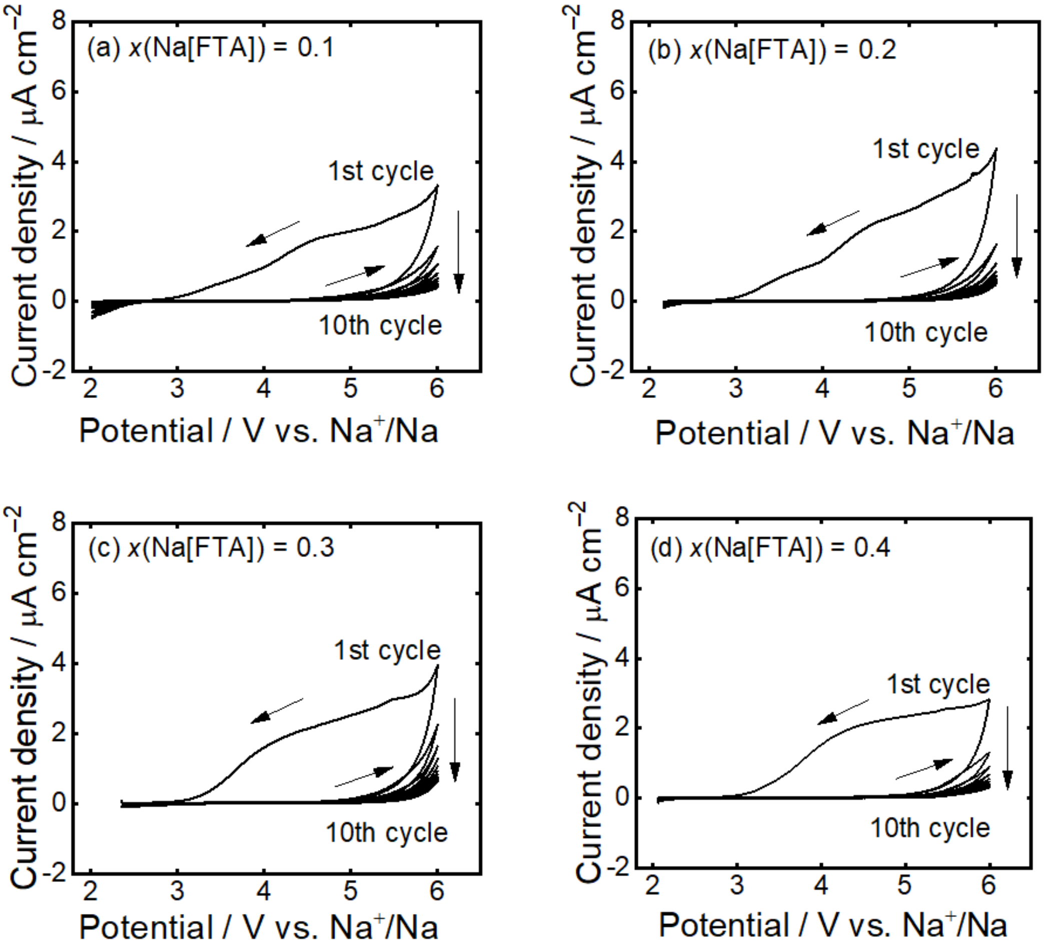

Figure 4-6. Cyclic voltammograms of an Al electrode at 298 K in the Na[FTA]-[C_3C_1pyrr][FTA] ILs at *x*(Na[FTA]) = (a) 0.1, (b) 0.2, (c) 0.3, and (d) 0.4 recorded at a scan rate of 1 mV s^{-1}.

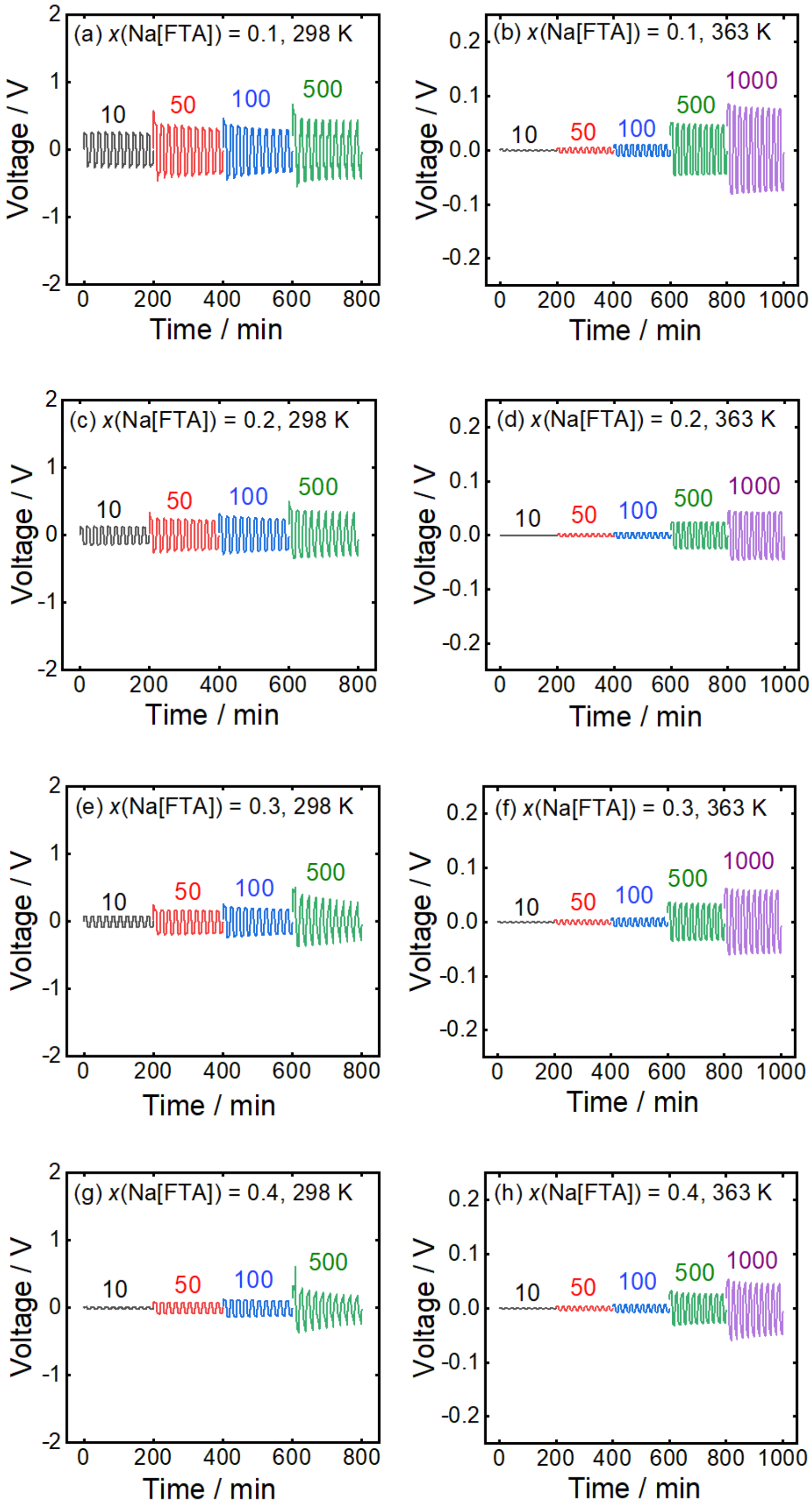

Figure 4-7. Na/Na symmetrical cell polarization voltage profiles at 298 and 363 K with the Na[FTA]-[C_3C_1pyrr][FTA] ILs (*x*(Na[FTA]) = (a, b) 0.1, (c, d) 0.2, (e, f) 0.3, and (g, h) 0.4). The unit of current density is μA·cm^{-2}.

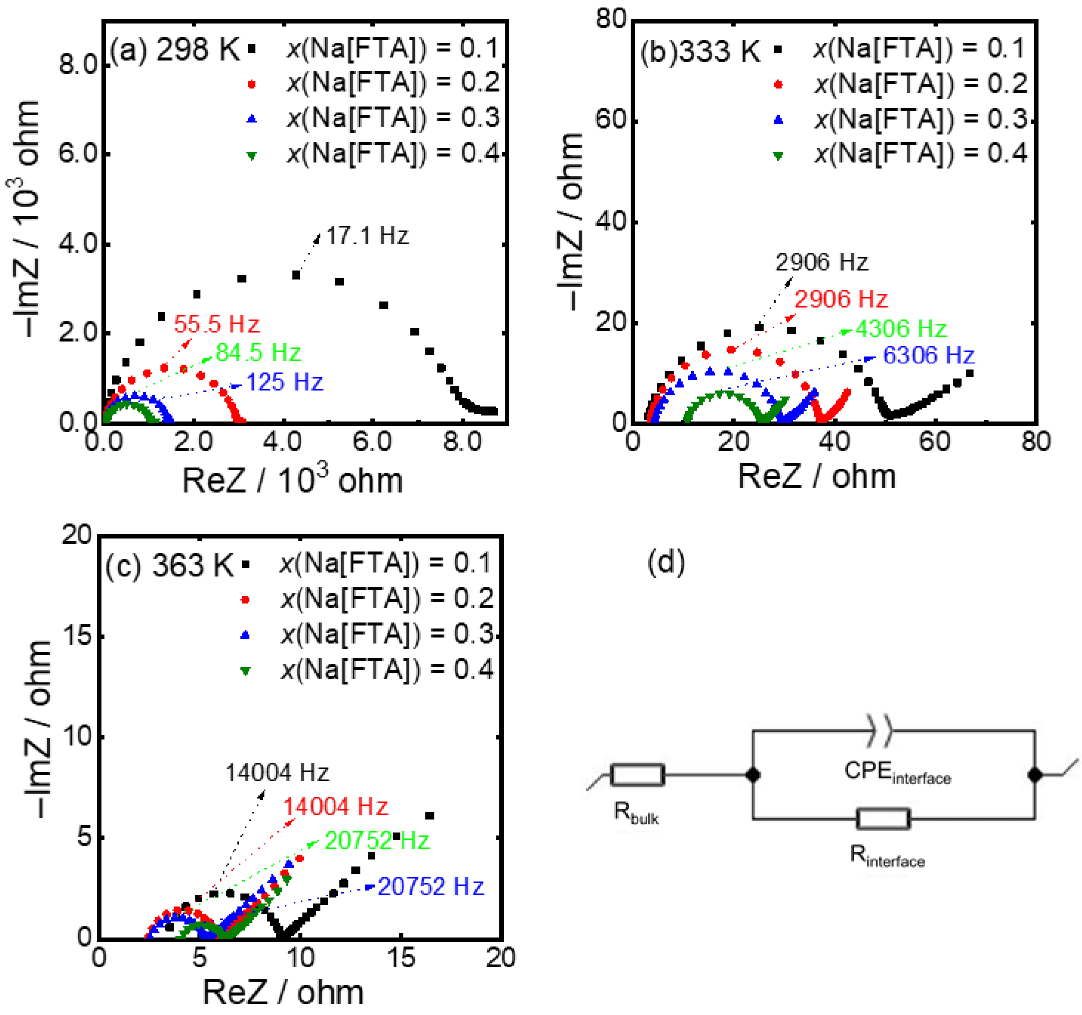

Figure 4-8. Nyquist plots of the Na/Na symmetric cells with the Na[FTA]-[C_3C_1pyrr][FTA] ILs (*x*(Na[FTA]) = 0.1−0.4) at (a) 298 K (characteristic frequencies are 17.1 Hz for *x*(Na[FTA]) = 0.1, 55.5 Hz for *x*(Na[FTA]) = 0.2, 84.5 Hz for *x*(Na[FTA]) = 0.3, 125 Hz for *x*(Na[FTA]) = 0.4), (b) 333 K (characteristic frequencies are 2906 Hz for *x*(Na[FTA]) = 0.1, 2906 Hz for *x*(Na[FTA]) = 0.2, 4306 Hz for *x*(Na[FTA]) = 0.3, 6306 Hz for *x*(Na[FTA]) = 0.4), and (c) 363 K (characteristic frequencies are 14004 Hz for *x*(Na[FTA]) = 0.1, 14004 Hz for *x*(Na[FTA]) = 0.2, 20752 Hz for *x*(Na[FTA]) = 0.3, 20752 Hz for *x*(Na[FTA]) = 0.4), in the frequency range of 100 kHz−10 mHz. (d) Equivalent circuit. AC amplitude = 10 mV.

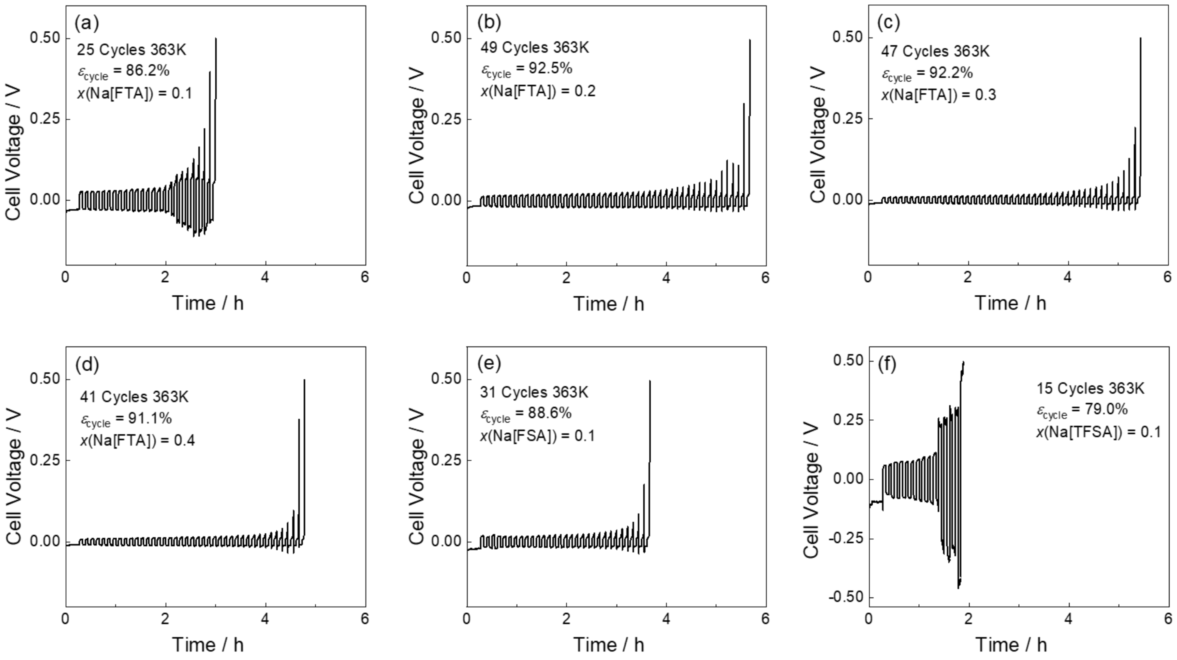

Figure 4-9. Voltage profiles during Na deposition/dissolution at 363 K in (a–d) Na[FTA]-[C_3C_1pyrr][FTA] at x(Na[FTA]) = 0.1–0.4, (e) Na[FSA]-[C_3C_1pyrr][FSA] at x(Na[FSA]) = 0.1, and (f) Na[TFSA]-[C_3C_1pyrr][TFSA] at x(Na[TFSA]) = 0.1. The working and counter electrodes were Al and Na plates, respectively. Na metal of 0.08 C cm^{-2} was deposited on the Al substrate, and 0.02 C cm^{-2} Na deposition and dissolution was repeated until the electrode potential reached 0.5 V vs. Na$^+$/Na during dissolution. The current density was ± 0.1 mA cm^{-2} for all tests.

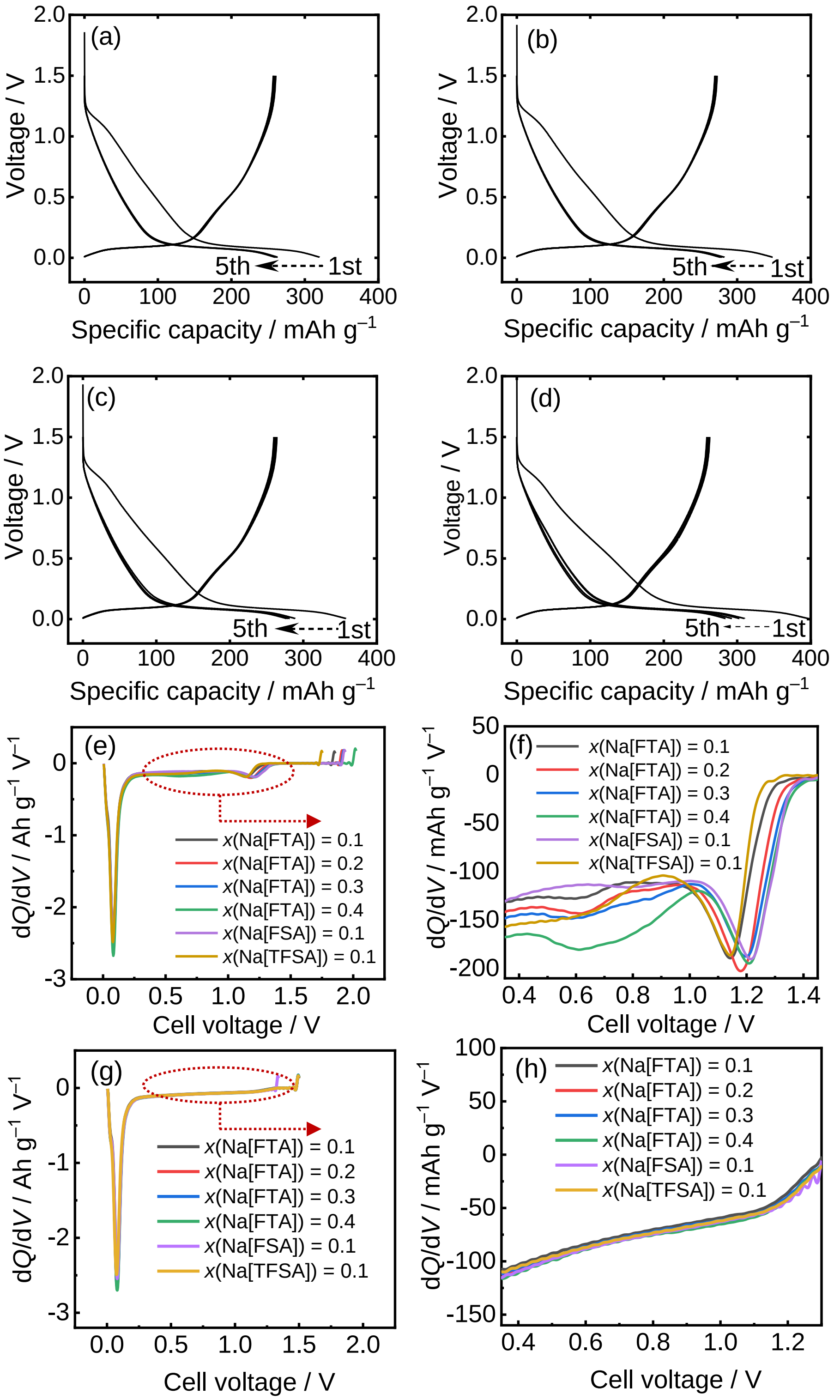

Figure 4-10. Charge-discharge curves of the Na/HC cells with the Na[FTA]-[C_3C_1pyrr][FTA] ILs at x(Na[FTA]) = (a) 0.1, (b) 0.2, (c) 0.3, and (d) 0.4 at 363 K. Charge-discharge rate: 20 mA g^{-1}. The corresponding differential capacity vs. voltage (dQ/dV) plots (e, f) and (g, h) show the first and fifth charge cycle behavior with those observed for Na[FTA]-[C_3C_1pyrr][FTA] ILs at x(Na[FTA]) = 0.1–0.4, Na[FSA]-[C_3C_1pyrr][FSA] at x(Na[FSA]) = 0.1 and Na[TFSA]-[C_3C_1pyrr][TFSA] at x(Na[TFSA]) = 0.1.

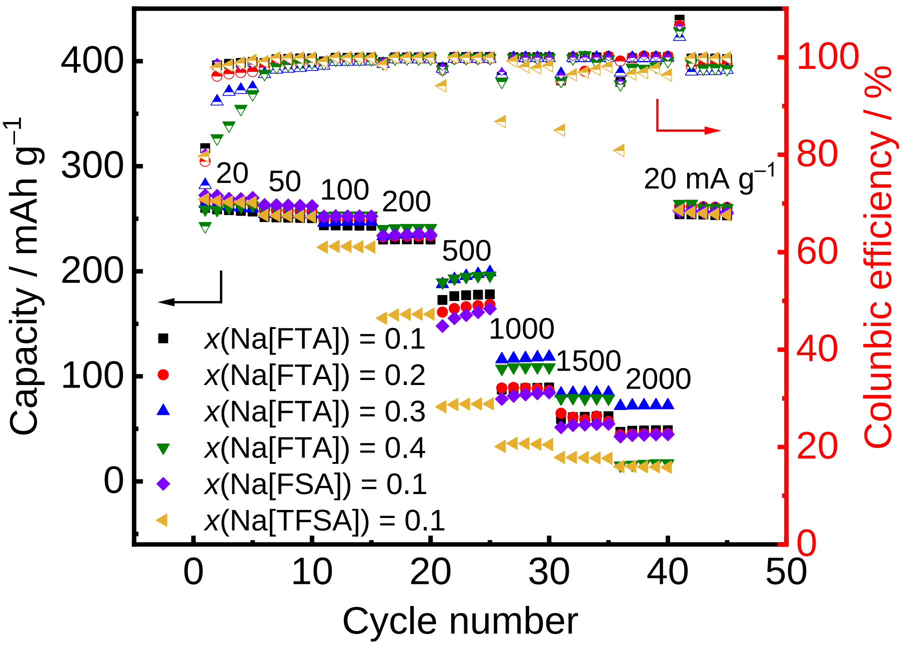

Figure 4-11. Rate capability of the Na/HC cells with Na[FTA]-[C_3C_1pyrr][FTA] at x(Na[FTA]) = 0.1–0.4, Na[FSA]-[C_3C_1pyrr][FSA] at x(Na[FSA]) = 0.1, and Na[TFSA]-[C_3C_1pyrr][TFSA] at x(Na[TFSA]) = 0.1 at 363 K. Charge-discharge rate: from 20 to 2000 mA g^{-1}. Cut-off voltages: 0.005–1.5 V. Coulombic efficiency is plotted with half-filled marks.

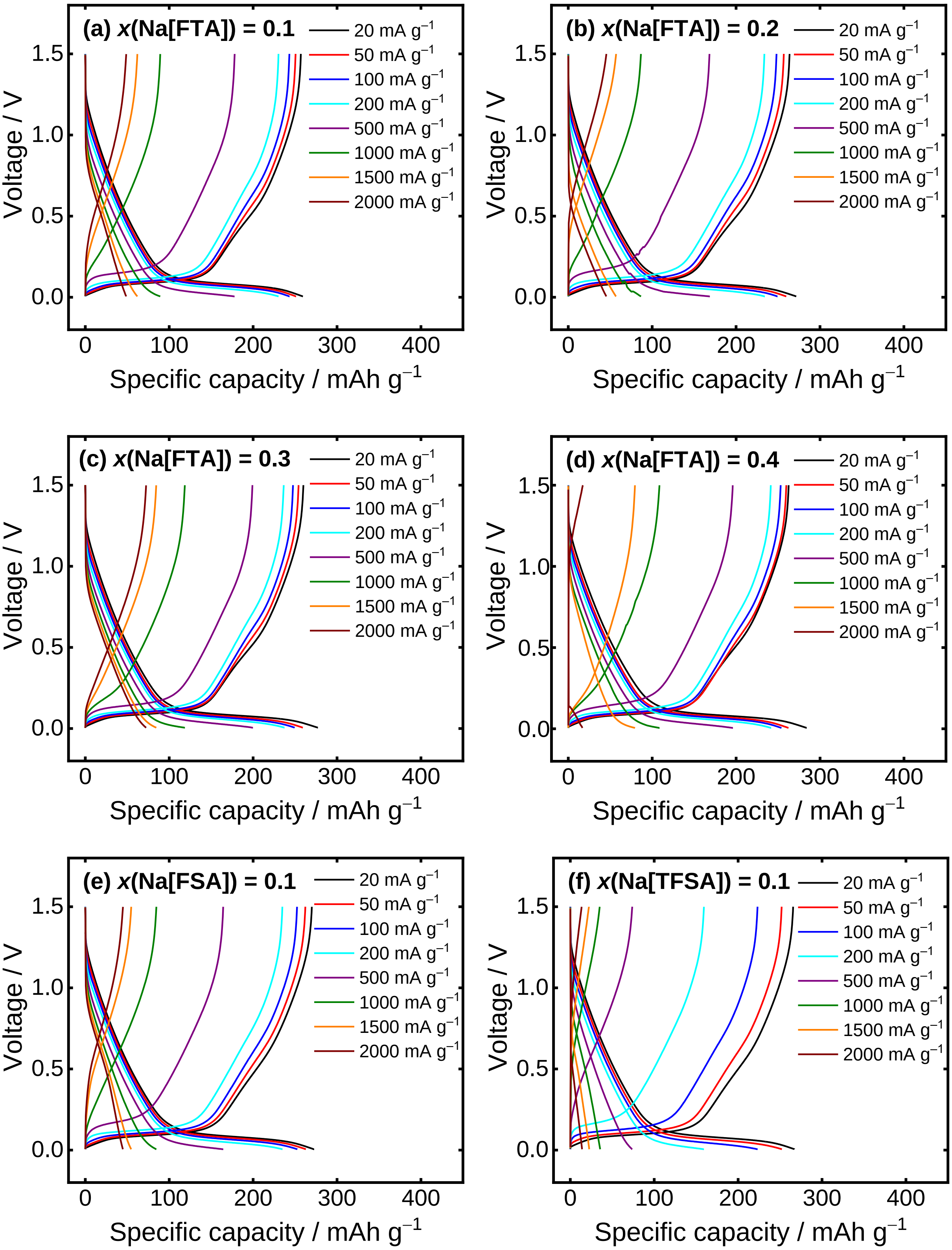

Figure 4-12. Charge-discharge curves of the HC/Na cells with (a–d) Na[FTA]-[C_3C_1pyrr][FTA] at x(Na[FTA]) = 0.1–0.4, (e) Na[FSA]-[C_3C_1pyrr][FSA] at x(Na[FSA]) = 0.1, and (f) Na[TFSA]-[C_3C_1pyrr][TFSA] at x(Na[TFSA]) = 0.1 at 363 K.

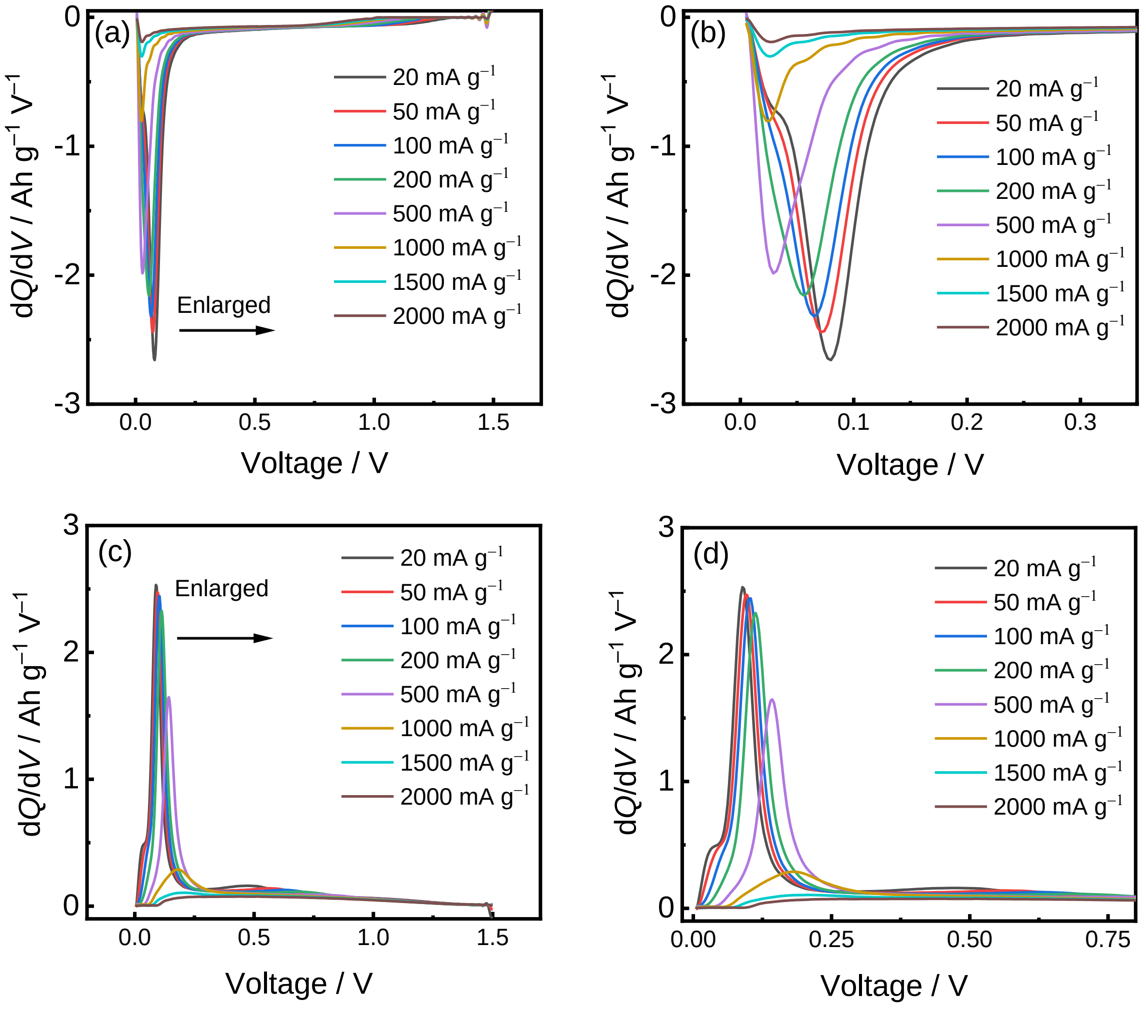

Figure 4-13. The d*Q*/d*V* plots of (a, b) charge and (c, d) discharge curves of the HC/Na cell with the Na[FTA]-[C_3C_1pyrr][FTA] IL at *x*(Na[FTA]) = 0.3 in charge-discharge rate from 20 to 2000 mA g^{-1} at 363 K.

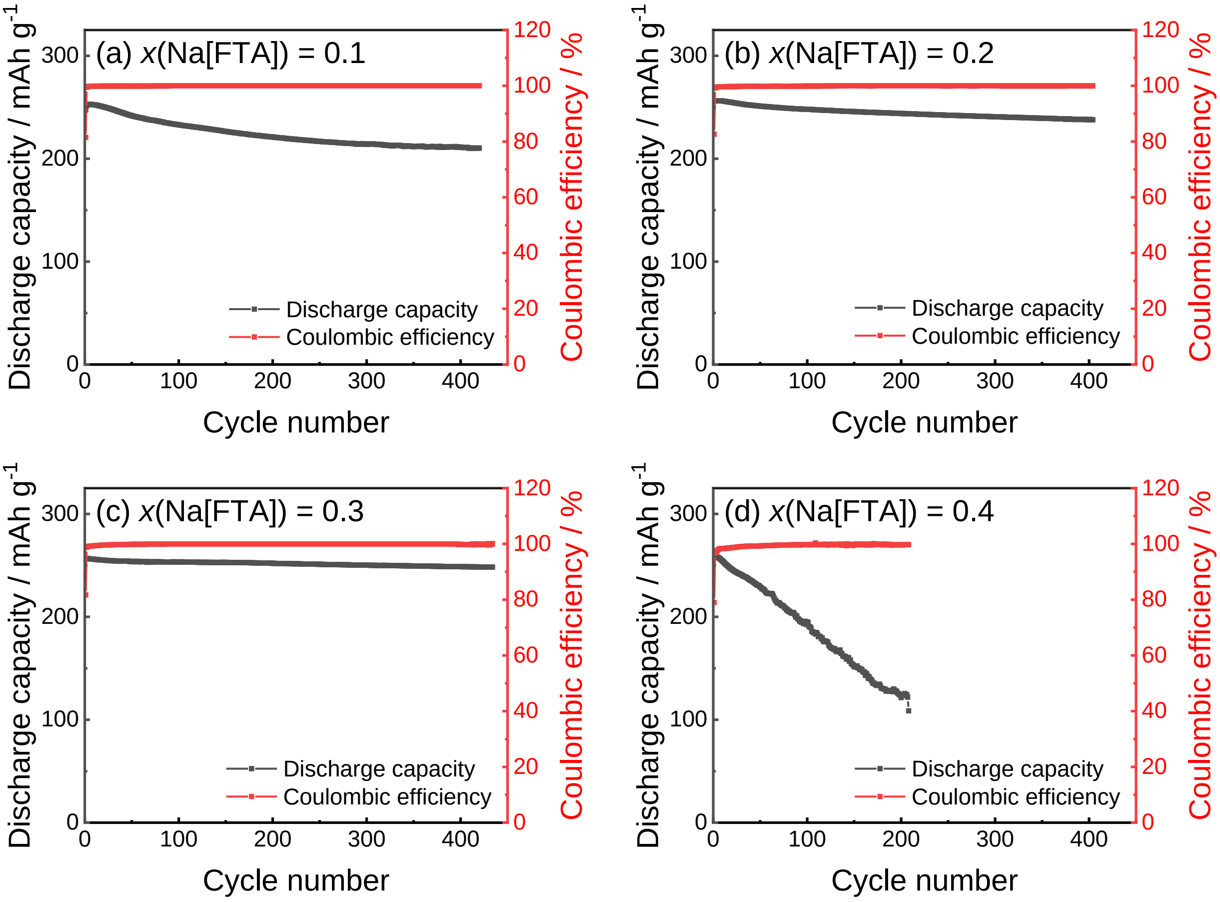

Figure 4-14. Cycling performance of the HC electrode at 363 K. Electrolyte: Na[FTA]-[C_3C_1pyrr][FTA] with *x*(Na[FSA]) = (a) 0.1, (b) 0.2, (c) 0.3, and (d) 0.4. Current rate: 200 mA g^{-1}. Cut-off voltages: 0.005–1.5 V.

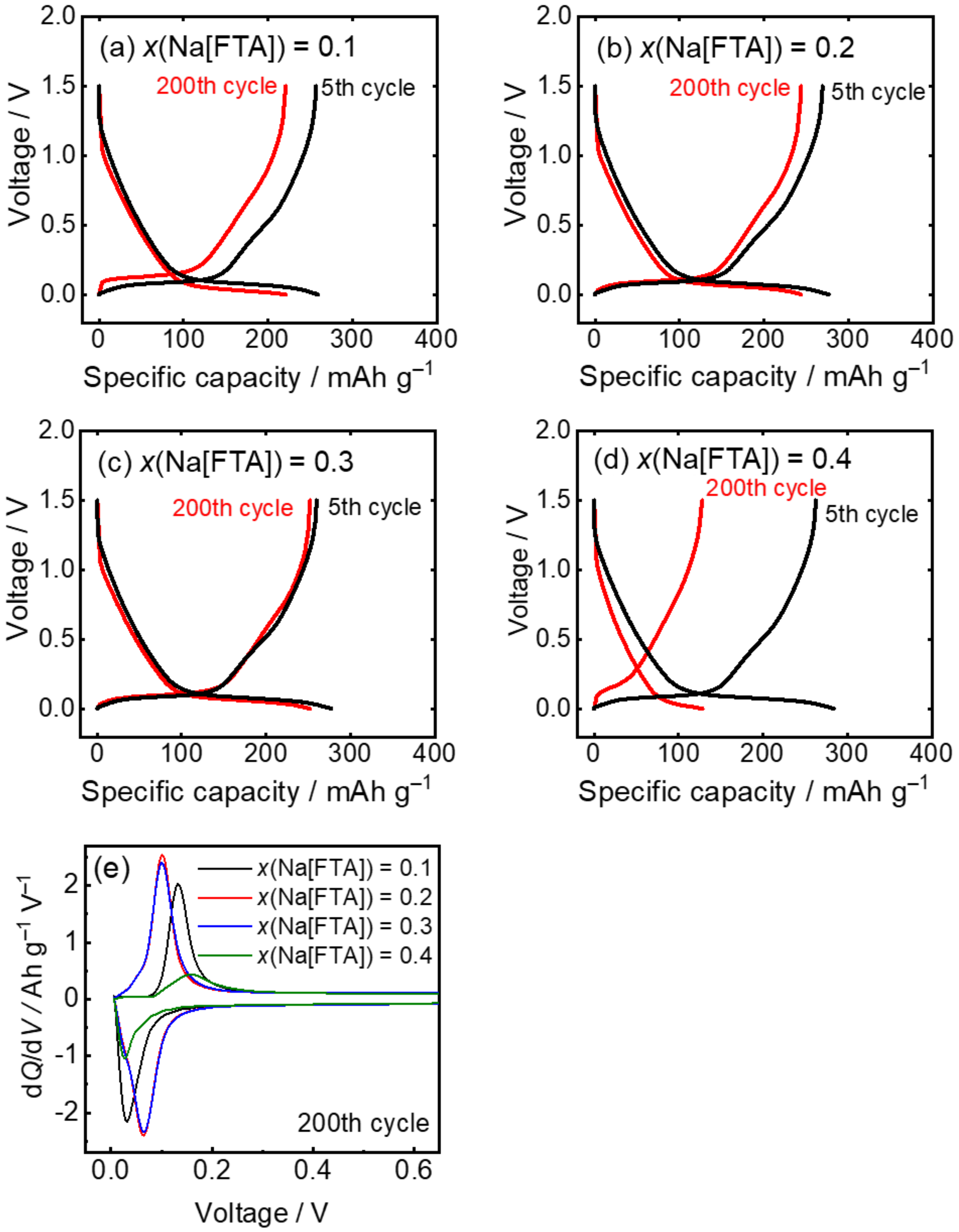

Figure 4-15. (a-d) Charge-discharge curves at the 200th cycle and (e) the corresponding dQ/dV plots of the HC/Na cells with the Na[FTA]-[C_3C_1pyrr][FTA] ILs at 363 K. Charge-discharge rate: 200 mA g^{-1}; x(Na[FTA]) = 0.1–0.4.

References

[1] J. P. Hallett, T. Welton, Chem. Rev., 111 (2011) 3508-3576.

[2] H. Ohno, Electrochemical Aspects of Ionic Liquids, John Wiley & Sons, 2005.

[3] D. Anseán, M. González, J. Viera, V. García, C. Blanco, M. Valledor, J. Power Sources, 239 (2013) 9-15.

[4] U. R. Koleti, C. Zhang, R. Malik, T. Q. Dinh, J. Marco, J. Energy Storage, 24 (2019) 100798.

[5] M. Ouyang, Z. Chu, L. Lu, J. Li, X. Han, X. Feng, G. Liu, J. Power Sources, 286 (2015) 309-320.

[6] J. Reiter, S. Jeremias, E. Paillard, M. Winter, S. Passerini, Phys. Chem. Chem. Phys., 15 (2013) 2565-2571.

[7] S. Jeremias, M. Carewska, L. Conte, S. Passerini, G. B. Appetecchi, RSC Adv., 3 (2013) 17755-17761.

[8] J. Song, B. Xiao, Y. Lin, K. Xu, X. Li, Adv. Energy Mater., (2018) 1703082.

[9] A. Ponrouch, D. Monti, A. Boschin, B. Steen, P. Johansson, M. Palacin, J. Mater. Chem. A, 3 (2015) 22-42.

[10] H. Matsumoto, N. Terasawa, T. Umecky, S. Tsuzuki, H. Sakaebe, K. Asaka, K. Tatsumi, Chem. Lett., 37 (2008) 1020-1021.

[11] K. Kubota, T. Nohira, T. Goto, R. Hagiwara, Electrochem. Commun., 10 (2008) 1886-1888.

[12] K. Matsumoto, Y. Okamoto, T. Nohira, R. Hagiwara, J. Phys. Chem. C, 119 (2015) 7648-7655.

[13] M. Forsyth, H. Yoon, F. Chen, H. Zhu, D. R. MacFarlane, M. Armand, P. C. Howlett, J. Phys. Chem. C, 120 (2016) 4276-4286.

[14] A. Basile, M. Hilder, F. Makhlooghiazad, C. Pozo-Gonzalo, D. R. MacFarlane, P. C. Howlett, M. Forsyth, Adv. Energy Mater., 8 (2018) 1703491.

[15] K. Matsumoto, T. Hosokawa, T. Nohira, R. Hagiwara, A. Fukunaga, K. Numata, E. Itani, S. Sakai, K. Nitta, S. Inazawa, J. Power Sources, 265 (2014) 36-39.

[16] D. Monti, E. Jónsson, M. R. Palacín, P. Johansson, J. Power Sources, 245 (2014) 630-636.

[17] J. S. Moreno, G. Maresca, S. Panero, B. Scrosati, G. Appetecchi, Electrochem. Commun., 43 (2014) 1-4.

[18] A. Moretti, S. Jeong, G. A. Giffin, S. Jeremias, S. Passerini, J. Power Sources, 269 (2014) 645-650.

[19] R.-S. Kühnel, J. Reiter, S. Jeong, S. Passerini, A. Balducci, Electrochem. Commun., 38 (2014) 117-119.

[20] J. Hwang, K. Matsumoto, R. Hagiwara, Adv. Sustainable Syst., 2 (2018) 1700171.

[21] R. Hagiwara, K. Matsumoto, J. Hwang, T. Nohira, Chem. Rec., 19 (2019) 758-770.

[22] M. Arnaiz, P. Huang, J. Ajuria, T. Rojo, E. Goikolea, A. Balducci, Batteries Supercaps, 1 (2018) 204-208.

[23] C. Ding, T. Nohira, R. Hagiwara, A. Fukunaga, S. Sakai, K. Nitta, Electrochim. Acta, 176 (2015) 344-349.

[24] H. Vogel, Phys. Z, 22 (1921) 645-646.

[25] G. Tammann, W. Hesse, Z. Anorg. Allg. Chem, 156 (1926) 245-257.

[26] G. S. Fulcher, J. Am. Ceram. Soc., 8 (1925) 339-355.

[27] M. Galiński, A. Lewandowski, I. Stępniak, Electrochim. Acta, 51 (2006) 5567-5580.

[28] W. Xu, E. I. Cooper, C. A. Angell, J. Phys. Chem. B, 107 (2003) 6170-6178.

[29] H. Tokuda, K. Hayamizu, K. Ishii, M. A. B. H. Susan, M. Watanabe, J. Phys. Chem. B, 108 (2004) 16593-16600.

[30] A. Noda, K. Hayamizu, M. Watanabe, J. Phys. Chem. B, 105 (2001) 4603-4610.

[31] D. R. MacFarlane, M. Forsyth, E. I. Izgorodina, A. P. Abbott, G. Annat, K. Fraser, Phys. Chem. Chem. Phys., 11 (2009) 4962-4967.

[32] C. Schreiner, S. Zugmann, R. Hartl, H. J. Gores, J. Chem. Eng. Data, 55 (2010) 4372-4377.

[33] K. R. Harris, J. Phys. Chem. B, 114 (2010) 9572-9577.

[34] H. Yoon, P. Howlett, A. Best, M. Forsyth, D. MacFarlane, J. Electrochem. Soc., 160 (2013) A1629-A1637.

[35] X.-F. Luo, A. S. Helal, C.-T. Hsieh, J. Li, J.-K. Chang, Nano Energy, 49 (2018) 515-522.

[36] D. Iermakova, R. Dugas, M. Palacín, A. Ponrouch, J. Electrochem. Soc., 162 (2015) A7060-A7066.

[37] J. Hwang, K. Matsumoto, R. Hagiwara, J. Phys. Chem. C, 122 (2018) 26857−26864.

[38] C.-Y. Chen, T. Kiko, T. Hosokawa, K. Matsumoto, T. Nohira, R. Hagiwara, J. Power Sources, 332 (2016) 51-59.

[39] C.-Y. Chen, K. Matsumoto, T. Nohira, C. Ding, T. Yamamoto, R. Hagiwara, Electrochim. Acta, 133 (2014) 583-588.

[40] T. Hosokawa, K. Matsumoto, T. Nohira, R. Hagiwara, A. Fukunaga, S. Sakai, K. Nitta, J. Phys. Chem. C, 120 (2016) 9628-9636.

[41] I. A. Shkrob, T. W. Marin, Y. Zhu, D. P. Abraham, J. Phys. Chem. C, 118 (2014)

19661-19671.

[42] M. Ishikawa, T. Sugimoto, M. Kikuta, E. Ishiko, M. Kono, J. Power Sources, 162 (2006) 658-662.

[43] S. Komaba, W. Murata, T. Ishikawa, N. Yabuuchi, T. Ozeki, T. Nakayama, A. Ogata, K. Gotoh, K. Fujiwara, Adv. Funct. Mater., 21 (2011) 3859-3867.

[44] K. Takada, Y. Yamada, E. Watanabe, J. Wang, K. Sodeyama, Y. Tateyama, K. Hirata, T. Kawase, A. Yamada, ACS Appl. Mater. Interfaces, 9 (2017) 33802-33809.

Chapter 5

Potassium Difluorophosphate as an Electrolyte Additive for Potassium Ion Batteries

5.1 Introduction

PIBs have shown their potential as LIB replacements. The redox potential of K^+/K (–2.93 V vs. standard hydrogen electrode) is lower than that of Na^+/Na (–2.71 V) and still very close to that of Li^+/Li (–3.04 V). This demonstrates prospects of a battery with a competitive energy density and high voltage operation capabilities.[1-6] Although K^+ has a larger ionic radius of 1.38 Å compared to Li^+ (0.76 Å) and Na^+ (1.02 Å), it has the smallest Stokes radius in certain solvents due to the weaker Lewis acidity, therefore solvating ability of K^+ is favorable to the transport behavior within the electrolyte and charge transfer at the electrolyte–electrode interface for PIBs.[7, 8]

The compatibility of well-established LIB components such as graphite negative electrodes in PIBs has also stimulated their advancement.[9] Graphite has been the common choice for negative electrodes for its ability to store cations, forming graphite intercalation compounds (GICs). However, the graphite negative electrodes are not suitable in SIBs since only a limited amount of Na^+ (< 40 mAh g^{-1}) can be stored within the graphitic layers. This is generally ascribed to the thermodynamic instability of Na–GICs,[10, 11] unless a solvent is cointercalated between two layers.[12, 13] On the other hand, K-GICs possess a rich variety of phases over a wide range of K stoichiometry, making them suitable for battery operations. Just like in the Li intercalation process, the structural properties of the K-GIC is dependent on the amount of K intercalants present in the graphitic layers at each stage.[14-17]

The staging mechanism of K-GICs consists of a sequential formation of KC_{60} (stage-5), KC_{48} (stage-4), KC_{36} (stage-3), KC_{24} (stage-2), and KC_8 (stage-1).[18] Formation of the KC_8 (stage-1 K-GIC) provides a theoretical capacity of 279 $mAhg^{-1}$.[19] Although previous works have reported the formation of phase-pure KC_8 under specific conditions,[20, 21] it is worth noting that the "fully" charged state of graphite is usually accompanied by the residual KC_{24} (stage-2 K-GIC) which remarkably diminishes the practically attainable capacity.[2, 8, 14, 22] The incomplete potassiation is generally attributed to the ineffectiveness of solid electrolyte–interphase (SEI) formed at the electrode surface in preventing continuous decomposition of the electrolyte, which eventually leads to excessive SEI buildup and large cell impedance.[23] Since the quantity of the SEI is determined by the electrolyte,[24] the selection and optimization of electrolytes are critical in harnessing the high performance of graphite anodes in PIBs. To tackle this issue, different approaches have been taken to develop advanced electrolytes for PIB operations. For instance, concentrated electrolyte ($K[N(SO_2F)_2]$:ethyl methyl carbonate with a molar ratio of 1:2.5) has been used to facilitate the formation of a robust inorganic SEI on the graphite surface.[20] There have also been attempts to optimize the solvent formulation to reduce the growth rate of SEI.[22]

In this chapter, the effects of the potassium difluorophosphate (KDFP) additive in a KPF_6-based organic electrolyte have been investigated. A three-electrode cell with a Pt or Al working electrode were used to analyze the basic electrochemical stability of the electrolytes with and without KDFP. Potassium deposition/dissolution was evaluated using K/Al cells and K/K symmetric cells, and subsequent analysis of interfacial behavior was performed through electrochemical impedance spectroscopy (EIS). The potassiation/depotassiation processes of the graphite electrode were confirmed by X-ray diffraction (XRD) and Raman spectroscopy. Additionally, in order to understand the improved electrochemical properties, X-ray photoelectron spectroscopy (XPS) was also performed to examine the different SEI components in the electrolyte with KDFP. The results were compared with a commonly used film-forming additive fluoroethylene carbonate (FEC) under the same conditions. This work has also employed galvanostatic intermittent titration technique (GITT) as well as rate capability and cycle tests to provide a comprehensive electrochemical evaluation of the graphite electrode.

5.2 Experimental

KPO_3 and KPF_6 (Aldrich, purity > 99%) were vacuum-dried at 353 K for 24 h before use. KDFP was synthesized through the reaction of KPO_3 and KPF_6 in the molar ratio of 2:1 at 593 K in a platinum crucible over three days.[25] The purity of the as-prepared KDFP was confirmed by X-ray powder diffraction (Figure 5-1). The as-prepared KDFP powder was weighed to the target weight ratio and added into 0.5 M KPF_6 in ethylene carbonate and diethylene carbonate (EC/DEC, in a 1:1 volume ratio, Kishida Chemical Co., Ltd., >99.0 % purity, water content < 10 ppm) and continuously stirred for 1 day in an Ar-filled glovebox until uniformity was achieved. Graphite electrodes were prepared by mixing graphite as an active material (particle size of 10 μm in average SNO-10, SEC Carbon) with carbon black (Wako Pure Chemical Industries, Japan), carboxyl methylcellulose (CMC), and styrene-butadiene rubber (SBR) at a weight ratio of 80:10:5:5 in NMP (Wako Pure Chemical Industries, >99.0 % purity) by a solid/liquid ratio of 0.51. The slurry was then pasted onto copper (Cu) foils and vacuum-dried at 333 K overnight. The electrodes with 10mm diameter were punched out from the foil and the electrodes were vacuum-dried at 383 K for 10 h before cell assembly. The average mass loading and density of prepared graphite electrode is 1.3 mg/cm^{-2}. and 0.7 g/cm^{-2}, respectively. Potassium metal (Kojundo Chemical Laboratory, purity 99.5%) was pressed onto an Al current collector and used as the counter electrode.

Cyclic voltammetry was carried out using a conventional three-electrode cell configuration under argon atmosphere at 298 K with an Al or Pt working electrode, a Pt wire counter electrode, and an Ag^+/Ag reference electrode. The reference electrode consisted of silver wire immersed in 0.05 mol kg^{-1} $AgSO_3CF_3$/electrolyte solution (0.5 M KPF_6-EC/DEC (1:1, v:v) with or without KDFP or FEC additive) filled in a glass tube with porous frit. The electrode potential in the three-electrode tests was converted to the K^+/K standard based on the experimentally determined K^+/K potential (–3.83 V vs. Ag^+/Ag, see Figure 5-2). The electrode potential was controlled and recorded by a potentiostat (Hokuto Denko Co., Ltd., HZ-5000). The efficiency of K metal deposition/dissolution was measured in 2032-type coin cells with a Cu plate working electrode (10 mm diameter, 0.2 mm thickness) and a K metal counter electrode. The K/K symmetric cells were assembled for electrochemical impedance and polarization tests with K metal on both sides of the cell. A glass fiber filter (Whatman, GF/A, thickness 260 μm) was used as the separator. Charge/discharge measurements were performed in a K/graphite half-cell using a charge-discharge unit (Hokuto Denko, HJ1001SD8) after resting for 1 h. Rate capability was tested at constant rates in the sequence of C/20, C/10, C/5, C/2, 1C, and C/20 (where 1 C corresponds to a current density of 279 mA g^{-1} based on the theoretical capacity of KC_8) within a voltage range of 0.001–2.5 V. Cycling tests were performed at a constant rate of C/3 in the same voltage range as the rate capability test. Galvanostatic intermittent titration technique (GITT) measurement was measured by applying a constant rate of C/20 for 30 min, followed by voltage relaxation for 2 h. The electrolytes utilized in the aforementioned electrochemical measurements were 0.5 M

KPF_6-EC/DEC (1:1, v:v) with 0 wt%, 0.1 wt%, and 0.2 wt% KDFP additive. The 0.5 M KPF_6-EC/DEC (1:1, v:v) electrolytes with 0.3 wt% and 3 wt% FEC additives were also examined in the same condition for comparison. Ionic conductivity of the electrolyte was measured by an AC impedance technique using a 3532-80 impedance analyzer (Hioki E.E. Corp.). Samples were sealed in a T-shaped cell with two stainless steel electrodes in the glove box and placed in a temperature-controlled thermostatic chamber (SU-242, ESPEC). The density of all studied electrolytes shows similar value and trend (Figure 5-6 (b)), which was measured with an oscillating U-tube density meter (DMA 4500 M, Anton Paar GmbH).

The samples for the XRD measurements were set in an airtight cell under a dry argon atmosphere. Raman spectra were collected by DXR3 Smart Raman (Thermo Fisher Scientific) using a 532 nm diode-pumped solid-state laser for fresh and (de)potassiated graphite electrodes. The samples for Raman spectroscopy were sealed in a glass cell and isolated from the air. The SEI layer components were analyzed using *ex-situ* XPS (JEOL, JPS-9030, Mg *K*α source). The electrodes samples for XPS were washed with EC/DMC and dried at 298 K under vacuum overnight and an airtight transfer vessel was used for transferring the sample into XPS.

5.3 Results and Discussion

In the preliminary test to ascertain the solubility of KDFP in 0.5 M KPF_6-EC/DEC, saturation of the additive was found to occur between concentrations of 0.2 and 0.3 wt%. Subsequently, 0.5 M KPF_6-EC/DEC electrolyte containing 0 wt% KDFP, 0.1 wt% KDFP, and 0.2 wt% KDFP were used in the assembly of three-electrode cells using Pt (anodic side) and Al (anodic and cathodic sides) working electrodes. To assess the electrochemical behavior of the electrodes in the electrolyte, cyclic voltammetry was performed at 298 K. As illustrated in Figure 5-3 (a), cyclic voltammograms obtained on the Pt electrode in 0.5 M KPF_6 EC/DEC with 0 wt% KDFP demonstrated a relatively low anodic potential limit of 4.40 V vs. K^+/K attained at a current density of 0.1 mA cm^{-2}. Higher anodic potential limits of 5.26 V and 5.42 V are observed in electrolyte with 0.1 wt% KDFP and 0.2 wt% KDFP, respectively. Previous reports on difluorophosphate additives (specifically LiDFP in $LiPF_6$-based electrolytes) have suggested that the addition of KDFP suppresses the generation of hydrolized products (mainly HPO_2F_2), extending the electrochemical stability window of the electrolyte [26, 27]. For comparison, as shown in Figure 5-3 (b), the addition of 0.3 wt% and 3 wt% FEC also improves the anodic potential limit to 5.22 and 5.48 V, respectively compared to the case without additive. As shown in Figure 5-3 (c) and (d), the negligible current (less than 1 μA cm^{-2} acquired on the Al electrode during anodic scan in all studied electrolytes proves the compatibility of Al as a current collector owing to the passivation layer on Al regardless of the addition of additives.[28]

Cathodic scans were thereafter performed on the Al electrode in the selected 0.5 M KPF_6-EC/DEC electrolytes. In the case of 0 wt% KDFP electrolyte, a current corresponding to K metal deposition was observed to occur from –0.4 V vs. K^+/K, as shown in Figure 5-3 (c), shortly followed by K metal dissolution around 0 V vs. K^+/K upon the anodic scan. It is noted that the corresponding Coulombic efficiency of K deposition/dissolution in the cyclic voltammograms increases from 5 % in 0 wt% KDFP electrolyte to 31 % and 40 % in the 0.1 wt% KDFP and 0.2 wt% KDFP, respectively. Comparably, as shown in Figure 5-3 (d), similar effects are observed with respect to FEC additives where Coulombic efficiencies are 26 % and

33 % in 0.3 wt% FEC and 3wt% FEC electrolytes, respectively. This suggests that FEC additives are not as effective as KDFP.

The Coulombic efficiency ($\varepsilon_{\mathrm{cycle}}$) of K metal deposition/dissolution on a Cu plate working electrode assembled with a K metal counter electrode in a coin cell was derived. The $\varepsilon_{\mathrm{cycle}}$ was calculated in accordance with Eq. (3-1).[29] As illustrated in Figure 5-4, voltage profiles of the electrodes in 0.5 M KPF_6-EC/DEC electrolytes containing varying weight ratios of KDFP or FEC were obtained at 298 K. The results indicate a gradual improvement of the $\varepsilon_{\mathrm{cycle}}$ with increasing concentrations of KDFP or FEC additives, confirming the favorable effect of additives on SEI formation on K metal surface. However, the larger polarization is observed in the case of FEC-added electrolytes, suggesting the different nature of SEI.

The compatibility of K metal electrodes in the electrolytes containing varying weight ratios of KDFP was further evaluated in K/K symmetric cells to exclude the effect from any positive or negative electrodes.[30, 31] The symmetric cells were cycled in each electrolyte at current densities in the sequence of 10, 50, 100, and 500 $\mu A\ cm^{-2}$ for 10 cycles. Each cycle consisted of 8-min deposition and 8-min dissolution with a 2-min rest in between. The resulting voltage profiles during the galvanostatic K metal deposition/dissolution tests are shown in Figure 5-5. As shown in Figure 5-5 (a), the overpotential of 55 mV observed in the 0 wt% KDFP electrolyte at 10 $\mu A\ cm^{-2}$ significantly increases with increasing current densities. On the other hand, the overpotentials observed at 10 $\mu A\ cm^{-2}$ significantly decrease with increasing concentrations of KDFP (*i.e.* 17 mV and 15 mV for 0.1 wt% KDFP and 0.2 wt% KDFP, respectively). Considering the similar ionic conductivities of these electrolytes (Figure 5-6), the major reason for the lower overpotential exhibited in the electrolytes with KDFP could primarily be attributed to reduced interfacial resistance through the SEI film.[31, 32] Previous studies for the electrolyte for LIB have reported similar improvements in the interfacial properties of the ionically conductive SEI components formed in electrolytes with LiDFP additives.[33, 34] Similar SEI components in the case of KDFP additives are also confirmed in XPS results as will be discussed in the later section. For comparison, the results acquired in the electrolyte with 0.3 wt% and 3 wt% FEC are shown in Figure 5-5 (d, e). Evidently, compared to electrolytes with KDFP, the total overpotential is greater and dramatically increases with increasing current density in the electrolytes with FEC (15 mV for 0.2 wt% KDFP vs.138 mV for 0.3 wt% FEC, respectively, at 10 μA cm^{-2}). These results could be associated with a more resistive SEI formed by FEC-derived products. Furthermore, the observations from K/K symmetric cells are in conformance with the deposition/dissolution tests performed on the K/Cu cells. It is also noteworthy that, the shape of voltage profiles in each cycle is steady with less polarization and stable from the early stage during the cycles with KDFP, whereas neat and FEC electrolyte required prolonged time to be stabilized.

To investigate the interfacial behavior of the SEI formed, EIS analysis was performed on the K/K symmetric cells after the formation of a stable SEI layer, which was achieved by cycling the cells at 10 μA cm^{-2} for 8 min over the course of three cycles. Figure 5-7 (f) illustrates a schematic of the equivalent circuit used for this analysis. The resulting electrolyte resistance R_{bulk} and interfacial resistances R_{int} resistances are listed in Table 5-1. The time-evolving EIS results illustrate that the R_{bulk} values remain low regardless of the amount of additive present, consistent with the ionic conductivity results shown in Figure 5-6. However, a dramatic decrease in the R_{int} values is manifested in the presence of KDFP, signifying that a stabilized interface is formed on the K. These results conform to the voltage profiles of the K/K symmetric cells shown in Figure 5-5. In the case of the FEC additive, as shown in Figure 5-7 (d, e) and Table 5-1, a progressive increase of R_{int} is observed in the presence of the additive, which verifies the inferior stability of the SEI formed. For the cells evaluated after storage for 5 days, the R_{int} value is more than ten times larger than that in the presence of KDFP.

To assess the effect of KDFP on the electrochemical behavior of graphite, cyclic voltammetry profiles of the graphite electrode in electrolytes with varying amounts of KDFP were measured in three-electrode cell at a scan rate of 5 mV s^{-1} between OCP and 0.01 V vs. K^+/K as shown in Figure 5-8. For the additive-free electrolyte, the CV curve shows a pair of redox peaks centered at ca. 0.2 V vs. K^+/K; an indication of the potassium intercalation/deintercalation into/from graphite. The relatively low initial Coulombic efficiency (36 %) achieved from the 0 wt% KDFP electrolyte is ascribed to the severe reductive decomposition of the electrolyte without an additive, as discussed above. In the case of electrolytes with 0.1 and 0.2 wt% KDFP, a significant increase in the current density is observed, which corresponds to the facile interfacial reaction. Moreover, a new reduction peak which appears at 0.6 V vs. K^+/K, depicts the reductive decomposition of KDFP. It is crucial to note that the initial Coulombic efficiency is remarkably improved to 64 % (0.1 wt% KDFP) and 75 % (0.2 wt% KDFP) despite the additional SEI created by KDFP decomposition. The higher Coulombic efficiency is most likely due to the preferential reduction of KDFP into a stable SEI layer on the graphite surface that suppresses the decomposition of other electrolyte components [33, 34]. This favorable initial SEI formation is postulated to facilitate the subsequent K intercalation/deintercalation into/from graphite. From Figure 5-8 (d), reduction of FEC is identified at the higher potentials of 1.3 and 1.0 V vs K^+/K than that in the case without FEC, however, only a limited improvement in Coulombic efficiency is obtained (41 %).

The K^+ intercalation/deintercalation behavior into/from graphite is examined by K/graphite half-cells. Figure 5-9 shows the initial three charge-discharge curves measured at C/20 (1C = 279 mA g^{-1}) and the corresponding dQ/dV plots. For the additive-free electrolyte, the charge curve consists of two regions. The first region slopes in the range of 0.4 and 0.2 V and the second is a voltage plateau at 0.15 V [22]. During the first charge, a charge capacity of 309 mAh g^{-1} was achieved in total (Figure 5-9 (a)). Besides, a small irreversible reduction peak, which is related to the decomposition of the electrolyte during the formation of SEI, was observed at 0.29 V (Figure 5-9 (f)). Three subsequent peaks corresponding to the phase transformation process to KC_{36}, KC_{24}, and KC_8 were also attained at 0.26, 0.20, and 0.15 V, respectively, in accordance with the previous study.[20] This is accompanied by a conspicuous change in the color of the graphite electrode from grey to gold, proving the formation of KC_8 (Figure 5-10).[14, 22] During the discharge process, the peaks observed at 0.28, 0.37, and 0.49 V in the dQ/dV plot correspond to the depotassiation steps of K-GICs (see Table 5-2 for voltage details).[20] A first discharge capacity of 266 mAh g^{-1} (Figure 5-9 (a)) is attained with a resultant initial Coulombic efficiency of 84.5 %. As shown in Figure 5-10, the appearance of the depotassiated electrode returns to dark grey, supporting the complete depotassiation to graphite.

In the presence of KDFP, relatively large reductive peaks emerged at ca. 0.36 V, indicating additional reduction associated with SEI formation, as had been detected earlier by the cyclic voltammetry results. The first discharge capacity of 273 and 274 mAh g^{-1} was obtained from 0.1 and 0.2 wt% KDFP electrolytes, respectively, which is fairly close to the theoretical capacity of 279 mAh g^{-1} for fully intercalated KC_8. Compared to the electrolyte without additives, slightly higher initial Coulombic efficiency of 86.1 % and 86.9 % are achieved in the electrolyte with the addition of 0.1 and 0.2 wt% KDFP, respectively. Importantly, the Coulombic efficiency of the subsequent cycles approaches 100 % with KDFP addition (95.9, 98.2, and 99.8 % of efficiencies in the second cycle for the addition of 0, 0.1 and 0.2 wt%, respectively), which also verifies the stable SEI formed in the presence of KDFP additive (see Table 5-3 for comparison). Likewise, the onset potential associated with the potassiation of graphite, shifts more positively/negatively during depotassiation/pottasiation, respectively (see Table 5-2 for comparison). This tendency further corroborates the positive influence of KDFP on reducing the reaction overpotential. The easier (de)potassiation process exhibited in this case is a result of a less resistive SEI film formed in the presence of KDFP.[33]

As shown in Figure 5-9 and summarized in Tables 2 and 3, the addition of FEC does not substantially contribute to improvement in the electrochemical behavior of graphite electrodes. The overpotential of (de)potassiation even increases by adding FEC, implying that an inferior, non-protective SEI layer is formed from the decomposition of FEC. This finding coincides a previous study whereby the graphite electrode in a KPF_6–based electrolyte with 2 wt% FEC could not withstand cycling over 5 times.[35] These results clearly suggest that some established additives used in LIBs may be ineffective or even detrimental for PIBs.

The effect of the additives on the structural change of GIC electrodes undergoing (de)potassiation was further investigated through *ex-situ* XRD and Raman spectroscopic analysis. As illustrated in Figure 5-11 and Figure 5-12, XRD patterns and Raman spectra of the pristine, fully charged, and fully discharged graphite electrodes in 0.5 M KPF_6-EC/DEC with 0, 0.1, and 0.2 wt% of KDFP were obtained.

As can be seen in Figure 5-11 (a), a sharp peak corresponding to an interlayer distance of 3.36 Å appears at 26.46° corresponding to the 002 diffraction line of the pristine graphite electrode.[36] After charging the cell at C/20 to 0.001 V in the electrolyte without additive, the 002 peak disappears, and two characteristic peaks assignable to KC_8 appear at 16.4 (5.40 Å) and 33.3° (2.69 Å). They are ascribed to the diffraction lines of 001 and 002, giving an interlayer distance of 5.38 Å. In previous works on the stage-1 K-GIC (KC_8), two different indexing manners (001 and 002 [18] or 004 and 008 [2, 37]) were proposed for these peaks, the latter taking account super lattice due to the periodic arrangements of K^+ in the graphite gallery. In addition to the diffraction peaks of KC_8, a small peak assigned to the 002 diffraction lines of the residual stage-2 K-GIC (KC_{24}) appears at 20.1°, indicating the incomplete potassiation of K-GIC. After discharging, the characteristic 002 peak of graphite is observed but with a lower intensity and a broader shape; indicating the original layered structure is recovered but with a lower crystallinity caused by the volume change during the intercalation/deintercalation. As shown in Figure 5-12 (a), the G band of the pristine graphite shifts from 1580 cm^{-1} to 1600 cm^{-1} after charging, confirming the existence of stage-2 K-GIC (KC_{24}) on the surface of charged graphite electrode (see the literature for assignments of the K-GIC Raman bands).[14, 18] The G and D bands of graphite which are also recovered after discharging, show consistency with the XRD results.

In the case of the 0.1 wt% KDFP electrolyte, the diffraction peak of KC_{24} disappears leaving only the ones assigned to KC_8 in the charged electrode (Figure 5-11 (b)). However, the corresponding Raman spectrum shows that a characteristic asymmetric band of KC_8 at 1430 cm^{-1} [38, 39] appears to be accompanied by a band of KC_{24} on the side of higher wavenumbers, implying that the stage-2 K-GIC still exists on the surface of the charged graphite electrode (Figure 5-12 (b)).[40] Interestingly, when the KDFP concentration in the electrolyte increased to 0.2 wt%, phase-pure KC_8 could exclusively be formed after charging, with characteristic peaks appearing at 16.50 (001, 5.37 Å) and 33.40° (002, 2.68 Å) [19] (Figure 5-11 (c)). Maximum intensity was observed on the typical KC_8 broad asymmetric peak [38] at around 1430 cm^{-1} (Figure 5-12 (c)). The complete and reversible formation of phase-pure KC_8 from the pristine graphite verified by these *ex-situ* analyses illustrates the best electrochemical performance [19] is attained with 0.2 wt% KDFP.

To gain deeper insight on the influence of the electrolyte additive on the (de)potassiation behavior of graphite, galvanostatic intermittent titration technique (GITT) [41] was employed to acquire charge/discharge profiles approaching to the thermodynamic equilibrium (Figure 5-13 (a), and (b)). The evolution of the quasi-equilibrium voltage vs. time (dV/dt) is shown in Figure 5-13 (c). Since the steady-state of phase transformation occurs in the voltage plateau, in theory, the voltage variation in this region should be zero. As can be seen, the measured dV/dt values remain constant at zero for a more prolonged state of (dis)charge in the case of 0.2 wt% KDFP than in the electrolyte without additive. This extended region of $dV/dt \approx 0$ indicates that for the selected electrode, a faster equilibrium is reached and favorable diffusion path in SEI layer is established with the aid of KDFP.

To draw a comparison, the (de)potassiation processes of graphite in the FEC containing electrolyte has also been investigated by XRD and Raman analyses. As shown in Figure 5-11 (d), the potassiated graphite shows a pair of strong diffraction peaks of KC_{24} with even greater intensity than those of KC_8. The residual KC_{24} seen after discharge indicates the poor reversibility of (de)potassiation in the electrolyte with FEC. These findings are further supported by the Raman spectra (Figure 5-12 (d)). Thus, the rapid capacity fading of graphite in the FEC-added electrolyte can be attributed to the irreversibility of K-GIC (de)potassiation process.

The rate performance of the K/graphite half-cell was further evaluated in the voltage range of 0.001–2.5 V at current densities of C/20, C/10, C/5, C/2, 1C, and C/20 at 298 K as shown in Figure 5-14. The results show significant improvements in the rate capability with increasing concentration of KDFP. After cycling at different rates, a reversible capacity as high as 272 mAh g^{-1} could be obtained from the electrolyte with 0.2 wt% KDFP at the current density of C/20. The corresponding charge-discharge curves shown in Figure 5-15 clearly indicate diminished polarization with regard to the electrolyte with 0.2 wt% KDFP. This further substantiates the dQ/dV results (Figure 5-9) reported in this study and additionally highlights the positive influence of KDFP additive on (de)potassiation kinetics. The minimal deviation from the equilibrium voltage observed in the GITT test performed on cells containing the KDFP additive, also substantiates that the presence of KDFP is advantageous in the formation of a more ionically conductive SEI that leads to the better (de)potassiation kinetics observed. Similar findings have been made in corresponding studies on the lithium analog, LiDFP , indicating enhanced rate capability in the performance of graphite electrodes for LIBs [33, 34].

Figure 5-16 (a) shows the cycle performance of K/graphite half-cells with varying amounts of KDFP evaluated in the voltage range of 0.001–2.5 V at a current density of C/3 and temperature of 298 K. As can be seen from the figure, the capacity of the cell without KDFP drastically decays after 40 cycles exhibiting low capacity retention (27.4 %) at the 100th cycle (discharge capacity of 56 mAh g^{-1}). In contrast, the cells containing the KDFP additive manifested significant enhancement in the cycling stability and discharge capacity retention. In particular, the discharge capacity retention of the cell with 0.2 wt% KDFP is 89.0 % at the 100th cycle and 76.8 % at the 400 cycles (discharge capacity: 181 mAh g^{-1}). Furthermore, the comparison of Coulombic efficiencies of the cells with and without KDFP over the initial 15 cycles presented in Figure 5-16 (b) shows that cells consisting of electrolytes with the additive need fewer cycles to achieve a Coulombic efficiency $\geq$ 99.9 %, indicating the formation of stable SEI film. These results clearly affirm the importance of adopting a suitable electrolyte additive for feasible PIB operations.

X-ray photoelectron spectroscopic analysis was carried out to ascertain the components of the SEI layer of graphite electrodes undergoing (de)potassiation and verify the possible effects of the additive on the electrochemical performance. Figure 5-17 shows K 2p, C 1s, O 1s, F 1s, and P 2p XPS spectra of GIC electrodes after 400 cycles in 0.5 M KPF_6-EC/DEC with 0 wt% and 0.2 wt% KDFP (see Table 5-4 for assignments). For the pristine graphite electrode, the characteristic peaks in the C 1s spectrum appearing at 284.4 eV and 285.3 eV can be assigned to be sp^2 and sp^3 carbon, respectively. The peak appearing at 290.9 eV in C 1s is considered to be indicative of π–π* transition (Figure 5-17).[42, 43] Partially oxidized graphite which results in weak peaks at 286.1 eV for C–O (also from CMC binder) and 287.2 eV for C=O, is also consistently observed in the O 1s spectra at 533.6 eV for C–O and 532.1 eV for C=O.[20, 44] Graphite electrodes cycled in both the electrolytes with and without the KDFP additive, showed significant increases in the intensities of C–O, C=O, and $-CO_3^{2-}$ peaks in the C 1s spectra (Figure 5-17 (a)), and the K–O peaks are observed at 528.8 eV in the O 1s spectra (Figure 5-17 (b)).[45, 46] These results validate the formation of the SEI layer by electrolyte decomposition and shows good agreement with previous works for potassium-ion batteries with KPF_6 electrolyte.[20, 44-46]

The main difference in the SEI constituents formed by electrolytes with and without additive can be observed in the F 1s and P 2p spectra. In both the electrolytes, the presence of CF_x, PF_x species (687.5 ± 1 eV), and KF (683.6 eV) are confirmed in F 1s spectra.[45] However, the KF ratio increases from 15.1 to 25.1 % in the presence of 0.2 wt% KDFP (Figure 5-17 (c)), in conformity with previous reports on the effect of LiDFP additive in LIBs.[33] Although KF species can be detected in the K metal counter electrode recovered from the electrolyte with 0.2 wt% KDFP, they are not detected in the electrolyte without the additive (Figure 5-18 (c)). Additional evidence of the distinctive SEI formed by the addition of KDFP is also furnished by the P 2p spectra as illustrated in Figure 5-17 (d). Two peaks associated with K_xPF_y and phosphate (PO_x) are observed at 137.7 and 133.7 eV, respectively. On the other hand, the spectrum of the electrode cycled in the electrolyte with 0 wt% KDFP shows only one peak of K_xPF_y at 137.6 eV. It can, therefore, be inferred that these phosphate species are created through the addition of KDFP into the electrolyte. According to the previous studies on the use of LiDFP additive in LIB electrolytes, phosphate species are considered to be favorable components of SEI during interfacial reactions and Li^+ diffusion.[33] In a similar manner, it is expected that the addition of KDFP could promote the formation of a stable and more ionically conductive SEI layer, which contributes to the facile reaction in the K/K symmetric and K/graphite cells observed in this system.

5.4 Conclusions

In conclusion, the feasibility of KDFP additive in KPF_6-based electrolytes was systematically investigated using K metal and graphite electrodes. Potassium metal deposition/dissolution tests and EIS measurements confirmed that a stable SEI with improved ionic conductivity is formed on the electrode surface during operation in the electrolyte containing KDFP. Furthermore, a high discharge capacity of 274 mAh g^{-1} (98.2 % of the theoretical value) was achieved from graphite electrodes in the electrolyte with 0.2 wt% KDFP as a result of the complete and reversible formation of phase-pure stage-1 K-GIC (KC_8). The electrolyte containing KDFP shows significant improvement of the rate performance and cycleability of graphite, delivering a 76.8 % capacity retention after 400 cycles with an averaged Coulombic efficiency of 99.99 %. It is important to note that such improvements could not be attained when FEC (another common additive) was used instead; attesting to the unique role of KDFP. Additional XPS analysis performed on the graphite electrodes after cycling in the electrolyte containing KDFP indicated that enriched KF and PO_x species were formed in the SEI layer, causing the improved interfacial properties and the diminished (de)potassiation overpotential. This study not only demonstrates a simple and effective way to acquire stage-1 K-GIC from high performance PIB electrolytes but also establishes the use of small amounts additives as a judicious way to boost the electrochemical performance of certain electrode materials.

Table 5-1. Fitting results of the EIS data for the K/K symmetric cells with 0.5 M KPF_6-EC/DEC electrolytes containing different amounts of KDFP or FEC.[a]

Additives	EIS component	1 h	12 h	1 day	3 day	5 day
0 wt% KDFP	R_{bulk} / Ω	9.49	36.65	41.96	63.24	114.9
	R_{int} / Ω	6175	7331	8061	11853	13914
	$C.F.$ / Hz	7.99	5.39	5.56	2.46	2.60
	Q / F $s^{\alpha-1}$	6.01×10^{-6}	6.04×10^{-6}	5.94×10^{-6}	6.01×10^{-6}	6.51×10^{-6}
	α	0.899	0.907	0.909	0.910	0.899
0.1 wt% KDFP	R_{bulk} / Ω	10.48	36.52	44.55	82.40	102.2
	R_{int} / Ω	2875	4062	5023	7585	8636
	$C.F.$ / Hz	18.38	11.83	11.83	5.69	5.69
	Q / F $s^{\alpha-1}$	5.10×10^{-6}	5.52×10^{-6}	5.43×10^{-6}	5.24×10^{-6}	5.21×10^{-6}
	α	0.840	0.881	0.883	0.886	0.886
0.2 wt% KDFP	R_{bulk} / Ω	6.707	22.31	32.38	67	103.79
	R_{int} / Ω	1 794	3 077	3 128	4 831	5 424
	$C.F.$ / Hz	25.97	11.84	11.84	7.99	7.99
	Q / F $s^{\alpha-1}$	6.27×10^{-6}	7.445×10^{-6}	7.13×10^{-6}	7.976×10^{-6}	7.195×10^{-6}
	α	0.904	0.881	0.887	0.861	0.881
0.3 wt% KDFP	R_{bulk} / Ω	9.887	18.38	30.53	52.61	101.2
	R_{int} / Ω	2110	2846	3606	4340	5110
	$C.F.$ / Hz	25.97	11.84	11.84	7.99	7.99
	Q / F $s^{\alpha-1}$	6.550×10^{-6}	7.367×10^{-6}	7.427×10^{-6}	7.113×10^{-6}	7.074×10^{-6}
	α	0.881	0.874	0.875	0.880	0.881
0.3 wt% FEC	R_{bulk} / Ω	23.63	36.21	82.34	107.96	145.64
	R_{int} / Ω	17909	40580	77062	181307	203896
	$C.F.$ / Hz	2.46	0.76	0.51	0.17	0.17
	Q / F $s^{\alpha-1}$	5.104×10^{-6}	5.242×10^{-6}	4.636×10^{-6}	4.581×10^{-6}	4.298×10^{-6}
	α	0.880	0.861	0.869	0.852	0.864
3 wt% FEC	R_{bulk} / Ω	19.01	64.38	79.69	108.4	208.6
	R_{int} / Ω	16246	40041	66 449	179735	223455
	$C.F.$ / Hz	2.60	1.12	0.51	0.16	0.11
	Q / F $s^{\alpha-1}$	4.994×10^{-6}	5.039×10^{-6}	4.722×10^{-6}	4.249×10^{-6}	4.028×10^{-6}
	α	0.893	0.842	0.883	0.840	0.852

[a] *C.F.*, Q, and α denote characteristic frequency, CPE parameter, and CPE exponent, respectively.

Table 5-2. The peak positions (unit: V) in the d*Q*/d*V* plots of the K/graphite cells in 0.5 M KPF_6-EC/DEC with different additives during the first charge and discharge processes. See Figures 5-9 for the corresponding d*Q*/d*V* plots.

Additive	SEI formation	Charge			Discharge		
		Potassiation			Depotassiation		
		KC_{36}	KC_{24}	KC_8	KC_8	KC_{24}	KC_{36}
Additive-free	0.295	0.264	0.201	0.151	0.279	0.367	0.485
0.1 wt% KDFP	0.351	0.263	0.228	0.172	0.265	0.352	0.464
0.2 wt% KDFP	0.358	0.280	0.241	0.184	0.261	0.350	0.462
0.3 wt% FEC	1.197	0.227	0.140	0.068	0.438	0.583	0.739
3 wt% FEC	1.245	0.035	0.079	0.136	0.410	0.518	0.680

Table 5-3. Coulombic efficiencies (%) of the K/graphite cells with 0.5 M KPF_6-EC/DEC electrolytes containing different amounts of KDFP or FEC. The charge-discharge rate is C/20.

Cycle number	0 wt% KDFP	0.1 wt% KDFP	0.2 wt% KDFP	0.1 wt% FEC	3 wt% FEC
1st	84.5	86.1	86.9	79.2	65.3
2nd	95.9	98.2	99.8	96.0	88.7
3rd	96.9	99.1	99.8	99.2	92.8

Table 5-4. Binding energy (eV) and assignments of the XPS data on the graphite and in 0.5 M KPF_6-EC/DEC electrolytes containing different amounts of KDFP.

	K2p	F1s	C1s	O1s	P2p
Graphite electrode					
0 wt% KDFP	295.2 (KF, $2p_{3/2}$) 292.5 (KF, $2p_{1/2}$)	687.5 (CF_x, PF_x) 683.6 (KF)	289.5 (CO_3^{2-}) 288.1 (C=O) 286.4 (C–O) 284.7 (C–C) 282.6 (K–C)	533.3 (C–O) 531.4 (C=O) 529.4 (K–O)	137.6 (K_xPF_y)
0.2 wt% KDFP	295.4 (KF, $2p_{3/2}$) 292.6 (KF, $2p_{1/2}$)	687.6 (CF_x, PF_x) 683.6 (KF)	289.5 (CO_3^{2-}) 288.0 (C=O) 286.4 (C–O) 284.6 (C–C) 282.9 (K–C)	533.6 (C–O) 531.7 (C=O) 528.8 (K–O)	137.7 (K_xPF_y) 133.7 (PO_x, Phosphate)
Pristine			290.9 (CF_x, PVDF) 287.2 (C=O) 286.1 (C–O) 285.3 (C, sp^3) 284.4 (C, sp^2)	533.6 (C–O) 532.1 (C=O)	
K metal					
0 wt% KDFP		687.5 (CF_x, PF_x)			
2 wt% KDFP		687.4 (CF_x, PF_x) 683.2 (KF)			

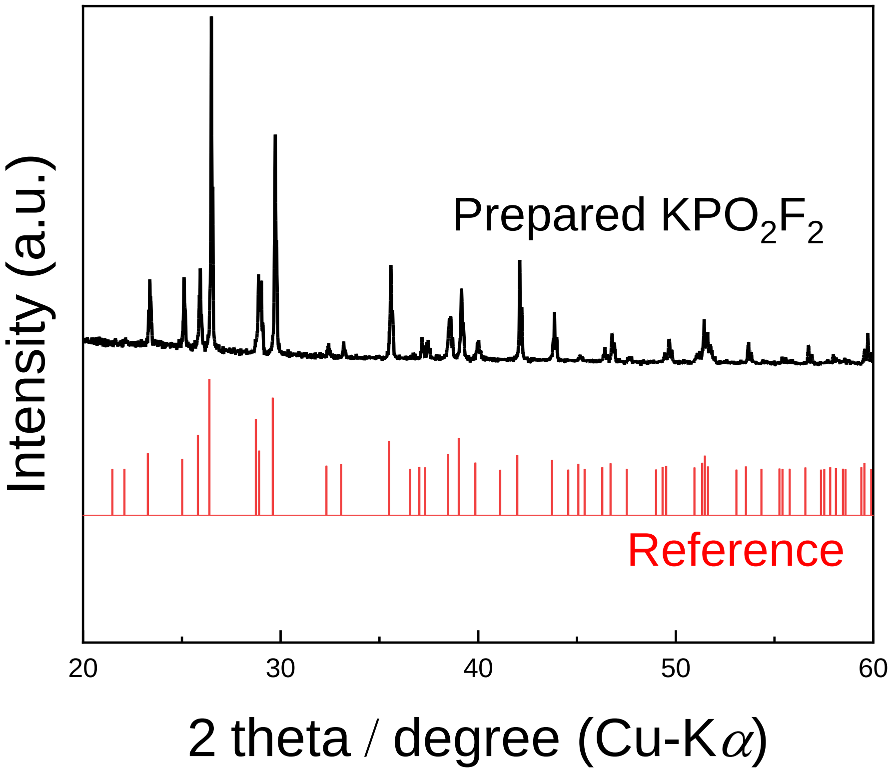

Figure 5-1. X-ray diffraction pattern of the prepared KDFP. The reference pattern of K[PO_2F_2] created from the single crystal X-ray diffraction data [47] is also shown for comparison.

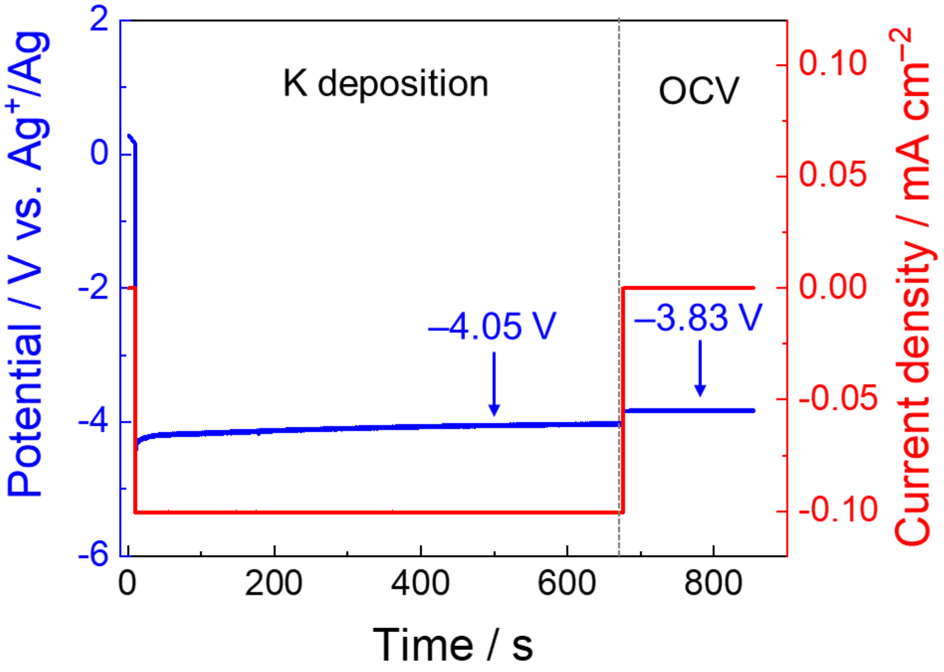

Figure 5-2. The voltage profile of K deposition/dissolution in 0.5 M KPF_6-EC/DEC on the Al working electrode (area: 0.25 cm^{-2}) with the Ag^+/Ag reference electrode and Pt counter electrode in a three-electrode cell. The K^+/K equilibrium potential in 0.5 M KPF_6-EC/DEC is determined to be –3.83 V vs. Ag^+/Ag by an open circuit potential (OCP) measurement after galvanostatic K metal deposition at 0.1 mA cm^{-2} in a three-electrode cell.

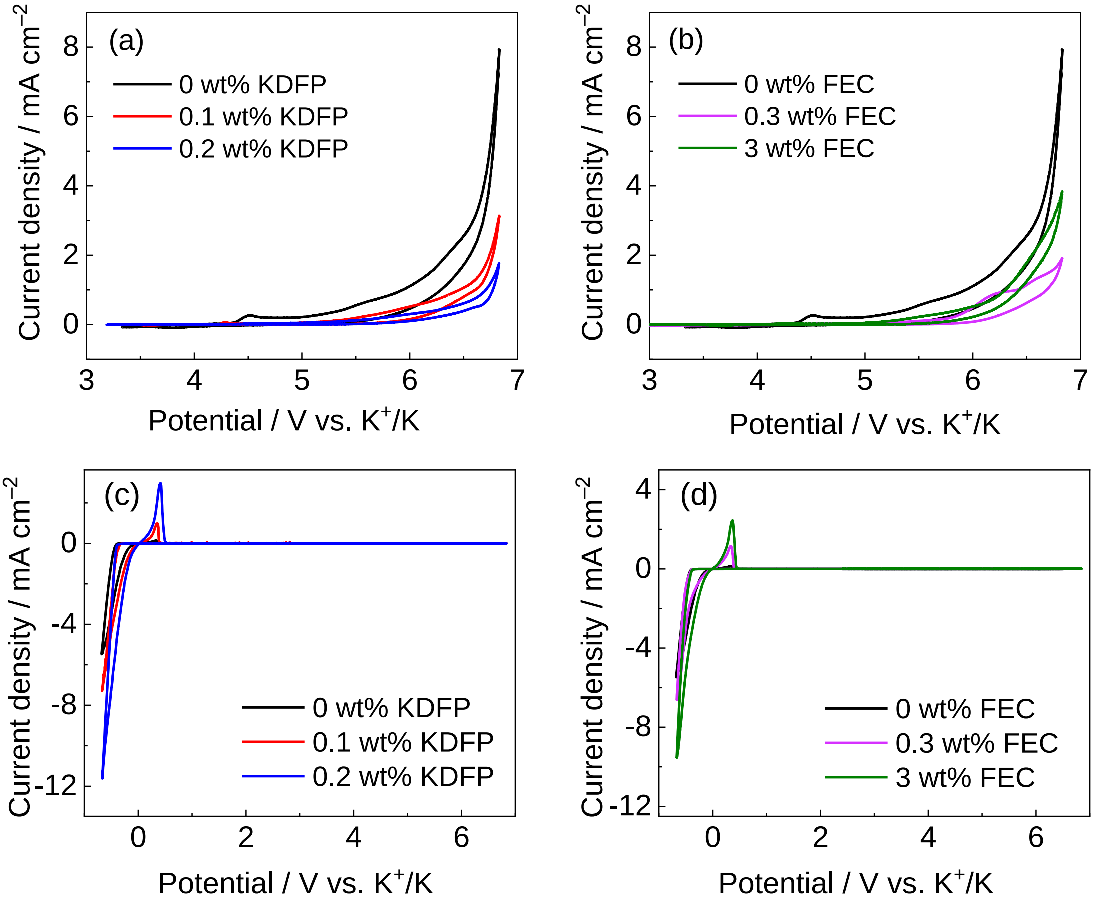

Figure 5-3. Cyclic voltammograms of Pt (anodic side) and Al (anodic and cathodic sides) electrodes in 0.5 M KPF_6-EC/DEC with varying weight ratios of (a, c) KDFP and (b, d) FEC additive. Scan rate: 5 mV s^{-1}.

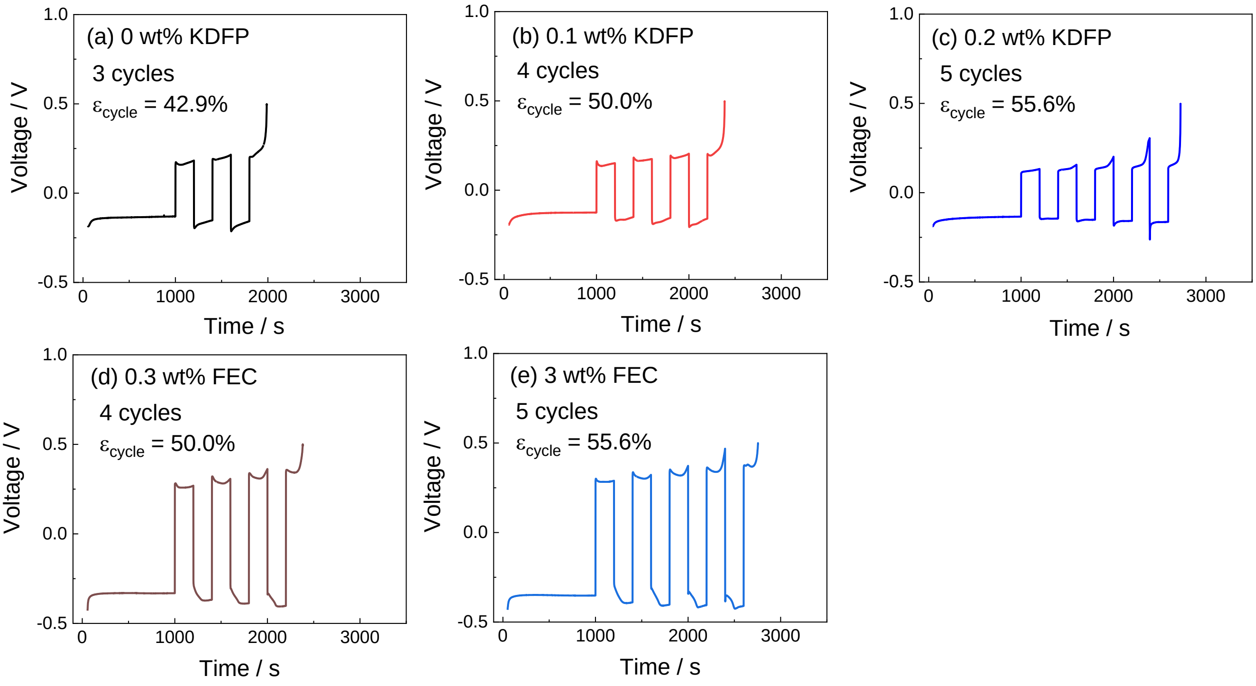

Figure 5-4. Voltage profiles during K deposition/dissolution in 0.5 M KPF_6-EC/DEC with (a) 0 wt% KDFP, (b) 0.1 wt% KDFP, (c) 0.2 wt% KDFP, (d) 0.3 wt% FEC, and (e) 3 wt% FEC at 298 K. The working and counter electrodes were Cu and K metal plates, respectively. K metal (0.1 C cm^{-2}) was pre-deposited on the Cu plate, followed by repeated dissolution and deposition at a capacity of 0.02 C cm^{-2} until the electrode potential reached 0.5 V vs. K^+/K during dissolution. The current density was ± 0.1 mA cm^{-2} for all the tests.

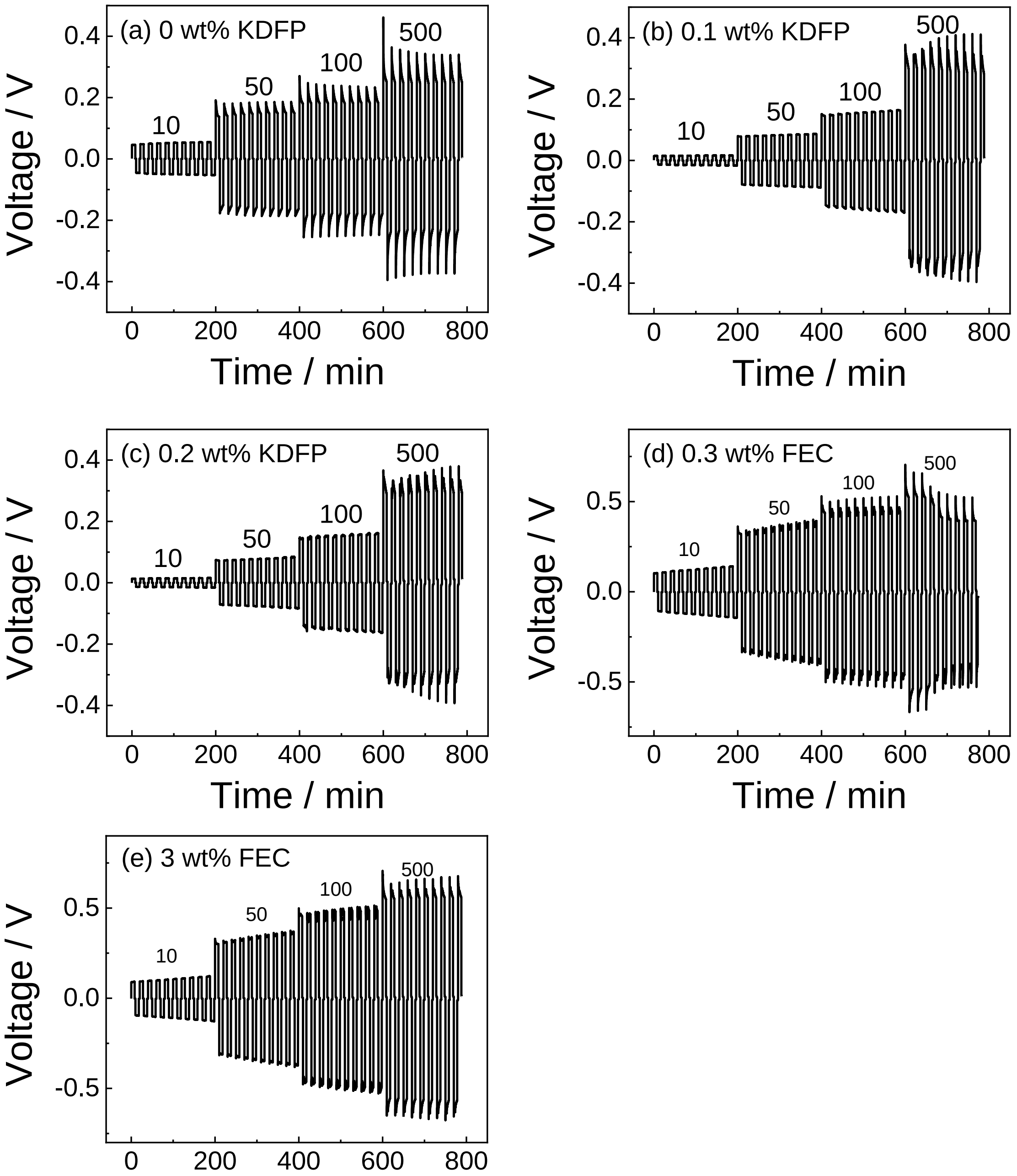

Figure 5-5. Voltage profiles of the K/K symmetrical cells during galvanostatic K metal deposition/dissolution in 0.5 M KPF_6-EC/DEC with (a) 0 wt% KDFP, (b) 0.1 wt% KDFP, (c) 0.2 wt% KDFP, (d) 0.3 wt% FEC, and (e) 3 wt% FEC additives at 298 K. The numbers shown in each panel denote current densities in μA cm^{-2}.

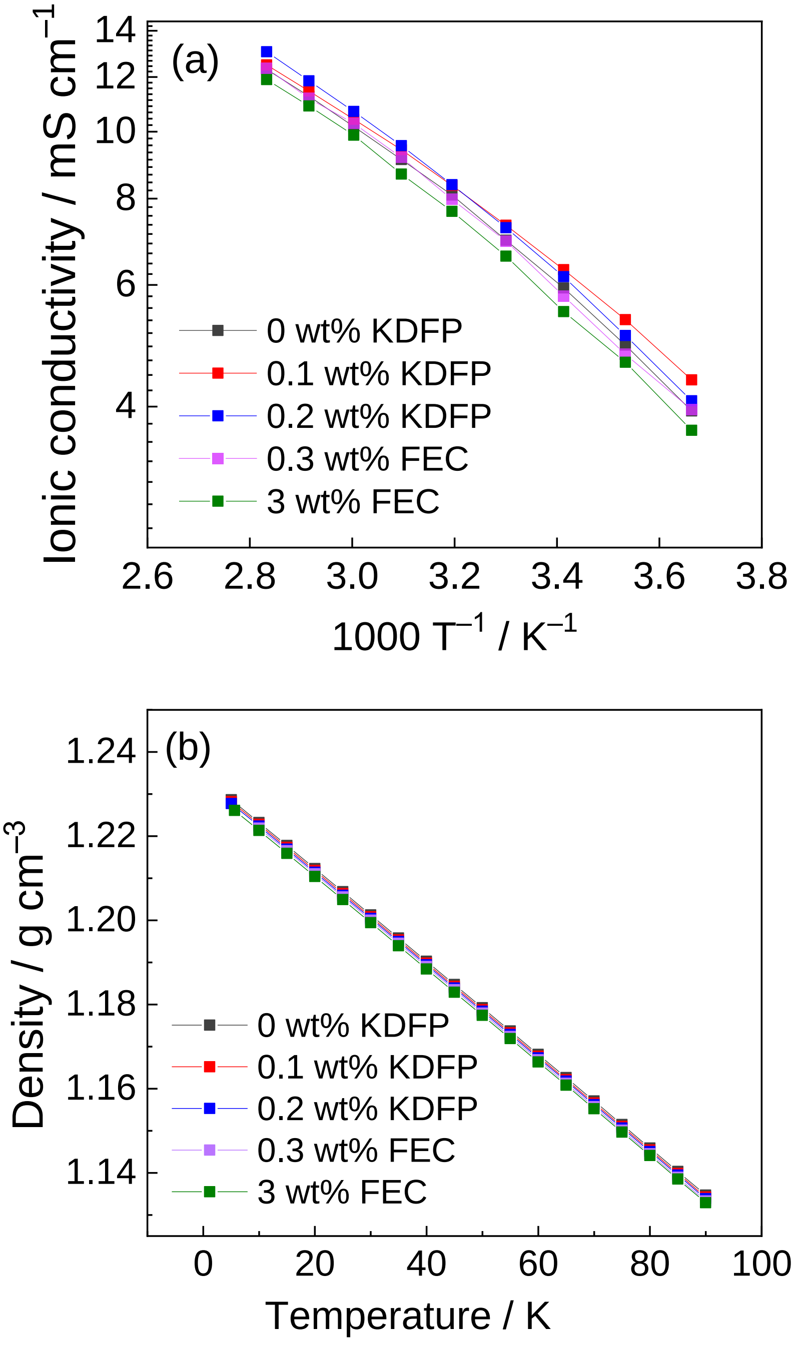

Figure 5-6. (a) Arrhenius plots of ionic conductivities and (b) densities of 0.5 M KPF_6-EC/DEC (1:1, v:v) without and with KDFP or FEC additives in the temperature range between 273 and 363 K.

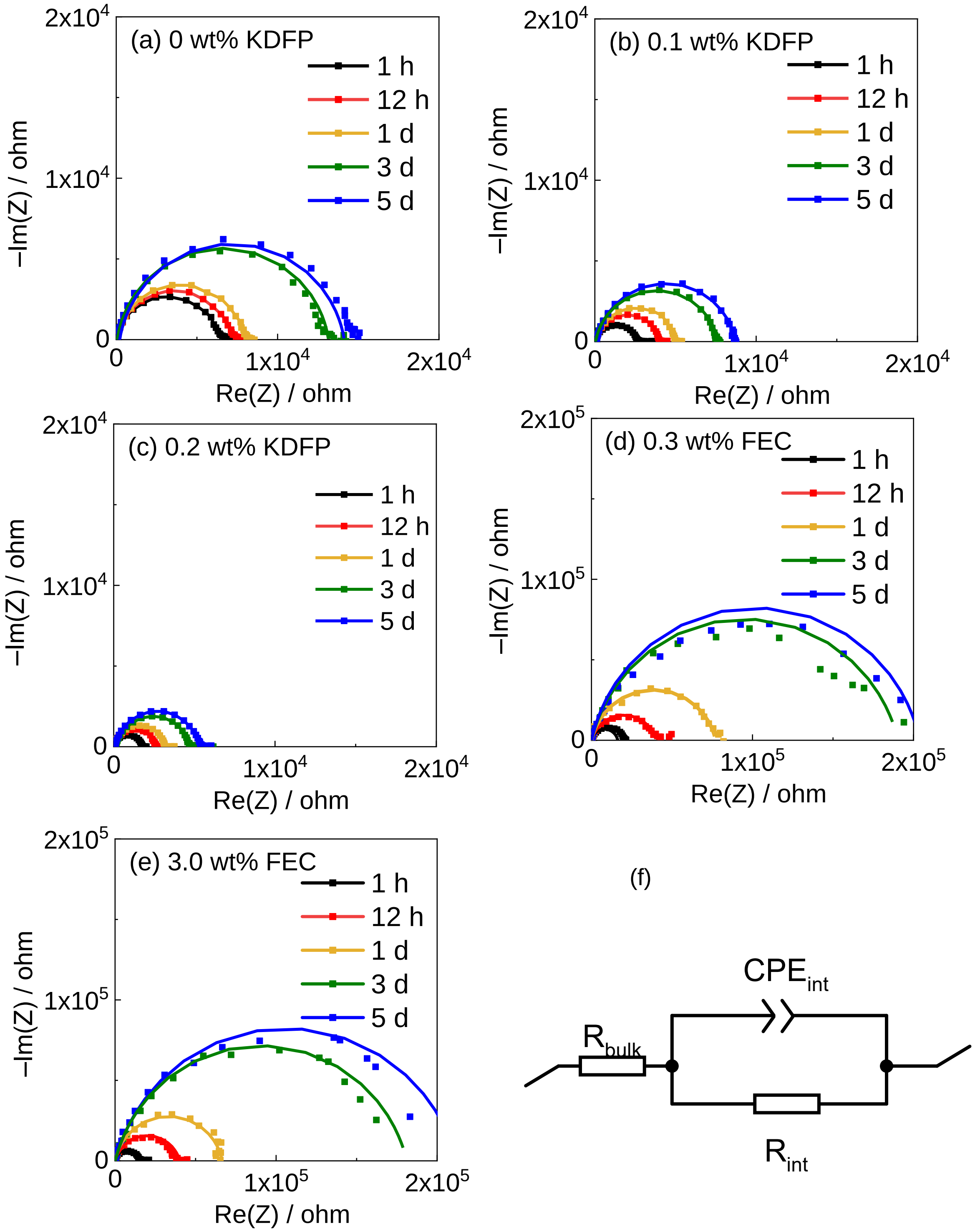

Figure 5-7. Nyquist plots and fitting lines of the K/K symmetric cells at 298 K using the 0.5 M KPF_6-EC/DEC electrolyte with (a) 0 wt% KDFP, (b) 0.1 wt% KDFP, (c) 0.2 wt% KDFP, (d) 0.3 wt% FEC, and (e) 3 wt% FEC in the frequency range of 100 kHz−10 mHz. (f) Equivalent circuit used for data fitting. AC amplitude: 10 mV.

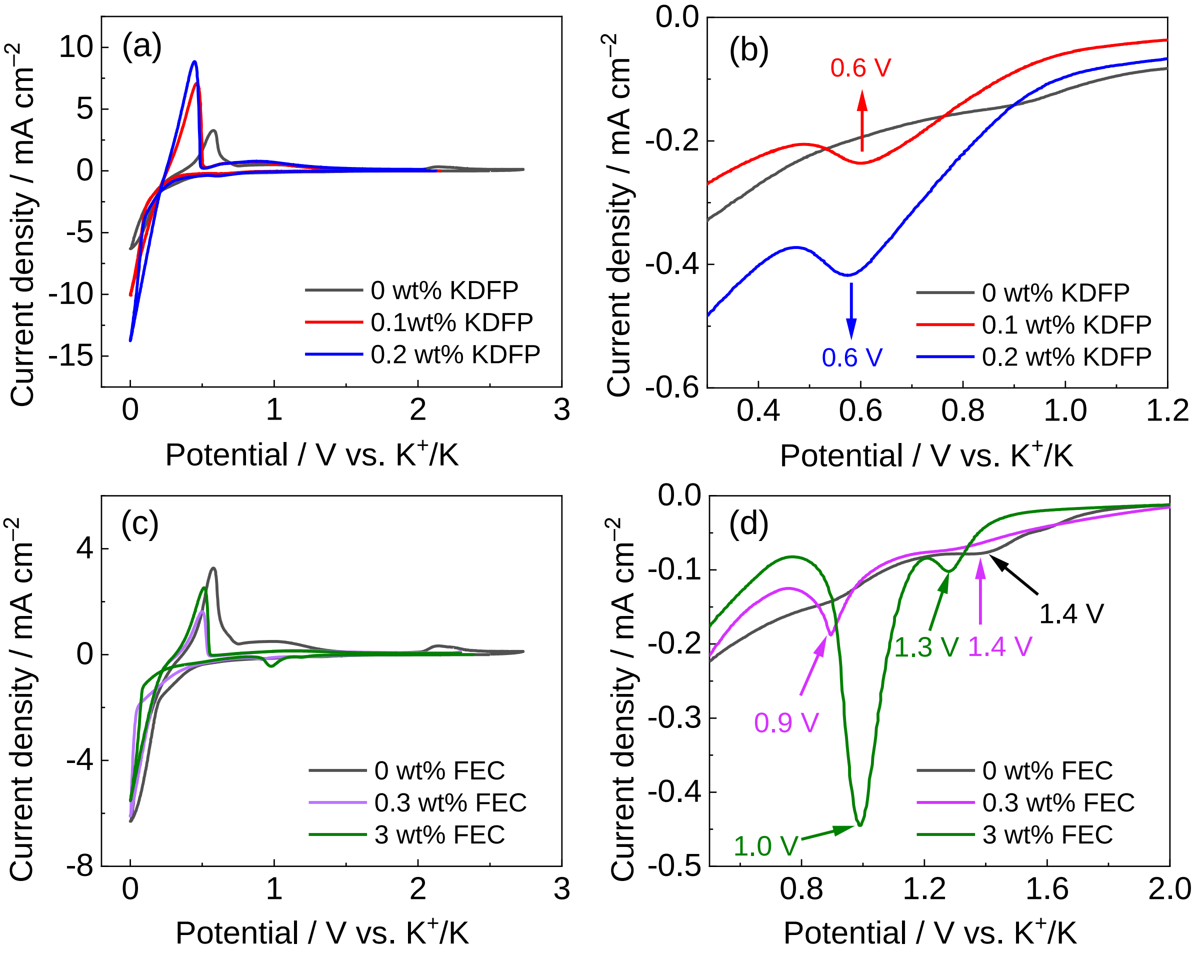

Figure 5-8. Cyclic voltammograms of graphite electrodes in 0.5 M KPF_6-EC/DEC with (a) 0 wt%, 0.1 wt%, and 0.2 wt% KFDP, (c) 0 wt%, 0.3 wt%, and 3 wt% FEC additives at 298 K. (b, d) are magnified figures of (a) and (c). Scan rate: 5 mV s^{-1}. Pt counter and Ag^+/Ag reference electrodes were used. The potential was converted to that against the K^+/K reference.

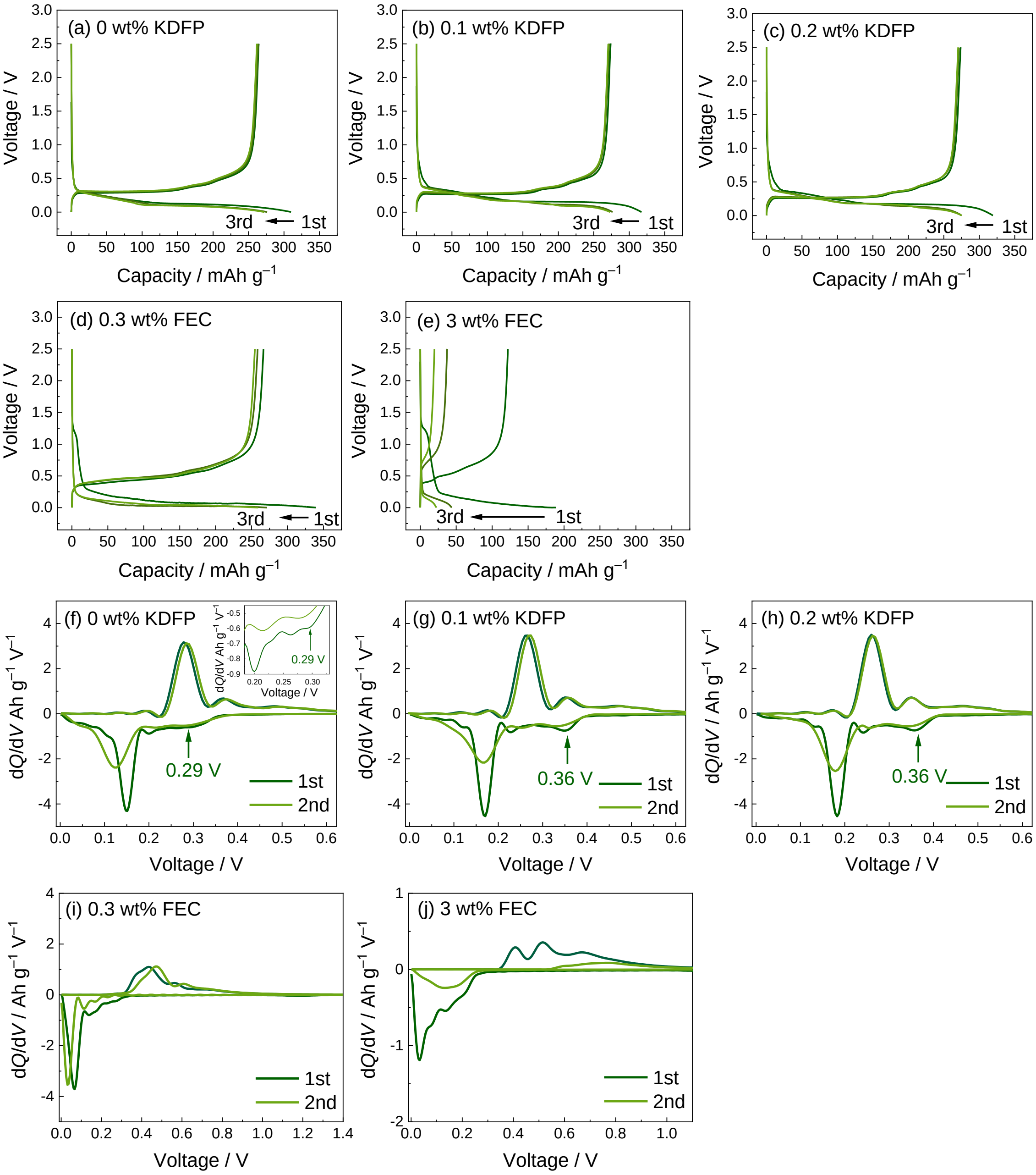

Figure 5-9. Charge-discharge curves of the K/graphite cells in 0.5 M KPF_6-EC/DEC with (a, f) 0 wt% KDFP, (b, g) 0.1 wt% KDFP, (c, h) 0.2 wt% KDFP, (d, i) 0.3 wt% FEC, and (e, j) 3 wt% FEC. Current density: C/20 (1C = 279 mA g^{-1}). The corresponding differential capacity vs. voltage (d*Q*/d*V*) plots of the first two charge-discharge cycles are shown in (f–j). (See Table 5-2 for the peak position during potassiation and depotassiation of the initial cycle.)

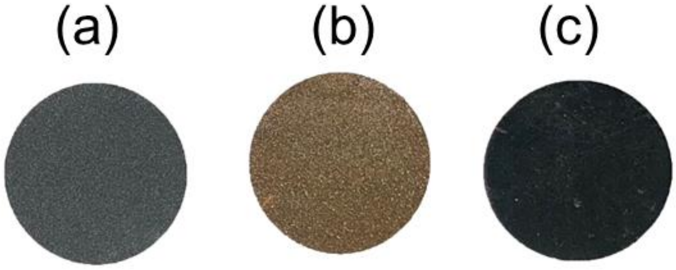

Figure 5-10. Photos of (a) as-prepared, (b) fully potassiated, and (c) fully depotassiated graphite electrodes obtained in 0.5 M KPF_6-EC/DEC by galvanostatic charge-discharge tests. C-rate: C/20 (1C = 279 mA g^{-1}).

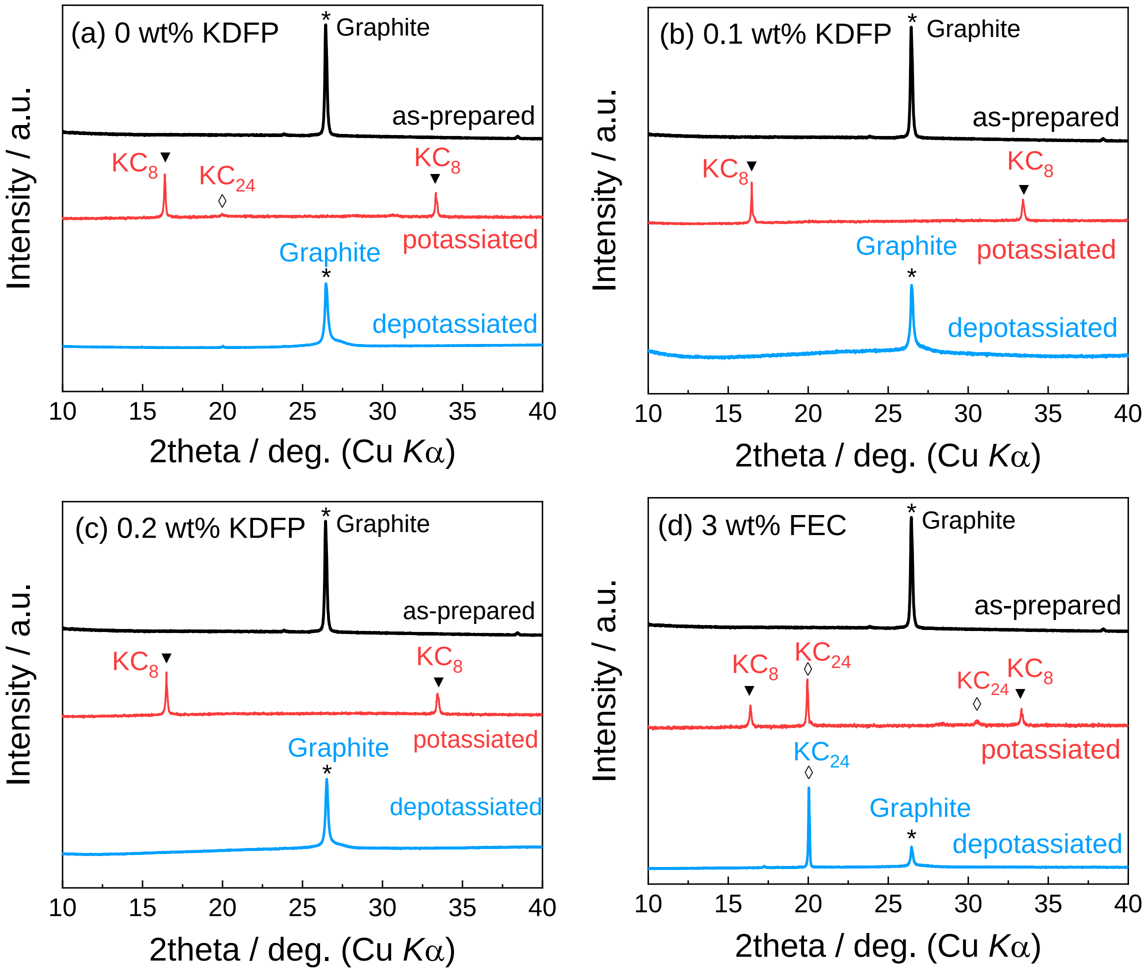

Figure 5-11. *Ex-situ* XRD patterns of graphite electrodes at pristine (black), fully potassiated (red), and fully depotassiated (blue) states. Electrolytes: 0.5 M KPF$_6$-EC/DEC with (a) 0 wt% KDFP, (b) 0.1 wt% KDFP, (c) 0.2 wt% KDFP, and (d) 3 wt% FEC.

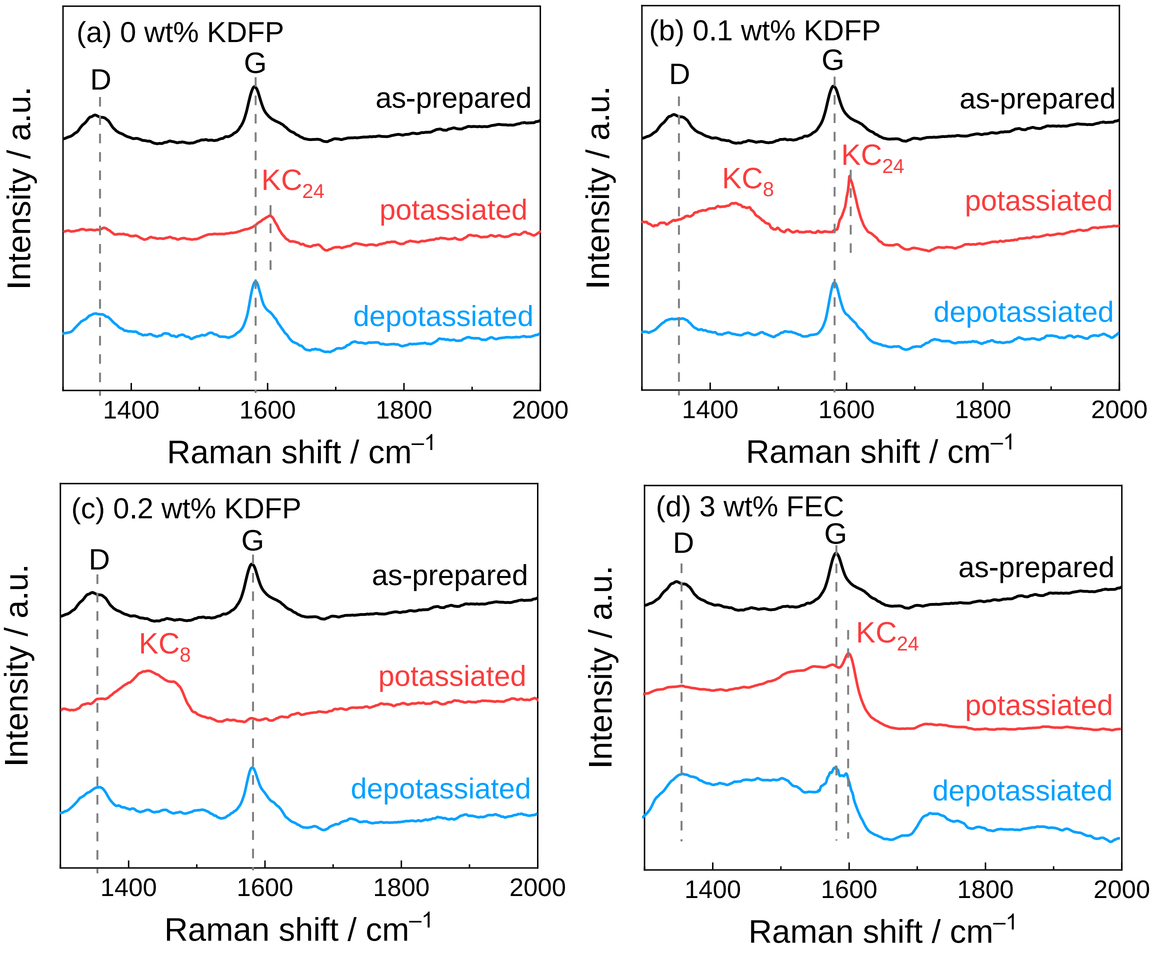

Figure 5-12. Raman spectra of graphite electrodes at pristine (black), fully potassiated (red), and fully depotassiated (blue) states. Electrolytes: 0.5 M KPF_6-EC/DEC with (a) 0 wt% KDFP, (b) 0.1 wt% KDFP, (c) 0.2 wt% KDFP, and (d) 3 wt% FEC.

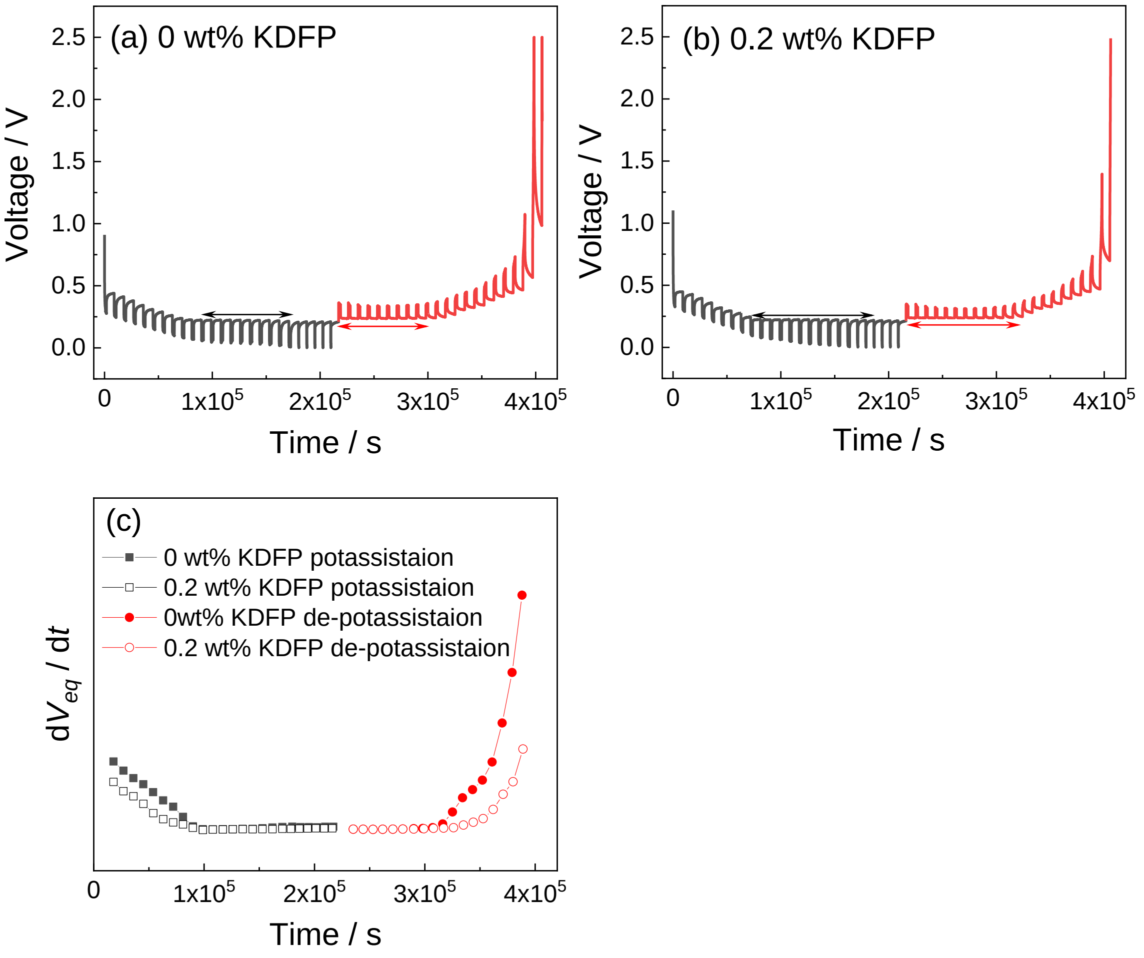

Figure 5-13. Galvanostatic intermittent titration technique (GITT) curves of graphite electrodes in 0.5 M KPF_6-EC/DEC with (a) 0 wt% and (b) 0.2 wt% KDFP. (c) Quasi-equilibrium voltage variation depends on the time change during charge-discharge process. GITT was measured by applying a constant rate of C/20 for 30 min followed by voltage relaxation for 2 h.

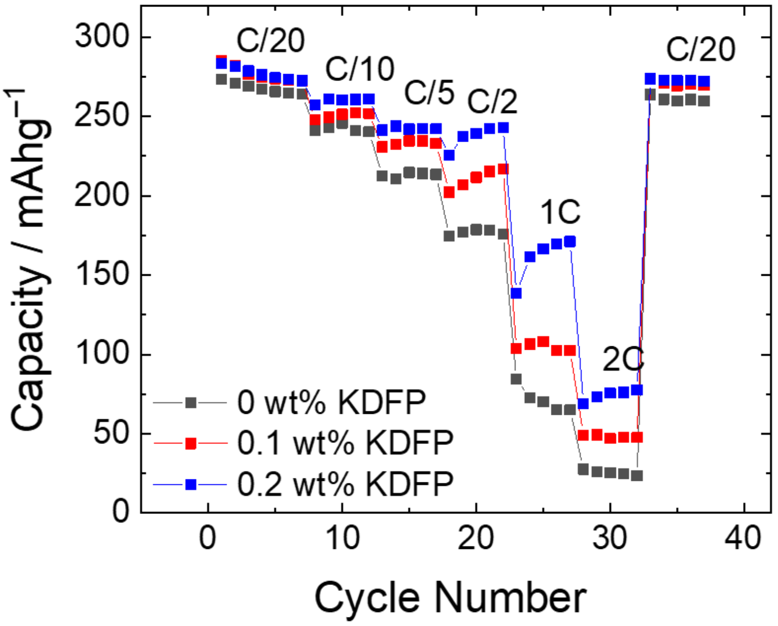

Figure 5-14. Rate capability of the K/graphite cells with 0.5 M KPF_6-EC/DEC electrolytes containing different amounts of KDFP at 298 K. Rate: C/20 to 2C. Cut-off voltages: 0.001–2.5 V.

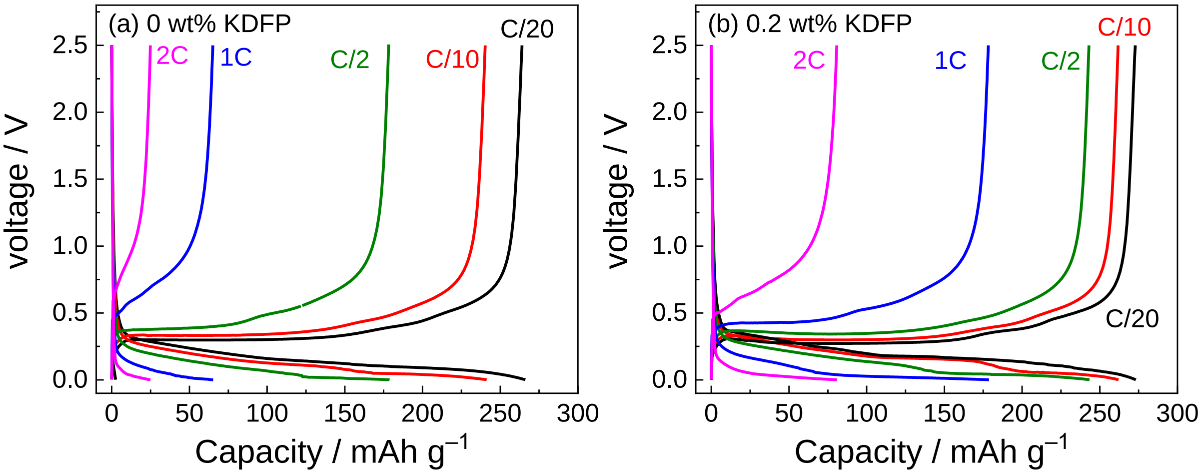

Figure 5-15. Charge-discharge curves of the K/graphite cells in 0.5 M KPF_6-EC/DEC with (a) 0 wt% and (b) 0.2 wt% KDFP during rate capability tests from C/20 to 2C at 298 K. Cut-off voltages: 0.001–2.5 V.

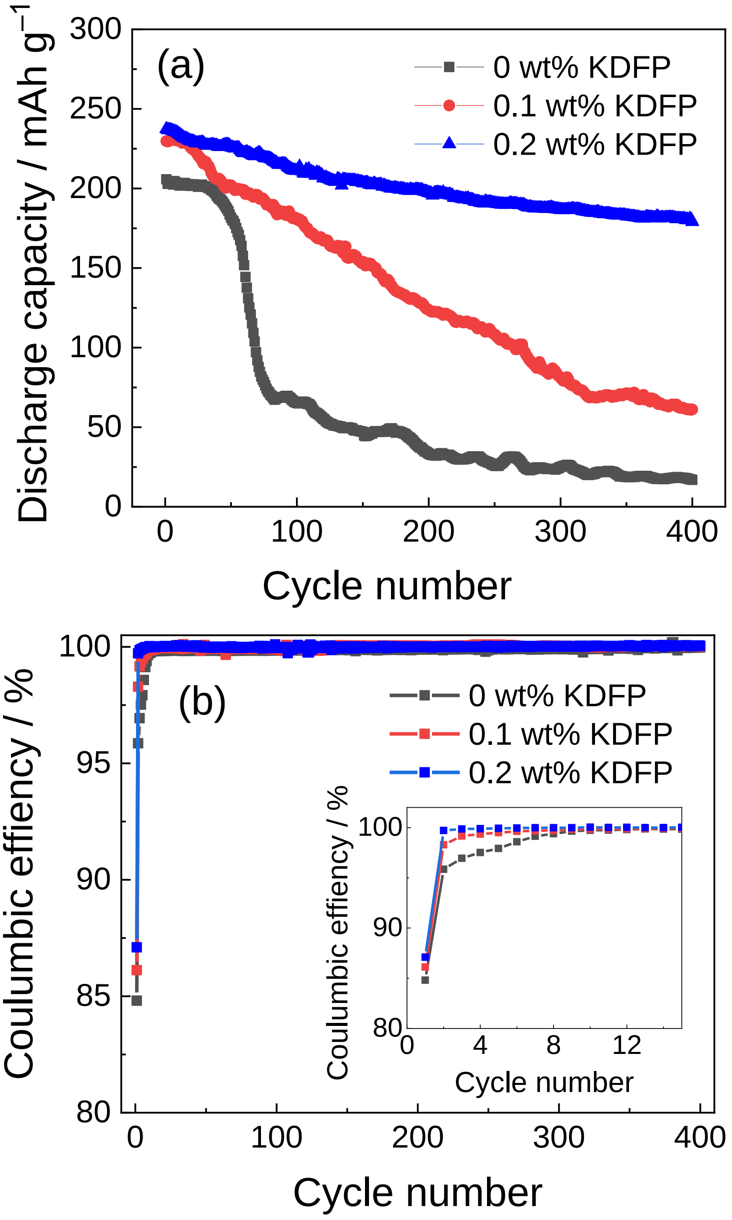

Figure 5-16. Cycle performance of the K/graphite cells with 0.5 M KPF$_6$-EC/DEC with 0 wt%, 0.1 wt%, and 0.2 wt% of KDFP. (a) Capacity retention and (b) Coulombic efficiency. C-rate: C/3. Cut-off voltage: 0.001–2.5 V.

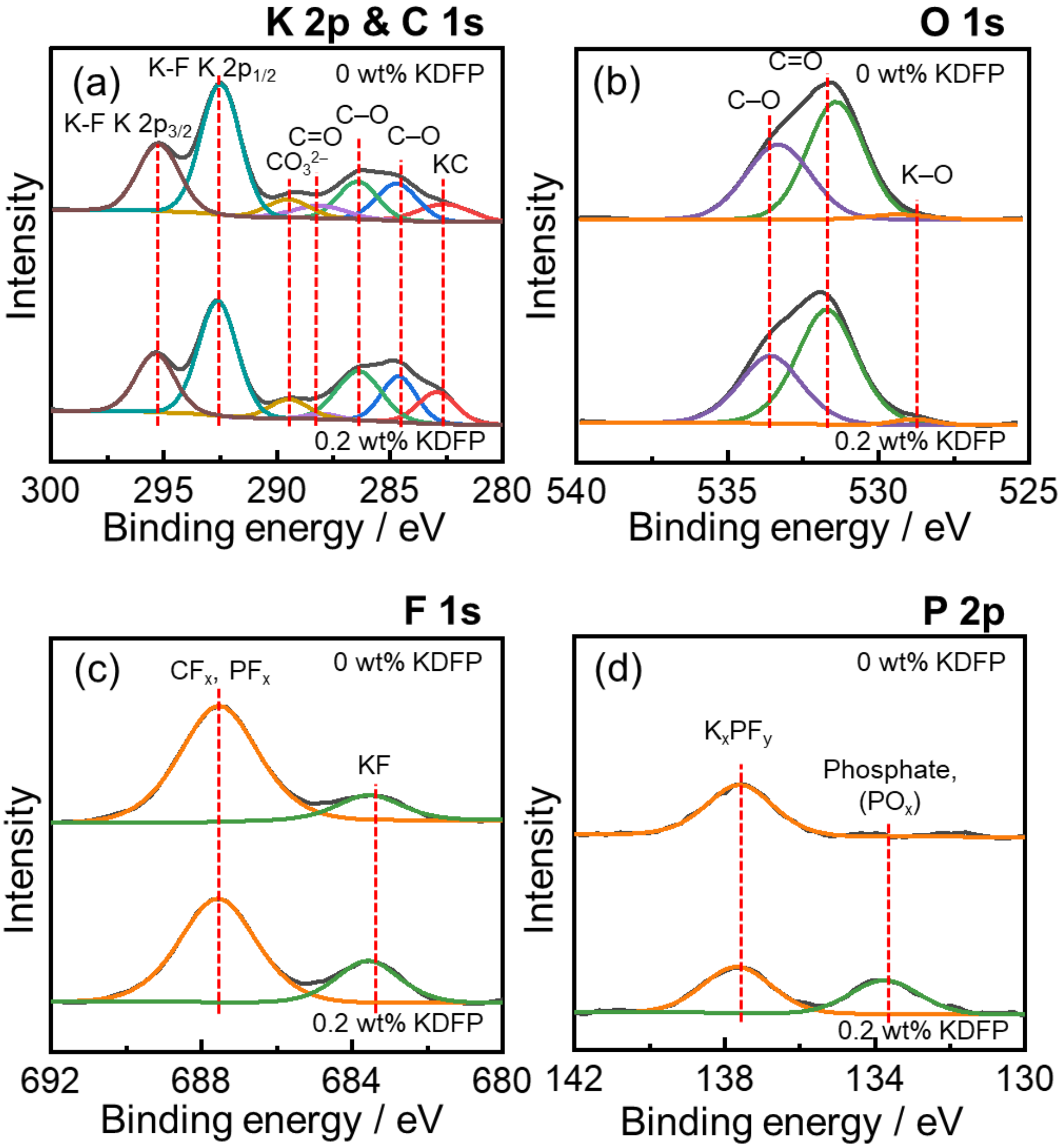

Figure 5-17. X-ray photoelectron spectra of SEI layers formed on graphite electrodes after 400 cycles in 0.5 M KPF_6 EC/DEC with and without KDFP additive in the (a) K 2p and C 1s, (b) O 1s, (c) F 1s, and (d) P 2p regions. The graphite electrodes after 400 cycles for XPS is in the fully depotassiation state. (See Table 5-4 for the binding energy of the peaks and SEI components)

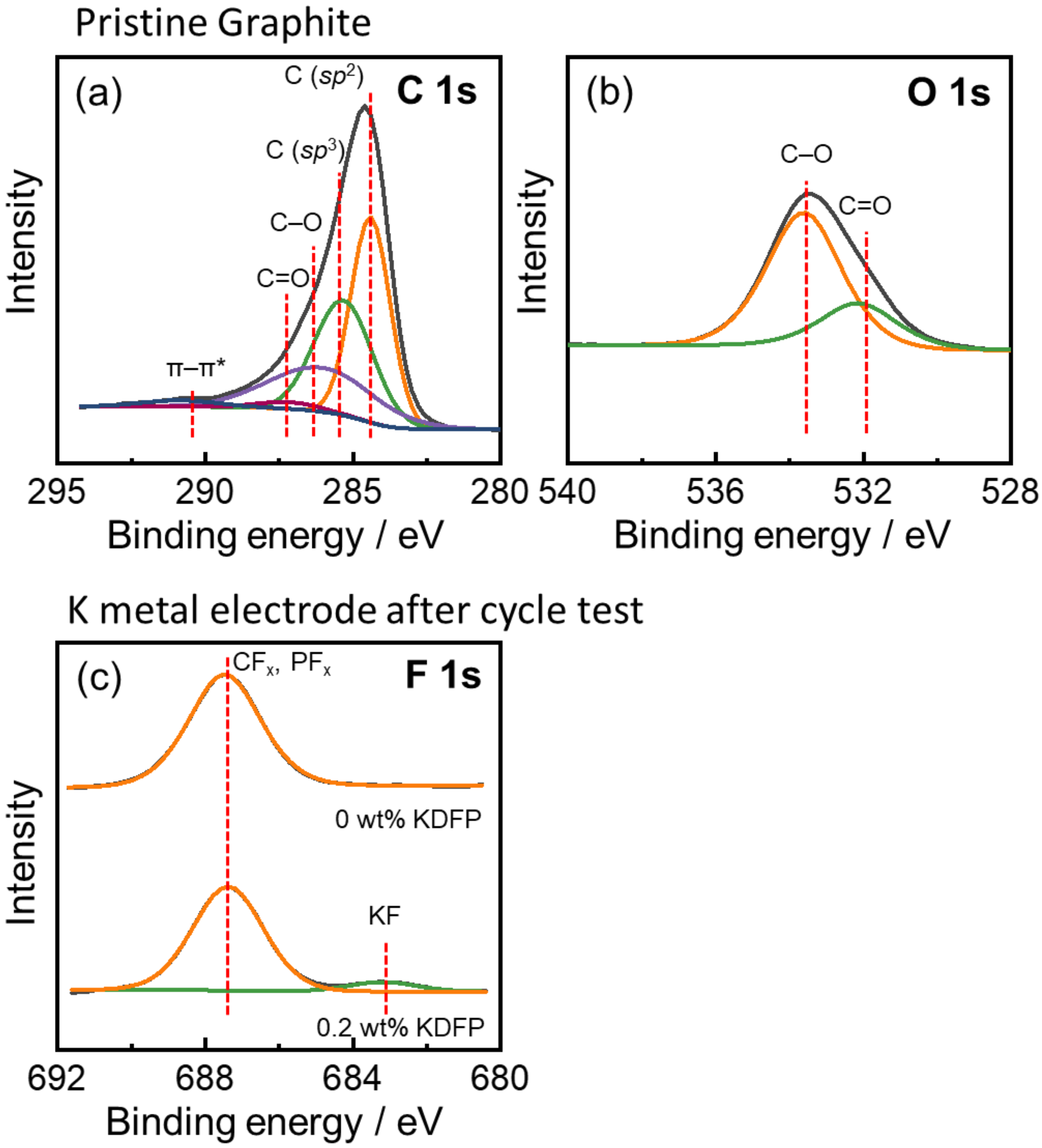

Figure 5-18. X-ray photoelectron spectra of the pristine graphite electrode (a) C 1s and (b) O 1s) and (c) K metal counter electrode (F 1s) after 400 cycles using 0.5 M KPF_6 EC/DEC with and without KDFP additive.

References

[1] K. Lei, F. Li, C. Mu, J. Wang, Q. Zhao, C. Chen, J. Chen, Energy Environ. Sci., 10 (2017) 552-557.

[2] S. Komaba, T. Hasegawa, M. Dahbi, K. Kubota, Electrochem. Commun., 60 (2015) 172-175.

[3] L. Fan, R. Ma, J. Wang, H. Yang, B. Lu, Adv. Mater., 30 (2018) 1805486.

[4] L. Fan, K. Lin, J. Wang, R. Ma, B. Lu, Adv. Mater., 30 (2018) 1800804.

[5] L. Fan, S. Chen, R. Ma, J. Wang, L. Wang, Q. Zhang, E. Zhang, Z. Liu, B. Lu, Small, 14 (2018) 1801806.

[6] S. Liu, J. Mao, Q. Zhang, Z. Wang, W. K. Pang, L. Zhang, A. Du, V. Sencadas, W. Zhang, Z. Guo, Angew. Chem., Int. Ed., 59 (2020) 3638-3644.

[7] Y. Matsuda, H. Nakashima, M. Morita, Y. Takasu, J. Electrochem. Soc., 128 (1981) 2552-2556.

[8] L. Wang, J. Yang, J. Li, T. Chen, S. Chen, Z. Wu, J. Qiu, B. Wang, P. Gao, X. Niu, J. Power Sources, 409 (2019) 24-30.

[9] Y. Li, Y. Lu, P. Adelhelm, M.-M. Titirici, Y.-S. Hu, Chem. Soc. Rev., 48 (2019) 4655-4687.

[10] G. Yoon, H. Kim, I. Park, K. Kang, Adv. Energy Mater., 7 (2017) 1601519.

[11] Y. Wen, K. He, Y. Zhu, F. Han, Y. Xu, I. Matsuda, Y. Ishii, J. Cumings, C. Wang, Nat. Commun., 5 (2014) 1-10.

[12] M. Goktas, C. Bolli, E. J. Berg, P. Novák, K. Pollok, F. Langenhorst, M. v. Roeder, O. Lenchuk, D. Mollenhauer, P. Adelhelm, Adv. Energy Mater., 8 (2018) 1702724.

[13] B. Jache, P. Adelhelm, Angew. Chem. Int. Ed., 53 (2014) 10169-10173.

[14] W. Luo, J. Wan, B. Ozdemir, W. Bao, Y. Chen, J. Dai, H. Lin, Y. Xu, F. Gu, V. Barone, Nano Lett., 15 (2015) 7671-7677.

[15] L. B. Ebert, Annu. Rev. Mater. Sci., 6 (1976) 181-211.

[16] M. S. Dresselhaus, G. Dresselhaus, Adv. Phys., 51 (2002) 1-186.

[17] T. Enoki, M. Suzuki, M. Endo, Graphite Intercalation Compounds and Applications, Oxford University Press, 2003.

[18] J. Liu, T. Yin, B. Tian, B. Zhang, C. Qian, Z. Wang, L. Zhang, P. Liang, Z. Chen, J. Yan, Adv. Energy Mater., 9 (2019) 1900579.

[19] Z. Jian, W. Luo, X. Ji, J. Am. Chem. Soc, 137 (2015) 11566-11569.

[20] L. Fan, R. Ma, Q. Zhang, X. Jia, B. Lu, Angew. Chem., Int. Ed., 58 (2019) 10500 –10505.

[21] J. C. Pramudita, V. K. Peterson, J. A. Kimpton, N. Sharma, Powder Diffr., 32 (2017) S43-S48.

[22] J. Zhao, X. Zou, Y. Zhu, Y. Xu, C. Wang, Adv. Funct. Mater., 26 (2016) 8103-8110.

[23] R. Rajagopalan, Y. Tang, X. Ji, C. Jia, H. Wang, Adv. Funct. Mater., (2020) 1909486.

[24] S. Wei, S. Choudhury, Z. Tu, K. Zhang, L. A. Archer, Acc. Chem. Res., 51 (2018) 80-88.

[25] K. Matsumoto, R. Hagiwara, Inorg. Chem., 48 (2009) 7350-7358.

[26] Y.-M. Song, C.-K. Kim, K.-E. Kim, S. Y. Hong, N.-S. Choi, J. Power Sources, 302 (2016) 22-30.

[27] C. Wang, L. Yu, W. Fan, J. Liu, L. Ouyang, L. Yang, M. Zhu, ACS Appl. Energy Mater., 1 (2018) 2647-2656.

[28] H. Yang, J. Hwang, Y. Wang, K. Matsumoto, R. Hagiwara, J. Phys. Chem. C, 123 (2019) 22018-22026.

[29] J. Hwang, H. Okada, R. Haraguchi, S. Tawa, K. Matsumoto, R. Hagiwara, J. Power Sources, 453 (2020) 227911.

[30] D. Iermakova, R. Dugas, M. Palacín, A. Ponrouch, J. Electrochem. Soc., 162 (2015) A7060-A7066.

[31] M. Forsyth, H. Yoon, F. Chen, H. Zhu, D. R. MacFarlane, M. Armand, P. C. Howlett, J. Phys. Chem. C, 120 (2016) 4276-4286.

[32] J. Hwang, K. Matsumoto, R. Hagiwara, J. Phys. Chem. C, 122 (2018) 26857−26864.

[33] K.-E. Kim, J. Y. Jang, I. Park, M.-H. Woo, M.-H. Jeong, W. C. Shin, M. Ue, N.-S. Choi, Electrochem. Commun., 61 (2015) 121-124.

[34] B. Yang, H. Zhang, L. Yu, W. Fan, D. Huang, Electrochim. Acta, 221 (2016) 107-114.

[35] X. Bie, K. Kubota, T. Hosaka, K. Chihara, S. Komaba, J. Mater. Chem. A, 5 (2017) 4325-4330.

[36] A. Eckmann, A. Felten, A. Mishchenko, L. Britnell, R. Krupke, K. S. Novoselov, C. Casiraghi, Nano Lett., 12 (2012) 3925-3930.

[37] W. Rüdorff, E. Schulze, Zeitschrift für anorganische und allgemeine Chemie, 277 (1954) 156-171.

[38] K. Ichimura, E. Takamura, M. Sano, Synth. Met., 40 (1991) 355-368.

[39] R. Nemanich, S. Solin, D. Guerard, Phys. Rev. B, 16 (1977) 2965-2972.

[40] J. Purewal, California Institute of Technology, Phd thesis, 2010.

[41] K. Tang, X. Yu, J. Sun, H. Li, X. Huang, Electrochim. Acta, 56 (2011) 4869-4875.

[42] F. Sette, G. Wertheim, Y. Ma, G. Meigs, S. Modesti, C. Chen, Phys. Rev. B, 41 (1990) 9766-9770.

[43] R. Blyth, H. Buqa, F. Netzer, M. Ramsey, J. Besenhard, P. Golob, M. Winter, Appl. Surf. Sci., 167 (2000) 99-106.

[44] Q. Zhang, J. Mao, W. K. Pang, T. Zheng, V. Sencadas, Y. Chen, Y. Liu, Z. Guo, Adv. Energy Mater., 8 (2018) 1703288.

[45] Y. Lei, D. Han, J. Dong, L. Qin, X. Li, D. Zhai, B. Li, Y. Wu, F. Kang, Energy Storage Mater., 24 (2020) 319-328.

[46] H. Wang, J. Hu, J. Dong, K. C. Lau, L. Qin, Y. Lei, B. Li, D. Zhai, Y. Wu, F. Kang, Adv. Energy Mater., 9 (2019) 1970168.

[47] R. Harrison, R. Thompson, J. Trotter, J. Chem. Soc. A, (1966) 1775-1780.

Chapter 6

Sodium Difluorophosphate as an Electrolyte Additive for Sodium Ion Batteries

6.1 Introduction

In line with the progress in lithium-ion batteries (LIBs), the importance of electrolytes has been less valued than the electrode materials considering the most effective design and cost consideration. However, electrolyte formulation is crucial for practical battery performance.[1] In commercialized LIBs, incorporating various types of additives is considered as an effective and economical way to optimize battery performance.[2-5] Recently, a steady progress in Na-ion batteries (SIBs) has been achieved by making use of techniques developed for LIBs.[6] In SIBs, fluoroethylene carbonate (FEC) has been a popular electrolyte additive after it was shown to improve the efficiency and stability of half cells.[1, 7] However, the performance and cycleability were actually lower in half-cells with FEC than without additive on some hard carbon electrodes.[8] Furthermore, some detrimental effects of FEC were also reported, including an increase in polarization in a two-electrode cell associated with a more resistive SEI layer formed on the Na metal counter electrode.[7, 9-11] Therefore, finding a functional additive with excellent film-forming and high conductivity properties could be an effective approach to obtain satisfactory electrochemical performance. In LIBs, difluorophosphate salts have been found to have good film-forming properties and are often effective in obtaining satisfactory electrochemical performance. Introduction of a small amount (< 2 wt%) of lithium difluorophosphate (LiDFP), which is an intermediate decomposition product of $LiPF_6$, into the electrolyte has been proven beneficial in (i) inhibiting the hydrolysis of $LiPF_6$ and restraining the generation of HPO_2F_2 [12-14] and (ii) forming a more ionically conductive surface film on the anode side. Consequently, electrodes in batteries containing the LiDFP- show fast Li^+ ion storage/release kinetics and good rate and cycling capability.[15] Chapter 5 also showed the effectiveness of potassium difluorophosphate (KDFP) in a electrolytic solution of potassium ion batteries. Despite such backgrounds, the functionality of their analogs in SIBs remains underexplored.

In this chapter, basic electrochemical behavior of sodium difluorophosphate (NaDFP) additive is investigated along with its effects on the electrochemical performance of a hard carbon (HC) electrode. The resulting electrochemical data is compared with the well-known film-forming additive FEC. In addition, cycle dependency of the electrochemical impedance spectroscopy (EIS) are investigated with the HC/HC symmetric cell.

6.2 Experimental

NaDFP was synthesized by the metathesis of $NaPF_6$ (Wako Pure Chemical Corporation, purity >99.7%) and KDFP prepared in Chapter 5.[16] The molar ratio of NaDFP:$NaPF_6$ reacted was 1:1.2. $NaPF_6$ and KDFP were dissolved in dehydrated tetrahydrofuran (THF; Wako, water content < 10 ppm, oxygen content < 1 ppm) (~200 cm^3 in a conical flask) by stirring at room temperature for 48 h with a sealed cap in the dry chamber. The solid precipitate was obtained by centrifuging the mixture. The acquired precipitate was washed with THF (~200 cm^3 in a conical flask) by stirring for 24h twice in the dry chamber. Absence of the impurity $NaPF_6$ in the product was checked by XRD. Recrystallization from THF solution by cooling down slowly from 353 K to 273 K sometimes helped growing large crystals of NaDFP, which was an easier way to separate them than that by filtration. The final product was dried under vacuum for 24 h at 353 K prior to use.

Powdery NaDFP was weighed and mixed into 1 M $NaPF_6$ in a mixed solvent of ethylene carbonate and diethylene carbonate (EC/DMC, in a 1:1 volume ratio, Kishida Chemical Co., Ltd., >99.0 % purity, water content < 10 ppm) to obtain a target electrolytic solution by stirring for one day until reaching uniformity. Saturation of NaDFP in 1 M $NaPF_6$-EC/DMC was found to occur when the concentration of NaDFP exceeds 1 wt% (0.08 mol kg^{-1}). Hard carbon (HC, Carbotron P, Kureha Battery Materials Japan Co., Ltd) powder, AB, and PVDF (85 : 10 : 5 in wt%) were uniformly mixed in NMP (solid/liquid ratio of 0.50). The obtained slurry was coated onto Al foil and vacuum-dried at 333 K overnight. The electrodes with 10 mm diameter were punched out from the foil and were vacuum-dried at 383 K for 10 h prior to cell assembly.

Electrochemical characterization of the HC electrode was carried out at 298 K using a 2032-type coin cell fabricated with the Na metal counter electrode. A glass fiber filter (Whatman, GF-A, 260 mm) was used as a separator. For the Na/HC cell, rate capability was tested at constant current rates of 20–500 mA $(g\text{-}HC)^{-1}$ within a voltage range of 0.005–1.5 V. The cycle tests were performed at a constant rate of 100 mA $(g\text{-}HC)^{-1}$ in the same voltage range with the rate capability test. The symmetric HC/HC cells for EIS were prepared with the HC electrodes after 1, 3, 10, and 20 cycles in Na/HC cell using the selected electrolytes (at the 80% SOC). The EIS measurements were performed with a VSP potentiostat (Bio-Logic) at 298 K over a frequency range from 1 or 100 mHz to 100 kHz with an ac amplitude of 10 mV.

6.3 Results and Discussion

Effects of the additives in 1 M $NaPF_6$-EC/DMC electrolyte (0.5 wt% NaDFP, 1 wt% NaDFP, 0.5 wt% FEC, and 3 wt% FEC) were measured in a two-electrode setup using Pt (positive potential region) and Al (positive and negative potential regions) working electrodes and Na metal counter electrode. The cyclic voltammograms of the Al electrodes at 298 K are shown in Figure 6-1. Although the first cycle exhibits a certain amount of current (less than 15 μA cm^{-2} at 7 V vs. Na^+/Na), it drastically decreases in the subsequent cycles and reaches a negligible level, suggesting the formation of an effective passivation layer on Al regardless of the addition of additives.[17] A careful observation suggests that the anodic current at 7 V vs. Na^+/Na with NaDFP additive is smaller than those for the neat and FEC-added electrolytes. Figure 6-2 (a) and (b) show the cyclic voltammograms of the Al electrode in the negative potential region. The cathodic and anodic currents corresponding to Na metal deposition and dissolution are observed at 0 V vs. Na^+/Na on the Al electrode. The corresponding Coulombic efficiency of Na metal deposition/dissolution in the cyclic voltammogram increases from 13.3% in the neat electrolyte to 21.5 % with 0.5 wt% NaDFP, and 26.7 % with 1 wt% NaDFP. The FEC-containing electrolytes give the low Coulombic efficiencies of 7.1 % and 15.2 % with 0.5 and 3 wt% FEC, respectively. Figure 6-2 (c) and (d) show the cyclic voltammograms of a Pt electrode in the high potential region, where irreversible decomposition of the electrolyte occurs. The neat electrolyte demonstrated a relatively low anodic limit of 4.7 V vs. Na^+/Na at a current density of 0.1 mA cm^{-2}. Higher anodic potential limits of 5.2 and 5.3 V compared with the neat electrolyte are observed in the electrolyte with 0.5 and 1 wt% NaDFP, respectively. The influence of the difluorophosphate salt on extending the electrochemical stability window of the electrolyte by suppressing the generation of hydrolysis products (mainly HPO_2F_2) has also been reported in previous reports in LIBs.[12, 18] On the other hand, the addition of 0.5 and 3 wt% FEC have little effect on the enhancement of the electrochemical stability.

Cycling of Na/Na symmetric cells was tested to clarify the electrochemical stability in terms of overpotential for the $NaPF_6$-based electrolytes containing different amounts of NaDFP or FEC. The compatibility of metal electrodes with various electrolytes with and without additive could be exclusively evaluated in Na/Na symmetric cells to avoid any effect from positive/negative electrode.[19, 20] The Na/Na symmetric cells were cycled with the sequence of constant currents of 10, 50, 100, 500, and 1000 μA cm^{-2} for 10 cycles. Figure 6-3 shows the resulting voltage profiles of the Na/Na symmetric cells. Each cycle consists of 8-min deposition (or dissolution) and 2-min rest between each step. Polarization of the additive-free $NaPF_6$ electrolyte is 3.83 mV (average potential value of 10 cycles) at 10 μA cm^{-2} and increases with increasing the current density, resulting in 210.6 mV at 1000 μA cm^{-2} (Figure 6-3 (a)). The polarization progressively decreases and stabilized with increasing the amount of NaDFP additive from 0.5 wt% (174.7 mV at 1000 μA cm^{-2}) to 1 wt% (122.4 mV at 1000 μA cm^{-2}) (Figure 6-3 (b) and (c)). Considering the similar ionic conductivities and thus bulk resistances of the electrolytes with and without additives (Figure 6-4), the major reason for the low polarization with KDFP additive is related to the low interfacial resistance, including ion migration in SEI films and charge transfer.[20, 21] For comparison, the results in the case of 0.5 and 3 wt% FEC addition were shown in Figure 6-4 (d) and (e). The polarization of the Na/Na symmetric cells becomes even larger by adding FEC compared with the neat electrolyte, suggesting the high interfacial resistances in the FEC-containing systems.

The performance of the $NaPF_6$-EC/DMC electrolyte with and without additive was further studied in terms of the performance of the HC negative electrode. Figure 6-5 shows the first and second charge-discharge curves of Na/HC cells and the corresponding dQ/dV plot in the selected electrolyte at a current density of 25 mA g^{-1}. Table 6-1 lists the first cycle Coulombic efficiencies of the HC electrodes. For the additive-free electrolyte, the initial charge provides a capacity of 342 mAh g^{-1}, including the irreversible capacity to form the SEI film. Two SEI formation peaks at 1.00 and 0.52 V are observed in the neat electrolyte in the corresponding dQ/dV plot, which disappeared in the second charge cycle. The following discharge curve consist of the plateau below 0.1 V and a slope region from 0.1 to 1.2 V, which are assigned to Na^+ insertion/extraction in nanopores and between graphene layers in hard carbon, respectively, according to the previous work.[22] The first discharge capacity of 260 mAh g^{-1} is attained with a resultant initial Coulombic efficiency of 75.8 %. Figure 6-6 shows the comparison of the dQ/dV plot. Addition of NaDFP leads to the shift of the SEI formation peak around 1.0 V to the lower potential but not for the one at 0.5 V

(Figure 6-6 (a)). Addition of 0.5 wt% FEC resulted in the appearance of a small peak at 1.2 V and shift of the peak at 0.5 to 0.7 V. Further addition of FEC (3 wt%) causes significant shifts of both the peaks by more than 0.2 V. The addition of FEC induces a slight increase of the difference in the overpotentials between charge and discharge (see insets in Figure 6-5 (d) and (e)), which is consistent with the previous report on HC [8]. Such a large overpotential is not observed in the cases of NaDFP, suggesting the SEI formed with FEC has a lower conductivity than those formed in an additive-free or NaDFP-containing electrolyte, which is in accordance with the high resistance value observed in FEC-containing electrolyte in the previous report.[10] Most of the previous works on FEC in SIBs show an inferior rate performance and the cycle test was conducted at a relatively low rate, such as C/10.[1, 7, 8, 23].

Rate performance of the Na/HC half-cell was further evaluated in the voltage range of 0.005–1.5 V by varying current densities in the sequence of 25, 50, 100, 250, 500, and 25 mA g^{-1} (three cycles for each current density). Figure 6-7 (a) and (b) show the resulting rate capability, where 260 mA g^{-1} corresponds to the rate of 1C for the present HC electrode as shown in Table 6-1. The rate capability significantly improves with the addition of NaDFP, achieving 165 and 178 mAh g^{-1} with 0.5 wt% and 1 wt% NaDFP, respectively, at 250 mA g^{-1} in contrast to the capacity of 93 mAh g^{-1} in the neat electrolyte. The FEC-containing electrolyte exhibits a considerable difference for the high-rate performance compared with the NaDFP-containing electrolytes. Only the capacities of 75 and 70 mAh g^{-1} are retained in the electrolytes with 0.5 and 3 wt% FEC, respectively, at a current density of 250 mA g^{-1}.[8]

Figure 6-8 shows the cycling performance of the Na/HC cell in $NaPF_6$ electrolyte with and without NaDFP or FEC additive. Without any additive, the discharge capacity in the neat electrolyte constantly deteriorates from the early cycles with the capacity retentions of 49.5% at the 250th cycle. In the presence of NaDFP additive, a stable cycle performance with capacity retentions of 72.8 and 76.6% is achieved after 250 cycles in the electrolytes containing 0.5 and 1 wt% NaDFP, respectively, providing 99.9% average Coulombic efficiency. In contrast, much lower capacity retention is obtained for 1 M $NaPF_6$ electrolyte containing FEC than those with NaDFP and the discharge capacities fluctuate during cycling. Cycle performance could be stabilized and maintained around 100 mAh g^{-1} after a few cycles with the aid of FEC, but there is not much improvement compared to the neat case.

The EIS test of the HC/HC symmetric cells in $NaPF_6$ electrolyte with and without NaDFP or FEC additive are conducted with HC electrodes after 1, 3, 10, and 20 cycles at 100 mA g^{-1}. As shown in Figure 6-9 (a-g), the Nyquist plots of the HC/HC symmetric cells consist of two semicircles in all the cases and an oblique line corresponding to a diffusion process. Figure 6-9 (h) displays a schematic drawing of the Nyquist plot for a symmetric cell; the semicircle in the high-frequency range is assigned to either the resistance of the SEI layer or the surface layer formed during cycles, which is named as R_h.[21, 24-27] The semicircle in the low-frequency range is ascribed to the charge transfer resistance, R_{ct}. Since the R_{ct} changes upon the SOC of each electrode,[28, 29] each electrode in the HC/HC symmetric cells is fixed in the 80% SOC after cycling. As shown in Figure 6-9 (a), both two semicircles significantly become larger with cycling in neat electrolyte, indicating the increase of R_h and R_{ct}. The presence of additives in the electrolyte significantly affects both the R_h and R_{ct}. The semicircles at high frequency in NaDFP-containing electrolytes exhibit less increase with 0.5 wt% NaDFP and almost no change with 1 wt% NaDFP after 20 cycles. (Figure 6-9 (b) and (c)), demonstrating the ability to hold low resistance of SEI and charge transfer during cycles with highly conductive SEI film formed with NaDFP. As shown in Figure 6-9 (d-g), the addition of FEC causes increases of R_h and R_{ct}, especially, the impact to R_{ct} is much more significant, reaching approximately three times larger than that of the neat electrolyte after 20 cycles in the case of 3 wt% FEC. These results demonstrate that the presence of NaDFP in the electrolyte has a strong beneficial effect on cycle performance and reducing interfacial resistance.

Ex-situ surface analysis of HC electrodes before and after cycling has been conducted by means of SEM deeper understanding of the surface films generated on the HC electrodes. The SEM images of the pristine HC electrode and HC electrodes after 3 and 20 cycles are provided in Figures 6-10 and 6-11, respectively. Figure 6-10 (a) shows a typical SEM image of the pristine HC electrodes. The hard carbon electrodes show an irregular shape with sharp edges.[30] The smooth and flat surface of HC particles becomes much rougher with the appearance of significant quantities of deposits on the surface after 3 cycles (Figure 6-10 (b)) and the quantity of the deposits is further increased after 20 cycles, covering the entire surface of the HC particle (Figure 6-11 (b)). A similar trend of morphology revulsion during cycles was reported for HC electrodes [31], and the presence of the surface deposits is consistent with the continuous formation of an SEI on the surface of HC electrode throughout the cycle. As shown in Figure 6-10 (c) and (d) and Figure 6-11 (c) and (d), the surface of the cycled electrodes with NaDFP additive has almost the same morphology with that of the uncycled electrode; smooth surface and sharp edges are preserved even after 20 cycles, indicating the excellent SEI nature formed with the aid of NaDFP. After 3 and 20 cycles in FEC-containing electrolyte, as shown in Figure 6-10 (e) and (f) and Figure 6-11 (e) and (f), a certain amount of surface deposits on HC along with cycles appear to be the features, distinguished from KDFP, which would cause the unstable cycle performance with low capacity retention.

6.4 Conclusions

In this chapter, the effects of the NaDFP additive on electrode performance were described, targeting its use in SIBs. With the addition of NaDFP, extension of electrochemical window was observed compared with the additive-free electrolyte. The gradual improvement of the Na metal deposition/dissolution efficiency with increasing concentrations of NaDFP additives confirmed the favorable effect of additives on SEI formation on Na metal surface, which was also reflected to the suppressed overpotentials during Na metal deposition/dissolution by the addition of NaDFP. Considering the similar ionic conductivities of the electrolytes with and without additives, the major reason for the lower overpotential with NaDFP was considered to be the lower interfacial resistance. The optimal electrochemical performance of the HC/Na cell was observed with the electrolyte containing 1 wt% NaDFP, achieving high rate capability and long cycle life. The EIS results of HC/HC symmetric cells during cycles confirmed the effect of NaDFP on reducing interfacial resistance. The SEM results confirmed that NaDFP- and FEC-containing electrolytes could form stable SEI film and prevent further decomposition of electrolyte compared with additive-free electrolyte.

Table 6-1. Charge-discharge capacities and Coulombic efficiencies of the Na/HC cells with 1 M $NaPF_6$-EC/DMC (1:1, v:v) electrolytes containing different amounts of NaDFP or FEC. The charge-discharge current density is 25 mA g^{-1}.

Additive	Charge capacity / mAh g^{-1}	Discharge capacity / mAh g^{-1}	Coulombic efficiency / %
neat electrolyte	342	260	75.8
0.5 wt% NaDFP	342	260	75.7
1 wt% NaDFP	342	260	76.1
0.5 wt% FEC	343	258	75.1
3 wt% FEC	344	256	74.6

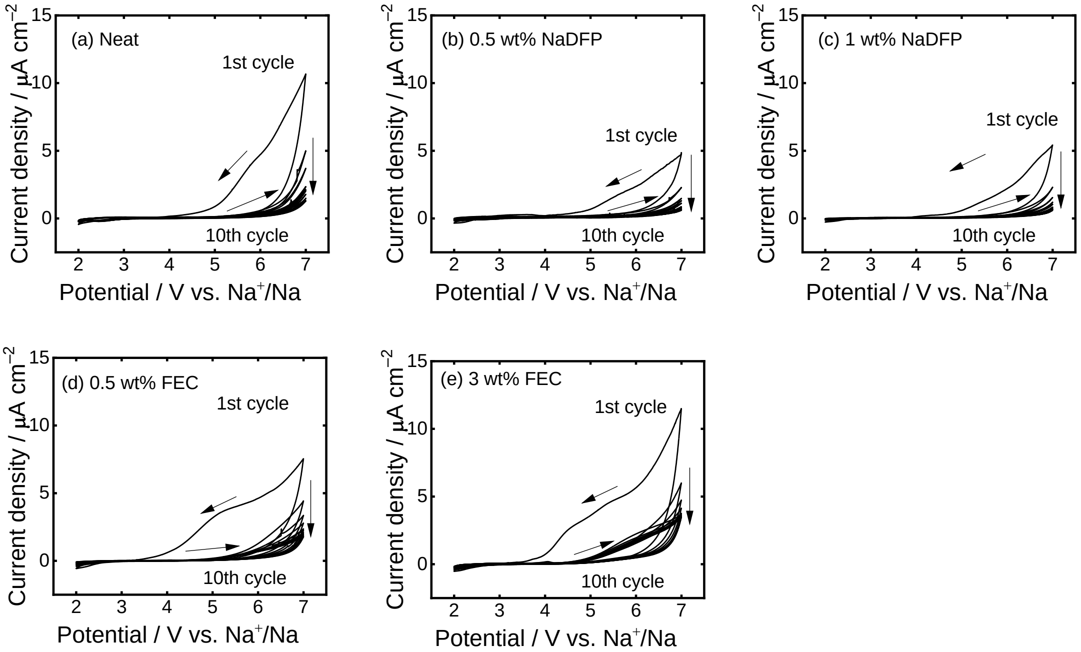

Figure 6-1. Cyclic voltammograms of an Al electrode at a scan rate of 5 mV s^{-1}. Electrolytes: 1 M $NaPF_6$-EC/DMC (1:1, v:v) with (a) 0 wt% additive (neat), (b) 0.5 wt% NaDFP, (c) 1 wt% NaDFP, (d) 0.5 wt% FEC, and (e) 3 wt% FEC.

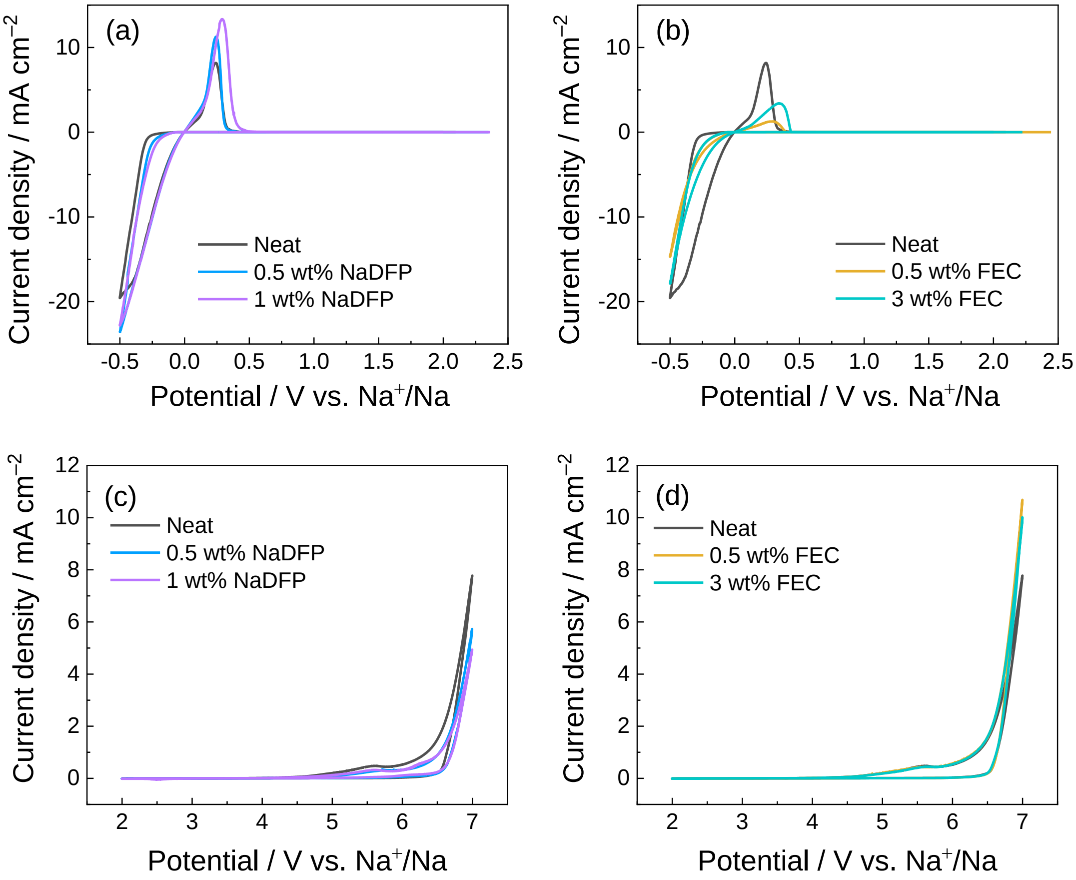

Figure 6-2. Cyclic voltammograms of (a, b) Al (positive potential region) and (c, d) Pt negative potential region) electrodes at a scan rate of 5 mV s^{-1}. Electrolytes: (a, c)1 M $NaPF_6$-EC/DMC (1:1, v:v) with 0 wt% additive (neat), 0.5 wt% NaDFP, and 1 wt% NaDFP, (b, d) 1 M $NaPF_6$-EC/DMC (1:1, v:v) with 0 wt% additive, 0.5 wt% FEC, and 3 wt% FEC.

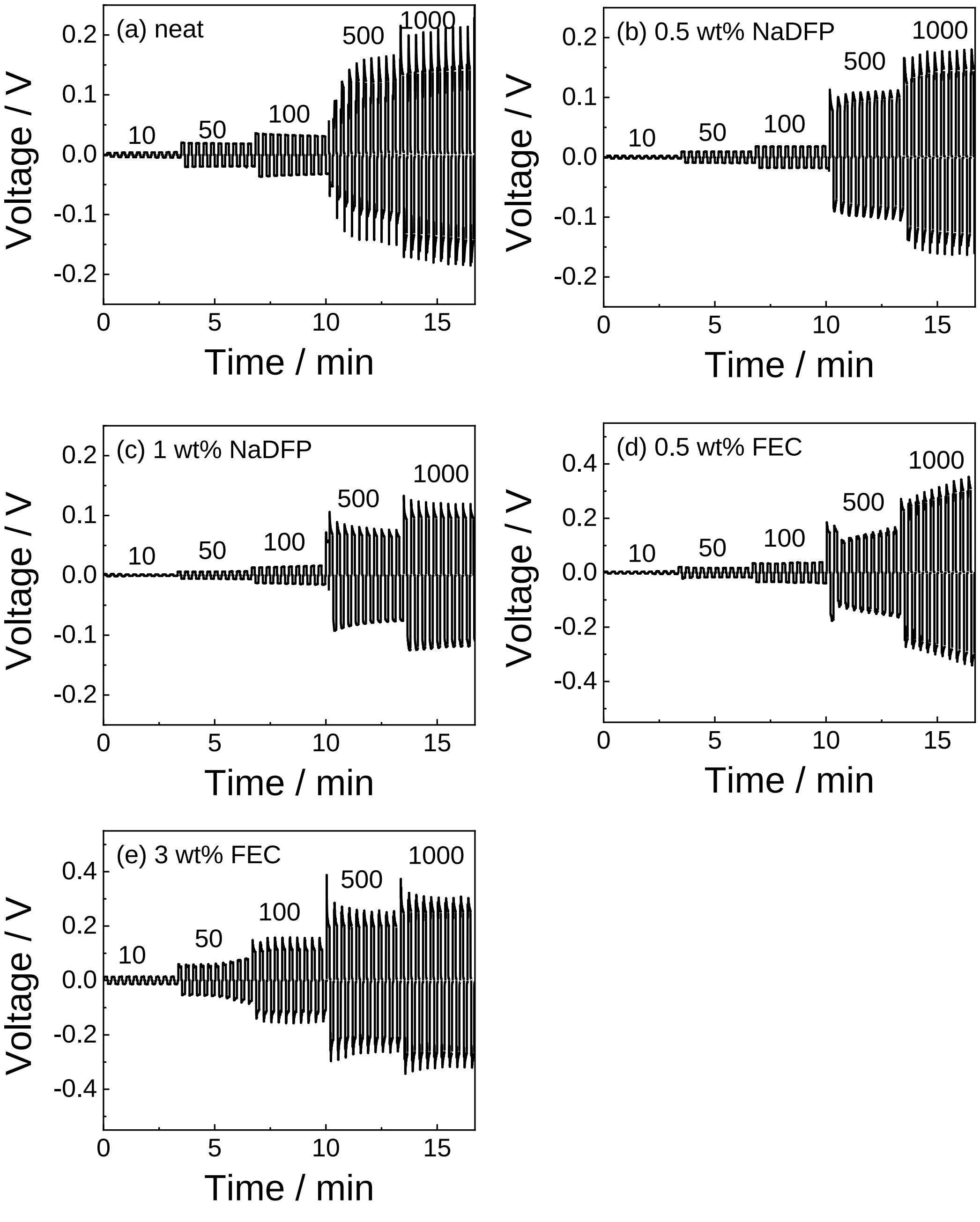

Figure 6-3. Voltage profiles of the Na/Na symmetrical cells during galvanostatic Na metal deposition/dissolution in 1 M $NaPF_6$-EC/DMC (1:1, v:v) with (a) 0 wt% additive (neat), (b) 0.5 wt% NaDFP, (c) 1 wt% NaDFP, (d) 0.5 wt% FEC, and (e) 3 wt% FEC. Current densities are shown in μA cm^{-2}.

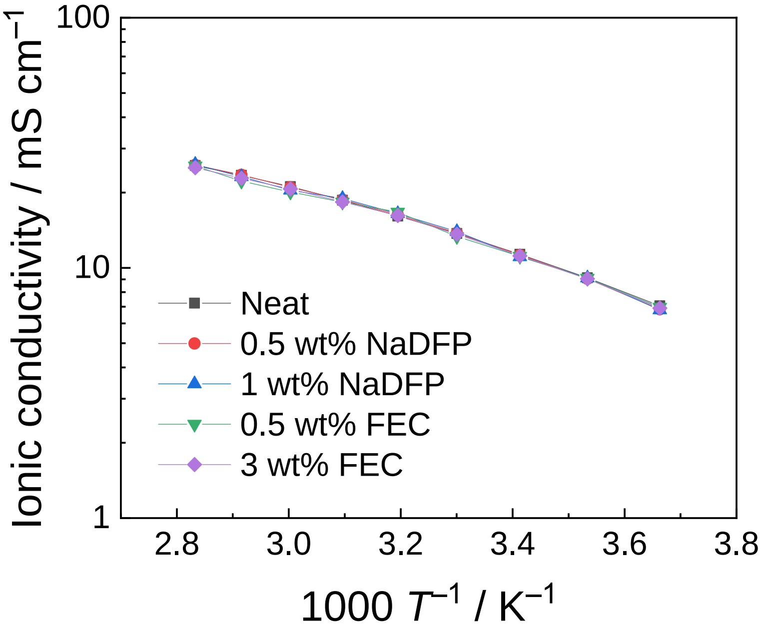

Figure 6-4. Arrhenius plots of ionic conductivities for 1 M $NaPF_6$-EC/DMC (1:1, v:v) without and with NaDFP or FEC additives in the temperature range between 298 and 363 K.

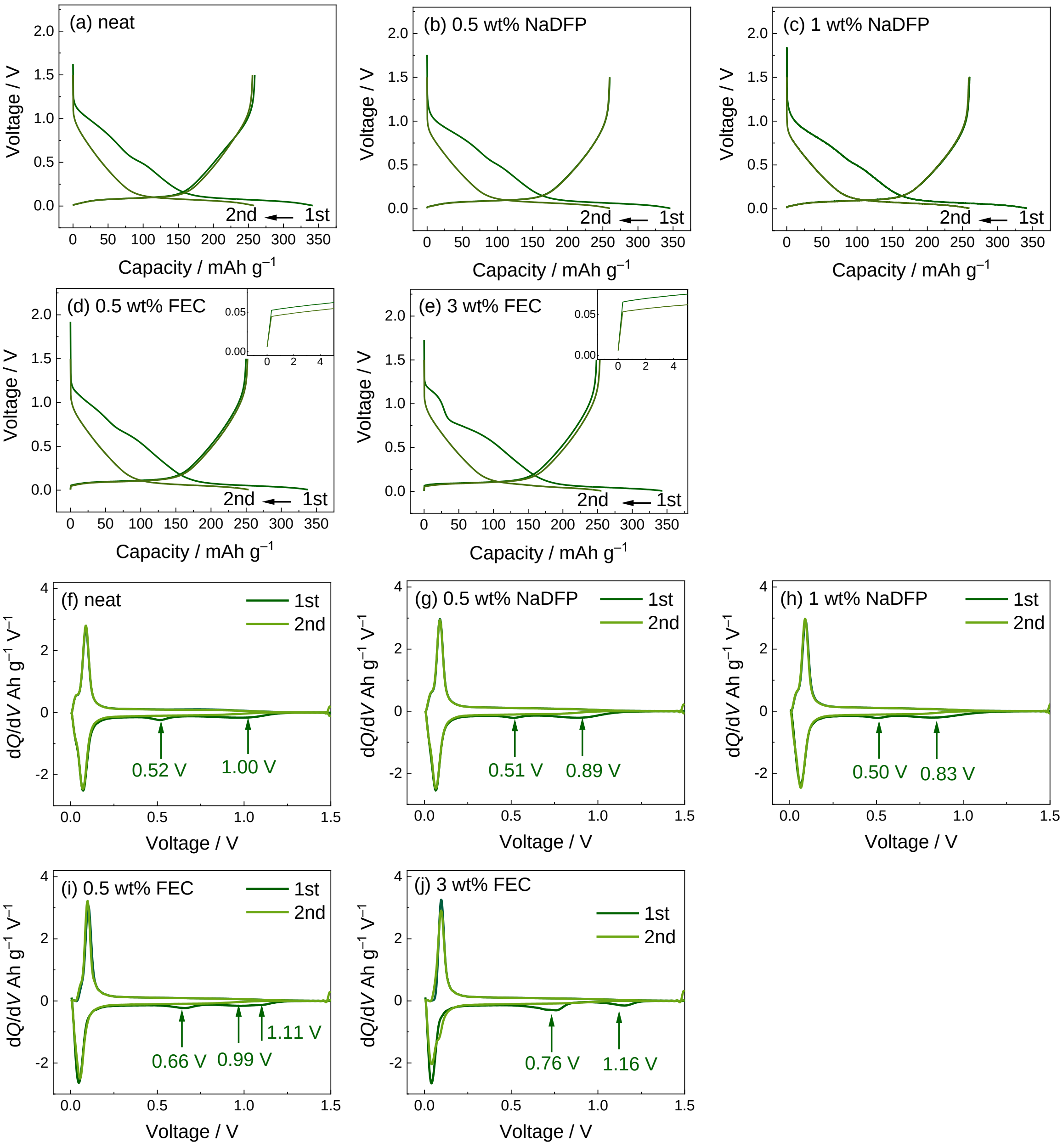

Figure 6-5. Charge-discharge curves and the corresponding dQ/dV plots of the Na/HC cells in 1 M $NaPF_6$-EC/DMC (1:1, v:v) with (a, f) 0 wt% additive (neat), (b, g) 0.5 wt% NaDFP, (c,h) 1 wt% NaDFP, (d, i) 0.5 wt% FEC, and (e, j) 3 wt% FEC. Current density: 25 mA g^{-1}. Cut-off voltage: 0.005–1.5 V.

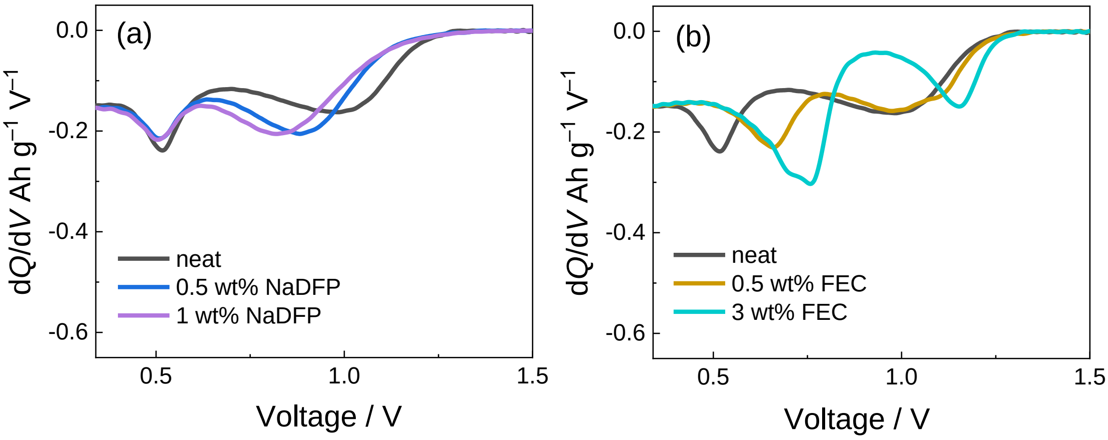

Figure 6-6. The d*Q*/d*V* plots of the first charge curve in (a)1 M $NaPF_6$-EC/DMC (1:1, v:v) with 0 wt% additive (neat), 0.5 wt% NaDFP, and 1 wt% NaDFP, (b) 1 M $NaPF_6$-EC/DMC (1:1, v:v) with 0 wt% additive (neat), 0.5 wt% FEC, and 3 wt% FEC.

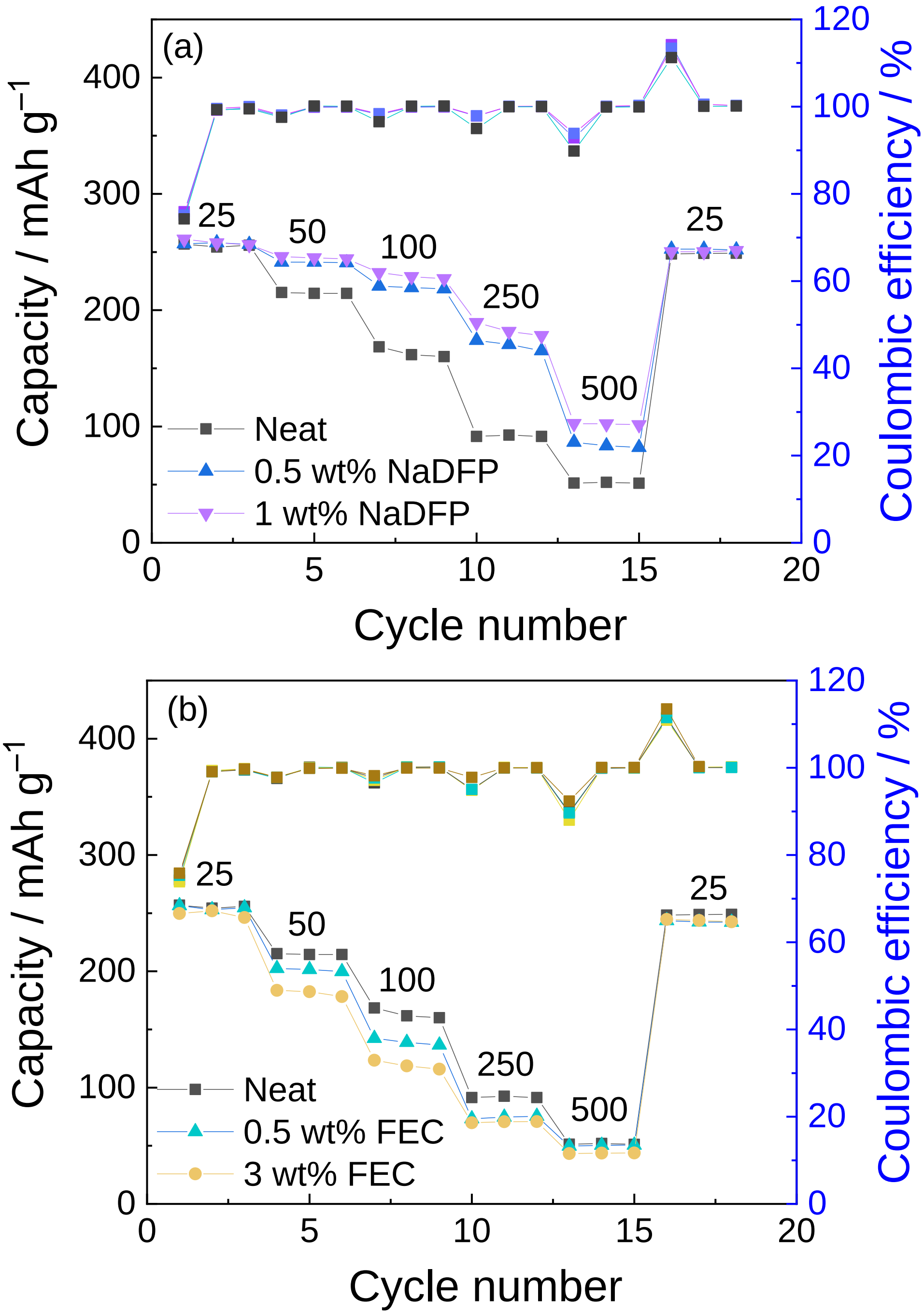

Figure 6-7. Rate capability of the Na/HC cells using 1 M $NaPF_6$-EC/DMC with and without NaDFP or FEC additives. Current density: 20−500 mA g^{-1}. Cut-off voltage: 0.005−1.5 V. Electrolytes: (a)1 M $NaPF_6$-EC/DMC (1:1, v:v) with 0 wt% additive (neat), 0.5 wt% NaDFP, and 1 wt% NaDFP and (b) 1 M $NaPF_6$-EC/DMC (1:1, v:v) with 0 wt% additive (neat), 0.5 wt% FEC, and 3 wt% FEC. Current densities are shown in mA g^{-1}.

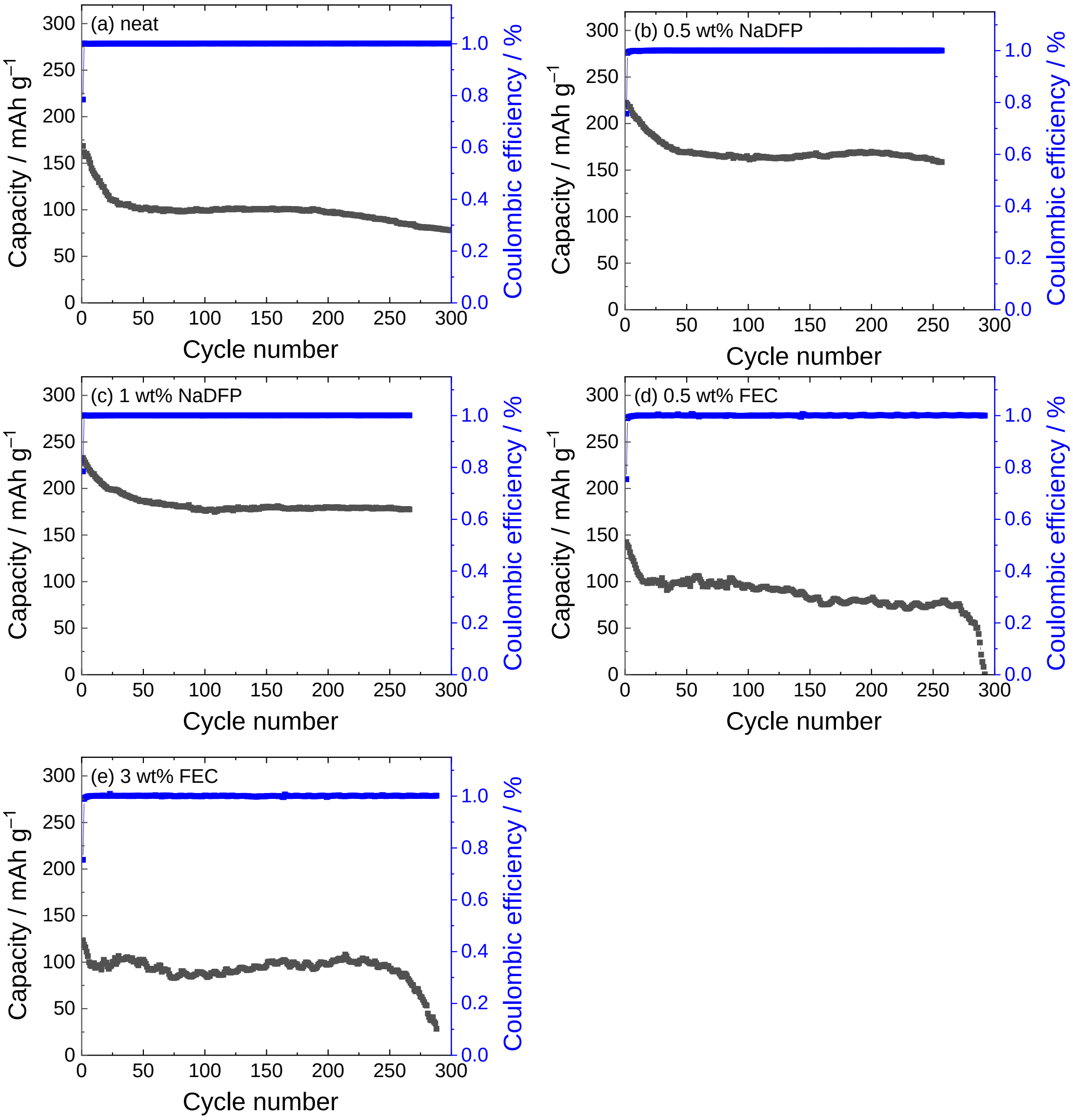

Figure 6-8. Cycle performance of the Na/HC cells with 1 M NaPF$_6$-EC/DMC with and without NaDFP or FEC additives. Current density: 100 mA g^{-1}. Cut-off voltage: 0.005−1.5 V. Electrolytes: 1 M NaPF$_6$-EC/DMC (1:1, v:v) with (a) 0 wt% additive (neat), (b) 0.5 wt% NaDFP, (c) 1 wt% NaDFP, (d) 0.5 wt% FEC, and (e) 3 wt% FEC.

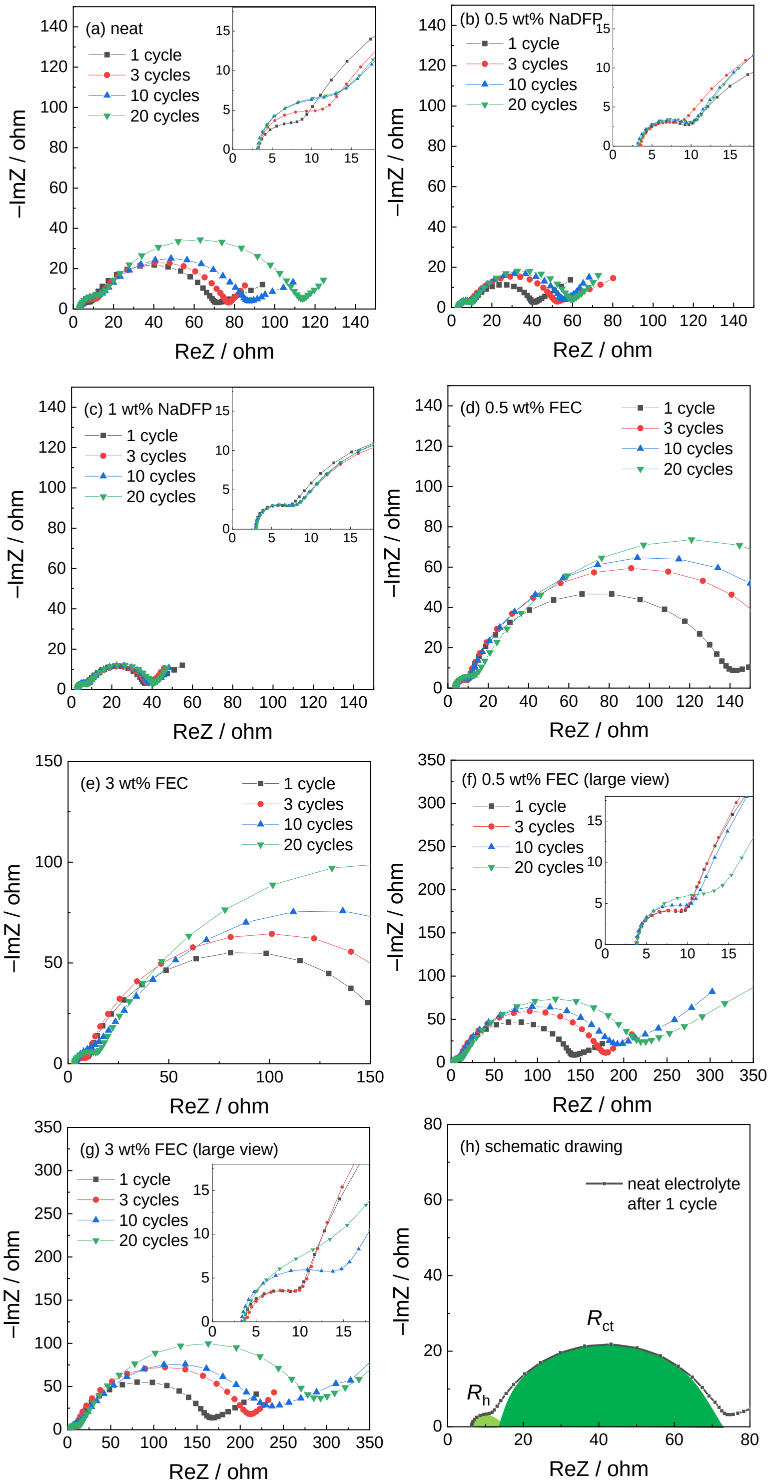

Figure 6-9. Nyquist plots of the HC/HC symmetric cells in 1 M $NaPF_6$-EC/DMC with different weight ratios of NaDFP or FEC additive at 298 K. Electrolytes: 1 M $NaPF_6$-EC/DMC (1:1, v:v) with (a) 0 wt% additive (neat), (b) 0.5 wt% NaDFP, (c) 1 wt% NaDFP, (d) 0.5 wt% FEC, and (e) 3 wt% FEC. (f) and (g) the wide-range views of (d) and (e), respectively. (h) the schematic drawing of the Nyquist plot for a HC/HC symmetric cell to show the relation between R_h and R_{ct}. Frequency range of 100 kHz−10 mHz. AC amplitude: 10 mV.

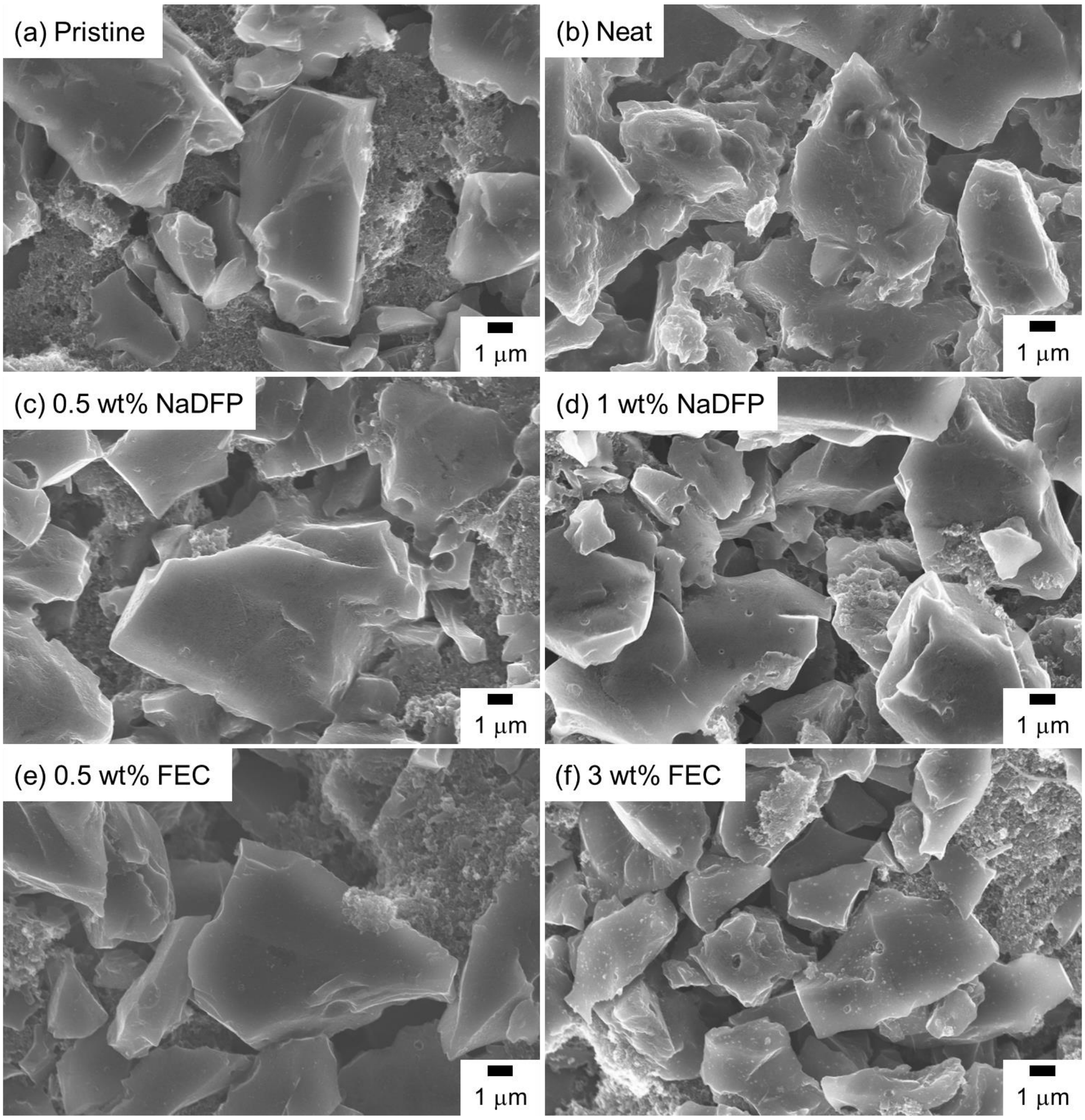

Figure 6-10. SEM images of the particle surface for (a) the pristine HC electrode and the HC electrode after 3 cycles at 298 K in (b) 0 wt% additive (neat), (c) 0.5 wt% NaDFP, (d) 1 wt% NaDFP, (e) 0.5 wt% FEC, and (f) 3 wt% FEC. Current density for cycle: 25 mA g^{-1}. Cut-off voltage for cycle: 0.005–1.5 V.

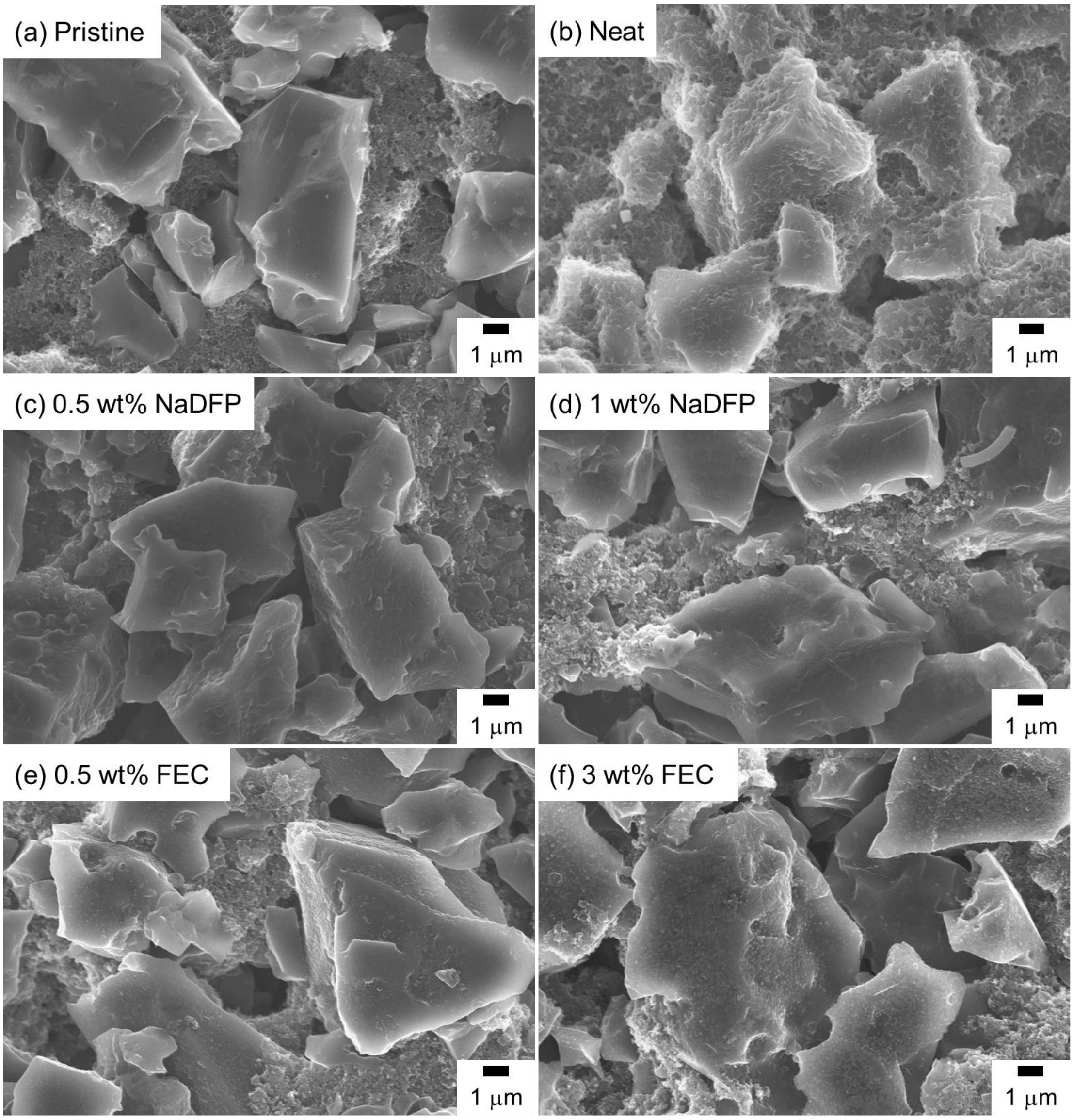

Figure 6-11. SEM images of the particle surface for (a) the pristine HC electrode and the HC electrode after 20 cycles at 298 K in (b) 0 wt% additive (neat), (c) 0.5 wt% NaDFP, (d) 1 wt% NaDFP, (e) 0.5 wt% FEC, and (f) 3 wt% FEC. Current density for cycle: 25 mA g^{-1}. Cut-off voltage for cycle: 0.005−1.5 V.

References

[1] J. Fondard, E. Irisarri, C. Courrèges, M. R. Palacín, A. Ponrouch, R. Dedryvère, J. Electrochem. Soc., 167 (2020) 070526.

[2] S. Mai, M. Xu, X. Liao, J. Hu, H. Lin, L. Xing, Y. Liao, X. Li, W. Li, Electrochim. Acta, 147 (2014) 565-571.

[3] J. Self, D. S. Hall, L. Madec, J. Dahn, J. Power Sources, 298 (2015) 369-378.

[4] X. Zuo, M. Zhao, X. Ma, X. Xiao, J. Liu, J. Nan, Electrochim. Acta, 245 (2017) 705-714.

[5] H. Zhang, W. Feng, J. Nie, Z. Zhou, J. Fluorine Chem., 174 (2015) 49-61.

[6] N. Yabuuchi, K. Kubota, M. Dahbi, S. Komaba, Chem. Rev., 114 (2014) 11636-11682.

[7] S. Komaba, T. Ishikawa, N. Yabuuchi, W. Murata, A. Ito, Y. Ohsawa, ACS Appl. Mater. Interfaces, 3 (2011) 4165-4168.

[8] A. Ponrouch, A. Goñi, M. R. Palacín, Electrochem. Commun., 27 (2013) 85-88.

[9] S. A. Webb, C. A. Bridges, G. M. Veith, J. Power Sources, 248 (2014) 1105-1117.

[10] H. Lu, L. Wu, L. Xiao, X. Ai, H. Yang, Y. Cao, Electrochim. Acta, 190 (2016) 402-408.

[11] B. Zhang, R. Dugas, G. Rousse, P. Rozier, A. M. Abakumov, J.-M. Tarascon, Nat. Commun., 7 (2016) 1-9.

[12] Y.-M. Song, C.-K. Kim, K.-E. Kim, S. Y. Hong, N.-S. Choi, J. Power Sources, 302 (2016) 22-30.

[13] B. Yang, H. Zhang, L. Yu, W. Fan, D. Huang, Electrochim. Acta, 221 (2016) 107-

114.

[14] G. Yang, J. Shi, C. Shen, S. Wang, L. Xia, H. Hu, H. Luo, Y. Xia, Z. Liu, RSC Adv., 7 (2017) 26052-26059.

[15] K.-E. Kim, J. Y. Jang, I. Park, M.-H. Woo, M.-H. Jeong, W. C. Shin, M. Ue, N.-S. Choi, Electrochem. Commun., 61 (2015) 121-124.

[16] K. Matsumoto, R. Hagiwara, Inorg. Chem., 48 (2009) 7350-7358.

[17] H. Yang, J. Hwang, Y. Wang, K. Matsumoto, R. Hagiwara, J. Phys. Chem. C, 123 (2019) 22018-22026.

[18] C. Wang, L. Yu, W. Fan, J. Liu, L. Ouyang, L. Yang, M. Zhu, ACS Appl. Energy Mater., 1 (2018) 2647-2656.

[19] D. Iermakova, R. Dugas, M. Palacín, A. Ponrouch, J. Electrochem. Soc., 162 (2015) A7060-A7066.

[20] M. Forsyth, H. Yoon, F. Chen, H. Zhu, D. R. MacFarlane, M. Armand, P. C. Howlett, J. Phys. Chem. C, 120 (2016) 4276-4286.

[21] J. Hwang, K. Matsumoto, R. Hagiwara, J. Phys. Chem. C, 122 (2018) 26857−26864.

[22] S. Komaba, W. Murata, T. Ishikawa, N. Yabuuchi, T. Ozeki, T. Nakayama, A. Ogata, K. Gotoh, K. Fujiwara, Adv. Funct. Mater., 21 (2011) 3859-3867.

[23] M. Dahbi, T. Nakano, N. Yabuuchi, T. Ishikawa, K. Kubota, M. Fukunishi, S. Shibahara, J.-Y. Son, Y.-T. Cui, H. Oji, Electrochem. Commun., 44 (2014) 66-69.

[24] D. Andre, M. Meiler, K. Steiner, C. Wimmer, T. Soczka-Guth, D. Sauer, J. Power Sources, 196 (2011) 5334-5341.

[25] F. Wohde, M. Balabajew, B. Roling, J. Electrochem. Soc., 163 (2016) A714.

[26] R. Alcantara, M. Jaraba, P. Lavela, J. Tirado, J. Electroanal. Chem., 566 (2004) 187-192.

[27] F. Croce, F. Nobili, A. Deptula, W. Lada, R. Tossici, A. D’epifanio, B. Scrosati, R. Marassi, Electrochem. Commun., 1 (1999) 605-608.

[28] C. Fleischer, W. Waag, H.-M. Heyn, D. U. Sauer, J. Power Sources, 260 (2014) 276-291.

[29] J. Gomez, R. Nelson, E. E. Kalu, M. H. Weatherspoon, J. P. Zheng, J. Power Sources, 196 (2011) 4826-4831.

[30] W. Cao, J. Zheng, D. Adams, T. Doung, J. P. Zheng, J. Electrochem. Soc., 161 (2014) A2087.

[31] Y. Pan, Y. Zhang, B. S. Parimalam, C. C. Nguyen, G. Wang, B. L. Lucht, J. Electroanal. Chem., 799 (2017) 181-186.

Chapter 7

Crystal Structure and Thermal Stability of Sodium Difluorophosphate

7.1 Introduction

The diverse structures of phosphates have been widely studied in various fields.[1-8] Among the variety of phosphates investigated in recent years, the fluorophosphates have drawn a lot of attention from researchers in inorganic chemistry.[9] Compared to orthophosphates, considering the fluorine atoms are covalently bound to the phosphorus atoms, fluorophosphates show additional compositional and structural diversity. For this reason, fluorophosphates [PO_xF_{4-x}] ($1 < x < 4$) species are reported to realize excellent optical properties.[10-12] In particular, difluorophosphates have been investigated in view of application as an electrolyte component in Li secondary batteries[13-15] and Na and K secondary batteries (Chapters 5 and 6), and thus difluorophosphates are promising systems searching for new functional materials. However, the crystal structure determination of difluorophosphates is a difficult subject because of the rigorous growth conditions required and relatively poor thermal stability and their low solubilities in aqueous and non-aqueous solvents. Many efforts have been made in the past to the preparation and structural characterization of these compounds. So far, several structures of difluorophosphates determined by single crystal diffraction analyses have been reported, including KPO_2F_2 (KDFP), [16] $RbPO_2F_2$ (RbDFP), [17] $CsPO_2F_2$ (CsDFP), [18] $NH_4PO_2F_2$ (NH_4DFP), [19] $AgPO_2F_2$ (AgDFP),

[20] and $LiPO_2F_2$ (LiDFP) [21]. However, there is still no data on the single crystal structure of sodium difluorophosphate ($Na[PO_2F_2]$, NaDFP). In this chapter, crystal structure of NaDFP, which has been determined for the first time, is discussed.

7.2 Experimental

KPO_3 and KPF_6 (Aldrich, purity > 99%) were dried under vacuum for 24 h at 80 °C before use. KDFP was synthesized by the reaction of KPO_3 and KPF_6 in the molar ratio of 2:1 by heating the starting material at 593 K in a platinum crucible over three days, as described in Chapter 5.[22] NaDFP was synthesized from $NaPF_6$ (Materials Electronic Chemicals Co., Ltd., purity >99%) and as-prepared KDFP by a metathesis reaction in a molar ratio of KDFP:$NaPF_6$ = 1:1.2. The starting materials, $NaPF_6$, and as-prepared KDFP were dissolved in dehydrated tetrahydrofuran (THF; Wako, water content < 10 ppm, oxygen content < 1 ppm) (~200 cm^3 in a conical flask) by stirring at room temperature for 48 h with a sealed cap in the dry chamber. The solid precipitate was isolated by centrifuging the mixture. The acquired precipitate was washed with THF (~200 cm^3 in a conical flask) by stirring for 24h twice in the dry chamber. The final product was dried under vacuum for 24 h at 353 K prior to use. Absence of the excess $NaPF_6$ in the product was checked by XRD. Single crystal samples of NaDFP with a cubic shape were grown by slowly cooling NaDFP-saturated $[C_2C_1im][FSA]$ ionic liquid from 363 K to room temperature.

Single-crystal X-ray diffraction measurements were performed using an R-axis Rapid II diffractometer (Rigaku Corporation) controlled by RAPID AUTO 2.40

software.[23] A selected crystal was put in a sealed quartz capillary under dry air atmosphere and mounted on the diffractometer under a cold dry-nitrogen flow. Data collection was performed at 113 K and consisted of 12 ω scans (130–190°, 5° per frame) at fixed φ (0°) and χ (45°) angles and 32 ω scans (0–160°, 5° per frame) at fixed φ (180°) and χ(45°) angles. The X-ray output was 50 kV–40 mA, and the exposure time was 1000 s deg^{-1}. Integration, scaling, and absorption corrections were performed using RAPID AUTO 2.40 software.[23] The structure was solved using SIR-92 [24] and refined by SHELXL-97 [25] linked to Win-GX [26]. Anisotropic displacement factors were introduced for non-hydrogen atoms, and hydrogen atoms were treated using an appropriate riding model.

7.3 Results and Discussion

X-ray crystallographic data and selected geometrical parameters are listed in Tables 7-1 and 7-2, respectively. Important contact distances and angles in the title compound are listed in Table 7-3. The NaDFP structure belongs to the *P*-1 space group. This is in contrast to KDFP, RbDFP and CsDFP which are isostructural with each other, belonging to the *Pnma* space group [16-18]. Figure 7-1 shows the molecular structure of $PO_2F_2^-$ which occupies the Wycoff site with the C_{2v} site symmetry, exhibiting the strong repulsion of two P=O double bonds. The P−F distances of 1.548(2), 1.557(2), 1.562(3), and 1.555(2) Å and the P−O distances of 1.471(3), 1.466(3), and 1.467(3) Å in NaDFP are averagely similar to those in KDFP (average P−F and P−O distances are 1.552 and 1.457 Å, respectively), RbDFP (average P−F and P−O distances are 1.562

and 1.461 Å, respectively) and CsDFP (average P−F and P−O distances are 1.56 and 1.47 Å, respectively) [16-18]. The Na1 atom is coordinated by five oxygen atoms in a square pyramidal way (Na···O distances of 2.316(3)−2.400(3) Å), but an additional fluorine atom has a secondary contact from the open phase of the square pyramid with the Na···F distance of 2.847(3) (Figure 7-2(a)). The coordination environment of Na2 is a distorted octahedron with four oxygen atoms (2.303(3)−2.364(3) Å) and two fluorine atoms (2.370(3) and 2.375(3) Å) being analogous to those in KDFP, RbDFP, and CsDFP (Figure 7-2(b)) [17, 18].

The consistency of the as-prepared NaDFP powder checked by X-ray powder diffraction was confirmed with the simulated result from the single-crystal analysis, as shown in Figure 7-3. The vibrational modes of DFP^- in NaDFP was analyzed by IR spectroscopy. Figure 7-4 shows the IR spectrum of NaDFP. Several strong absorption bands between 1400 and 800 cm^{-1} of the as-synthesized NaDFP are assigned to the stretching modes of DFP^-, which agrees with the calculated data of KDFP.[22] The bands observed at 1305 and 1145 cm^{-1} are assigned to the asymmetric and symmetric stretching bands of P–O2, respectively. The bands at 888 and 835 cm^{-1} are assigned to the asymmetric and symmetric stretching of P–F2, respectively. The strong absorption band in the lower frequency region (498 cm^{-1}) are based on the complicated combination modes, including scissoring, rocking, and wagging modes.

Thermal stability of the as-synthesized NaDFP was examined by the thermal gravimetric (TG) and differential thermal analysis (DTA). As shown in Figure 7-5, a slow weight loss process is observed in the TG curve from room temperature to 453 K, which is caused by the hygroscopic nature of the metal difluorophosphates. When the temperature exceeds 453 K, the weight loss is distinct and reaches 5 wt% loss at 515 K. The following TG curve shows the two-step weight loss behavior between 453–790 K, corresponding to two endothermic peaks around 507 and 584 K, resulting in a total weight loss of ca. 46%, which is attributed to the decomposition of NaDFP. These observations suggest the following two alternative decomposition reactions (Eq. (7-1, 7-2)):

$$\mathrm{NaDFP} \rightarrow \mathrm{NaPO_3F} + \mathrm{POF_3}\uparrow \text{ (theoretical weight loss = 46.2 wt.\%)} \quad (7\text{-}1)$$

$$2\mathrm{NaDFP} \rightarrow \mathrm{Na_2P_2O_7} + \mathrm{PF_5}\uparrow + \mathrm{POF_3}\uparrow \text{ (theoretical weight loss = 51.1 wt.\%)} \quad (7\text{-}2)$$

The weight loss process slows down significantly above 790 K, and an endothermic peak around 902 K is observed during this region as judged from the DTA curve, which is the typical endothermic phase transition of diphosphate [20, 27] indicate the existence of $Na_2P_2O_7$.

7.4 Conclusions

In this chapter, structure and thermal properties of NaDFP have been investigated by single-crystal XRD, IR spectroscopy, and TG-DTA analysis. The molecular structure of DFP^- in NaDFP has a C_{2v} symmetry with other difluorophosphates. Two crystallographically independent Na^+ ions coexist in the as-synthesized NaDFP. The two Na atoms have different coordination environments; Na1 is in a square pyramidal oxygen coordination with one secondary fluorine contact and Na2 is in a distorted octahedral coordination with four oxygen and two fluorine atoms. IR identified the absorption bands of DFP^- in NaDFP. The TG-DTA traces confirmed the thermal stability of the as-synthesized NaDFP.

Table 7-1. Summary of crystallographic data and refinement results for NaDFP.

	NaDFP
formula	$NaPO_2F_2$
fw	123.96
T / K	113
crystal system	triclinic
space group	$P-1$
a / Å	6.708(5)
b / Å	6.844(6)
c / Å	8.540(7)
α / °	63.937(17)
β / °	78.750(13)
γ / °	83.826(17)
V / Å^3	343.3(5)
Z	4
ρ_{calc} / g cm^{-3}	2.385
μ / mm^{-1}	0.804
R_1 [a]	0.0369
wR_2 [b]	0.1062
cryst size / mm^3	0.30×0.10×0.10

[a] $R_1 = \Sigma||F_o| - |F_c||/\Sigma|F_o|$.

[b] $wR_2 = [\Sigma w(F_o^2 - F_c^2)^2/\Sigma w(F_o^2)^2]^{1/2}$.

Table 7-2. Selected bond lengths (Å) and angles (˚) in NaDFP.

bond length / Å		bond angles / ˚	
P1-O1	1.471(3)	O2-P1-O1	121.38(16)
P1-O2	1.466(3)	O2-P1-F1	109.86(16)
P1-F1	1.548(2)	O1-P1-F1	108.68(14)
P1-F2	1.557(2)	O2-P1-F2	109.52(13)
P2-O3	1.466(3)	O1-P1-F2	107.20(14)
P2-O4	1.467(3)	F1-P1-F2	97.54(13)
P2-F3	1.562(3)	O3-P2-O4	121.87(16)
P2-F4	1.555(2)	O3-P2-F4	108.79(14)
		O3-P2-F3	108.53(15)
		O4-P2-F4	109.27(14)
		O4-P2-F3	108.60(14)
		F4-P2-F3	96.89(13)

Table 7-3. Selected contact distances (Å) and angles (˚) in NaDFP.

bond length / Å		bond angles / ˚	
Na1···O2	2.316(3)	O2···Na1···O4	93.44(11)
Na1···O4	2.350(3)	O2···Na1···O3	103.66(10)
Na1···O3	2.392(3)	O2···Na1···O1	174.62(10)
Na1···O1	2.400(3)	O2···Na1···F4	78.47(9)
Na1···F4	2.847(3)	O4···Na1···O3	93.06(11)
Na2···O3	2.303(3)	O4···Na1···O1	86.96(10)
Na2···O4	2.304(3)	O4···Na1···F4	152.54(9)
Na2···O1	2.364(3)	O3···Na1···O1	81.67(9)
Na2···F3	2.370(3)	O4···Na1···F4	152.54(9)
Na2···F2	2.375(3)	O1···Na1···F4	98.76(9)
		O3···Na2···O4	138.94(11)
		O3···Na2···O1	84.36(9)
		O3···Na2···F3	84.28(10)
		O3···Na2···F2	103.73(9)
		O4···Na2···O1	88.93(10)
		O4···Na2···F3	88.92(11)
		O4···Na2···F2	83.90(9)
		O1···Na2···F3	104.46(10)
		O4···Na2···F2	83.90(9)
		F3···Na2···F2	82.25(9)

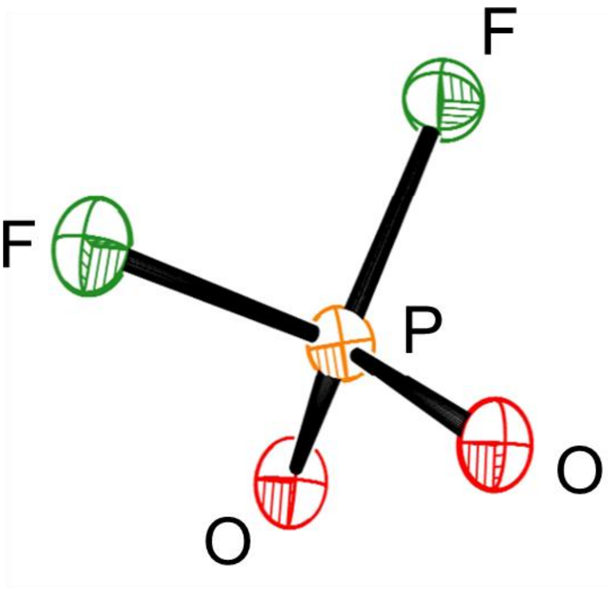

Figure 7-1. Molecular structure of DFP^- in NaDFP at 113 K. Thermal ellipsoids are shown at the 50 % probability level.

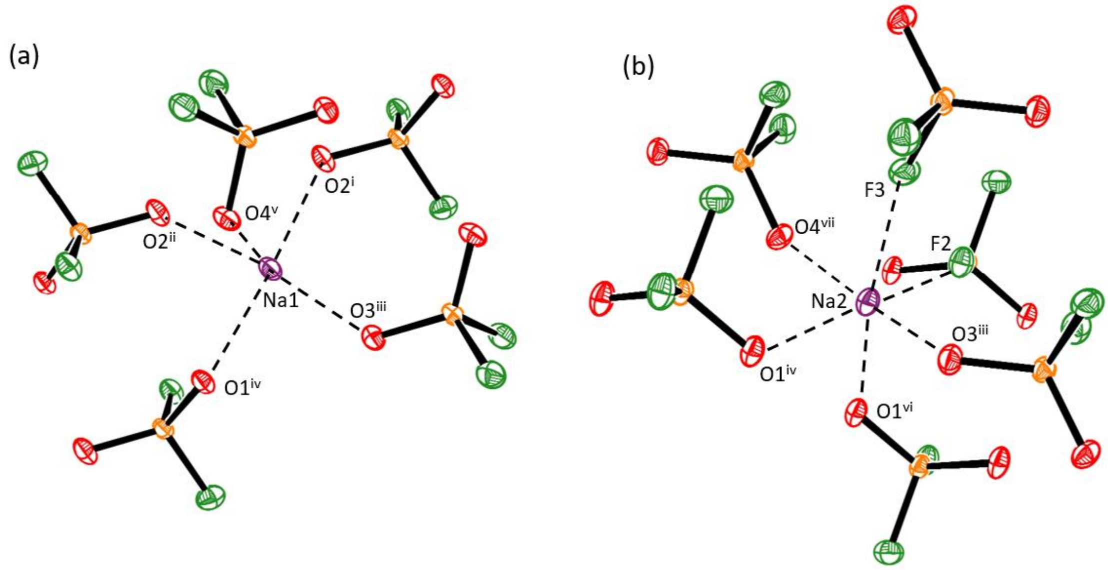

Figure 7-2. Coordination environments of (a) Na1 and (b) Na2 in NaDFP [symmetry code: (i) x+1, y−1, z; (ii) −x+2, −y, −z+2; (iii) −x+2, −y, −z+2; (iv) x+1, y, z; (v) x, y−1, z+1; (vi) −x+1, −y, −z+2; (vii) −x+2, −y+1, −z+1]. Thermal ellipsoids are shown at the 50 % probability level.

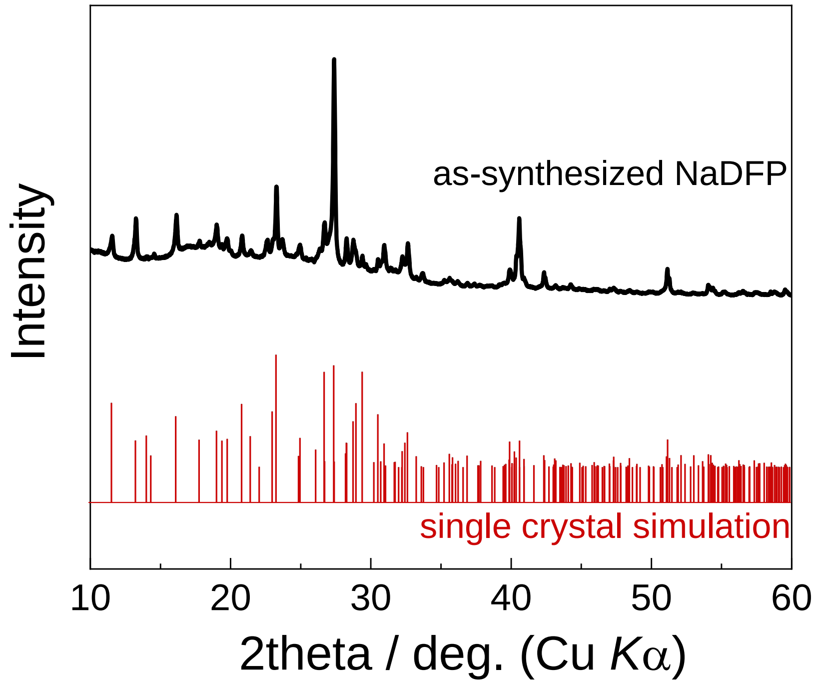

Figure 7-3. X-ray powder diffraction pattern of the as-synthesized NaDFP. The reference pattern of NaDFP created from the single-crystal X-ray diffraction data is also shown for comparison.

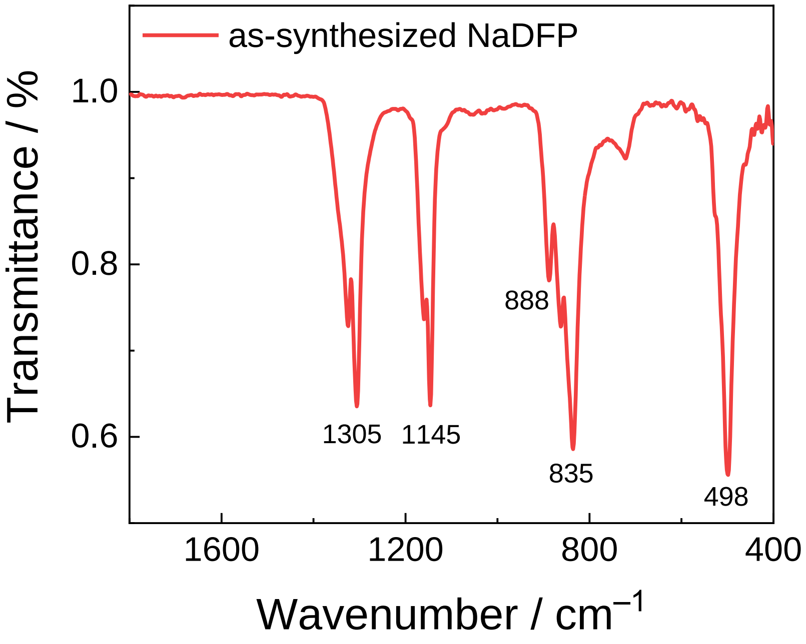

Figure 7-4. The IR spectra of the as-synthesized NaDFP. The absorption bands at 1305 and 1145 cm^{-1} are assigned to ν_{as}(PO_2) and ν_s(PO_2) modes , respectively. The absorption bands at 888 and 835 cm^{-} are assigned to ν_{as}(PF_2) and ν_s(PF_2).[1]. The vibrational modes (δ_s(PF_2) – δ_s(PO_2), ρ_r(PF_2) – ρ_w(PO_2), and ρ_w(PF_2) – ρ_r(PO_2)) are observed as one band around 498 cm^{-1}.

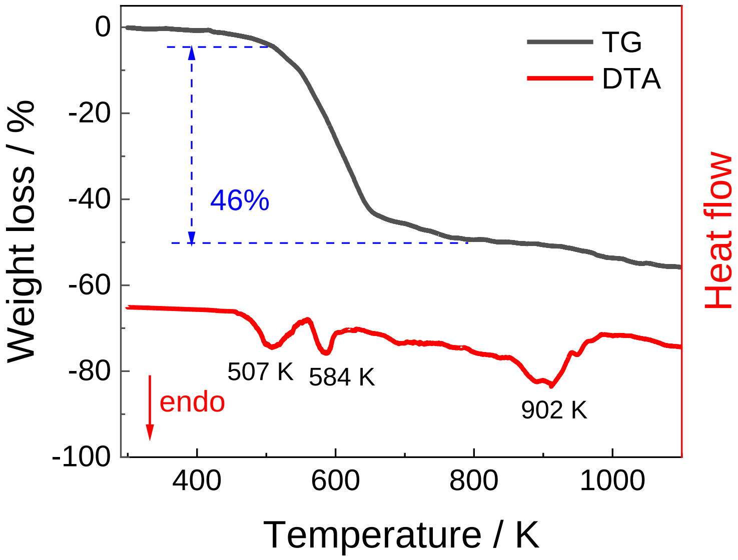

Figure 7-5. The TG-DTA curves of as-synthesized NaDFP. Scan rate: 1 K min^{-1}.

References

[1] G. Clark, A. Tai, Science, 107 (1948) 505-505.

[2] Y. Fang, J. Zhang, L. Xiao, X. Ai, Y. Cao, H. Yang, Adv. Sci., 4 (2017) 1600392.

[3] J. Qiao, L. Ning, M. S. Molokeev, Y.-C. Chuang, Q. Liu, Z. Xia, J. Am. Chem. Soc., 140 (2018) 9730-9736.

[4] Y.-X. Ma, Y.-P. Gong, C.-l. Hu, J.-G. Mao, F. Kong, J. Solid State Chem., 262 (2018) 320-326.

[5] D. Schildhammer, G. Fuhrmann, L. L. Petschnig, K. Wurst, D. Vitzthum, M. Seibald, H. Schottenberger, H. Huppertz, Inorg. Chem., 56 (2017) 2736-2741.

[6] H. Yu, W. Zhang, J. Young, J. M. Rondinelli, P. S. Halasyamani, Adv. Mater., 27 (2015) 7380-7385.

[7] A. Choudhury, S. Natarajan, C. N. R. Rao, Chem. Commun., (1999) 1305-1306.

[8] P. H. Abelson, Science, 283 (1999) 2015-2016.

[9] S. G. Jantz, L. van Wüllen, A. Fischer, E. Libowitzky, E. J. Baran, M. Weil, H. A. Höppe, Eur. J. Inorg. Chem., 2016 (2016) 1121-1128.

[10] B. Zhang, G. Shi, Z. Yang, F. Zhang, S. Pan, Angew. Chem. Int. Ed., 56 (2017) 3916-3919.

[11] G. Han, Y. Wang, B. Zhang, S. Pan, Chem. Eur. J, 24 (2018) 17638-17650.

[12] Y. Wang, B. Zhang, Z. Yang, S. Pan, Angew. Chem. Int. Ed., 57 (2018) 2150-2154.

[13] C. Wang, L. Yu, W. Fan, J. Liu, L. Ouyang, L. Yang, M. Zhu, ACS Appl. Energy Mater., 1 (2018) 2647-2656.

[14] C. Wang, L. Yu, W. Fan, R. Liu, J. Liu, L. Ouyang, L. Yang, M. Zhu, J. Alloys

Compd., 755 (2018) 1-9.

[15] K.-E. Kim, J. Y. Jang, I. Park, M.-H. Woo, M.-H. Jeong, W. C. Shin, M. Ue, N.-S. Choi, Electrochem. Commun., 61 (2015) 121-124.

[16] R. Harrison, R. Thompson, J. Trotter, J. Chem. Soc. A, (1966) 1775-1780.

[17] W. Granier, J. Durand, L. Cot, J. Galigne, Acta. Cryst. B, 31 (1975) 2506-2507.

[18] J. Trotter, S. Whitlow, J. Chem. Soc. A, (1967) 1383-1386.

[19] R. Harrison, J. Trotter, J. Chem. Soc. A, (1969) 1783-1787.

[20] P. J. Malinowski, D. Kurzydłowski, W. J. D. T. Grochala, Dalton Trans., 44 (2015) 19478-19486.

[21] G. Han, Y. Wang, H. Li, Z. Yang, S. Pan, Chem. Commun., 55 (2019) 1817-1820.

[22] K. Matsumoto, R. Hagiwara, Inorg. Chem., 48 (2009) 7350-7358.

[23] RAPID AUTO, version 2.40; Rigaku Corporation: Tokyo, Japan, 2006.

[24] A. Altomare, G. Cascarano, C. Giacovazzo, A. Guagliardi, J. Appl. Crystallogr., 26 (1993) 343-350.

[25] G. M. Sheldrick, Acta Crystallogr., Sect. A: Found. Crystallogr., 64 (2008) 112-122.

[26] L. J. Farrugia, J. Appl. Crystallogr., 32 (1999) 837-838.

[27] M. Weil, M. Puchberger, E. Füglein, E. J. Baran, J. Vannahme, H. J. Jakobsen, J. Skibsted, Inorg. Chem., 46 (2007) 801-808.

Chapter 8

General Conclusions

SIB and PIB researches currently prosper, benefitting from using know-how gained from 30 years of LIBs. The role of the electrolyte is, in large part, responsible for the life-length and the realistically possible performance in terms of practically accessible capacity, rate capability, safety, etc.. In this study, functional electrolytes were synthesized and their effects on practical SIBs and PIBs performance were investigated, including thermal, physical, structural, and electrochemical properties.

In Chapter 2, general experimental procedures were described. Further details on the experiments were mentioned in each chapter.

In Chapter 3, a hybrid inorganic-organic ionic liquid based on sodium bis(fluorosulfonyl)amide (Na[FSA]) and [*N*-ethyl-*N*-methylpyrrolidinium][FSA] ([C_2C_1pyrr][FSA]) was investigated as an electrolyte for SIBs operation over an extended temperature and a Na^+ ion fraction ranges. The phase diagram of this binary system revealed a wide liquid-phase temperature range at Na[FSA] mole fractions ranging from 0.3 to 0.7 near room temperature, where the 0.7 mole fraction equates with a molar concentration of 5.42 mol L^{-1}. The viscosity and molar ionic conductivity were consistent with the fractional Walden rule, and the temperature dependence of these physical parameters obeys the Vogel−Tammann−Fulcher equation. The optimal Na[FSA] content of the ionic liquid occurred at mole fractions between 0.3 and 0.7 based on the sodium metal deposition/dissolution behavior and the rate and cycle properties of a NASICON-type cathode, $Na_3V_2(PO_4)_3/C$ (NVPC). The highest cycle efficiency, ε_{cycle}, of Na metal deposition/dissolution was observed at x(Na[FSA]) = 0.6 (ε_{cycle} = 93.3%). Although Na/NVPC half-cell tests indicate a maximum rate and cycle performance at x(Na[FSA]) = 0.6 (83.5% retention at 100 C (11700 mA g^{-1}) and 80% retention after 4000 cycles at 2 C (234 mA g^{-1})), NVPC/NVPC symmetric cell tests indicated that the greater Na[FSA] fraction provided better rate performance and that half-cell tests with a Na metal electrode did not provide reliable data for the target electrode/electrolyte system.

In Chapter 4, thermal, physical, and electrochemical properties of the inorganic-organic hybrid ionic liquid electrolyte system, Na[FTA]-[C_3C_1pyrr][FTA], (FTA^- = (fluorosulfonyl)(trifluoromethylsulfonyl)amide and $C_3C_1pyrr^+$ = *N*-methyl-*N*-propylpyrrolidinium) were investigated in view of application to SIBs. The asymmetric FTA^- structure provided a wide liquid-phase temperature range, especially at low x(Na[FTA]) (x(Na[FTA]) = molar fraction of Na[FTA]) and low temperature range. Glass transition at 170 – 209 K was the only observed thermal behavior in the x(Na[FTA]) of 0.0–0.4. Temperature dependence of viscosity and ionic conductivity obeyed the Vogel–Tammann–Fulcher equation, and the correlation between molar conductivity and viscosity followed the fractional Walden rule. The anodic potential limits were above 5 V vs. Na^+/Na at 298 and 363 K. The high compatibility with Al substrate was confirmed at high potentials owing to FTA-derived passivation layers. The noticeable effects of x(Na[FTA]) are observed for the electrochemical performance of Na metal and hard carbon electrodes. In both the cases, a moderate concentration, x(Na[FTA]) of 0.2–0.3, enables favorable charge-discharge behavior. At 363 K, the discharge capacities of the hard carbon electrode at x(Na[FTA]) of 0.3 are 260 and 236 mAh g^{-1} at the current densities of 20 and 200 mA g^{-1}, respectively. The optimum cycling performance occurred at x(Na[FTA]) = 0.3, which provided satisfactory capacity retention (97.0% retention after 400 cycles) and high average Coulombic efficiency (>99.9%).

In Chapter 5, potassium difluorophosphate (KDFP) was demonstrated for the first time as an electrolyte additive to overcome the high polarization in PIBs by forming a stable and K-conducting solid–electrolyte interphase (SEI) on graphite electrode. With the optimal addition of 0.2 wt% KDFP, significant improvement in terms of (de)potassiation kinetics, capacity retention (76.8% after 400 cycles with KDFP vs. 27.4% after 100 cycles without KDFP) as well as average Coulombic efficiency (~99.9 % during 400 cycles) has been affirmed for a graphite electrode. Moreover, the KDFP-containing electrolyte also enables the K/K symmetric cell to be durably cycled with a smaller interfacial resistance compared to the case without KDFP. X-ray diffraction and Raman analyses confirmed the reversible formation of a phase-pure stage-1 potassium-graphite intercalation compound (KC_8) with the aid of KDFP. The enhanced electrochemical performance by the KDFP addition was discussed based on the analysis of the SEI layer on graphite and K metal electrodes by X-ray photoelectron spectroscopy.

In Chapter 6, the as-synthesized sodium difluorophosphate (NaDFP) was used as an electrolyte additive to enhance the electrochemical performance on a hard carbon electrode. A wider electrochemical window was achieved with NaDFP additive compared with a neat electrolyte. The effect of NaDFP on Na metal deposition/dissolution behavior was investigated on Na/Na symmetric cells. A reversible capacity of around 259 mAh g^{-1} was achieved for the HC electrodes in the selected electrolyte with the reversible sodium insertion. The optimum electrochemical performance of the HC/Na half-cell occurred on an electrolyte with 1 wt% NaDFP and was characterized by superior charge/discharge rate performance and excellent cycling stability over 80 cycles (78.1% capacity retention after 80 cycles). The EIS and SEM results confirmed the effect of NaDFP on forming a high ionic conductivity and stable SEI film.

In Chapter 7, the structure, geometric, and thermal properties of NaDFT were investigated by single-crystal X-ray diffraction analysis, infrared spectroscopy, and thermogravimetric analysis. In the title compound, the DFP^{-} has C_{2v} symmetry and two crystallographically independent Na^{+} ions coexist. The coordination environment of Na1 is a distorted trigonal bipyramid with five oxygen atoms, and Na2 was a distorted octahedron with four oxygen atoms and two fluorine atoms in cis position. The 5% weight loss in thermogravimetric analysis showed its decomposition at 515 K.

This study demonstrates that functional electrolytes can achieve advanced electrochemical performance in Na and K secondary batteries and from a robust SEI film to improve the operation performance. Two new ILs systems, Na[FSA]-[C_2C_1pyrr][FSA] and Na[FTA]-[C_3C_1pyrr][FTA], have been established and investigated. The acquired wide liquid phase temperature range suggests the possibility of extending the applications of secondary battery systems based on these ILs. The Na secondary batteries equipped with the aforementioned ILs showed excellent rate and cycle ability. The functional electrolytes additive, KDFP and NaDFP, for K and Na secondary batteries manifest their exclusive effect on forming a ionic conducive SEI film on electrolyte. Further, the single-crystal analysis of NaDFP has been revealed for the first time.

List of Publications

Chapter 3

Huan Yang, Jinkwang Hwang, Yushen Wang, Kazuhiko Matsumoto, Rika Hagiwara

The Journal of Physical Chemistry C, **123** (2019) 22018-22026.

"*N*-Ethyl-*N*-Methylpyrrolidinium bis(fluorosulfonyl)amide ionic liquid electrolytes for sodium secondary batteries: Effects of Na ion concentration"

Chapter 4

Huan Yang, Xu-Feng Luo, Kazuhiko Matsumoto, Jeng-Kuei Chang, Rika Hagiwara

Journal of Power Sources, **470** (2020) 228406.

"Physicochemical and electrochemical properties of the (fluorosulfonyl)(trifluoromethylsulfonyl)amide ionic liquid for Na secondary batteries"

Chapter 5

Huan Yang, Chih-Yao Chen, Jinkwang Hwang, Keigo Kubota, Kazuhiko Matsumoto, Rika Hagiwara

ACS Applied Materials & Interfaces, **12** (2020) 36168−36176.

“Potassium difluorophosphate as an electrolyte additive for potassium ion batteries”

Chapter 6

Huan Yang, Jinkwang Hwang, Yuto Tonouchi, Kazuhiko Matsumoto, Rika Hagiwara

Journal of Power Sources (to be submitted)

“Effects of sodium difluorophosphate as an electrolyte additive for sodium ion batteries”

Acknowledgment

First and foremost, I would like to express my sincere gratitude to my supervisor Prof. Rika Hagiwara for his invaluable guidance and continuous support of my Ph. D. study and related research. I would like to say sincerely thankful words to Associate Professor Kazuhiko Matsumoto for his patience and assistance in instructing me about my research work. Without his valuable advice, I could not achieve the current research results. I am greatly indebted to Assistant Professor Kouji Yasuda for his helpful comments. I own a deep sense of gratitude to my “deskmate”, Dr. Jinkwang Hwang, for his insightful suggestions and constant encouragement.

I would also like to thank all the present and former laboratory members in Energy Chemistry Laboratory. It is an unforgettable and meaningful thing for my whole life to be a member of you. In particular, I sincerely thank Mr. Shubham Kaushik, Mr. Hiroki Yamamoto, and Mr. Di Wang. Special thanks are also expressed to Ms. Naoko Sakamoto for her various help and heedful care.

Finally, I would like to thank my parents for their unreserved love and support, which are my motivation to move forward.

There are still too many thanks needed to be written here. Thank you all who are related to this study.

Huan Yang

September, 2020